ADVANCES IN PHASE CONTRAST IMAGING USING FULLY AND PARTIALLY COHERENT WAVEFIELDS

A thesis submitted for the degree of

Doctor of Philosophy

Mario Alejandro Beltran Toro

BSc (Hons)

School of Physics

Monash University

Australia.

December 2014

Copyright Notices

Notice 1

Notice 2

Contents

Abstract

X-ray phase contrast imaging enables the visualization of an object's features that otherwise would be impossible to obtain with conventional absorption based X–ray imaging. The first part of this thesis focuses specifically on propagation–based phase contrast imaging (PBI). It has a particular emphasis on the quantitative image reconstruction under the assumption that the source of illumination is fully coherent. It presents the existing methods of extracting quantitative information as well as original ones developed in this thesis. The second part of this thesis takes a purely theoretical route, which focuses on studying the forward problem of aberrated optical systems under partially coherent illumination.

This thesis begins with a general overview and review of the relevant literature including the theory of coherent X–ray wavefield diffraction, partial coherence, phase–contrast X–ray imaging, and phase–contrast tomography. Particular emphasis is given to PBI.

We then move to the original work that involved developing a method to carry out quantitative PBI based tomography on multi–material samples using only a single view per tomographic projection. The samples considered here are those for which (i) the complex refractive index of each component of the sample is known, and (ii) the component materials are spatially quantized. The method was applied to tomographic data obtained at the SPring–8 synchrotron facility in Japan. The sample used was a multi–material test phantom. The refractive index distribution of the test phantom was recovered in three dimensions with a single phase contrast image per projection. The method was applied successfully and was very stable under the presence of noise, opening the possibility of significant dose reduction incurred by samples.

The next step in this work sees the application of the aforementioned method to complex biological organs. The chosen organs were the thorax of a rabbit pup and an excised rat brain. Experimental data were also acquired at the SPring–8 synchrotron facility in Japan. Tomographic slices containing the refractive index distribution for each organ were reconstructed using a single phase contrast image per projection. Signal–to–noise ratios for each reconstructions showed significant improvements of up 200 fold compared to absorption contrast reconstructions of the same slices.

Finally, this thesis treats the problem of arbitrary aberrations in linear shift–invariant optical systems. This involves mathematically establishing a series of expressions considering arbitrary forms of phase contrast modalities as well as taking into account partially coherent illumination. Expressions are presented for the output cross spectral density under the space–frequency formulation of statistically stationary partially coherent fields. This could broaden the applicability of phase contrast to sources of lower quality.

General Declaration

In accordance with Monash University Doctorate Regulation 17 / Doctor of Philosophy and Master of Philosophy (MPhil) regulations the following declarations are made:

I hereby declare that this thesis contains no material which has been accepted for the award of any other degree or diploma at any university or equivalent institution and that, to the best of my knowledge and belief, this thesis contains no material previously published or written by another person, except where due reference is made in the text of the thesis.

This thesis includes 2 original papers published in peer reviewed journals. The core theme of the thesis is advances in phase contrast imaging using fully and partially coherent wavefields. The ideas, development and writing up of all the papers in body of the thesis were the principal responsibility of myself, the candidate, working within the School of Physics under the supervision of Marcus J. Kitchen and David M. Paganin.

The inclusion of co-authors reflects the fact that the work came from active collaboration between researchers and acknowledges input into team-based research.

Signed:

Mario Alejandro Beltran Toro

Acknowledgements

I would like to express my gratitude to my supervisors Dr. Marcus Kitchen and Associate Professor David Paganin for their constant support, fantastic leadership, patience, enthusiasm, kindness and treating me as an equal throughout my PhD candidature. Without Marcus's extensive experience in experimental physics this project would have not been possible. David has played a crucial role in my development as an independent researcher, always encouraging me to think outside the box and explore new avenues, even if these avenues are outside the field of coherent X–ray optics.

I have had the fortune to be part of a creative and dynamic team that is the School of Physics. I am very grateful to Dr. Tim Petersen for his valuable input into chapter 6 and to Dr. Kaye Morgan for helping me produce the supplementary movie of the reconstructed lung airways. Also, much gratitude goes to a number of current and former staff members, namely Dr. Imants Svalbe, Dr. Daniele Pelliccia, Dr. Mathew Dimmock and Dr. John Gilliam.

All experiments in this research were conducted at the 8 GeV Super Photon Ring (SPring–8) with the approval of the Japan Synchrotron Radiation Research Institute. My acknowledgments to Kentaro Uesugi and Dr Naoto Yagi for their assistance. Also, many thanks to Professor Stuart Hooper and his team of Physiologists who came along to the synchrotron facility and conducted the animal procedures.

As a recipient of a Faculty of Science Dean's Postgraduate Research Scholarship I thank the Monash University Faculty of Science for their financial support during my candidature.

Many thanks to my fellow past and present students, Dr. Gary Ruben, Dr. Shane Kennedy, Dr. Shekhar Chandra, Dr. Naomi Schofield, Dr. Richard Bear, Dr Ben Farmer, Elliot Hutchinson, Wan Zahidi Zakwan, Samuel Eastwood, Katie Lee, Katie Auchettl, Rhiannon Murrie, Freda Rothschild, Andrew Leong, David Palamara, Timothy Dolley, Amelia Frasner-McKelvie, Tessa Charles, Jacob Tosado. I must single out Jeremy Brown for his assistance with writing Latex documents.

This journey would have been far more difficult without the affection and support of my family and friends. A special huge goes to my 'Brates', George Sinadinos (El Griego Loco), Domago Dragicevic and Zlatko Basic (El Balcanico). You guys are the coolest. A warm thankyou to the sweet Alma Basic. Also, a big thankyou to the Latino gang, Pili Torres, Andrea Aguilera, Tino Guzman, Pilar Aguilera and Marta Avila. I appreciate the support of my sisters, Carol Patricia Beltran Toro, Marcela Isabel Beltran Toro (La Chola) and Claudia Elena Beltran Toro. And finally, I'd like thank my beloved parents Bernardita

del Carmen Toro Correa and Mario del Carmen Beltran Herrera for their endless love and support; this thesis is dedicated to them.

Thesis overview

Since Wilhelm Conrad Röntgen first discovered X–rays, a cornucopia of X–ray applications have been cultivated. These applications range from biomedical sciences through to materials engineering and they continue to expand their influence in many scientific areas. With their high energy, X–rays can penetrate through matter such as light metals, biological tissue and ceramics. This makes X–rays an excellent tool for probing matter. One of the most impacting applications is their use in medicine as a non–invasive diagnostic imaging tool.

The most commonly used X–ray imaging technique is two dimensional absorption–based X–ray radiography. This technique involves illuminating an object with a beam of X–rays and recording the intensity distribution of the transmitted beam by means of a spatially resolved detector or film. The image contrast arises from the difference in the transverse intensity resulting from the variation in the attenuation coefficient across the object. The attenuation coefficient of a specific material within the object is dependent on the imaginary part of its complex refractive index (Als–Nielsen and McMorrow [2]). Absorption–based X–ray imaging works well when the density variations within the object are relatively large. For example, a human chest radiograph reveals high contrast of the ribs as result of the high difference in attenuation coefficient between bone and soft tissue. Unfortunately, when the transverse differences in attenuation of the transmitted intensity are small the internal features become difficult or impossible to visualize with this technique. This has limited applications, especially when it comes to imaging to samples such as biological specimens.

One way to improve visualization is with the use of Computed Tomography (CT) scanners. The invention of CT scanners enabled the field of X–ray imaging to enter an extra spatial dimension. With CT one can obtain a three–dimensional reconstruction of the internal structure of an object, thus providing valuable morphological detail. X–ray CT is based on the idea that X–rays will travel approximately along straight ray–paths through the object (Kak and Slaney [43]). Under conventional CT the transmitted intensities recorded at various projection angles provide knowledge of the line–integrals of the linear attenuation coefficient distribution of the object (Kak and Slaney [43]). By acquiring a sufficient number of projections these integrals can be inverted and one can recover the

three dimensional distribution of the object's linear attenuation coefficient. However, in cases where the object contains small features that have low absorption, conventional CT provides very little contrast to resolve them. One way to overcome this is by taking longer exposures for each acquisition. This, however will impose a higher radiation dose, which can be detrimental to the sample. Dose consideration is particularly important for *in vivo* studies, and thus methods requiring large numbers of projections are of limited use for biomedical applications.

One of the ways to overcome the limitations set by conventional absorption contrast imaging is to turn to the field of phase–contrast imaging. Phase–contrast exploits the wave nature of light, where X–ray beams are described in terms of a complex wavefield that carries phase and amplitude information (Zernike [93], Bonse and Hart [7], Teague [82]). Here, the phase of the wavefield undergoes shifts as X–rays are transmitted through the object. These phase–shifts are rendered visible in the detected intensity via the aid of optical setups that are able to convert phase variations into intensity variations. The induced phase–shifts are dependent on the real part of the object's complex refractive index $n = 1 - \delta + i\beta$. At typical X–ray energies (100 eV–100 keV) the real part (δ) is in the order of $\sim 10^3$ times larger than the imaginary part β. This yields the possibility of achieving high contrast at potentially lower radiation doses. This promises to be incredibly beneficial, particularly when it comes to CT. An important note is that the key ingredient to carry out phase–contrast imaging experiments is the need for an X–ray beam that exhibits some degree of coherence. All radiation sources can be characterized by their degree of coherence (Born and Wolf [8]). In optical terms, a beam's degree of coherence can be loosely defined as a measure of the ability of the field to interfere. Chapter 3 covers all the main concepts and quantities concerning coherence theory.

A number of phase–contrast methods exist, most of which are discussed in Chapter 3. In terms of experimental applications the original results of this thesis focus exclusively on propagation–based phase–contrast imaging (PBI). For PBI, images are collected at a non–zero distance downstream of the object and the contrast arises as result of Fresnel diffraction. The great advantage that PBI offers over alternative phase–contrast methods is that it does not require any additional optical elements between the object and detector. This simplicity makes it well suited for potential biomedical or industrial applications.

When propagation–based phase–contrast imaging is combined with CT, weakly absorbing features of an object can be more readily visualised in 3D. The setup is identical to that of conventional CT with the exception that now the detector is positioned at some increased propagation distance from the object's exit plane and the X–ray source requires a moderate degree of spatial coherence. Normally, propagation–based X–ray phase contrast tomography experiments are performed using highly coherent synchrotron beams or microfocus laboratory sources. In most cases the end goal with PCT is to recover the three dimensional complex refractive index distribution of an object. However, although PBI can improve the visualization of weakly absorbing features in an object, quantitative information (i.e. the complex refractive index) cannot be directly inferred from the raw

phase contrast X–ray images (Cloetens *et al.* [16]). In order to obtain such information, phase retrieval methods are required. Including phase retrieval in the reconstruction step gives rise to 'quantitative propagation–based phase–contrast tomography' (see section 3.4 of chapter 3).

Phase retrieval is any process that involves finding the phase of a complex wavefield given measurements of field moduli (Gerchberg and Saxton [29]). This is also known as the phase problem. A cornucopia of phase retrieval methods for extracting quantitative information from intensity measurements alone have been developed to obtain the projected phase and absorption information of the object (Gerchberg and Saxton [29], Teague [82], Gureyev and Nugent [37], Paganin and Nugent [66], Gureyev [35]). Notwithstanding their successes, these methods often require multiple intensity measurements, impose strong restrictions on the object under study, or apply iterative solution techniques. Acquiring multiple images can prove problematic for correct alignment of images and induces a higher radiation dose. Several phase retrieval methods require the object to be "weak" such that they provide little to no absorption contrast with limited phase gradients introduced by the sample. Since most inanimate materials and biological tissues cannot be considered as weak objects, phase retrieval algorithms developed under these approximations have only limited use for biomedical imaging or materials science applications. Iterative phase retrieval algorithms can also be problematic as convergence to the correct solution cannot be guaranteed and are computationally more intensive than analytic solutions.

Considering the above limitations, a great challenge exist to discover a means for performing high contrast quantitative propagation-based phase–contrast tomography using a single image per projection. For the case of a single–material object illuminated by paraxial coherent X–rays, there have been a number of tomographic studies using a single view per projection. These phase–contrast tomography investigations, which incorporate the effects of both absorption and phase contrast, extend the seminal work for the phase–contrast tomography of pure phase objects by Bronnikov [11]. The majority of this literature is reviewed in chapter 3. Further advancements were made by Paganin *et al.* [65]. In their work a noise–robust deterministic phase retrieval algorithm to reconstruct the projected linear attenuation coefficient of an object comprised of a single material using a single PBI image was developed. This enables the performance of quantitative PBI tomography with a single image per projection, as was performed by Mayo *et al.* [52]. In spite of their achievement their method is still heavily restricted to sample being comprised of a single material. The associated algorithm is extensively described in Chapter 4.

This thesis embarks on the task of developing a quantitative PBI tomographic method that can be extended to samples composed of multiple materials under the strict condition that only one image per projection is acquired. Also, the method should be analytic and stable in the presence of noise. In chapter 4 a method is derived that enables analytic propagation–based phase retrieval tomography to be performed on a multi–material object in which the spatially–dependent complex refractive index is quantized (i.e. it takes one of a series of distinct values). The algorithm makes use of a single PBI image per projection,

separately and selectively reconstructing each interface between any given pair of distinct materials. Having separately reconstructed the interfaces between different distinct pairs of materials, a spliced three–dimensional image of all materials present in the sample can then be computed.

In chapter 4 the phase retrieval method is successfully applied experimentally using a test object. Chapter 5 takes the next step by showing that the method can be applied to complex biological organs, without using any chemical contrast enhancements. Experiments were performed specifically on the thorax of a newborn New Zealand white rabbit pup and the excised brain of an adult Sprague Dawley rat. The aim was to determine whether our method could be applied to complex structures without imposing additional radiation dose than conventional CT and to measure a possible gain in signal–to–noise ratio (SNR) of the reconstructed images.

Throughout the majority of this thesis the results are based on the key assumption that the X–ray source is a well behaved, fully coherent field. Despite the great technological advances made in achieving X–ray sources of high coherence (i.e. synchrotron beams, lasers) it is impossible to achieve perfect coherence in practice. In Chapter 6 this assumption is dropped in order extend our applications to X–ray sources that exhibit partial coherence. Work relating to a partially coherent treatment specifically for propagation-based phase contrast imaging has been previously reported (Gureyev [34], Zysk *et al.* [94], Petruccelli *et al.* [69]). In most of these studies the space–frequency description of partially coherent fields was utilised as the fundamental starting point (Wolf [88]). This thesis also uses the space–frequency description for partially coherent fields.

From an optical perspective, phase contrast can be interpreted as a form of optical aberration. In fact, PBI is directly linked to the "defocus" aberration. In this context, an aberrated imaging system may be defined as one whose transverse spatial distribution of output intensity is not equal to the transverse spatial distribution of the input intensity, up to transverse and multiplicative scale factors, together with the smearing effects of finite resolution. Almost all aberrated imaging systems exhibit phase contrast; that is, they have a spatial distribution of the output intensity which is influenced by the functional form of the input wavefronts (input phase distribution). Examples of aberrated imaging systems yielding phase contrast include Zernike phase contrast (Zernike [93]), propagation–based phase contrast (Wilkins *et al.* [85]), differential phase–contrast (Förster *et al.* [26]), inline holography (Gabor [27]), etc.

In chapter 6 we consider the generalized differential phase contrast associated with aberrated linear shift–invariant optical imaging systems employing statistically stationary partially coherent scalar radiation, for which the output spatial distribution of spectral density (i.e., the output image) can be modelled using the transfer function formalism. Chapter 6 extends previously reported work by Paganin and Gureyev [64], which restricted consideration to the generalized differential phase contrast of fully coherent scalar fields imaged using aberrated linear shift–invariant optical systems. Establishing a mathematical expression that integrates the theory of aberrations with the theory of partial coherence

enables arbitrary phase–contrast imaging modes to be implemented on a wider range of radiation sources.

2

Theory of X–ray wavefield diffraction

2.1 Introduction

In this chapter we cover the fundamental background theory of optical wavefield diffraction, which is of primary importance for this thesis. This background serves as a pre–requisite for later discussions on phase–contrast X–ray imaging when considering cases where optical elements are absent (i.e. PBI). We begin with a derivation of the electromagnetic (EM) wave equations from Maxwell's equations in section 2.2. The angular–spectrum method for the spatial propagation of EM wavefields is discussed in section 2.3. This the leads to the special cases of Fresnel and Fraunhofer diffraction which are described in sections 2.4 and 2.5, respectively. Lastly, the theory concerning partially coherent fields from a statistical stand point is covered in section 2.6.

2.2 Electromagnetic wave equations in free space

Since the discovery that light is electromagnetic radiation governed by Maxwell's equations, which unite electric and magnetic phenomena, these equations have been the main pillars in describing classical optical behaviour. This section reviews the derivation of the electromagnetic wave equations in free space (vacuum). We begin by stating Maxwell's equations in a dielectric medium (Jackson [42]):

$$\nabla \cdot \mathbf{E}(\mathbf{r}, t) = \frac{\rho(\mathbf{r}, t)}{\epsilon_0}, \tag{2.1a}$$

$$\nabla \cdot \mathbf{B}(\mathbf{r}, t) = 0, \tag{2.1b}$$

$$\nabla \times \mathbf{E}(\mathbf{r}, t) = -\frac{\partial \mathbf{B}(\mathbf{r}, t)}{\partial t}, \tag{2.1c}$$

$$\nabla \times \mathbf{B}(\mathbf{r}, t) = \mu_0 \mathbf{J}(\mathbf{r}, t) + \mu_0 \epsilon_0 \frac{\partial \mathbf{E}(\mathbf{r}, t)}{\partial t}. \tag{2.1d}$$

Here, $\mathbf{E}(\mathbf{r}, t)$ is the electric field and $\mathbf{B}(\mathbf{r}, t)$ is the magnetic field. $\mathbf{r} = (x, y, z)$ represents the position vector in three–dimensional Cartesian coordinates. Time is denoted by t. The symbols $\nabla \cdot$ and $\nabla \times$ are the three–dimensional gradient and curl operators, respectively. The

charge density is denoted by $\rho(\mathbf{r}, t)$, and the current density by $\mathbf{J}(\mathbf{r}, t)$. The constants μ_0 and ϵ_0 are the permeability and permittivity of free space, respectively. Equation (2.1a) is the differential form of Gauss's law, which states that "the net electric flux through any enclosed surface is proportional to the total charge enclosed within that surface". Equation (2.1b) is Gauss's law for magnetism. Equation (2.1c) is Faraday's law of induction and Eqn. (2.1d) is Ampère's law. In the absence of material media (free space) it can be assumed that charge and current densities are zero, therefore Eqns. (2.1a) and (2.1d) simplify to:

$$\nabla \cdot \mathbf{E}(\mathbf{r}, t) = 0, \tag{2.2a}$$

$$\nabla \times \mathbf{B}(\mathbf{r}, t) = \mu_0 \epsilon_0 \frac{\partial \mathbf{E}(\mathbf{r}, t)}{\partial t}. \tag{2.2b}$$

Taking the curl of Eqn. (2.1c) gives

$$\nabla \times \nabla \times \mathbf{E}(\mathbf{r}, t) = -\frac{\partial}{\partial t}[\nabla \times \mathbf{B}(\mathbf{r}, t)]. \tag{2.3}$$

Substituting Eqn. (2.2b) into Eqn. (2.3) and making use of the identity

$$\nabla \times \nabla \times \mathbf{f} = \nabla(\nabla \cdot \mathbf{f}) - \nabla^2 \mathbf{f}, \tag{2.4}$$

arrives us at the following:

$$\nabla[\nabla \cdot \mathbf{E}(\mathbf{r}, t)] - \nabla^2 \mathbf{E}(\mathbf{r}, t) = -\mu_0 \epsilon_0 \frac{\partial^2 \mathbf{E}(\mathbf{r}, t)}{\partial t^2}. \tag{2.5}$$

Using Eqn. (2.2a) brings us to the wave equation for electric fields in vacuum known as the d'Alembert wave equation:

$$\left(\nabla^2 - \mu_0 \epsilon_0 \frac{\partial^2}{\partial t^2}\right) \mathbf{E}(\mathbf{r}, t) = 0. \tag{2.6}$$

With the application of similar logic one can also derive the wave equation for magnetic fields in vacuum. This provides the following pair of equations:

$$\left(\nabla^2 - \mu_0 \epsilon_0 \frac{\partial^2}{\partial t^2}\right) \mathbf{E}(\mathbf{r}, t) = 0, \tag{2.7a}$$

$$\left(\nabla^2 - \mu_0 \epsilon_0 \frac{\partial^2}{\partial t^2}\right) \mathbf{B}(\mathbf{r}, t) = 0. \tag{2.7b}$$

Given the d'Alembert wave Eqns. (2.7) one can deduce the speed at which the electric and magnetic disturbances propagate though vacuum. Consider a plane wave propagating

in the positive z–direction that is a solution to Eqn. (2.7). Such waves have the form $\Im \sin(kz - \omega t + \phi)$. Here, $\Im$ is the amplitude, ϕ is the relative phase, $k = 2\pi/\lambda$ is the wavenumber for a given wavelength λ, $\omega = 2\pi\nu$ is the angular frequency corresponding to a particular frequency ν, and t is time. Substituting this plane wave into the d'Alembert wave equations gives the following:

$$\mu_0 \epsilon_0 \omega^2 - k^2 = 0. \tag{2.8}$$

Since $c = \nu\lambda$, where c is the speed at which the electric and magnetic disturbances propagate in vacuum, Eqn. (2.8) gives the relation

$$c = \frac{1}{\sqrt{\mu_0 \epsilon_0}}. \tag{2.9}$$

By using measured values of μ_0 and ϵ_0 it was found that the value of c coincides with that of the speed of light in vacuum, which had already been experimentally reported. This was the key link that led to the discovery that light was electromagnetic radiation.

The pair of Eqns. in (2.7) contain six spatial components for the free space electric and magnetic disturbances. Each make up six decoupled scalar differential equations of identical form. It is this decoupling that enables the electric and magnetic disturbances to be described by a single complex scalar wave equation (Paganin [67]):

$$\left(\nabla^2 - \frac{1}{c^2}\frac{\partial^2}{\partial t^2}\right)\Psi(\mathbf{r}, t) = 0. \tag{2.10}$$

Equation (2.10) is known as the d'Alembert wave equation for scalar fields. Here the squared modulus $|\Psi(\mathbf{r}, t)|^2$ corresponds to the optical intensity. Note that when it comes to incorporating optical polarization effects the scalar d'Alembert form becomes invalid[1].

If we consider complex scalar wavefields that are strictly monochromatic, represented as a function of space and time, such fields can be expressed as a product of spatial and temporal components (Paganin [67], Born and Wolf [8]):

$$\Psi(\mathbf{r}, t) = \psi(\mathbf{r}) \exp(-i\omega t), \tag{2.11}$$

where ω denotes angular frequency. When substituting Eqn. (2.11) into the d'Alembert wave equation (Eqn. (2.10)) the time component can be separated out as a common factor:

---

[1]The transition from vector to scalar electromagnetic optics is not immediately apparent and is somewhat involved. Literature on this subject that covers the rigorous treatment on how to make such transition can be found in Green and Wolf [32], Wolf [87], Marathay and Parrent [51], Nieto-Vesperinas [63], Born and Wolf [8].

$$\left[\nabla^2\psi(\mathbf{r}) + \frac{\omega^2}{c^2}\psi(\mathbf{r})\right]\exp(-i\omega t) = 0. \tag{2.12}$$

Since

$$\exp(-i\omega t) \neq 0, \tag{2.13}$$

this factor can be canceled in Eqn. (2.12) and hence we arrive at the time–independent scalar wave equation:

$$(\nabla^2 + k^2)\psi(\mathbf{r}) = 0, \tag{2.14}$$

with $k = \frac{\omega}{c}$. This equation is known as the 'Helmholtz equation', which governs the spatial evolution of the function $\psi(\mathbf{r})$ corresponding to a specific monochromatic angular frequency. This equation is pivotal to the theory of diffraction, which essentially involves constructing a solution to this equation, as we will show in the following section.

2.3   The angular spectrum representation of plane waves

The angular spectrum method provides a formalism that enables the calculation of the forward propagated wavefield over a specified plane perpendicular to the optic axis z, given the boundary value of that disturbance over a parallel plane with a smaller z value (see Fig. 2.1). This is achieved by finding a general solution to Helmholtz equation given specific boundary values (Goodman [30], Mandel and Wolf [50], Paganin [67]). The development shown in this section is based on that shown in Paganin [67].

We begin by considering the scenario in Fig. 2.1. Here an object is placed along the optic axis 'z'. The complex wavefield $\psi(\mathbf{r}_\perp, z = 0)$ denotes the spatial part of the beam at the plane $z = 0$, which correspond to the object's exit plane. We wish to calculate the wavefield at some forward distance $\psi(\mathbf{r}_\perp, z \geq 0)$, under the assumption that the half–space $z \geq 0$ corresponds to vacuum. For the scenario in Fig. 2.1 the source lies upstream of the object.

It can be demonstrated by direct substitution that elementary plane waves are solutions to the Helmholtz equation. Such waves have the form

$$\psi^{\mathrm{PW}}(x, y, z) = \exp[i(k_x x + k_y y + k_z z)]. \tag{2.15}$$

Note that this is only true if $k^2 = k_x^2 + k_y^2 + k_z^2$. Here (k_x, k_y, k_z) are components of the wave–vector $\mathbf{k}$. The magnitude of this vector ($|\mathbf{k}|$) equals $k = 2\pi/\lambda$, with λ being the
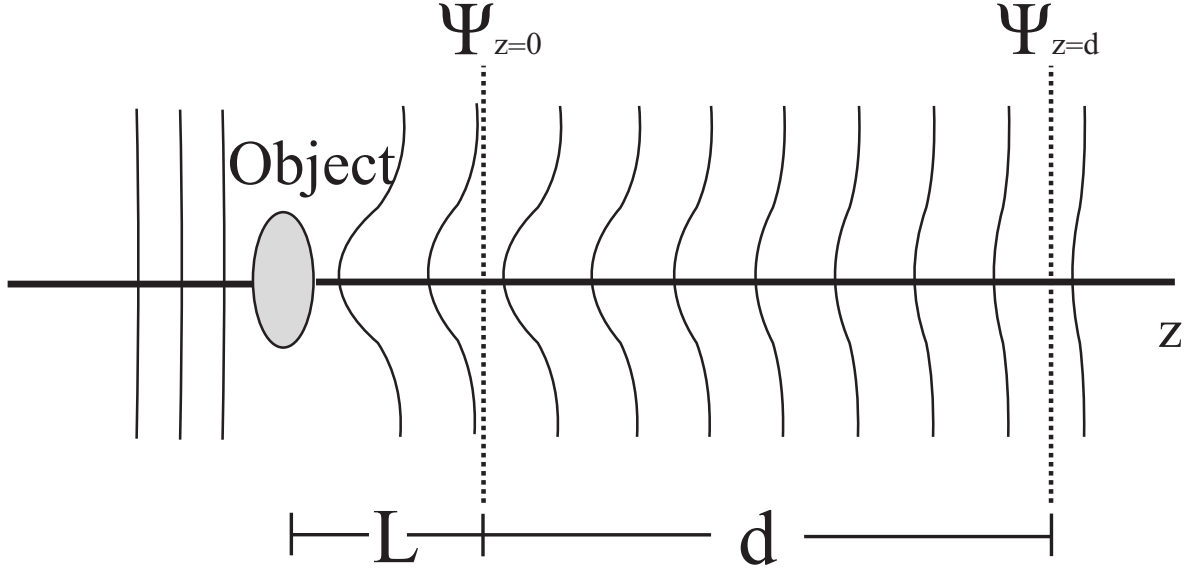
Figure 2.1: Propagation of scalar wavefields.

X-ray wavelength. Since the z direction represents the direction of propagation, it proves convenient to isolate the z component of the wave–vector as:

$$k_z = \sqrt{k^2 - (k_x^2 + k_y^2)}. \tag{2.16}$$

Note that the positive branch of the square root has been chosen on account of the assumption that the field is forward propagating. This enables the elementary plane wave to be re–expressed as:

$$\psi^{\mathrm{PW}}(x, y, z) = \exp[i(k_x x + k_y y)] \exp\left[iz\sqrt{k^2 - (k_x^2 + k_y^2)}\right]. \tag{2.17}$$

Note that the $z = 0$ boundary value of the plane wave is

$$\psi(x, y, z = 0) = \exp[i(k_x x + k_y y)], \tag{2.18}$$

and

$$\exp\left[iz\sqrt{k^2 - (k_x^2 + k_y^2)}\right] \tag{2.19}$$

is the propagation factor termed the *free space propagator*. Now we express an arbitrary unpropagated wavefield in terms of a Fourier integral

$$\psi(\mathbf{r}_\perp, z = 0) = \frac{1}{2\pi} \iint_{-\infty}^{\infty} \widetilde{\psi}(k_x, k_y, z = 0) \exp[i(k_x x + k_y y)] dk_x dk_y. \tag{2.20}$$

Here, $\widetilde{\psi}(k_x, k_y, z = 0)$ denotes the Fourier transform of $\psi(x, y, z = 0)$ with respect to $\mathbf{r}_\perp = (x, y)$, with $\mathbf{k}_\perp = (k_x, k_y)$ being Fourier–space coordinates dual to $\mathbf{r}_\perp = (x, y)$. Note that from a physical point of view Eqn. (2.20) is a Fourier decomposition of the unpropagated wavefield into a series of plane waves of the form $\exp[i(k_x x + k_y y)]$. To obtain the wavefield at $z = d$ one need only to multiply the integrand Eqn. (2.20) by the free space propagator in Eqn. (2.19) leading to:

$$\psi(\mathbf{r}_\perp, z = d) = \frac{1}{2\pi} \iint_{-\infty}^{\infty} \widetilde{\psi}(k_x, k_y, z = 0) \exp\left[id\sqrt{k^2 - k_x^2 - k_y^2}\right]$$
$$\times \exp[i(k_x x + k_y y)]dk_x dk_y.$$
$$(2.21)$$

This expression is known as the angular–spectrum representation of the propagated wavefield. It is an exact solution to the Helmholtz equation that solves the boundary value problem of determining the propagated field $\psi(\mathbf{r}_\perp, z = d)$ as a result of forward propagating the field $\psi(\mathbf{r}_\perp, z = 0)$ in free space by a distance $z = d$.

It is possible to make further simplification of the process which describes free space diffraction. Basically, the aim is to express Eqn. (2.21) in terms of a diffraction operator, which acts upon the unpropagated wavefield that in turn produces a propagated wavefield at some forward distance d. This operator form can be written as:

$$\psi(\mathbf{r}_\perp, z = d) = \mathfrak{D}_d \psi(\mathbf{r}_\perp, z = 0). \qquad (2.22)$$

The linear operator $\mathfrak{D}_d$ takes the form:

$$\mathfrak{D}_d = F_{\mathbf{k}_\perp}^{-1} \exp\left[id\sqrt{k^2 - |\mathbf{k}_\perp|^2}\right] F_{\mathbf{r}_\perp}. \qquad (2.23)$$

Here, $F_{\mathbf{r}_\perp}$ represents the forward Fourier transform with respect to $\mathbf{r}_\perp$ and $F_{\mathbf{k}_\perp}^{-1}$ represents the corresponding inverse Fourier transform with respect to $\mathbf{k}_\perp = (k_x, k_y)$. $\mathbf{k}_\perp$ is dual to $\mathbf{r}_\perp$. The forward and inverse Fourier transform conventions used in this thesis are:

$$\widetilde{G}(\mathbf{k}_\perp) = \frac{1}{2\pi} \iint_{-\infty}^{\infty} G(\mathbf{r}_\perp) \exp[-i(\mathbf{r}_\perp \cdot \mathbf{k}_\perp)]d\mathbf{r}_\perp$$
$$G(\mathbf{r}_\perp) = \frac{1}{2\pi} \iint_{-\infty}^{\infty} \widetilde{G}(\mathbf{k}_\perp) \exp[i(\mathbf{r}_\perp \cdot \mathbf{k}_\perp)]d\mathbf{k}_\perp \qquad (2.24)$$

where, $\widetilde{G}(\mathbf{k}_\perp)$ is the Fourier transform of the function $G(\mathbf{r}_\perp)$.

The operator form of the angular spectrum method implies the following procedure to calculate the propagated wavefield: (i) Take the Fourier transform of the unpropagated field with respect to $\mathbf{r}_\perp$; (ii) multiply the result by the free space propagator in Eqn. (2.19); (iii) take the inverse Fourier transform with respect to $\mathbf{k}_\perp$ of this result, which yields the desired propagated field $\psi(\mathbf{r}_\perp, z = d)$.

2.4 Fresnel diffraction

This section provides a derivation of the Fresnel diffraction integral. Fresnel diffraction is seen as a limiting case of the angular–spectrum method. This limiting case corresponds to the 'Fresnel regime', which essentially states that propagation distances should be small enough such that most features of the diffracting object are still distinguishable within the diffracted image. When propagation distances are sufficiently small relative to the diffracting object the image is said to be in the Fresnel regime, which applies to both near and intermediate fields. To this end it is useful to introduce the quantity known as the Fresnel number that is defined by the formula (Goodman [30], Paganin [67]):

$$N_F = \frac{D^2}{\lambda d}, \tag{2.25}$$

where D is the characteristic length scale over which the object varies appreciably. As we shall see below, the Fresnel number gives an approximate indication as to how far a distance downstream of the direction of propagation is required to produce either a Fresnel (near or intermediate field) or Fraunhofer (far field) image given a certain object size and radiation wavelength.

We begin the derivation of the Fresnel diffraction integral by restating the angular spectrum in operator form (Paganin [67]) as:

$$\psi(\mathbf{r}_\perp, z = d) = F_{\mathbf{k}_\perp}^{-1} \exp\left[id\sqrt{k^2 - |\mathbf{k}_\perp|^2}\right] F_{\mathbf{r}_\perp} \psi(\mathbf{r}_\perp, z = 0). \tag{2.26}$$

In the Fresnel regime the wavefields propagate paraxially. This implies that the vector's normal wavefronts make small angles with respect to the optic axis as they forward propagate. Under this condition the binomial approximation is made to the free space propagator in Eqn. (2.19):

$$\sqrt{k^2 - |\mathbf{k}_\perp|^2} \approx k - \frac{|\mathbf{k}_\perp|^2}{2k}. \tag{2.27}$$

As a result the angular spectrum formalism under Fresnel diffraction becomes:

$$\psi(\mathbf{r}_\perp, z = d) = \exp(ikd)F_{\mathbf{k}_\perp}^{-1} \exp\left[\frac{-id\,|\mathbf{k}_\perp|^2}{2k}\right] F_{\mathbf{r}_\perp} \psi(\mathbf{r}_\perp, z = 0). \tag{2.28}$$

Here we see that the free space propagator now takes the form $\exp\left[\frac{-id|\mathbf{k}_\perp|^2}{2k}\right]$. The term $\exp(ikd)$ is a constant phase factor. In order to express Eqn. (2.28) as a diffraction integral, use can be made of the Fourier convolution theorem (Winthrop and Worthington [86]). This gives the real space form of the free space propagator, which sees the Fresnel diffraction integral written as (Paganin [67]):

$$\psi(\mathbf{r}_\perp, z = d) = -\frac{ik\exp(ikd)}{2\pi d}\exp\left[\frac{ik\,|\mathbf{r}_\perp|^2}{2d}\right]\int_{-\infty}^{\infty}\psi(\mathbf{r}'_\perp, z = 0)\exp\left[\frac{ik\,|\mathbf{r}'_\perp|^2}{2d}\right]$$

$$\times\exp\left[\frac{-ik}{d}(\mathbf{r}_\perp\cdot\mathbf{r}'_\perp)\right]d\mathbf{r}'_\perp. \tag{2.29}$$

Here $\mathbf{r}'_\perp = (x', y')$. We close this section with reference to Fig. 2.2. Here we show forward simulated diffraction intensity images of Fig. 2.2 (a) using a numerical implementation of Eqn. (2.28). Both images display the squared modulus of the propagated wavefield. The size of the image in Fig. 2.2 (a) is 225×225 pixels with a pixel size of 1 μm. The unpropagated field was calculated using the equation $\psi(\mathbf{r}_\perp, z = 0) = \sqrt{I_{Image}}e^{i\phi_{image}}$. For each simulation the intensity was set to $I_{Image} = 1$ assuming a non–absorbing object[2]. Also, the maximum phase shift was 4.6 radians for a wavelength of $\lambda = 6.2 \times 10^{-10}$ m as shown in Fig. 2.2 (a). Fig. 2.2 (b) shows an image calculated at a propagation distance $d = 0.01$ m (the near field $N_F = 5.8$) and (c) shows an image calculated at $d = 0.10$ m (the intermediate field $N_F = 0.6$). Here, the characteristic length scale is $D = 6$ μm.

2.5   Fraunhofer diffraction

Fraunhofer diffraction is the case where propagation distances are relatively large. Fraunhofer diffraction patterns are also termed as 'far field' images. This section shows that the expression in Eqn. (2.29) permits an easy transition to the far field. At very large propagation distances (the far field) the Fresnel number is much less than unity:

$$N_F \ll 1. \tag{2.30}$$

Under this condition the first exponential term that appears inside the integral in Eqn. (2.29) tends to unity and thus can be ignored (Paganin [67]). This in turn brings us to the "Fraunhofer diffraction integral" (Goodman [30]):

$$\psi(\mathbf{r}_\perp, z = d) \rightarrow -\frac{ik\exp(ikd)}{2\pi d}\exp\left[\frac{ik\,|\mathbf{r}_\perp|^2}{2d}\right]\int_{-\infty}^{\infty}\psi(\mathbf{r}'_\perp, z = 0)\exp\left[\frac{-ik}{2d}(\mathbf{r}_\perp\cdot\mathbf{r}'_\perp)\right]d\mathbf{r}'_\perp. \tag{2.31}$$

In a more compact form Eqn. (2.31) can be expressed as:

---

[2]This assumption is often known as the "pure phase object" assumption/approximation. This implies that the wavefield is assumed to only undergoes phase variation and not intensity variations as it travels through the object.
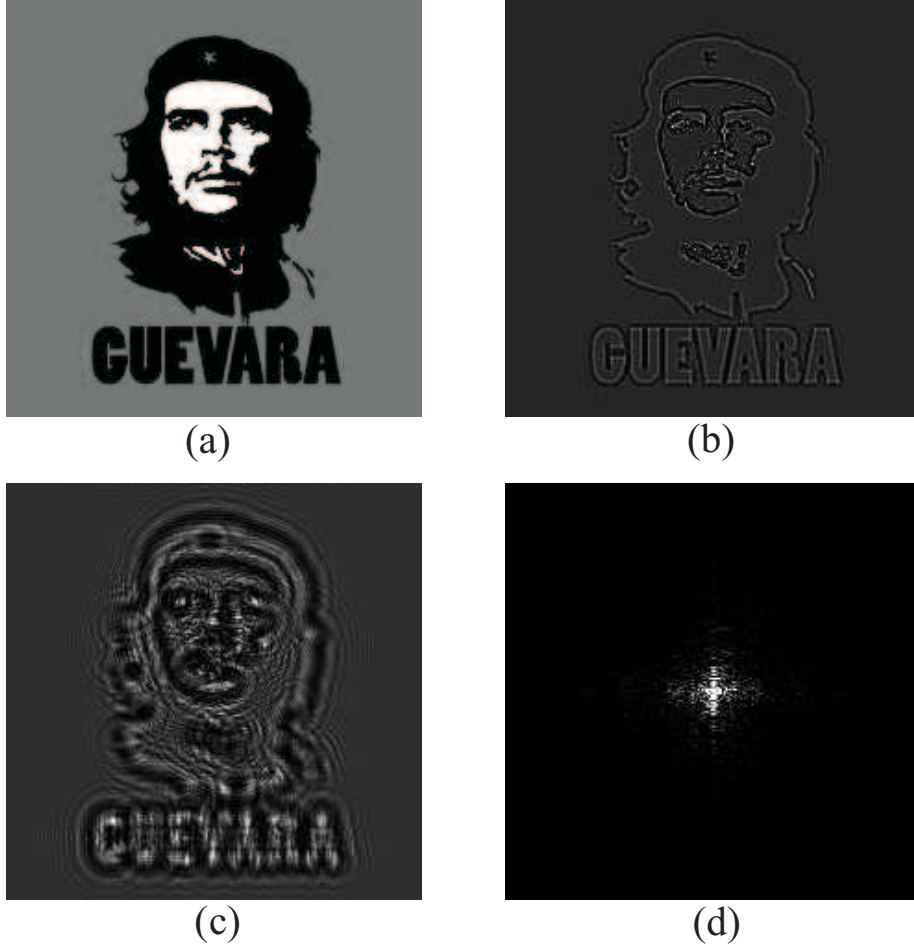
Figure 2.2: Examples of Fresnel and Fraunhofer diffraction. (a) is the unpropagated phase image used for forward simulations of Fresnel and Fraunhofer diffraction images. (b) shows a Fresnel diffraction image in the near field, with $N_F = 5.8$. (c) also shows a Fresnel diffraction image in the intermediate field, with $N_F = 0.6$. (d) shows a far field Fraunhofer diffraction pattern in a logarithmic scale, with $N_F \ll 1$.

$$\psi(\mathbf{r}_\perp, z = d) \rightarrow -\frac{ik \exp(ikd)}{2\pi d} \exp\left[\frac{ik |\mathbf{r}_\perp|^2}{2d}\right] \times \widetilde{\psi}\left(\mathbf{k}_\perp = \frac{k\mathbf{r}_\perp}{d}, z = 0\right). \tag{2.32}$$

Here, $\widetilde{\psi}\left(\mathbf{k}_\perp = \frac{k\mathbf{r}_\perp}{d}, z = 0\right)$ is the two–dimensional Fourier transform of the unpropagated wavefield with respect to $\mathbf{r}_\perp$. Note that Eqn. (2.32) tells us that the Frounhofer diffraction pattern is the Fourier transform of the exit–surface ($z = 0$) wavefield uptream of the diffracting object multiplied by a modulated "scale factor" given by the expanding spherical wave term $\exp\left[\frac{ik\mathbf{r}_\perp^2}{2d}\right]$. By taking the squared modulus of Eqn. (2.32) we find that:

$$I \propto \left|\widetilde{\psi}\left(\mathbf{k}_\perp = \frac{k\mathbf{r}_\perp}{d}, z = 0\right)\right|^2, \tag{2.33}$$

$$I \propto \frac{1}{d^2}.$$ (2.34)

From these relations we note that in the far field the intensity distribution obeys the inverse square law. Like the operator form of the Fresnel diffraction this result can be very easily numerically implemented. It has the advantage that the Fourier transform is only needed to be applied once followed by the squared modulus. A far field ($N_F \ll 1$) diffraction image calculated by numerically applying Eqn. (2.33) to the phase map in Fig. 2.2 (a) is shown in Fig. 2.2 (d).

2.6 Partially coherent wavefields

So far in this chapter we have considered optical fields that are monochromatic with a well defined phase and amplitude as they propagate. However, this is not case in most optical scenarios. In nature all optical fields experience random fluctuations (Wolf [90]). The theory of partial coherence is concerned with the quantitative description of such stochastically fluctuating optical fields (Wolf [90]). This section discusses the mathematical tools and concepts used to treat partially coherent fields. The theory presented in this section forms the fundamental basis for the results derived in chapter 6 where the theory of optical aberrations and partially coherent fields is combined.

2.6.1 Theory of stochastic optical waves

Before proceeding into the description of partially coherent fields this section introduces some elementary mathematical concepts necessary for understanding the partial coherence description of stochastic optical waves.

We begin by considering the variable $x(t)$, which represents a field at some point in space at time t. Suppose that $x(t)$ can be measured in a series of experiments. Also, let $^1x(t), ^2x(t), ^3x(t), ..., ^kx(t)$ be the outcomes of such experiments. It can be said that one has an *ensemble of realizations* or an ensemble of *sample functions* of the random function $x(t)$. For all random processes the concept of an "average value" immediately comes to mind. In this section, we focus on two types of averages. First, we consider the concept of a *time average* that for a given realization of the ensemble is defined as (Wolf [90]):

$$\left\langle ^kx(t) \right\rangle_t = \lim_{T \to \infty} \frac{1}{2T} \int_{-T}^{T} {}^kx(t)dt.$$ (2.35)

Here the angular brackets with the subscript t denotes the time average taken over the time interval $-T \le t < T$. The other kind of average we consider is the *ensemble average* or the *expectation value*, given by:

$$\langle x(t) \rangle_e = \lim_{N \to \infty} \frac{1}{N} \sum_{k=1}^{N} {}^k x(t). \tag{2.36}$$

Here the ensemble average is denoted by the angular brackets with the subscript e (ensemble).

To end this section we give a brief discussion on *Ergodicity*. A statistically stationary process[3] is said to be *ergodic* when averages taken over the $-\infty < t < \infty$ interval of a typical realization ${}^k x(t)$ of the random process is equal to the corresponding ensemble average (Wolf [90]):

$$\left\langle {}^k x(t) \right\rangle_t = \langle x(t) \rangle_e . \tag{2.37}$$

For the statistical description of partially coherent wavefields considered in this thesis the processes are assumed to be statistically stationary and ergodic. Essentially, this means that: 1) there is no need to distinguish between time averages and ensemble averages; 2) the statistics of the experiment are independent of the origin of time (Wolf [90]).

2.6.2 Interference, visibility and time–average intensity

A basic feature of optical wavefields that are partially coherent is the ability to form interference patterns. Interference occurs when two or more wavefields add to produce a superposed wavefield. This is visualised in the measured intensity as interference fringes. It is the contrast of the fringes that largely defines the degree of coherence. The notion of the 'quality' of interference fringes can be evaluated using the Michelson fringe visibility, defined as (Wolf [90]):

$$V = \frac{I_{max} - I_{min}}{I_{max} + I_{min}}. \tag{2.38}$$

For a typical interference fringe we denote its maximum intensity as I_{max} and its minimum intensity as I_{min}.

Another important quantity in the theory of partial coherence is the time–averaged intensity. At optical and higher temporal frequency ranges the temporal fluctuations of the field are very rapid, making instantaneous intensity measurements impractical. The expression for the time–averaged intensity is obtained by simply adapting Eqn. (2.35) (Wolf [90]) to give:

$$\langle I \rangle_t = \lim_{T \to \infty} \frac{1}{2T} \int_{-T}^{T} I(t) dt. \tag{2.39}$$

---

[3] Statistically stationary processes are those in which the statistics of the random variable are independent of the origin of time.

The time interval $-T \leq t < T$, which in practice will always be non–infinite, must be large in relation to the bandwidth $\Delta\omega$ of light (i.e. $T \gg 1/\Delta\omega$).

2.6.3   Temporal and spatial coherence

Temporal and spatial coherence are key concepts when it comes to understanding the underlying theory of partially coherent fields.
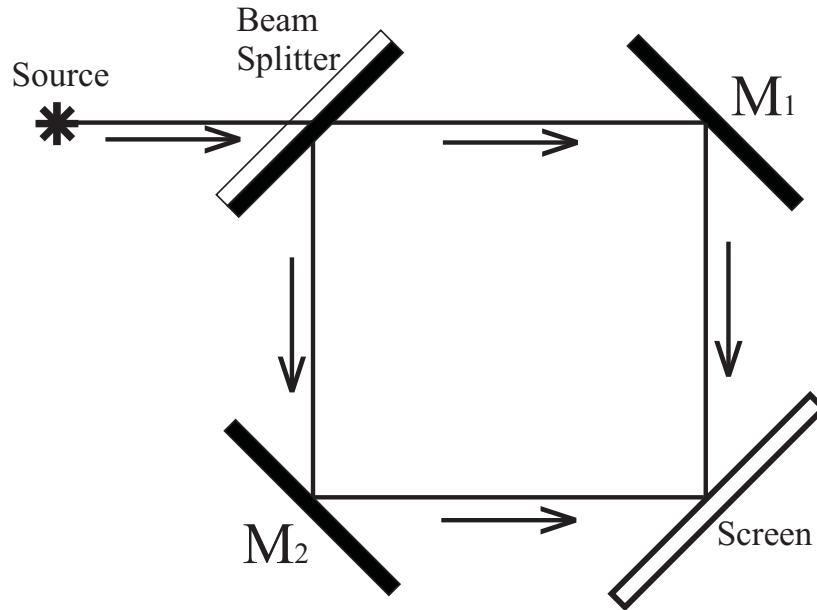
Figure 2.3: Diagram of a Mach–Zehnder interferometer as a means of illustrating and understanding the concept of temporal coherence. M_1 and M_2 are mirrors.

To understand temporal coherence consider the Mach–Zehnder interferometry setup presented in Fig. 2.3. Here we have a source emanating a quasi-monochromatic[4] beam of light with a frequency bandwidth $\Delta\omega$. When the beam reaches the beam splitter it divides it into two separate beams. Each of the beams is reflected perpendicularly from the mirrors M_1 and M_2 and eventually meet at the screen yielding interference fringes. It is the forming of these fringes which is said to be a manifestation of *temporal coherence* between the two beams. The contrast of the interference fringes depends on the time delay Δt due to the difference in path length of the beams. It has been experimentally verified that interference fringes are observed provided that (Wolf [90]):

$$\Delta t \leqslant \frac{2\pi}{\Delta\omega}. \tag{2.40}$$

This defines the *coherence time*, which can be seen as an indicator of the duration in which the phase and amplitude of a propagating wavefield is defined. Naturally, there is a

---

[4] *Quasi–monochromatic* light beams are partially coherent fields, which are characterised by the property defined as the effective bandwidth $\frac{\Delta\omega}{\bar{\omega}} \ll 1$, where $\bar{\omega}$ is the mean temporal frequency. Further, to be quasi–monochromatic we also require $\Delta\omega \neq 0$.

corresponding path length delay associated with the coherence time. This is referred to as the *coherence length* (Wolf [90]):

$$\Delta \bar{l} = \frac{2\pi c}{\Delta \omega} = \frac{\bar{\lambda}^2}{\Delta \lambda}.$$

(2.41)

Here, $\bar{\lambda}$ is the mean wavelength and $\Delta \lambda$ is the effective wavelength range.

We now turn to concepts regarding spatial coherence. The Young interferometer in Fig. 2.4 aids us with an illustrative example. Like in the temporal coherence example the light emitted from the extended incoherent source of length σ is also assumed to be quasi-monochromatic. When the light rays emitted from an arbitrary point on the source reach the pinholes Q_1 and Q_2 placed on the screen Y equidistantly from the optic axis, two secondary wavefronts are produced at each pinhole. An interference pattern resulting from the superposition of the two wavefronts is formed at the screen B. At the point P fringes will be observed as long as the pinholes are situated within an area of

$$\Delta A \approx \frac{L_1^2 \bar{\lambda}^2}{\sigma^2}.$$

(2.42)

This quantity is termed the coherence area. It can be appreciated that as the distance L_1 becomes greater the coherence area increases quadratically. Equation (2.42) verifies a well known fact whereby spatial coherence improves as light propagates further from the source of emittance and reduces with larger source size σ (Wilkins *et al.* [85]).
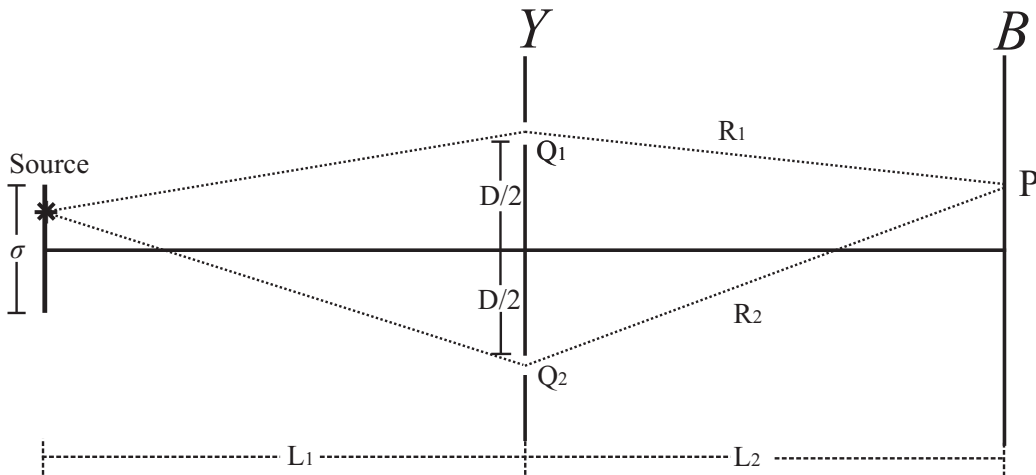
Figure 2.4: Diagram of Young's interference experiment used for the conceptual understanding of spatial coherence. σ is the length of the line source. Q_1 and Q_2 are pinholes on an opaque screen Y separated by distance D from one another. L_1 is the distance from the source to the screen Y and L_2 is the distance from the screen Y to the screen B.

2.6.4   The mutual coherence function

The mutual coherence function provides us with a more general treatment of partial coherence theory. Instead of relying on the visibility of fringes as a method of quantification of the degree of coherence, the mutual coherence function employs a direct application of the theory of random variables presented in section 2.6.1 to describe partially coherent optical fields (Born and Wolf [8], Wolf [90]).

Consider once again Young's interference experiment in Fig. 2.4. Let $\Psi(Q_1, t)$ and $\Psi(Q_2, t)$ be the complex wavefields incident at each pinhole at time t. The scattered wavefields due to each pinhole will generate an interference pattern in the neighbourhood surrounding point P located on the screen B. The field at point P, once $\Psi(Q_1, t)$ and $\Psi(Q_2, t)$ have reached this point, will be given by the principle of superposition as:

$$\Psi(P, t) = K_1 \Psi(Q_1, t - t_1) + K_2 \Psi(Q_2, t - t_2). \tag{2.43}$$

Here, $t_1 = \frac{R_1}{c}$ and $t_2 = \frac{R_2}{c}$ are the respective times it takes light to travel to P from Q_1 and Q_2. The factors K_1 and K_2 are complex numbers (propagators) that depend on the shape of the pinholes. Taking the squared modulus of Eqn. (2.43), followed by the time average of the result, brings us to the time-average intensity at point P (Born and Wolf [8], Wolf [90]):

$$
\begin{aligned}
\bar{I}(P) &= \left\langle |K_1 \Psi(Q_1, t - t_1) + K_2 \Psi(Q_2, t - t_2)|^2 \right\rangle \\
&= \left\langle |K_1 \Psi(Q_1, t - t_1)|^2 \right\rangle + \left\langle |K_2 \Psi(Q_2, t - t_2)|^2 \right\rangle \\
&\quad + 2 \left| K_1 K_2^* \right| \operatorname{Re} \left\langle \Psi(Q_1, t - t_1) \Psi^*(Q_2, t - t_2) \right\rangle.
\end{aligned}
\tag{2.44}
$$

Here, Re denotes the real component of the corresponding term. Also, note that here the subscript on the angular brackets has been dropped denoting the assumption that time–averages are equal to the ensemble average since we have assumed an ergodic process.

Setting

$$\bar{I}_1(P) = \left\langle |K_1 \Psi(Q_1, t - t_1)|^2 \right\rangle \tag{2.45}$$

and

$$\bar{I}_2(P) = \left\langle |K_2 \Psi(Q_2, t - t_2)|^2 \right\rangle \tag{2.46}$$

allows Eqn. (2.44) to be re-written as:

$$\bar{I}(P) = I_1(P) + I_2(P) + 2 \left| K_1 K_2^* \right| \operatorname{Re} \left\langle \Psi(Q_1, t - t_1) \Psi^*(Q_2, t - t_2) \right\rangle. \tag{2.47}$$

Here, one can evidently see that the third term on the right–hand side of Eqn. 2.47 is an interference term. Introduce the time lag τ, which denotes the relative time difference that the photons have as they travel to the point P at speed c via either of the two pinholes at Q_1 and Q_2:

$$\tau = \frac{R_1 - R_2}{c}. \tag{2.48}$$

This, together with the assumption of stationarity, enables the term inside the angular brackets in Eqn. (2.47) to be written as:

$$\langle \Psi(Q_1, t + \tau)\Psi^*(Q_2, t)\rangle \equiv \Gamma(Q_1, Q_2, \tau). \tag{2.49}$$

This is the *mutual coherence* function. Eqn. (2.49) can also be viewed as a measure of the degree of correlation between $\Psi(Q_1, t)$ and $\Psi(Q_2, t)$ (Born and Wolf [8], Wolf [90]). In this context, it can be said that if $\Psi(Q_1, t)$ and $\Psi(Q_2, t)$ are fully uncorrelated, then the interference fringes will not be visible. In the opposite case if $\Psi(Q_1, t)$ and $\Psi(Q_2, t)$ are fully correlated then the interference fringes will yield maximal visibility (Born and Wolf [8], Wolf [90]). Therefore, a certain degree of correlation is needed between the wavefields at Q_1 and Q_2 so that fringes can exist. A correlation that gives fringes between maximal and minimal visibility is referred to as having an *intermediate degree of coherence*, which correspond to partially coherent fields (Born and Wolf [8], Wolf [90]).

The following normalized form of the mutual coherence function gives us the *complex degree of coherence*:

$$\gamma(Q_1, Q_2, \tau) = \frac{\Gamma(Q_1, Q_2, \tau)}{\sqrt{\Gamma(Q_1, Q_1, \tau = 0)\Gamma(Q_2, Q_2, \tau = 0)}}. \tag{2.50}$$

A quantitative relation between the complex degree of coherence and the visibility of fringes is given via:

$$V = |\gamma(Q_1, Q_2, \tau)| \tag{2.51}$$

where, the modulus of the complex degree of coherence function gives a value that lies between zero and unity:

$$0 \leqslant |\gamma(Q_1, Q_2, \tau)| \leqslant 1. \tag{2.52}$$

Here, a value of unity corresponds to complete coherence, conversely, a value of zero corresponds to complete incoherence. All other values correspond to partial coherence.

2.6.5 The cross–spectral density and spectral density

The cross–spectral density and the spectral–density are used as an alternative description for partially coherent fields rather than a space–time correlation function (i.e. the mutual coherence function Γ and the complex degree of coherence γ). The cross–spectral density W was originally introduced as the Fourier transform of the mutual coherence function with respect to the time lag τ (Wolf [88]):

$$W(\mathbf{r}_1, \mathbf{r}_2, \omega) = \frac{1}{2\pi} \int_{-\infty}^{\infty} \Gamma(\mathbf{r}_1, \mathbf{r}_2, \tau) e^{i\omega\tau} d\tau. \tag{2.53}$$

However, it was later discovered to also be a correlation function itself, associated with an ensembles of realizations that are functions of position and temporal frequency instead of position and time. This is demonstrated by considering an optical field in a closed domain D in free–space. Generally, it can be shown that the cross–spectral density of the field at any pair of points $\mathbf{r}_1$ and $\mathbf{r}_2$ in D may be expressed in a series (Wolf [88, 90]):

$$W(\mathbf{r}_1, \mathbf{r}_2, \omega) = \sum_n \lambda_n(\omega) \varsigma_n^*(\mathbf{r}_1, \omega) \varsigma_n(\mathbf{r}_2, \omega). \tag{2.54}$$

The functions ς_n are eigenfunctions and λ_n the eigenvalues of the integral equation (Wolf [90]):

$$\int_D W(\mathbf{r}_1, \mathbf{r}_2, \omega) \varsigma_n(\mathbf{r}_1, \omega) d^3\mathbf{r}_1 = \lambda_n(\omega) \varsigma_n(\mathbf{r}_2, \omega), \tag{2.55}$$

where $d^3\mathbf{r}_1$ is the three–dimensional differential element of $\mathbf{r}_1$ and the quantities $\lambda_n(\omega)$ are positive real eigenvalues (i.e. $\lambda_n(\omega) > 0$, $(n \geq 0)$). The eigenfunctions ς_n may take the form of an orthonormal set over the domain D:

$$\int_D \varsigma_n^*(\mathbf{r}, \omega) \varsigma_m(\mathbf{r}, \omega) d^3\mathbf{r} = \widehat{\delta}_{mn}. \tag{2.56}$$

Here, $\widehat{\delta}_{mn}$ is the Kronecker delta symbol.

To show that the cross–spectral density can be expressed as a correlation function using the expansion in Eqn. (2.54), first begin by considering the ensemble of sample functions of the form (Wolf [88]):

$$\psi(\mathbf{r}, \omega) = \sum_n a_n(\omega) \varsigma_n(\mathbf{r}, \omega), \tag{2.57}$$

where $a_n(\omega)$ are random coefficients such that

$$\langle a_n^*(\omega)a_m(\omega)\rangle_\omega = \lambda_n(\omega)\widehat{\delta}_{mn}. \tag{2.58}$$

Here, $\lambda_n(\omega)$ are the same quantities that appear in integral Eqn. (2.55). Now constructing the correlation function $\langle \psi^*(\mathbf{r}_1, \omega)\psi(\mathbf{r}_2, \omega)\rangle_\omega$ one obtains

$$\langle \psi^*(\mathbf{r}_1, \omega)\psi(\mathbf{r}_2, \omega)\rangle_\omega = \sum_{n,m} \langle a_n^*(\omega)a_m(\omega)\rangle_\omega \varsigma_n^*(\mathbf{r}_1, \omega)\varsigma_m(\mathbf{r}_2, \omega), \tag{2.59}$$

where upon using the relation in Eqn. (2.58) we arrive at:

$$\langle \psi^*(\mathbf{r}_1, \omega)\psi(\mathbf{r}_2, \omega)\rangle_\omega = \sum_n \lambda_n(\omega)\varsigma_n^*(\mathbf{r}_1, \omega)\varsigma_n(\mathbf{r}_2, \omega). \tag{2.60}$$

Noting that the right hand side of Eqn. (2.60) equates to the right had side of Eqn. (2.55), we have established the result that the cross–spectral density is indeed a correlation function, as given by (Wolf [88]):

$$W(\mathbf{r}_1, \mathbf{r}_2, \omega) = \langle \psi^*(\mathbf{r}_1, \omega)\psi(\mathbf{r}_2, \omega)\rangle_\omega. \tag{2.61}$$

The essence of Eqn. (2.61) is that the cross–spectral density of a statistically stationary fluctuating field in the domain D may be expressed, for all pairs of points in D, as a cross–correlation of ensembles $\{\psi(\mathbf{r}, \omega)\}$ of space–frequency realizations $\psi(\mathbf{r}, \omega)$, all of which have the same angular frequency ω (Wolf [88]).

The spectral–density[5] is given by $S(\mathbf{r}, \omega) \equiv W(\mathbf{r}, \mathbf{r}, \omega)$ which is also expressed as:

$$S(\mathbf{r}, \omega) = \langle \psi^*(\mathbf{r}, \omega)\psi(\mathbf{r}, \omega)\rangle_\omega. \tag{2.62}$$

Equation (2.62) may intuitively lead to the belief that it represents the average squared modulus of the Fourier frequency components of the field $\Psi(\mathbf{r}, t)$. However, Eqn. (2.62) should be viewed as the space–dependent part of a member of a statistical ensemble of monochromatic realizations, all of frequency ω (Wolf [90]). This is also true for Eqn. (2.61). Hence when it comes to the space–frequency description of partially coherent fields it is crucial to differentiate between a monochromatic field of frequency ω and an ensemble of monochromatic fields all which have the same frequency ω (Wolf [90]).

---

[5]Note that the spectral–density and the intensity of the spatial part of a monochromatic wavefield (i.e. $\Psi(\mathbf{r}, t) = \psi(\mathbf{r}, \omega)e^{-i\omega t}$) are equivalent in the special case where the ensemble characterizing the stochastic process contains only a single member.

2.7   Concluding remarks

The material of the present chapter, which reviews the theory of X–ray diffraction together with the theory of partially coherent fields, is supplemented in chapter 3 by a review of phase–contrast X–ray imaging, phase retrieval and tomography. The background material reviewed in both chapters 2 and 3 constitute the underpinning prior knowledge upon which the original research of chapters 4, 5, and 6 is based.

Phase contrast X–ray imaging, phase retrieval and tomography

<div style="text-align: right">3</div>

3.1 Introduction

This chapter presents an overview of phase–contrast imaging theory and methods. The theory and methods covered are those that have the highest relevance in the development of this thesis. We begin by briefly discussing the interaction of X-rays with matter in section 3.2, mainly emphasizing the derivation of the *projection approximation*, which plays a key role in the work presented in chapters 4 and 5. In section 3.3 the theory of image formation (the forward problem) with conventional phase–contrast techniques is covered. In section 3.4, analytic ways to perform phase retrieval (the inverse problem) are discussed. Finally, we end this chapter by discussing tomographic principles and phase–contrast tomography in section 3.5. This last–mentioned topic is also essential background for chapters 4 and 5.

3.2 Interactions of X–rays with matter

At macroscopic scales, the interactions between X–rays and matter is quantified by the complex refractive index[1]:

$$n(\mathbf{r}) = 1 - \delta(\mathbf{r}) + i\beta(\mathbf{r}). \tag{3.1}$$

The imaginary component $\beta(\mathbf{r})$ is directly proportional to the linear attenuation coefficient μ of the material via $\beta = \mu\lambda/4\pi$ (Als–Nielsen and McMorrow [2]). The real component $\delta(\mathbf{r})$ is the refractive index decrement from unity and is responsible for refraction effects (Als–Nielsen and McMorrow [2]). Both quantities can be calculated given knowledge of the properties of the material at the subatomic scale. For instance, one may calculate $\delta(\mathbf{r})$ with the formula (Als–Nielsen and McMorrow [2]):

---

[1]Note, that a static scatterer has been assumed, since $n = n(\mathbf{r})$ rather than $n = n(\mathbf{r}, t)$.

$$\delta = \frac{r_e \lambda^2}{2\pi} \sum_j N_j f_{1j}. \tag{3.2}$$

Similarly, the linear attenuation coefficient μ can be calculated with the formula (Als–Nielsen and McMorrow [2]):

$$\mu = r_e \lambda \sum_j N_j f_{2j}. \tag{3.3}$$

The parameter N_j denotes the concentration of atoms per unit of volume for a particular type j of atoms. The classical electron radius is labelled as r_e. The quantities f_1 and f_2 in Eqns. (3.2) and (3.3) respectively represent the real and imaginary components of the atomic scattering factor in the forward direction.

3.2.1   The projection approximation

Consider the scenario in Fig. 3.1. Here, we have the case where incoming X-rays (incident wavefield) impinge on an object at its entrance plane $z = z_{entry}$, travel through it, and eventually exit the object at the plane $z = z_{exit}$. The projection approximation links the wavefield at the entrance plane $z = z_{entry}$ to the wavefield at the exit plane $z = z_{exit}$ using knowledge of the object's complex refractive index.
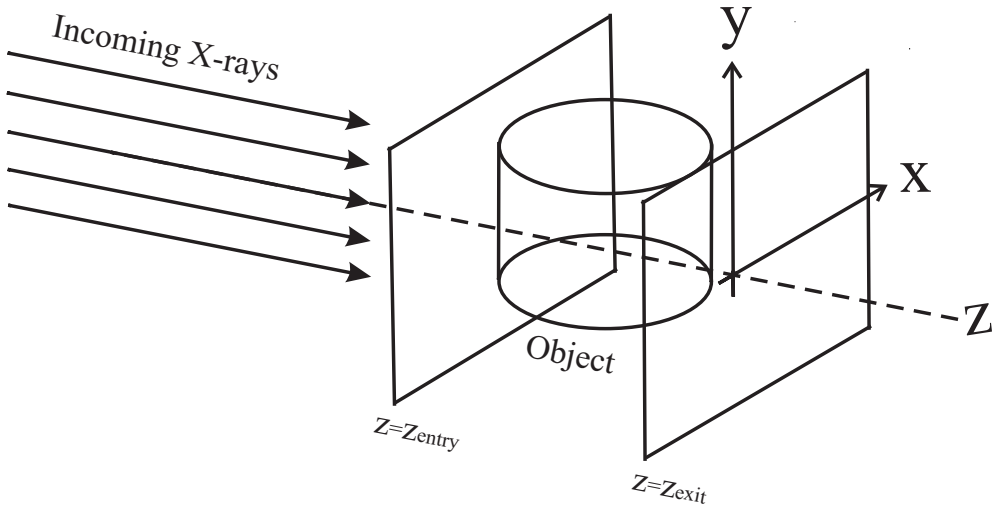
Figure 3.1: Schematic illustration of the projection approximation.

The projection approximation is derived from first principles using the "inhomogeneous paraxial wave equation" as a starting point (Paganin [67]):

$$\left(2ik\frac{\partial}{\partial z} + \nabla_\perp^2 + k^2[n^2(\mathbf{r}) - 1] \right) \psi(\mathbf{r}) = 0. \tag{3.4}$$

The inhomogeneous paraxial wave equation can be viewed as the Helmholtz wave equation (see Eqn. (2.14)) in the presence of material media instead of vacuum, under the paraxial limit[2]. We remind the reader that in optics the term "paraxiality" implies that the propagating wavefield travels in a direction almost parallel to the optic axis. Mathematically this enables second order derivatives with respect to z to be ignored. $n(\mathbf{r})$ is the refractive index distribution function of the object defined by the Cartesian coordinates $\mathbf{r} = (x, y, z)$ shown in Fig. 3.1. The essence of the projection approximation is that it assumes there is a continuous accumulation of the phase and amplitude shifts along independent straight line X–ray paths, which allows for the determination of the wavefield at the exit plane $z = z_{exit}$. Now, since the transverse Laplacian operator $\nabla_\perp^2 \equiv \frac{\partial^2}{\partial x^2} + \frac{\partial^2}{\partial y^2}$ couples adjacent ray trajectories, under the projection approximation this operator can be ignored leading to the following partial differential equation Paganin [67]:

$$\frac{\partial}{\partial z}\psi(\mathbf{r}) \approx \frac{k}{2i}[1 - n^2(\mathbf{r})]\psi(\mathbf{r}). \tag{3.5}$$

As depicted in Fig. 3.1, the lower boundary is given by the plane $z = z_{entry}$ and the upper boundary is given by the plane $z = z_{exit}$. With these boundary values one can obtain a solution of Eqn. (3.5) for the exit wavefield $\psi(\mathbf{r}_\perp, z = z_{exit})$, which is of the form (Paganin [67]):

$$\psi(\mathbf{r}_\perp, z = z_{exit}) \approx \exp\left\{\frac{k}{2i}\int_{z=z_{entry}}^{z=z_{exit}}[1 - n^2(\mathbf{r})]dz\right\}\psi(\mathbf{r}_\perp, z = z_{entry}). \tag{3.6}$$

At X–ray energies, the refractive index in Eqn. (3.1) is very close to unity. This allows us to make the approximation (Paganin [67]):

$$1 - n^2(\mathbf{r}) \approx 2[\delta(\mathbf{r}) - i\beta(\mathbf{r})]. \tag{3.7}$$

Substituting the approximation in Eqn. (3.7) into Eqn. (3.6) gives

$$\begin{aligned}
\psi(\mathbf{r}_\perp, z = z_{exit}) &\approx \exp\left\{-ik\int_{z=z_{entry}}^{z=z_{exit}}[\delta(\mathbf{r}) - i\beta(\mathbf{r})]dz\right\}\psi(\mathbf{r}_\perp, z = z_{entry})\\
&= \underbrace{\exp\left[-k\int_{z=z_{entry}}^{z=z_{exit}}\beta(\mathbf{r})dz\right]}_{\textit{Exponential decay}}\underbrace{\exp\left[-ik\int_{z=entry}^{z=exit}\delta(\mathbf{r})dz\right]}_{\textit{Phase change}}\psi(\mathbf{r}_\perp, z = z_{entry}).
\end{aligned}$$
$$\tag{3.8}$$

Separating the exponential terms in Eqn. (3.8) enables us to appreciate how the phase and amplitude shifts imparted on the wavefield traversing the object are related to $\delta(\mathbf{r})$ and $\beta(\mathbf{r})$. Hence, under the projection approximation, the phase–shift from $z = z_{entry}$ to $z = z_{exit}$ is:

---

[2]A formal derivation of the inhomogeneous paraxial wave equation can be found in (Paganin [67]).

$$\Delta\phi(\mathbf{r}_\perp) = -k \int_{z=z_{entry}}^{z=z_{exit}} \delta(\mathbf{r})dz. \tag{3.9}$$

Taking the squared modulus of Eqn. (3.8) gives an expression for the intensity at $z = z_{exit}$:

$$\mathrm{I}(\mathbf{r}_\perp, z = z_{exit}) = \exp\left[-2k \int_{z=z_{entry}}^{z=z_{exit}} \beta(\mathbf{r})dz\right] \mathrm{I}(\mathbf{r}_\perp, z = z_{entry}). \tag{3.10}$$

Eqn. (3.10) is the well–known Beer–Lambert law of attenuation for inhomogeneous objects (Als-Nielsen and McMorrow [2], Paganin [67]).

3.3   Phase–contrast imaging techniques

When a semi-transparent object such as biological tissue is illuminated with X-rays the intensity detected at the exit plane of the object will display little to no contrast. This can be circumvented by implementing phase–contrast techniques. Phase–contrast imaging is any optical technique where phase–shifts imparted on the wavefield are rendered visible in the measured intensity. The phase–shifts result from the variations in the refractive index in the object.

3.3.1   Zernike–type phase contrast imaging

Frits Zernike is considered to be the pioneer of phase-contrast microscopy and hence why this technique it bears his name (Zernike [93]). Zernike–type phase-contrast imaging makes use of optical lenses, exploiting the fact that their focal planes contain Fourier transforms of the incident input wavefields. At this plane a filter is placed that acts as a phase retarder that induces phase variations on the zero spatial frequency of the previously mentioned Fourier transform. These changes become manifest in the intensity at the image (detector) plane. Such a system is shown in Fig. 3.2. At the plane $z = 0$ in Fig. 3.2 a lens (L_1) is placed that focuses the rays at the plane $z = f$. At $z = f$ a small transparent on-axis filter produces a $\pi/2$ phase retardation on the light concentrated on this point. The lens (L_2) positioned at $z = 2f$ undoes the effect of (L_1), effectively acting as inverse Fourier transform and ultimately yielding a phase contrast image.

The beauty of utilising Zernike–type phase contrast imaging is that the detected intensity is directly proportional to the input phase, thus allowing direct inference of this quantity (Zernike [93]). Note that this statement is only valid provided the sample is fully transparent and the transverse phase shifts are small. Mathematically, this is simple to illustrate. Beginning with the weak–phase approximation (Zernike [93]), the wavefield in the plane $z = 0$ can be written as:

$$\exp[i\phi(\mathbf{r}_\perp)] \approx 1 + i\phi(\mathbf{r}_\perp), \quad |\phi(\mathbf{r}_\perp)| \ll 1. \tag{3.11}$$
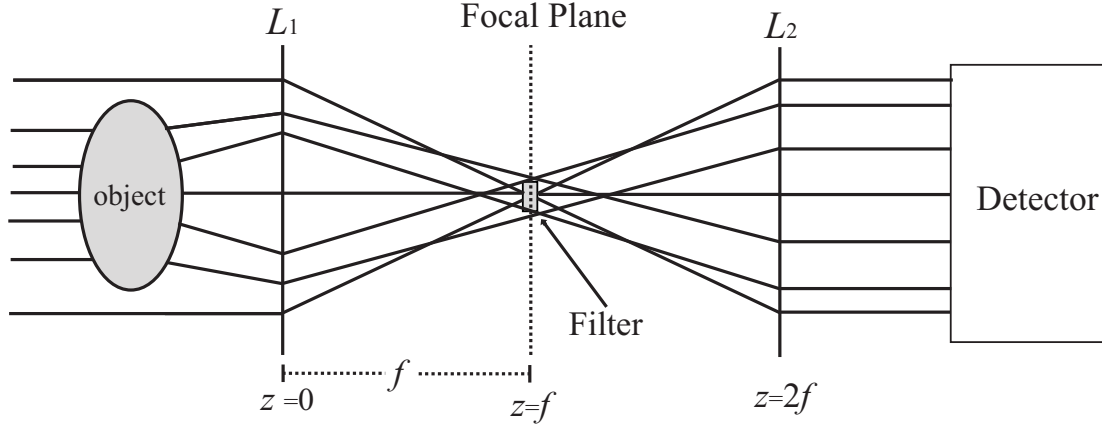
Figure 3.2: Schematic diagram showing Zernike-type phase contrast imaging.

Under this approximation one may view the input wavefield as a superposition of an unscattered function "1" plus a scattered complex function $i\phi$. At the focal point $z = f$ the majority of the light concentrated will be that of the unscattered function. Here, the filter acts as an $e^{i\pi/2}$ multiplier transforming "1" into a complex value $e^{i\pi/2} = i$. Therefore, under a Zernike–type system the input wavefield undergoes the following transformation:

$$\psi_{in}(\mathbf{r}_\perp) \approx 1 + i\phi(\mathbf{r}_\perp) \longrightarrow i + i\phi(\mathbf{r}_\perp). \tag{3.12}$$

Therefore, the intensity at the detector plane, given by the squared modulus, will yield (Zernike [93]):

$$I(\mathbf{r}_\perp) = |\psi(\mathbf{r}_\perp)|^2 \approx 1 + 2\phi(\mathbf{r}_\perp). \tag{3.13}$$

Notice that since phase variations are small the second order term in $\phi(\mathbf{r}_\perp)$ has been ignored.

An example of an X–ray Zernike phase–contrast image is shown in Fig. 3.3 where the buried copper interconnects of a integrated circuit can be clearly seen. The set up used to acquire this image is a more contemporary implementation of Zernike phase contrast that can be found in (Neuhäusler *et al.* [62]).

3.3.2 Differential interference phase contrast imaging

In differential interference contrast (DIC) imaging systems the contrast is produced by making the exit wavefield interfere with a transversely–shifted replica of itself. Consider a thin transparent sample such that when illuminated by a coherent beam of X–rays with a planar wavefront, the wavefield exiting the sample is given by $\exp[i\phi(x, y)]$. Suppose the imaging system is able to create a replica of this wavefield transversely shifted by a distance ε in the x–direction (i.e. $\exp[i\phi(x + \varepsilon, y)]$). By appropriate choice of Cartesian
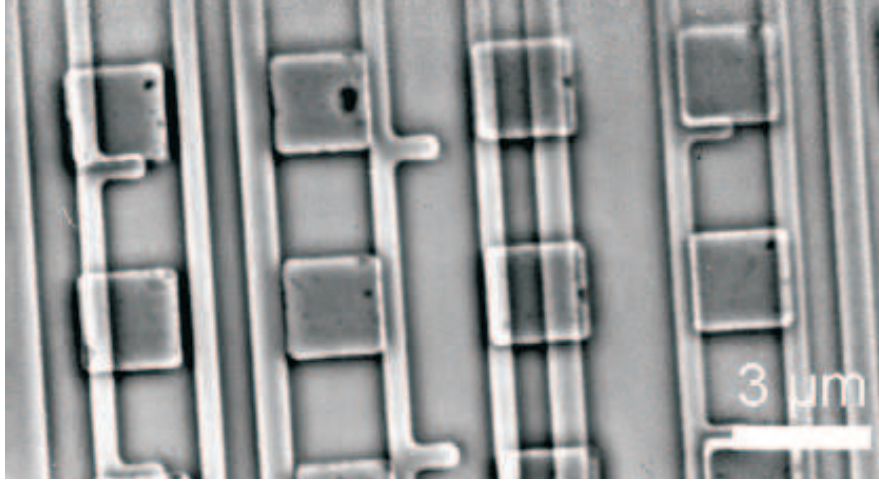
Figure 3.3: Zernike phase contrast micrograph image of an integrated circuit. The image was acquired using a X–ray microscope. Image was taken from Neuhäusler *et al.* [62].

coordinates there is no loss of generality in assuming the previously mentioned transverse shift to be in the *x*–direction. If the original and the transversely displaced fields are then superposed, such an interaction can be viewed as mapping input to output fields as (Paganin [67]):

$$\exp[i\phi(x, y)] \rightarrow \exp[i\phi(x, y)] + \exp[i\phi(x + \varepsilon, y)]. \tag{3.14}$$

The output intensity of the interferogram will be the squared modulus of the right–hand–side of Eqn. (3.14):

$$I(x, y) = \left| \exp[i\phi(x, y)] + \exp[i\phi(x + \varepsilon, y)] \right|^2. \tag{3.15}$$

If ε is assumed to be sufficiently small, a first–order Taylor approximation can be made to the phase $\phi(x + \varepsilon, y)$:

$$\phi(x + \varepsilon, y) \approx \phi(x, y) + \varepsilon \frac{\partial \phi(x, y)}{\partial x}. \tag{3.16}$$

By substituting Eqn. (3.16) into Eqn. (3.15) the output intensity reduces to

$$I(x, y) = 2 \left(1 + \cos \left[\varepsilon \frac{\partial \phi(x, y)}{\partial x} \right] \right). \tag{3.17}$$

Here, we see that the output image exhibits phase–contrast, given that the output intensity is dependent on *x*–derivatives of the phase. Since the contrast of the intensity is dependent on the derivative of the phase one may say that the system displays *differential interference*

contrast (DIC). If one takes the Taylor–series expansion of the cosine term one may see that this type of DIC is of second order in ε since (Paganin [67]):

$$\cos\left[\frac{\partial\phi(x,y)}{\partial x}\right] = 1 - \frac{1}{2}\left[\frac{\partial\phi(x,y)}{\partial x}\right]^2 + ... \tag{3.18}$$

Note that further improvements to DIC that makes the contrast proportional to first order in ε can be made with the introduction of a phase bias ϕ_B into the shifted replica. However, since this thesis does not make use of this method we find that illustrating this does not add significant insight. The derivation of the intensity expression under DIC when a phase bias is introduced can be found in (Paganin [67]). Literature regarding the experimental implementation and demonstration of X–ray differential interference contrast is reported by (Kaulich *et al.* [44]).

3.3.3 Interferometry

Interferometry is one of the most traditional methods for achieving phase–contrast. The idea behind this method is rather simple. It involves dividing the incident beam by splitting it into two separate beams then later recombining them in order to form an interference pattern or interferogram. One of the beams is utilised as a reference wavefield with its properties known *a priori* and another is used to probe a sample of interest. In the X–ray regime interferometers require a high degree of spatial and temporal coherence. Ulrich Bonse and Michael Hart designed the first X–ray interferometer known as the Bonse-Hart interferometer (Bonse and Hart [7]). The schematic layout of the design is shown in Fig. 3.4. Here, we see how an incident beam of X–rays is split into two by the beam splitter. The beam that serves as a reference wavefield is labelled ψ_R. The other beam is used to probe the sample and is labelled ψ_S. A transmission mirror is then used to recombine the beams which allow interference of the beams by the analyser crystal, which subsequently records the intensity (I_M) measured by the detector. We can describe the wavefield that exits the sample as $\psi_S = \exp(i\phi_S)$ and denote the reference wavefield as $\psi_R = \exp(i\phi_R)$. We can then simply say that the interference wavefield formed at the detector ψ_M will be the superposition of ψ_S and ψ_R, yielding:

$$\psi_M = \psi_S + \psi_R. \tag{3.19}$$

Taking the squared modulus yields the intensity I_M:

$$\begin{aligned}
I_M &= |\psi_S + \psi_R|^2 \\
&= 2 + 2\mathrm{Re}(\psi_S\psi_R^*) \\
&= 2\left[1 + \cos(\phi_S - \phi_R)\right].
\end{aligned}$$
$$\tag{3.20}$$
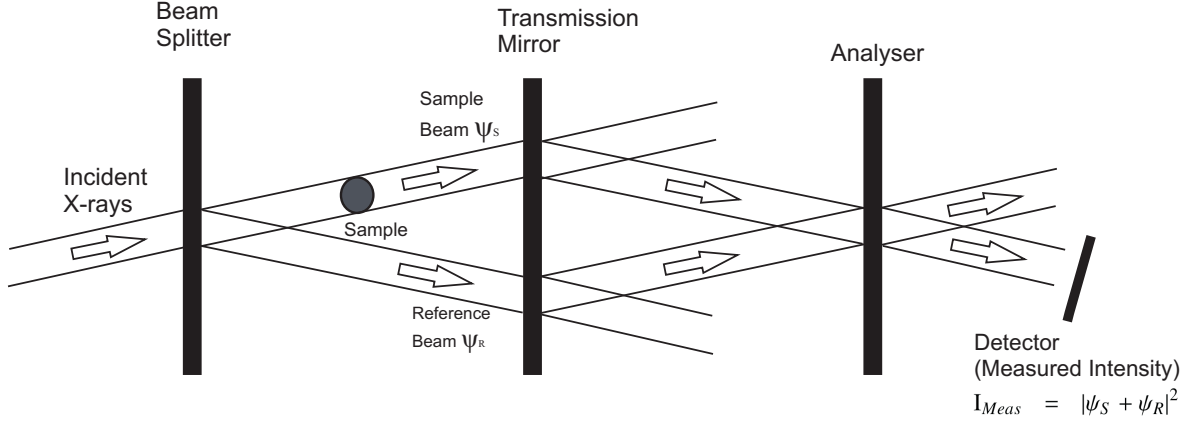
Figure 3.4: Schematic diagram illustrating the setup for a Bonse-Hart inferometer.

Note that the manipulations in Eqn. (3.20) assume that the normalised intensities $I_R = \psi_R \psi_R^*$ and $I_S = \psi_S \psi_S^*$ both equal unity. Also, we see from Eqn. 3.20 that interferograms can be interpreted as phase–contrast images whose measured intensity responds to transverse phase variations. X–ray interferometry is known to be very sensitive. In fact, it said to be the most sensitive of all the phase contrast techniques (Momose [54]). The contrast is manifest as a series of interference fringes. Some of its drawbacks, in addition to the high spatial and temporal coherence requirements, are that the optics need to be in an environment of extremely high stability. This creates great challenges, particularly when it comes to optical alignment (Momose [54]). Other interferometer designs exist, these include: Michelson, Mach–Zehnder, Fabry-Perot and Twyman-Green interferometers among others. However, like the Bonse–Hart interferometer they all require high spatial and temporal coherence as well as stable optics.

3.3.4   Analyser–based phase contrast imaging

Another well–known method for rendering phase contrast is via the use of an analyser crystal. This method is widely referred to as analyser–based phase contrast imaging (ABI) and has been applied in many imaging studies. Much of the seminal work done on ABI is found in Förster *et al.* [26], Somenkov [76], Ingal and Beliaevskaya [41], Davis *et al.* [23, 22], Davis [21], Davis and Stevenson [24] , Chapman *et al.* [14]. A schematic picture illustrating a conventional ABI setup is shown in Fig. 3.5. Essentially, ABI is relies on Bragg diffraction phenomena to render phase variations visible. The analyser crystal is positioned in such a way that its atomic planes satisfy the Bragg condition for a given X-ray energy. This is determined by Bragg's law:

$$n\lambda = 2d_s \sin(\theta_B), \tag{3.21}$$

where n is an integer, d_s is the spacing between the atomic planes and θ_B is the Bragg angle. Theoretically, under this condition the incident beam is mostly reflected. However,
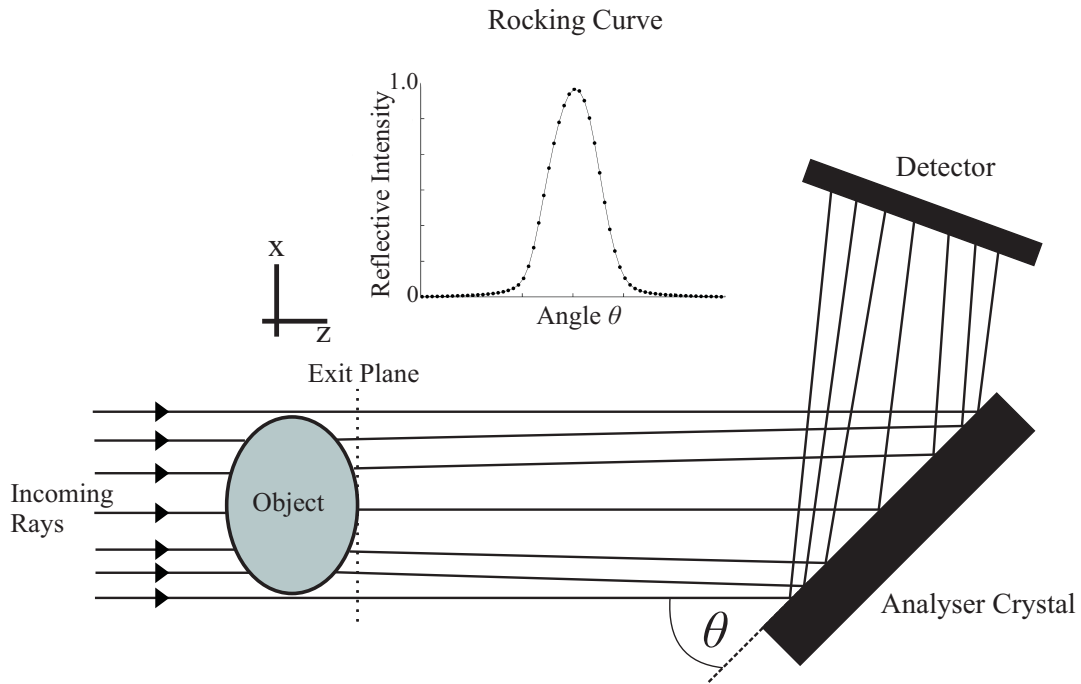
Figure 3.5: Schematic diagram illustrating the setup for analyser–based phase contrast imaging.

reflection not takes place in the crystal exactly at $\theta = \theta_B$, but also for a narrow angular range $\Delta\theta$. This is termed the Bragg reflection where its angular dependency of reflection is called the "rocking curve". In ABI the plane of diffraction is determined by the orientation of the crystal Bragg planes with respect to the incoming beam, which in turn determines the transverse direction in which the beam renders phase changes visible. Therefore ABI is only sensitive to phase changes in only one transverse direction; namely those that are parallel to the diffraction plane. The intensity at the detector is proportional to the gradient of the rocking curve. If the analyser is aligned at the half intensity point of the rocking curve then the intensity at the detector is approximately proportional to the first derivative of the phase with respect to x. Examples of images of a PMMA rod acquired using ABI at different orientations are shown in Fig. 3.6. Figure 3.6 (a) shows the image acquired with the analyser crystal oriented at the Bragg peak $\theta = \theta_B$. Here, the outer and inner edges of the rod are clearly seen. Figure 3.6 (b) shows the images acquired with the analyser crystal oriented at an angle corresponding to the right side of the rocking curve's half width at half maximum (HWHM) point. Here, greater enhancement of the rod's edges is seen. Note that at this crystal orientation the contrast is proportional to the first derivative with respect to x.

It has been shown that ABI produces high contrast images and it requires only a single optical element which reduces alignment issues. However, such advantages are also accompanied with some disadvantages. The most common of these is that it requires a high degree of temporal coherence to satisfy the Bragg condition. This makes it harder to

apply using laboratory sources, particularly for imaging large moving samples; thereby making clinical applications difficult to implement.
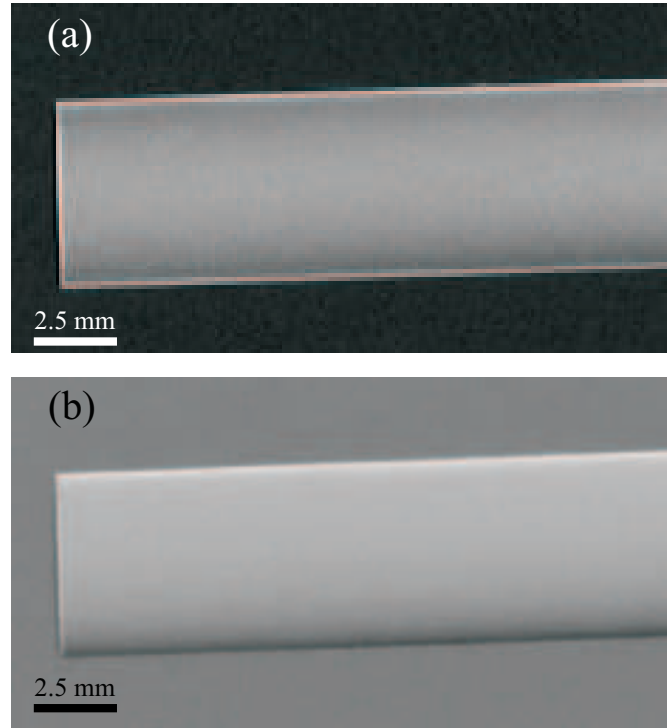
Figure 3.6: X–ray analyser–based phase–contrast images of a PMMA rod using 20 keV X–rays. (a) Imaged recorded at $\theta = \theta_B$. (b) Image recorded at the HWHM intensity point of the rocking curve (right side). Images acquired from Lewis *et al.* [49].

3.3.5   Grating–based differential phase–contrast imaging

Gratings are optical elements composed of equally spaced grid lines that can also be used to render phase variations visible. In the last decade the use of gratings in phase–contrast imaging has been adapted to X–ray sources, where various methods have been developed (Momose *et al.* [55], Weitkamp *et al.* [84], Takeda *et al.* [79], McDonald *et al.* [53]). Grating–based differential phase–contrast relies on the Talbot self–imaging effect. This effect arises as of result Fresnel diffraction from a periodic grating. It has been shown that at regular propagation distances the image of the grating is repeated (Talbot [80]). The distance where repeated images of the grating is formed is given by integer multiples of

$$d_T = \frac{2p_0^2}{\lambda}, \tag{3.22}$$

where d_T is the first Talbot distance of the grating G_0 and p_0 is its period (see Fig. 3.7).

In recent years grating–based X–ray differential phase–contrast imaging has attracted significant attention (David *et al.* [20], Momose *et al.* [55], Takeda *et al.* [79]). It has
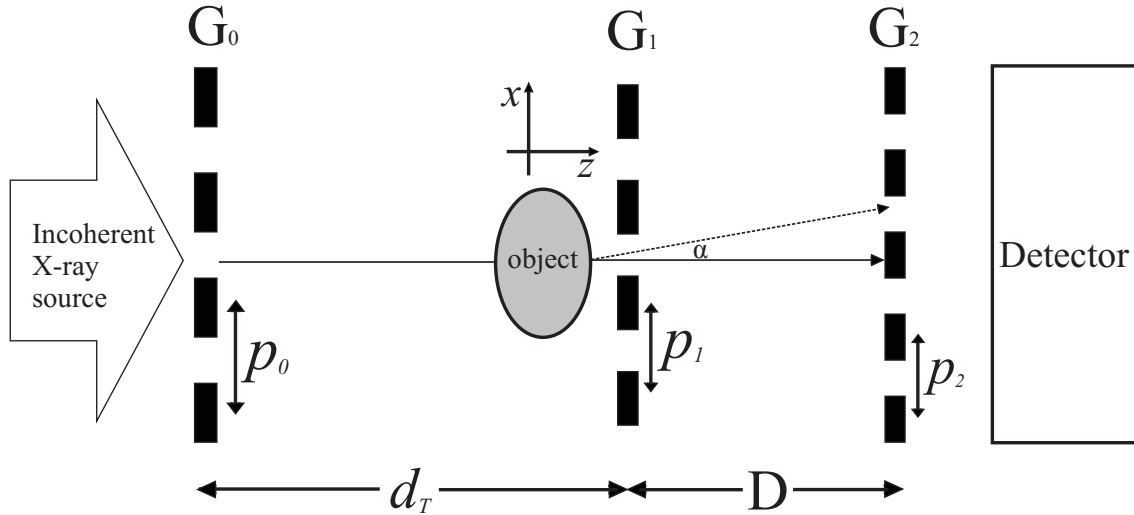
Figure 3.7: Schematic diagram illustrating the setup to perform grating–based differential phase–contrast imaging used by Pfeiffer *et al*. [71].

enabled the performance of high sensitivity phase–contrast imaging experiments with low-brilliance incoherent sources (i.e. X–ray tubes Pfeiffer *et al*. [71]). Due to its incredibly high sensitivity it has been shown to have enormous potential in biomedical imaging (Pfeiffer *et al*. [71], Herzen *et al*. [39], Stutman *et al*. [77], Donath *et al*. [25], Zambelli *et al*. [92]). Its sensitivity can be so great that many samples have to be immersed in water to reduce some of the high phase contrast signal produced in the intensity image caused by the sharp variation in refractive index between certain interfaces (i.e tissue/water). The elemental work in grating–based X–ray differential phase–contrast with low–brilliance sources was pioneered by Pfeiffer *et al*. [71]. The basic setup used is shown in Fig. 3.7. Here, grating G_0, which acts as an absorbing mask with transmitting slits, is placed close the X–ray tube anode that is used to created an array of individually partially coherent sources. This provides a beam with sufficient spatial coherence for differential phase–contrast image formation. A second and third grating G_1 and G_2 is placed at distances d_T and $d_T + D$ from G_0, respectively. The sample is positioned just before G_1. The distance D corresponds to the first Talbot distance of the grating G_1 which is determined by the formula (Talbot [80]):

$$D = \frac{2p_1^2}{\lambda}.$$ (3.23)

Here p_1 is the period of the grating G_1. The gratings G_1 and G_2 are responsible for producing differential phase–contrast where the image formed at the detector displays a phase contrast similar to that of analyser–based phase contrast imaging (Pfeiffer *et al*. [71]). Essentially, as the X–ray beam traverses the sample it undergoes a slight refraction causing angular deviations of the X–ray beam. The central idea behind grating interferometry depends on locally detecting these angular deviations. The angular deviations are directly

proportional to local gradients of the phase shifts imparted by the sample and are quantified by the following (Born and Wolf [8]):

$$\alpha = \frac{\lambda}{2\pi}\frac{\partial}{\partial x}\phi(x, y), \tag{3.24}$$

where, α denotes the refraction angle. Note that if the sample is weakly absorbing then the detected intensity is a direct measure of the phase gradients $\frac{\partial \phi(x,y)}{\partial x}$. In this case the total phase shifts of the sample can be recovered by simply integrating along the x–direction.

Further advancements have been made by Morgan *et al.* [58, 57, 56] where grid–based differential phase–contrast is performed with only one two–dimensional grating and can retrieve quantitative information using only a single exposure. Here, differential phase contrast is achieved in both the x and y directions. An initial exposure of the grid alone (no sample) is taken with a high spatial resolution detector positioned at the first Talbot distance. The sample is then placed just after the grid. This causes distortions to the image of the grid as a result of phase gradients induced by the sample. By using correlation analysis, the intensity shifts in small regions of images taken of the grid alone and of the grid plus sample allows the phase gradients in both the x and y–direction to be simultaneously retrieved using simple geometric relations. Images obtained of an airway interface of a mouse using only one two–dimensional grating with a single exposure are shown in Fig. 3.8. A raw image (unprocessed) is shown in Fig. 3.8 (a) where the magnified region displays the features of the two–dimensional grating pinholes. Figure 3.8 (b) shows an image of the phase gradients in the x–direction $\left(\frac{\partial \phi(x,y)}{\partial x}\right)$ and (c) the phase gradients in the y–direction $\left(\frac{\partial \phi(x,y)}{\partial y}\right)$. Figure 3.8 (d) is the retrieved projected thickness calculated from Figs. 3.8 (b) and (c).

The advancements made by Morgan *et al.* [58, 57, 56] avoid issues of optical alignment, however it still has some limitations. One of these limitations is resolution, which is restrained to the pinhole size of the grating. Another limitation is object size. When imaging larger objects (i.e the lungs) the grating needs to be highly absorbing in order to visualise the grid pattern, which is essential to carry out the correlation analysis. This implies some of the radiation is lost in making the grid pattern visible.

3.3.6   Propagation–based phase contrast imaging

Phenomena such as light focused through a glass lens and ripples observed in the bottom of a swimming pool are everyday examples of phase–contrast. These examples in particular occur thanks to the propagation of light used to visualise phase changes inferred by an object as intensity variations. This type of phase–contrast is widely known as "propagation–based phase–contrast" (PBI) and, in a way, has already been introduced in chapter 2 where Fresnel diffraction was discussed. Figure 3.9 shows a schematic depiction of a normal PBI setup where a detector is positioned at a distance d from the object. One of the major
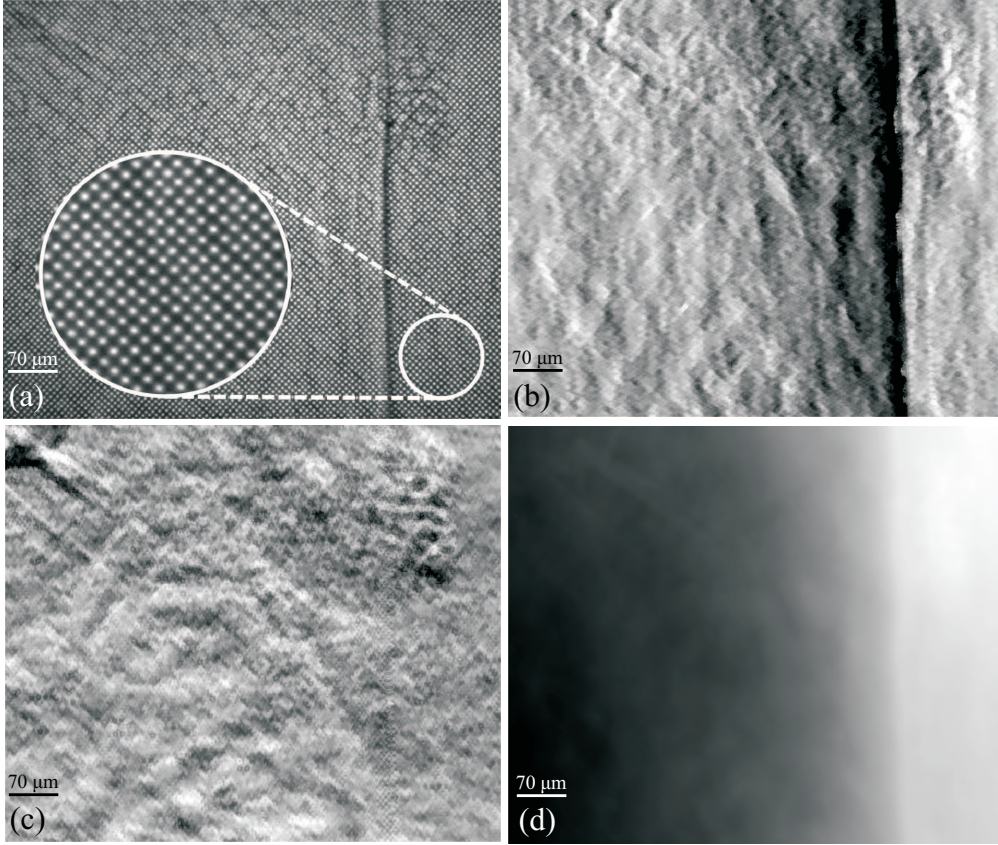
Figure 3.8: Images of an airway interface acquired using X–ray single–grating phase–contrast imaging techniques. (a) Shows a raw image taken at the first Talbot distance. (b) shows the phase gradients in the *x*-direction of (a). (c) shows the phase gradients in the *y*-direction of (a). (d) shows the projected thickness of the airway interface seen in (a). Images taken from Morgan *et al.* [57].

advantages PBI possesses is that it requires no optical elements between the object and detector in order to render a phase–contrast image.

We recall the Fresnel diffraction integral in Fourier operator form to formulate the theory of PBI (see Eqn. (2.28) of chapter 2):

$$\psi(\mathbf{r}_\perp, z = d) = \exp(ikd)\mathrm{F}^{-1}_{\mathbf{k}_\perp} \exp\left[\frac{-id\,|\mathbf{k}_\perp|^2}{2k}\right] \mathrm{F}_{\mathbf{r}_\perp}\psi(\mathbf{r}_\perp, z = 0). \qquad (3.25)$$

Here, $\psi(\mathbf{r}_\perp, z = d)$ denotes the complex wavefield formed at the detector plane, while $\psi(\mathbf{r}_\perp, z = 0)$ denotes the complex wavefield at the plane where X-rays just exit the object (see Fig. 3.9). If we consider a small propagation distance d then one can make the following approximation to the Fourier space propagator:

$$\exp\left[\frac{-id\,|\mathbf{k}_\perp|^2}{2k}\right] \approx 1 - \frac{id\,|\mathbf{k}_\perp|^2}{2k}. \qquad (3.26)$$
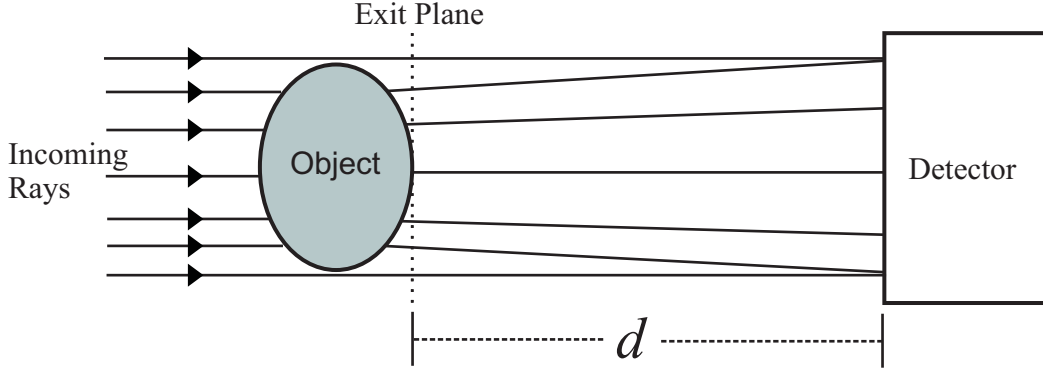
Figure 3.9: Schematic diagram illustrating propagation-based phase-contrast imaging.

Now, since we are interested in linking phase effects with the propagated intensity, for convenience we assume the exit scalar wavefield at $z = 0$ has the form $\exp[i\phi(\mathbf{r}_\perp, z = 0)]$. This omits attenuation in the intensity at $z = 0$, implying the object is transparent. By invoking the Fourier derivative theorem and making use of Eqn. (3.26), Eqn. (3.25) becomes

$$\psi(\mathbf{r}_\perp, z = d) = \exp(ikd)\left[1 + \frac{id\nabla_\perp^2}{2k}\right]\exp[i\phi(\mathbf{r}_\perp, z = 0)]. \qquad (3.27)$$

The intensity is obtained by taking the squared modulus, which gives:

$$I(\mathbf{r}_\perp, z = d) = 1 + 2Re\left\{\frac{id}{2k}\exp[-i\phi(\mathbf{r}_\perp, z = 0)]\nabla_\perp^2\exp[i\phi(\mathbf{r}_\perp, z = 0)]\right\}. \qquad (3.28)$$

With further manipulation one can arrive at the following, to first order in d (Bremmer [10]):

$$I(\mathbf{r}_\perp, z = d) = 1 - \frac{d}{2k}\nabla_\perp^2\phi(\mathbf{r}_\perp, z = 0)]. \qquad (3.29)$$

Arriving at the result in Eqn. (3.29) helps appreciate the essence of all propagation-based phase-contrast literature, in the regime of large Fresnel number (i.e. $N_f \gg 1$; see also section 2.4 of chapter 2). Here the forward propagation of the intensity is directly proportional to the transverse Laplacian of the exit surface phase. This forms the most fundamental concept for the majority of research studies done with PBI. It essentially provides phase contrast at high spatial frequencies. Physically, this yields enhancement of features where strong phase gradients occur, namely in boundaries between different refracting media. These enhancements are displayed in the intensity image as phase contrast fringes. An example of an X–ray PBI image is shown in Fig. 3.10, corresponding to the inflated lungs of a newborn rabbit pup. Here phase–contrast fringes can be appreciated throughout the images which enable enhancement of the features, particularly at their

boundaries. The strong speckle pattern[3] is seen as the result of the multiple refractions incurred by the beam as it propagated through the air pockets (alveoli) in the lungs (Kitchen *et al.* [46]).
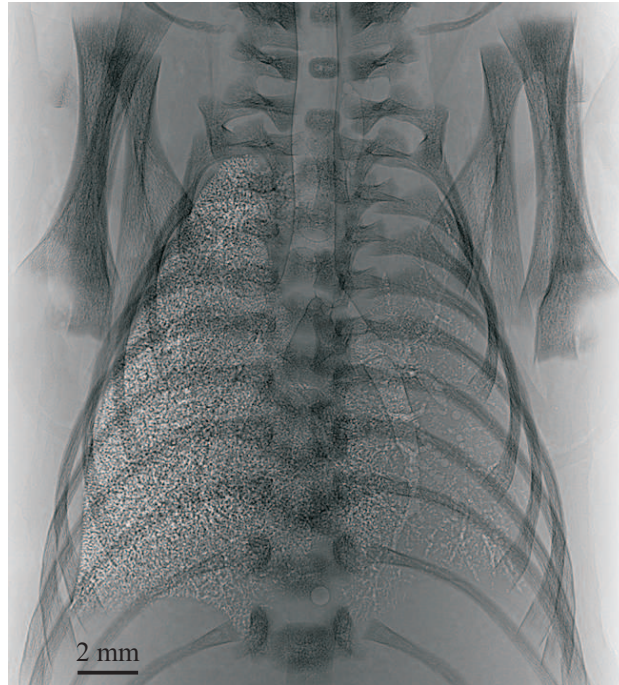
Figure 3.10: X–ray propagation-based phase–contrast images of the lungs of a newborn rabbit pup. Image acquired using 25 keV X–rays and a propagation distance $d = 2\ m$.

We close this section by making some remarks on the benefits of PBI. Aside from its practical simplicity, it has also been successfully applied using polychromatic sources (Wilkins *et al.* [85]). This was done by restricting the source size and having a long source–to–object distance to meet the spatial coherence requirements. Moreover, the magnification resulting from point source illumination can improve resolution (Wilkins *et al.* [85]). When is comes to medical imaging applications, PBI has already found its way to the clinic. For example, Konica Minolta Pty. Ltd. developed an X–ray mammography unit based on PBI (Tanaka *et al.* [81]). The image contrast and quality shows significant improvement over conventional attenuation based X–ray mammography. Due to these great advantages of PBI we have chosen to focus on this technique for the bulk of the thesis, providing new image reconstruction approaches and experimental data in chapter 4 and chapter 5. As such, we focus exclusively on quantitative propagation–based phase–contrast methods for the remainder of this chapter.

---

[3]Speckle patterns appear as a result of multiple wavefronts of the same frequency interfering with each other. Each wavefront has a different amplitude such that when added together the intensity varies randomly (Born and Wolf [8]).

3.4 Phase retrieval methods

Up until now we have been discussing the various methods to render phase variations as intensity variations as a result of the phase–contrast imaging system. These are examples of what is referred to as the 'forward problem'. In practice, detectors only measure the intensity but not the phase distribution of a complex scalar wavefield (i.e. $I = |\psi|^2 = A^2$) hence all phase (ϕ; complex) information is lost. In this section we discuss the associated 'inverse problem', which involves measuring or retrieving quantitative information about a sample from either one or a series of phase-contrast images. Phase retrieval is an example of the 'inverse problem' whereby either analytic or iterative methods can be used to calculate phase distributions from intensity measurements. In recent years, problems of phase retrieval have created their own area of study in the field of coherent X-ray optics and have generated a vast amount of literature. Despite all the advances made in the area of phase retrieval, it is still an ongoing problem. Difficulties associated with phase retrieval arise due to practical limitations. This section discusses some of he successfully applied phase retrieval algorithms that are valid within the Fresnel regime, that is, near ($N_F \gg 1$) and intermediate ($N_F \approx 1$) fields (see section 2.4 of chapter 2).

3.4.1 The transport–of–intensity equation

When we consider contrast formed as result of free–space propagation in the near Fresnel regime, where $N_f \gg 1$ (i.e. PBI), the paraxial approximation proves advantageous. Plenty of the analytical phase retrieval methods in the literature are developed using the transport–of–intensity equation (TIE) (Teague [82]). To derive the TIE, firstly we consider the inhomogeneous paraxial wave Eqn. (3.4) in free-space (i.e. $n(\mathbf{r}) = 1$). Considering this, Eqn. (3.4) reduces to:

$$\left(2ik\frac{\partial}{\partial z} + \nabla_\perp^2\right)\psi(\mathbf{r}) = 0.$$

(3.30)

Expressing the complex scalar wavefield in terms of its intensity and phase as[4]:

$$\psi = \sqrt{I}\exp(i\phi),$$

(3.31)

and inserting Eqn. (3.31) into Eqn. (3.30), expanding all terms, cancelling similar ones and factoring out $\exp(i\phi)$ gives the following:

$$-ik\frac{1}{\sqrt{I}}\frac{\partial I}{\partial z} - 2\sqrt{I}\frac{\partial \phi}{\partial z} + \nabla_\perp^2\sqrt{I} - i\frac{1}{\sqrt{I}}\nabla_\perp I \cdot \nabla_\perp\phi - i\frac{1}{\sqrt{I}}I\nabla_\perp^2\phi - \sqrt{I}(\nabla_\perp\phi)^2 = 0. \quad (3.32)$$

---

[4]Note, that the $\mathbf{r}$ dependence of the functions ψ, I and ϕ have been momentarily dropped for simplicity.

Taking the imaginary part gives the resulting equation;

$$-k\frac{1}{\sqrt{I}}\frac{\partial I}{\partial z} - \frac{1}{\sqrt{I}}\nabla_\perp I \cdot \nabla_\perp \phi - \frac{1}{\sqrt{I}}I\nabla_\perp^2 \phi = 0. \tag{3.33}$$

We factor out $1/\sqrt{I}$ and use the identity $\nabla \cdot (A\nabla B) = \nabla A \cdot \nabla B + A\nabla^2 B$ to give the following continuity equation, commonly known as the transport-of-intensity equation (Teague [82]):

$$\nabla_\perp \cdot [I(\mathbf{r})\nabla_\perp \phi(\mathbf{r})] = -k\frac{\partial I(\mathbf{r})}{\partial z}. \tag{3.34}$$

This second order elliptic partial differential equation is as an expression that describes the local conservation of optical energy as wavefields evolve from one plane $z = z_1$ to another infinitesimally separated parallel plane $z = z_2$.

Numerous algorithms exist that numerically solve for the phase function ϕ using the TIE as a basis, by treating I and $\partial I/\partial z$ in Eqn. (3.34) as measurable input data. One of the commonly used algorithms of Paganin and Nugent [66] uses the TIE to recover phase information via the following relation:

$$\phi(\mathbf{r}_\perp) = -k\nabla_\perp^{-2}\left(\nabla_\perp \cdot \left\{ \frac{1}{I(\mathbf{r}_\perp)}\nabla_\perp \left[\nabla_\perp^{-2}\frac{\partial I(\mathbf{r}_\perp)}{\partial z} \right] \right\}\right). \tag{3.35}$$

The intensity derivative $\partial I/\partial z$ can be approximated by taking the difference over two images closely spaced together separated by $|z_2 - z_1|$, as shown Fig. 3.11. It is important to note that Eqn. (3.35) calculates the phase $\phi(\mathbf{r}_\perp)$ at the plane distanced half-way between $z = z_1$ and $z = z_2$. Equation (3.35) can be easily numerically implemented by making use of the discrete Fast Fourier transform as:

$$\phi(\mathbf{r}_\perp) = k F_{k_x,k_y}^{-1} \frac{k_x}{k_x^2 + k_y^2} F_{x,y} \left\{ \frac{1}{I} F_{k_x,k_y}^{-1} \frac{k_x}{k_x^2 + k_y^2} F_{x,y} \left(\frac{I_{z_2} - I_{z_1}}{|z_2 - z_1|} \right) \right\}. \tag{3.36}$$

Here $F_{x,y}$ denotes the forward Fourier transform with respect to (x, y) and F_{k_x,k_y}^{-1} denotes the inverse Fourier transform with respect to (k_x, k_y). Note that implementation of Eqn. (3.36) requires two intensity images collected at separate distances as inputs. This implies that the imaged sample in theory incurs around twice the radiation dose than if only one image was required, which limits its applicability in areas such as biological imaging. Also, in cases where during experiments the images are collected at separate instances, issues of alignment often arise. This also makes it more difficult to correct the non uniformities across the beam. Another drawback of Eqn. (3.36) is its numerical instability under the presence of low spatial frequency noise originating due to zeroes in the term $k_x/(k_x^2 + k_y^2)$.
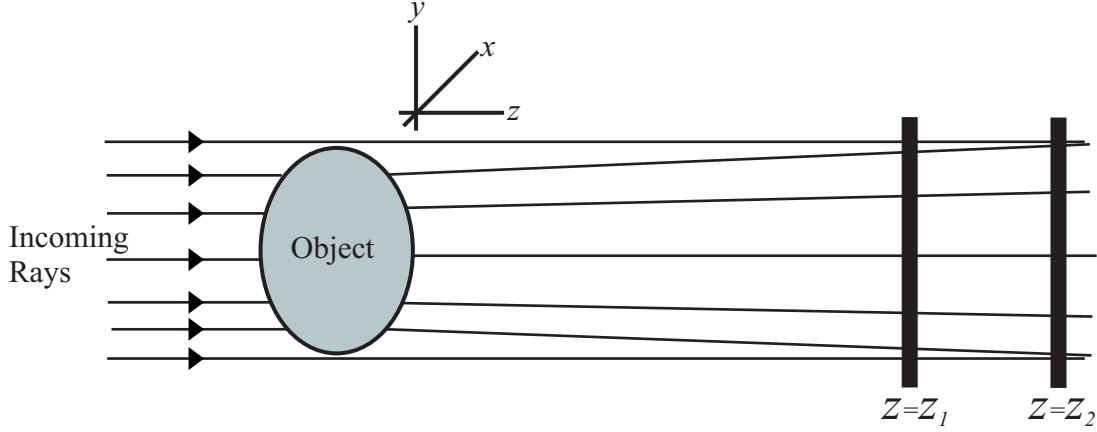
Figure 3.11: Illustration of imaging setup in order to perform phase retrieval with two parallel closely spaced intensity images.

3.4.2   The contrast–transfer function

Generally, diffraction effects due to free-space propagation can be quantified in terms of a 'transfer function' acting upon an input wavefield that yields the output wavefield. The free-space propagator function used in Eqn. (2.28) for Fresnel diffraction is such a transfer function. The contrast–transfer function (CTF) method makes use of the Fourier spectrum analysis of the intensity pattern under Fresnel diffraction and was first formulated by Guigay *et al.* [33]. There, the author assumes the object satisfies the "weak phase–amplitude approximation" and later takes the Fourier transform of the intensity distribution created at a propagation distance z that lies within the Fresnel regime. The "weak phase–amplitude approximation" is given by

$$\exp[-\mu(x, y) + i\phi(x, y)] \approx 1 - \mu(x, y) + i\phi(x, y). \tag{3.37}$$

The functions $\mu(x, y)$ and $\phi(x, y)$ are the absorption and phase function at the contact plane $z = 0$. They are defined as line integrals along the real and imaginary component of the object's complex refractive index. This approximation ultimately lead to the following expression known as the contrast–transfer function formulation (Guigay *et al.* [33]):

$$\widetilde{I}(k_x, k_y) = \widehat{\delta}(k_x, k_y) - 2\cos\left[\frac{\lambda z}{4\pi}(k_x^2 + k_y^2)\right]\widetilde{\mu}(k_x, k_y) + 2\sin\left[\frac{\lambda z}{4\pi}(k_x^2 + k_y^2)\right]\widetilde{\phi}(k_x, k_y) \tag{3.38}$$

The Fourier transform of the intensity is denoted by $\widetilde{I}(k_x, k_y)$ with k_x and k_y being dual to the coordinates x and y, respectively. The functions $\widetilde{\mu}(k_x, k_y)$ and $\widetilde{\phi}(k_x, k_y)$ are the Fourier transforms of the functions $\mu(x, y)$ and $\phi(x, y)$, respectively. $\widehat{\delta}(k_x, k_y)$ is defined here as the Dirac-delta function.

With the expression in Eqn. (3.38) a number of phase retrieval algorithms have been developed. We state here the algorithm derived by Turner *et al.* [83] as it of one of the

most relevant algorithms that competes with the key algorithms derived in this thesis (see Eqn. (4.21)). The algorithm of Turner *et al.* [83] has a restriction that only allows it to be applied to objects comprised of a single material, in addition to the approximation of monochromatic scalar paraxial radiation. Under these restrictions the phase $\phi(\mathbf{r}_\perp, z = 0)$ exiting the object is given by:

$$\phi(\mathbf{r}_\perp, z = 0) = \mathrm{F}_{k_x,k_y}^{-1}\left[\frac{\delta}{2\left(\beta \cos\left[\frac{\lambda z}{4\pi}(k_x^2 + k_y^2)\right] + \delta \sin\left[\frac{\lambda z}{4\pi}(k_x^2 + k_y^2)\right]\right)}\mathrm{F}_{x,y}\left\{\frac{\mathrm{I}(\mathbf{r}_\perp, z = d)}{\mathrm{I}_0} - 1\right\}\right].$$

(3.39)

Note that to implement Eqn. (3.39) one requires *a priori* knowledge of the object's complex refractive index, namely δ and β. Also, it is key to notice that zeroes appear in the denominator thus producing singularities in the solution that may cause an over amplification of certain spatial frequencies. This represents a genuine loss of information (Turner *et al.* [83]). The problem of singularities may be circumvented by taking additional images at a range of propagation distances z.

3.5   Phase and amplitude computed tomography

Tomography is the science that involves the study of sections or slices of an object. The problem of recovering a two–dimensional function (slice) from projections (line integrals) over rotating angles is one that was brought to light and solved by Johan Radon [72]. Tomographic techniques have broad applications especially in areas such as diagnostic medicine where apparati, known as Computed Tomography (CT) scanners, are used to obtain three–dimensional images that enable visualisation of the internal structure of organs in a non-invasive manner. The fundamental principles of tomography are covered in section 3.5.1. Section 3.5.2 discuses the application of tomography to phase–contrast X–ray imaging. Methods that combine the phase retrieval and tomographic process in single–step approach are discussed in section 3.5.3.

3.5.1   Tomography principles and the Fourier slice theorem

This section describes the mathematical procedure that enables the reconstruction of a two–dimensional slice from a series of projections. A two–dimensional slice can be described by the complex function $f(x_1, x_2)$. First, one needs to set up an appropriate coordinate system that conveniently describes straight–line ray paths along a function $f(x_1, x_2)$ for a given angle Ω about the origin. Figure 3.12 shows a two–dimensional function $f(x_1, x_2)$ with a series of straight parallel lines used to define integrals along straight ray–paths that comprise a projection of $f(x_1, x_2)$ at a given angle Ω. The variable s is the distance from the origin to an arbitrary line. Each line has a normal vector $\widehat{n} = (\cos \Omega, \sin \Omega)$ that can be
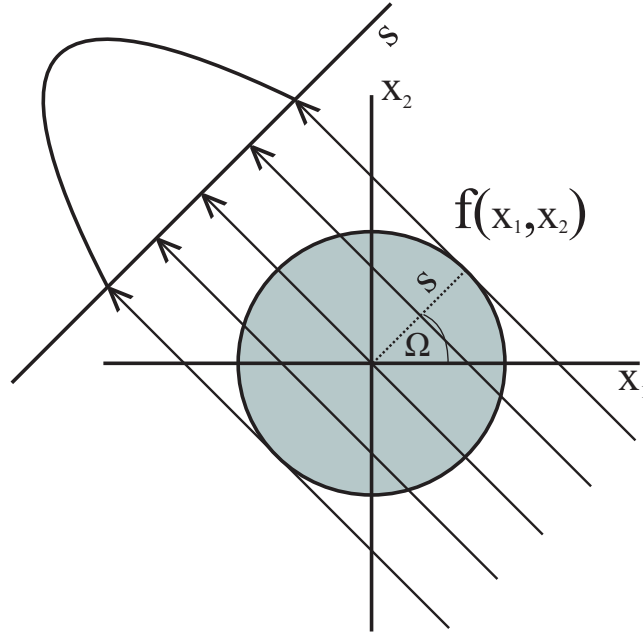
Figure 3.12: Digram showing a series of parallel line integrals along the object function $f(x_1, x_2)$. s and Ω are polar coordinates. s is the radius from the origin which becomes the independent variable in the projection space. Ω is the angle from the x axis which rotates over π radians.

used to describe straight lines across the plane for any angle Ω with the equation (Kak and Slaney [43]):

$$x_1 \cos \Omega + x_2 \sin \Omega = s. \tag{3.40}$$

The range of values taken by s and Ω are $0 \le \Omega < \pi$ and $-\infty \le s < \infty$ respectively. The line integrals along $f(x_1, x_2)$ defines the Radon transform:

$$\Re[f](s, \Omega) = \int_{-\infty}^{\infty} \int_{-\infty}^{\infty} f(x_1, x_2) \widehat{\delta}(s - x_1 \cos \Omega - x_2 \sin \Omega) dx_1 dx_2. \tag{3.41}$$

Here, $\Re$ is the symbol defining the Radon transform which maps f on to (s, Ω) space. The Radon transform of a function is also known as a 'sinogram' since projections of a distinct feature follows a sinusoidal path along varying angles (see Fig. 3.13 (b)). Equation 3.41 utilises the Dirac delta function labelled here as $\widehat{\delta}(x)$.

Before proceeding we recall the Fourier transform convention used in this thesis:

$$F_s \{G\} = \frac{1}{\sqrt{2\pi}} \int_{-\infty}^{\infty} G(s) \exp(-i\nu s) ds. \tag{3.42}$$

Here, the variable ν is dual to s.

The aim of tomography is to invert the Radon transform in Eqn. (3.41) in order to recover the function $f(x_1, x_2)$. This can be achieved by invoking the 'Fourier slice theorem' (Kak and Slaney [43]). The Fourier slice theorem states that the one–dimensional Fourier transform of each one–dimensional projection with respect to s is directly related to the two dimensional Fourier transform of $f(x_1, x_2)$ with respect to (x_1, x_2). With the definition in Eqn. (3.42) one may prove, by changing the order of integration and making the change of variables $\zeta_1 = v \cos \Omega$ and $\zeta_2 = v \sin \Omega$, that the continued one–dimensional Fourier transform of all of the projections is equal to the two–dimensional Fourier transform of the function $f(x_1, x_2)$. This is demonstrated in Eqn. (3.43) (Kak and Slaney [43]):

$$
\begin{aligned}
F_s \{\Re[f]\} &= \frac{1}{\sqrt{2\pi}} \int_{-\infty}^{\infty} \left[\int_{-\infty}^{\infty} \int_{-\infty}^{\infty} f(x_1, x_2) \widehat{\delta}(s - x_1 \cos \Omega - x_2 \sin \Omega) dx_1 dx_2 \right] \exp(-ivs) ds \\
&= \frac{1}{\sqrt{2\pi}} \int_{-\infty}^{\infty} \int_{-\infty}^{\infty} \left[\int_{-\infty}^{\infty} \exp(-ivs) \widehat{\delta}(s - x_1 \cos \Omega - x_2 \sin \Omega) ds \right] f(x_1, x_2) dx_1 dx_2 \\
&= \frac{1}{\sqrt{2\pi}} \int_{-\infty}^{\infty} \int_{-\infty}^{\infty} \exp[-i(vx_1 \cos \Omega + vx_2 \sin \Omega)] f(x_1, x_2) dx_1 dx_2 \\
&= \sqrt{2\pi} \times \frac{1}{2\pi} \int_{-\infty}^{\infty} \int_{-\infty}^{\infty} \exp[-i(x_1 \zeta_1 + x_2 \zeta_1)] f(x_1, x_2) dx_1 dx_2 \\
&= \sqrt{2\pi} \times F_{x_1,x_2}[f](\zeta_1, \zeta_2). \quad\quad (3.43)
\end{aligned}
$$

With the relation $F_s \{\Re[f]\} = \sqrt{2\pi} \times F_{x_1,x_2}[f](\zeta_1, \zeta_2)$ one is able to invert the Radon transform and recover the function $f(x_1, x_2)$. This process is known as filtered backprojection, which is implemented as the following operation:

$$
\begin{aligned}
f(x_1, x_2) &= \frac{1}{\sqrt{2\pi}} F_{\zeta_1,\zeta_2}^{-1} [F_s \{\Re[f]\}] \\
&= \frac{1}{\sqrt{2\pi}} \times \frac{1}{2\pi} \int_{-\infty}^{\infty} \int_{-\infty}^{\infty} F_s \{\Re[f]\} \exp[i(x_1 \zeta_1 + x_2 \zeta_2)] d\zeta_1 d\zeta_2. \quad (3.44)
\end{aligned}
$$

In words, the operation in Eqn. (3.44) describes the following procedure: (i) take the one–dimensional Fourier transform of each row of the Radon transform (sinogram) with respect to s; (ii) take the two–dimensional inverse Fourier transform of the result with respect to (ζ_1, ζ_2) to recover the function $f(x_1, x_2)$. Alternatively, Eqn. (3.44) can be expressed in a more compact form which gives further physical insight. This can be shown by changing the variables inside the integral into their corresponding polar coordinates (v, Ω). The polar form of the differential elements $d\zeta_1$ and $d\zeta_2$ can be calculated via the Jacobian matrix:

$$
\begin{aligned}
d\zeta_1 d\zeta_2 &= d(v \cos \Omega) d(v \sin \Omega) \\
&= \left| \det \begin{pmatrix} \frac{\partial}{\partial v}(v \cos \Omega) & \frac{\partial}{\partial \Omega}(v \cos \Omega) \\ \frac{\partial}{\partial v}(v \sin \Omega) & \frac{\partial}{\partial \Omega}(v \sin \Omega) \end{pmatrix} \right| dv d\Omega. \\
&= |v| \, dv d\Omega. \quad\quad (3.45)
\end{aligned}
$$
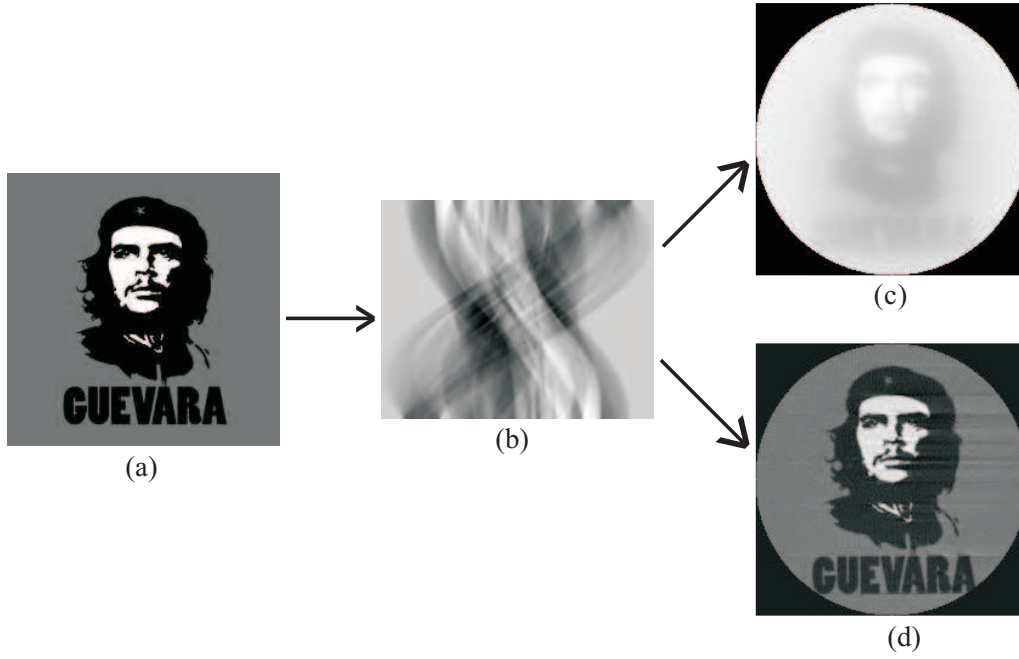
Figure 3.13: Figure showing a CT simulation of the image in (a). (b) is the sinogram of (a) produced with 180 projections. (c) shows a reconstruction of the sinogram in (b) without filtering before backprojecting. (d) also shows a reconstruction of the sinogram in (b) but this time the sinogram is filtered with the function $|\nu|$ before backprojecting. (a) has a size of 225×225 pixels.

Hence, Eqn. (3.44) becomes

$$f(x_1, x_2) \quad = \quad \frac{1}{2\pi} \int_0^\pi \left[\frac{1}{\sqrt{2\pi}} \int_{-\infty}^\infty F_s \{\Re[f]\} |\nu| \exp[i\nu s] d\nu \right] d\Omega. \qquad (3.46)$$

It can be seen that the inner integral of Eqn. (3.46) displays the form of a Fourier convolution, which enables it to be re–written in the more abbreviated form:

$$f(x_1, x_2) = \frac{1}{2\pi} \int_0^\pi F_\nu^{-1} |\nu| F_s \{\Re[f]\} \, d\Omega. \qquad (3.47)$$

This helps clarify why Eqn. (3.47) carries the name of filtered backprojection as a Fourier filtering process naturally appears in the inversion. In this case the Radon transform $\Re[f](s, \Omega)$ is Fourier filtered with the function $|\nu|$ known as the Ram–Lak filter (Ramachandran and Lakshminarayanan [73]). The filtering process is essential when reconstructing real tomographic data sets given that only a finite number of projections can be acquired. Having a finite number of projections has consequences of under–sampling high spatial frequency information of the function. To compensate for this drawback the sinogram (Radon transform) is filtered with a high–pass Fourier filter before backprojecting into real space (x_1, x_2). The effects of filtering the sinogram before backprojecting can be shown

in Fig. 3.13. The Radon transform of Fig. 3.13 (a) in shown in Fig. 3.13 (b). The back-projected reconstruction with and without filtering of Fig. 3.13 (b) is shown in Fig. 3.13 (d) and Fig. 3.13 (c), respectively, where the difference in backprojection reconstruction quality is clearly evident.

Also important is the number of projections acquired in a tomographic data set. Naturally, the higher the number of projections taken the better the object information is sampled, therefore the higher the quality of the reconstructed image. This is demonstrated in Fig. (3.14). Here tomographic simulations were performed with varying number of projections. We see how increasing the number of projections improves the reconstruction quality. Normally, when tomographic experiments are performed an optimal number of projections is estimated. This estimation mainly depends on the number of pixels the imaged object covers over the detector window (Kak and Slaney [43]).
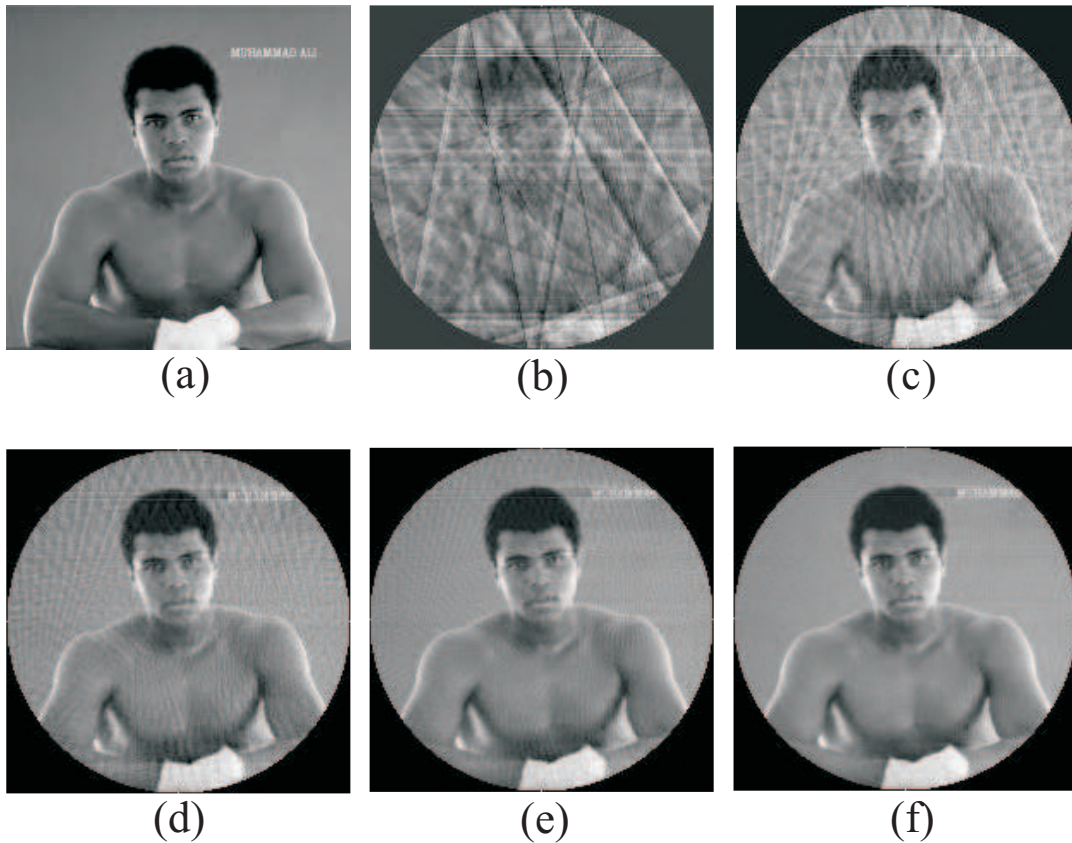
Figure 3.14: CT simulations with varying number of projections. (a) is the original image with size of 200×200 pixels. (b) CT reconstruction performed with 10 projections. (c) reconstruction with 30 projections. (d) reconstruction with 60 projections. (e) reconstruction with 90 projections. (f) reconstruction with 180 projections.

3.5.2 Theory of phase–contrast tomography

Phase contrast tomography allows visualisation of the internal structures of weakly absorbing objects. Also, it allows the quantitative reconstruction of the real part of the three–dimensional complex refractive index distribution. In this case the real part is denoted as $\delta(x_1, x_2, x_3)$. In simple terms the core idea of phase–contrast tomography is to merge phase–retrieval methods with tomographic principles. In general this is done in a two–step process. First, the phase $\phi_0(s, u, \Omega)$ of the exit wavefield is calculated at each tomographic projection. Second, the phase–retrieved images are then backprojected, thus obtaining $\delta(x_1, x_2, x_3)$. This follows directly from the projection approximation where the exit phase function can be expressed as a Radon transform (Bronnikov [11]):

$$
\begin{aligned}
\phi_0(s, u, \Omega) &= -k \int_{-\infty}^{\infty} \int_{-\infty}^{\infty} \delta(x_1, x_2, u)\widehat{\delta}(s - x_1 \cos \Omega - x_2 \sin \Omega) dx_1 dx_2 \\
&= -k \Re[\delta](s, u, \Omega).
\end{aligned}
\tag{3.48}
$$

The introduced variable u is used to represent the vertical axis at the projected plane. Given this relation, the real part of the complex refractive index distribution is calculated via:

$$
\delta(x_1, x_2, x_3) = -\frac{1}{2\pi k} \int_0^\pi F_{\nu,\xi}^{-1} |\nu| \, F_{s,u} \{\phi_0(s, u, \Omega)\} \, d\Omega.
\tag{3.49}
$$

The coordinate ξ is dual to u. Note, that the two dimensional forward and inverse Fourier transforms in Eqn. (3.49) have been defined as:

$$
\begin{aligned}
F_{s,u}\{G\} &= \frac{1}{2\pi} \int_{-\infty}^{\infty} G(s, u) \exp[-i(\nu s + \xi u)] ds du, \\
F_{\nu,\xi}^{-1}\{\widetilde{G}\} &= \frac{1}{2\pi} \int_{-\infty}^{\infty} \widetilde{G}(\nu, \xi) \exp[i(\nu s + \xi u)] d\nu d\xi.
\end{aligned}
\tag{3.50}
$$

3.5.3 Single–step approach

In the context of X-ray phase contrast imaging, the seminal work was derived by Bronnikov [11, 12]. In this work, phase retrieval and tomography are combined into a single–step approach. The omission of the phase retrieval process to each tomographic image holds advantages in terms of computational efficiency. This derivation used Fresnel diffraction theory to relate the intensity downstream from the object to its projected exit phase in the near Fresnel regime. This implies that the propagation distance should be small enough such that only a single fringe is formed at the detector. Additionally, the imaged object is considered to be a 'pure phase object', which is non–absorbing. To begin, the intensity of the incoming wavefield is uniform (i.e. $I_{in} = 1$). The exit phase is then calculated via:

$$
\phi_0(s, u, \Omega) = k F_{\nu,\xi}^{-1} \left\{ \frac{1}{d(\nu^2 + \xi^2)} F_{s,u} [I_d(s, u, \Omega) - 1] \right\},
\tag{3.51}
$$

where $I_d(s, u, \Omega)$ is the phase–contrast intensity formed at a distance d downstream from the object for an arbitrary tomographic angle Ω. Substituting Eqn. (3.51) into the filtered backprojection formula in Eqn. (3.49) allows the merger of functions in Fourier space, which enables the complex refractive index $\delta(x_1, x_2, x_3)$ to be calculated with the formula:

$$\delta(x_1, x_2, x_3) = -\frac{1}{2\pi} \int_0^\pi F_{\nu,\xi}^{-1} \frac{|\nu|}{d(\nu^2 + \xi^2)} F_{s,u} \{I_d(s, u, \Omega) - 1\} \, d\Omega. \tag{3.52}$$

Further adjustments to this formulation were made by Gureyev *et al.* [38]. As opposed to the non–absorbing and small d restrictions, the formulation of Gureyev *et al.* [38] combines the CTF–based phase retrieval approach discussed in section 3.4.2 with Eqn. (3.49). This way the object is now only restricted to the "single–material weak phase–amplitude approximation". Also, their method is valid at higher propagation distances within the Fresnel regime. The formula is given by

$$\begin{aligned}
\delta(x_1, x_2, x_3) &= -\frac{1}{2\pi} \int_0^\pi F_{\nu,\xi}^{-1} \left[\widetilde{g}(\nu, \xi) F_{s,u} I_d(s, u, \Omega) - 1 \right] d\Omega \\
\widetilde{g}(\nu, \xi) &= \frac{|\nu|}{2 \left\{ \sin[\frac{\lambda d}{4\pi}(\nu^2 + \xi^2)] + \frac{\beta}{\delta} \cos[\frac{\lambda d}{4\pi}(\nu^2 + \xi^2)] \right\}}.
\end{aligned} \tag{3.53}$$

Note that this method inherits the same limitations that arise from the CTF based approach. This is mainly the over amplification of certain spatial frequencies, thus suffering from numerical instability at certain distances d.

3.6   Concluding remarks

Chapters 2 and 3 have reviewed the theoretical and experimental background that will be employed throughout the remainder of this thesis. The remaining chapters of the thesis comprise original research that builds upon this background.

2D and 3D X–ray phase retrieval of multi–material objects

<div style="text-align: right">4</div>

4.1   Introduction

In chapter 3 it was shown that phase–contrast X–ray imaging is a very powerful tool for visualizing weakly absorbing features inside a sample as the changes in the phase of the X–ray wavefield induced by variations in refractive index across the sample are rendered visible in the measured intensity. Out of the various phase–contrast imaging modalities discussed in chapter 3 we saw how propagation–based X–ray phase contrast imaging (PBI) omits the need for any optical elements between the illuminating radiation and the detector, thus making it one of the simplest phase–contrast X–ray imaging modalities in terms of practicality. For this reason we focus on this modality in this chapter.

When PBI is combined with computed tomography (CT) the visualization of an object's internal structure is significantly improved over conventional absorption–based CT (Cloetens *et al*. [18]). However, this only provides a better qualitative 3D image but infers no quantitative information about the imaged object. The combinations of phase retrieval methods with CT makes quantitative phase–contrast imaging in 3D possible. In section 3.5.3 algorithms that perform phase and amplitude computed tomography were discussed, namely those derived by Bronnikov [11, 12] and Gureyev *et al*. [38]. These algorithms carry out the phase retrieval and tomography procedure in a single step, which provides greater numerical efficiency. Also, they possess the advantage of only requiring a single PBI image per projection. Nevertheless, they are still restricted to samples comprised of a single–material and that are weakly absorbing. Also, these methods are unstable under the presence of low spatial frequency noise.

Paganin *et al*. [65] developed a phase retrieval algorithm that is robust under the presence of noise and also only requires a single phase-contrast image. This algorithms includes the effects of absorption and phase contrast without making any weak–based approximations. It has been successfully applied in subsequent tomographic investigations Mayo *et al*. [52]. However, the the algorithm is still restricted to single–material objects and only operates within the validity of the TIE.

In this chapter[1], the work of Paganin *et al.* [65] is extended by presenting a noise-robust method to perform quantitative phase contrast tomography on a multi–material object where its complex refractive index is spatially quantized. The algorithm uses a single PBI image per tomographic projection. This allows the object under study to incur no additional radiation dose compared to that imparted in conventional absorption contrast tomography. The method involves separately reconstructing each interface between any given pair of distinct materials. Once all interfaces are quantitatively reconstructed each of these can used to produce a single spliced tomogram with all interfaces exhibiting the correct refractive index distribution. Section 4.2.1 of the chapter reviews the phase retrieval derived by Paganin *et al.* [65]. Section 4.2.2 shows the derivation of the extension to the work of Paganin *et al.* [65], which constitutes the original work crucial to this chapter and to chapter 5. An experimental implementation in shown in Section 4.3. Some concluding remarks are given in section 4.4.
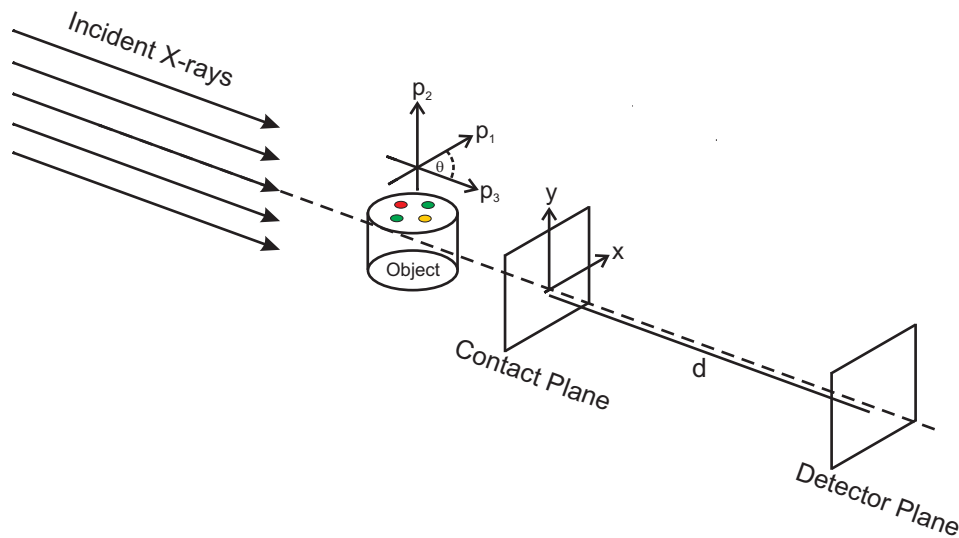
Figure 4.1: Experimental setup showing the imaging geometry and coordinate system for propagation-based phase contrast tomography.

4.2   Theory

In this section we outline the theory for quantitative phase-amplitude tomography of a multi-material object with a quantized distribution of complex refractive indices (i.e. a "spatially quantized object"). Section 4.2.1 reviews an existing theory for two–dimensional (2D) single-image propagation-based phase retrieval of a one–material object, with section 4.2.2 generalizing this to the case of 2D single–image phase retrieval of an object of a given material which is embedded in a matrix of a second material. Section 4.2.3 generalizes this

---

result to the case of three–dimensional (3D) propagation–based phase–contrast imaging of spatially–quantized objects, given a single image per projection.

4.2.1 Two–dimensional phase retrieval for a binary object

In this derivation we consider a radiation source that is paraxial and monochromatic. For such sources the phase and intensity of a wavefield downstream of the object under study obeys the Transport–of–Intensity equation (TIE) (Teague *et al.* [82]). Therefore we begin by restating the TIE (see also Eqn. (3.34)):

$$\nabla_\perp \cdot \left[I(\mathbf{r}_\perp, z) \nabla_\perp \phi(\mathbf{r}_\perp, z) \right] = -k \frac{\partial I(\mathbf{r}_\perp, z)}{\partial z}. \tag{4.1}$$

We remind the reader that the intensity and phase of the scalar wavefield are denoted by $I(\mathbf{r}_\perp, z)$ and $\phi(\mathbf{r}_\perp, z)$, the position vector $\mathbf{r}_\perp = (x, y)$ is perpendicular to the optic axis z, $\nabla_\perp = \left(\frac{\partial}{\partial x}, \frac{\partial}{\partial y} \right)$ is the transverse gradient operator, and $k = \frac{2\pi}{\lambda}$ is the wave number.

We then consider an object with complex refractive index distribution:

$$n(\mathbf{p}) = 1 - \delta(\mathbf{p}) + i\beta(\mathbf{p}) \tag{4.2}$$

where δ quantifies the refractive properties of the object, and

$$\beta = \frac{\lambda \mu}{4\pi}, \tag{4.3}$$

quantifies absorptive properties of the object. λ is the radiation wavelength and μ is the linear attenuation coefficient. The position vector $\mathbf{p} = (p_1, p_2, p_3)$ represents the object's coordinate system as illustrated in Fig. 4.1. For an object composed of a single material "1"(including voids; herein referred to as a binary object), $n(\mathbf{p})$ takes only the values $1 - \delta_1 + i\beta_1$ or unity. For normally incident plane-wave illumination of an optically thin single–material object, the intensity and phase at the contact plane ($z = 0$) is given by the projection approximation (see section 3.2.1 of chapter 3), such that

$$I(\mathbf{r}_\perp, z = 0) = I_0 \exp \left[-\mu_1 T_1(\mathbf{r}_\perp) \right], \tag{4.4}$$

and

$$\phi(\mathbf{r}_\perp, z = 0) = -k\delta_1 T_1(\mathbf{r}_\perp), \tag{4.5}$$

with Eqn. (4.4) being the Beer-Lambert law of absorption. $T_1(\mathbf{r}_\perp)$ is the projected thickness of the object (projected in the z–direction) and I_0 is the uniform incident intensity. By

substituting $I(\mathbf{r}_\perp, z = 0)$ and $\phi(\mathbf{r}_\perp, z = 0)$ into the TIE (Eqn. (4.1)) we obtain the following expression:

$$\delta_1 I_0 \nabla_\perp \cdot \{\exp\left[-\mu_1 T_1(\mathbf{r}_\perp)\right] \nabla_\perp \cdot T_1(\mathbf{r}_\perp)\} = \frac{\partial I(\mathbf{r}_\perp, z)}{\partial z}. \tag{4.6}$$

We make use of the identity

$$\nabla_\perp \cdot \{\exp\left[-\mu_1 T_1(\mathbf{r}_\perp)\right] \nabla_\perp \cdot T_1(\mathbf{r}_\perp)\} = -\frac{1}{\mu_1} \nabla_\perp^2 \exp\left[-\mu_1 T_1(\mathbf{r}_\perp)\right]. \tag{4.7}$$

One is then able to re-express Eqn. (4.6) as

$$-\frac{I_0 \delta_1}{\mu_1} \nabla_\perp^2 \exp\left[-\mu_1 T_1(\mathbf{r}_\perp)\right] = \frac{\partial I(\mathbf{r}_\perp, z)}{\partial z}. \tag{4.8}$$

Now the derivative $\frac{\partial I(\mathbf{r}_\perp, z)}{\partial z}$ can be approximated by taking the intensity difference across two closely spaced planes separated by a distance d. In this case we consider one of the measured intensities to be at the contact plane $z = 0$ and the other at some close distance $z = d$. That is,

$$\begin{aligned}
\frac{\partial I(\mathbf{r}_\perp, z)}{\partial z} &\approx \frac{I(\mathbf{r}_\perp, z = d) - I(\mathbf{r}_\perp, z = 0)}{d} \\
&= \frac{I(\mathbf{r}_\perp, z = d) - I_0 \exp\left[-\mu_1 T_1(\mathbf{r}_\perp)\right]}{d}.
\end{aligned}$$

$$\tag{4.9}$$

With this approximation one is able to rearrange Eqn. (4.8) in order to obtain the following

$$\left[-\frac{d\delta_1}{\mu_1} \nabla_\perp^2 + 1\right] \exp\left[-\mu_1 T_1(\mathbf{r}_\perp)\right] = \frac{I(\mathbf{r}_\perp, z = d)}{I_0}. \tag{4.10}$$

By Fourier transforming both sides one can make use of the Fourier derivative theorem

$$\mathbf{F}_{\mathbf{r}_\perp} \left\{\nabla_\perp^2 G(\mathbf{r}_\perp)\right\} = -\mathbf{k}_\perp^2 G(\mathbf{r}_\perp), \tag{4.11}$$

enabling the projected thickness $T_1(\mathbf{r}_\perp)$ to be calculated as (Paganin *et al.* [65]):

$$T_1(\mathbf{r}_\perp) = -\frac{1}{\mu_1} \ln\left(\mathbf{F}_{\mathbf{k}_\perp}^{-1} \left\{\frac{1}{\frac{d\delta_1}{\mu_1} \mathbf{k}_\perp^2 + 1} \mathbf{F}_{\mathbf{r}_\perp}\left[\frac{I(\mathbf{r}_\perp, z = d)}{I_0}\right]\right\}\right). \tag{4.12}$$

Here $\mathbf{F}_{\mathbf{k}_\perp}$ and $\mathbf{F}_{\mathbf{r}_\perp}^{-1}$ are respectively the two–dimensional forward and inverse Fourier transforms with respect to $\mathbf{r}_\perp$, and $\mathbf{k}_\perp = (k_x, k_y)$ are the Fourier coordinates dual to $\mathbf{r}_\perp$ (see

Fig. 4.1). This algorithm assumes the "near field approximation" that d be sufficiently small that the Fresnel number be significantly larger than unity, that is

$$N_F = \frac{l^2}{\lambda(D_l + d)} \gg 1, \tag{4.13}$$

where l is the characteristic transverse length scale associated with the wavefield at the exit surface of the object and D_l is the distance from the smallest feature to the exit surface (see e.g. Paganin *et al*. [67]). For a given wavelength and spatial resolution we can therefore estimate the minimum feature size that can be imaged and still satisfy the near field approximation.

A mathematically identical form of Eqn. (4.12), which allows for the recovery of the projected electron density $\rho(\mathbf{r}_\perp)$, has also been derived via a different approach by Wu *et al*. [91]. In their derivation, the authors assumed the energies of the incident X–rays must range from 60 to 500 keV. Their derivation is not restricted to a single material object, but enables the same mathematical simplification as the single material assumption made in deriving Eqn. (4.12) when lower energy X–rays are considered.

4.2.2 Two–dimensional phase retrieval of a ternary object

This section extends the phase retrieval algorithm in Eqn. (4.12) by generalizing to the case of a ternary object (two materials including voids). To this end, consider an object made of material "j" with projected thickness $T_j(\mathbf{r}_\perp)$ embedded in another object made of material "1" with projected thickness $T_1(\mathbf{r}_\perp)$. We seek to recover $T_j(\mathbf{r}_\perp)$ from a single PCI image. Introduce the total projected thickness (Myers *et al*. [60]):

$$A(\mathbf{r}_\perp) = T_j(\mathbf{r}_\perp) + T_1(\mathbf{r}_\perp). \tag{4.14}$$

Under the projection approximation the intensity and phase at the contact plane are given by (see section 3.2.1 of chapter 3):

$$I(\mathbf{r}_\perp, z = 0) = I_0 \exp\left[-\mu_j T_j(\mathbf{r}_\perp) - \mu_1 T_1(\mathbf{r}_\perp)\right], \tag{4.15}$$

and

$$\phi(\mathbf{r}_\perp, z = 0) = -k\left[\delta_j T_j(\mathbf{r}_\perp) + \delta_1 T_1(\mathbf{r}_\perp)\right]. \tag{4.16}$$

By substituting Eqns. (4.14), (4.15) and (4.16) in the TIE (Eqn. (4.1)) we obtain the following non–linear differential equation with respect to $T_j(\mathbf{r}_\perp)$:

$$\left(\delta_j - \delta_1\right) I_0 \exp\left[-\mu_1 A(\mathbf{r}_\perp)\right] \nabla_\perp \cdot \left\{\exp\left[-(\mu_j - \mu_1)T_j(\mathbf{r}_\perp)\right] \nabla_\perp \cdot T_j(\mathbf{r}_\perp)\right\} +$$

$$\delta_1 I_0 \exp\left[-\mu_1 A(\mathbf{r}_\perp)\right] \nabla_\perp \cdot \left\{\exp\left[-(\mu_j - \mu_1)T_j(\mathbf{r}_\perp)\right] \nabla_\perp \cdot A(\mathbf{r}_\perp)\right\} = \frac{\partial I(\mathbf{r}_\perp, z)}{\partial z}.$$

$$(4.17)$$

Assuming that the total projected thickness $A(\mathbf{r}_\perp)$ varies slowly across the plane $\mathbf{r}_\perp = (x, y)$, spatial derivatives of $A(\mathbf{r}_\perp)$ can be neglected. As such, the second term on the left hand side of Eqn. (4.17) can be ignored, thus the non–linear differential equation in Eqn. (4.17) simplifies to:

$$\left(\delta_j - \delta_1\right) I_0 \exp\left[-\mu_1 A(\mathbf{r}_\perp)\right] \nabla_\perp \cdot \left\{\exp\left[-(\mu_j - \mu_1)T_j(\mathbf{r}_\perp)\right] \nabla_\perp \cdot T_j(\mathbf{r}_\perp)\right\} = \frac{\partial I(\mathbf{r}_\perp, z)}{\partial z}.$$

$$(4.18)$$

To proceed we follow the procedure used for the binary case by making use of the identity in Eqn. (4.7) in a slightly modified form:

$$\nabla_\perp \cdot \left\{\exp\left[-(\mu_j - \mu_1)T_j(\mathbf{r}_\perp)\right] \nabla_\perp \cdot T_j(\mathbf{r}_\perp)\right\} = -\frac{1}{\mu_j - \mu_1} \nabla_\perp^2 \exp\left[-(\mu_j - \mu_1)T_j(\mathbf{r}_\perp)\right].$$

$$(4.19)$$

Subsequently, expressing the right hand side of Eqn. (4.18) as a first–order finite difference approximation of two closely spaced measured intensities of the planes $z = 0$ and $z = d$, yields:

$$\left[-\frac{d(\delta_j - \delta_1)}{(\mu_j - \mu_1)} \nabla_\perp^2 + 1\right] \exp\left[-(\mu_j - \mu_1)T_j(\mathbf{r}_\perp)\right] = \frac{I(\mathbf{r}_\perp, z = 0)}{I_0 \exp\left[-\mu_1 A(\mathbf{r}_\perp)\right]}. \qquad (4.20)$$

Fourier transform both sides of Eqn. (4.20), use the Fourier derivative theorem, and inverse transform to obtain the following expression for $T_j(\mathbf{r}_\perp)$ (Beltran *et al.* [6]):

$$T_j(\mathbf{r}_\perp) = \frac{1}{\mu_j - \mu_1} \ln\left(F_{\mathbf{k}_\perp}^{-1}\left\{\frac{1}{\frac{d(\delta_j - \delta_1)}{(\mu_j - \mu_1)}\mathbf{k}_\perp^2 + 1} F_{\mathbf{r}_\perp}\left[\frac{I(\mathbf{r}_\perp, z = d)}{I_0 \exp[-\mu_1 A(\mathbf{r}_\perp)]}\right]\right\}\right). \qquad (4.21)$$

To employ this algorithm one requires *a priori* knowledge of the total projected thickness $A(\mathbf{r}_\perp)$ in addition to the values δ_j, δ_1 and μ_j, μ_1 corresponding to the different materials in the object. If an object is of complicated shape and is known to contain no internal voids, then $A(\mathbf{r}_\perp)$ can be found using techniques such as laser profilometry (Myers *et al.* [60]). In the case of tomography, a more convenient and practical approach to obtain $A(\mathbf{r}_\perp)$ for each projection angle can be used. By utilizing Eqn. (4.12) the encasing material can first

be correctly reconstructed tomographically. Internal and external voids can then be located by computationally searching for a predefined threshold in each slice of the reconstructed volume. $A(\mathbf{r}_\perp)$ may then be calculated for each projection angle. On an additional note, for point source illumination it is necessary to account for image magnification in both Eqn. (4.12) and Eqn. (4.21). Both equations will be altered by identical factors (see Kitchen *et al.* [45]).

4.2.3 Three–dimensional phase retrieval for spatially quantized objects

This section combines the phase retrieval algorithms in Eqns. (4.12) and (4.21) with tomography principles to enable interface–specific phase retrieval tomography, using a single propagation-based X–ray phase contrast image per projection (see section 3.5.1). For both absorption and phase contrast tomography we utilize a conventional filtered backprojection (FBP) algorithm to reconstruct a two–dimensional slice of the imaged object (Kak and Slaney [43]). Fourier–transform–based FBP utilizing projection phase–contrast images processed using Eqn. (4.12), allows one to "focus in" on an interface between air (cavities) and the encasing object "1", enabling any voids within the encasing material to be quantitatively reconstructed. Here δ_1 and β_1 take the values corresponding to the encasing object "1". For objects with spatially quantized refractive indices, such as shown in Fig. 4.2, the "correct" interfaces will be sharply reconstructed.
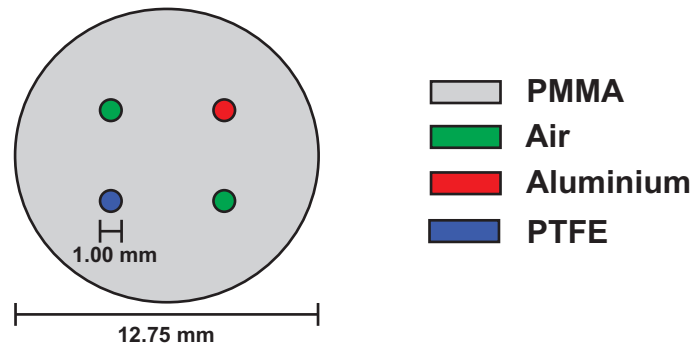
Figure 4.2: Top view of the test object used to demonstrate interface–specific phase retrieval tomography using a single propagation–based X–ray phase contrast image per projection.

Interfaces between embedded objects "j" (where $j = 2, 3, ...$) and the encasing object "1", will be incorrectly reconstructed using the aforementioned procedure. However, such incorrectly reconstructed interfaces will bear a characteristic local signature of either (i) residual phase–contrast fringes, or (ii) blurred interfaces. Moreover, such "incorrect" interfaces (e.g. between materials "j" and "1") may be quantitatively (sharply) reconstructed by repeating the FBP analysis using inputs derived by inserting $(\Delta\delta)_{j1} \equiv \delta_j - \delta_1$ and $(\Delta\mu)_{j1} \equiv \mu_j - \mu_1$ into Eqn. (4.21), provided the material of interest is not in contact with or

in the immediate vicinity of either another embedded object or a cavity. From a series of FBP reconstructions for each distinct pair of material interfaces present in the sample, one can build up a quantitative 3D map of all materials. These can be spliced together into a composite tomographic reconstruction, for which all interfaces between each distinct pair of materials is sharply reconstructed. This is the core idea underpinning our procedure for phas-e-amplitude tomography of a multi–material object with spatially quantized complex refractive index distribution, given a single propagation–based phase contrast image per projection.

Crucial to the success of the splicing procedure described above is the idea that "incorrect" interfaces are only locally polluted (in three dimensions) by locally incorrect choices for δ and μ (Mayo *et al.* [52]). How may one quantify the smoothing artefacts for interfaces which are incurred as a result of a locally incorrect filtering parameter, $\alpha = \frac{d\delta}{\mu}$, being utilized in Eqn. (4.12) at a given interface? In regions where over-smoothing occurs (i.e. where α is overestimated), the amount of blurring ("bleed width") of an "incorrect" interface can be estimated by analysing the low-pass Fourier filter in Eqn. (4.12), which has the form of a Lorentzian function. This Lorentzian can be rewritten as

$$\frac{1}{\alpha \mathbf{k}_\perp^2 + 1} = \frac{1}{\varepsilon \mathbf{k}_\perp^2 + 1} \times \left(\frac{\varepsilon \mathbf{k}_\perp^2 + 1}{\alpha \mathbf{k}_\perp^2 + 1} \right). \tag{4.22}$$

In the case of a medium "j" embedded in an encasing medium "1", $\varepsilon = \frac{d(\delta_j - \delta_1)}{(\mu_j - \mu_1)}$ is the ratio in Eqn. (4.21) that will correctly reconstruct this particular interface. Equation (4.22) allows us to approximately interpret the operation of Eqn. (4.12) (using α rather than ε) on this interface as the correct Lorentzian function multiplied by the ratio of quadratic functions on the right side of Eqn. (4.22). This quotient is a Fourier filter that locally causes either an over- or under-smoothing artefact in the vicinity of the "incorrect" interface. Incidentally, in the case of oversmoothing, when $\frac{\varepsilon}{\alpha} < 1$, this ratio of quadratic functions is a Lorentzian function that has been vertically scaled by a factor $\frac{\alpha - \varepsilon}{\varepsilon}$ and shifted positively along the vertical axis by $\frac{\varepsilon}{\alpha}$, with a maximum value of unity (see Fig. 4.3 (a)). In the opposite case, when $\frac{\varepsilon}{\alpha} > 1$, we have an inverted Lorentzian, giving rise to a high-pass filter that leaves a characteristic fringe representing under-compensated phase contrast (see Fig. 4.3 (b)). In either case, one has a clear signature associated with "incorrect" interfaces, which allows them to be unambiguously identified and thereby enabling one to "focus in" upon a particular material interface of interest.

Oversmoothing is a particular problem since it will cause an object to appear to "bleed" beyond its physical boundaries, potentially encroaching the space of other features in the object. This "bleed width" can be estimated via the optical uncertainty principle:

$$\Delta \mathbf{x} \Delta \mathbf{k} \geq 1, \tag{4.23}$$

where $\Delta \mathbf{x}$ is the uncertainty in real space (i.e., the "bleed width") and $\Delta \mathbf{k}$ is the uncertainty in reciprocal space. Take $\Delta \mathbf{k}$ as the half–width at half–maximum (HWHM) of the second

quotient on the right–hand side of Eqn. (4.22), relative to the asymptotic baseline of $\frac{\varepsilon}{\alpha}$, as displayed in Fig. 4.3 (a). Subsequently, using Eqn. (4.23) we obtain a simple lower bound for the associated bleed width that is, somewhat surprisingly, independent of ε:

$$\Delta \mathbf{x} \geq \sqrt{\alpha} \qquad (4.24)$$

We close this section by noting that this "bleed width", associated with interfaces other than those selected via a given choice for α, is constructive insofar as it "tags" particular over–smoothed interfaces as not corresponding to the particular interface of interest, but rather to an interface with $\varepsilon < \alpha$. Under–smoothed interfaces are also tagged, as corresponding to $\varepsilon > \alpha$, via the signature of incompletely–compensated phase contrast fringes.
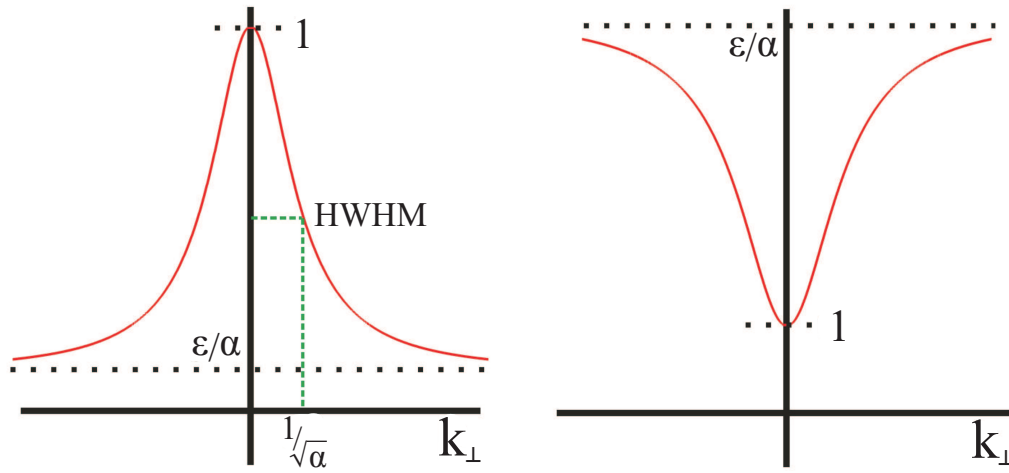
Figure 4.3: Graphs of the Fourier filter $\frac{\varepsilon \mathbf{k}_\perp^2 + 1}{\alpha \mathbf{k}_\perp^2 + 1}$ are shown. (a) shows the case when $\varepsilon/\alpha < 1$, leading to an over–smoothed reconstruction and (b) shows the case when $\varepsilon/\alpha > 1$, leading to an under–smoothed reconstruction.

4.3 Experimental results and discussion

Here we give an synchrotron–based experimental implementation of the theory developed above. Section 4.3.1 discusses the experimental setup. Section 4.3.2 reports 2D phase–amplitude retrieval of multi–material spatially quantized objects with embedded features that are non-overlapping in projection (cf. sections 4.2.1 and 4.2.2). This requirement for non-overlap in projection is relaxed is section 4.3.3, which implements 3D phase–amplitude retrieval of multi–material spatially quantized objects, given a single propagation–based X–ray phase contrast image per projection (cf. section 4.2.3).

4.3.1   Experimental setup

X–ray propagation–based phase–amplitude computed tomography experiments were per-
formed in Hutch 3 of beamline 20B2 at the SPring-8 synchrotron radiation source, Japan
(proposal 2009A1882). The beamline employs a bending magnet source with a Si(111)
double–crystal monochromator (Goto *et al.* [31]). A monochromatic X–ray beam of 24
keV provided acceptable phase and attenuation contrast for materials of relatively low
atomic number. This energy is also commensurate with the diagnostic X–ray energies
used in mammography (Abrami *et al.* [1]). Phase and absorption contrast images were
recorded with the detector positioned at distances of $d = 1$ m and $d = 10$ cm from the
object, as shown in Fig. 4.1. An optically coupled Hamamatsu CCD camera (C4880-41S)
with a 10 μm thick gadolinium oxysulfide (Gd_2O_2S) phosphor was used to acquire each
data set. The images had a window size of 3000 x 1500 pixels and an effective pixel size of
5.9 μm, which gave a region of interest (ROI) of 17.70 mm (H) $\times$ 8.85 mm (V). For each
tomographic data set, 1800 projections were collected over 180° of rotation, each acquired
with an exposure time of 2.5 s. Flat field images (no object in the beam) were recorded
every 43 projections. Frequent flat field recordings were required due to instabilities in
beam position with time. Dark field images also were acquired with the main beam shutter
closed at the beginning and end of each scan to correct for the detector dark current offset.
Prior to quantitative analysis, all phase–contrast images were flat–field and dark–field
corrected to compensate for both illumination non–uniformities and CCD dark current.
The flat and dark field correction method performed for each tomographic image is shown
in Eqn. (4.25) below:

$$\text{Corrected Image} = \frac{I_{Image} - I_{Dark\ field}}{I_{Flat\ field} - I_{Dark\ field}}. \tag{4.25}$$

The imaged object was a PMMA (Polymethyl-methacrylate $C_5H_8O_2$; commonly
known as Perspex) cylinder 10 mm in height and 12.75 $\pm$ 0.05 mm in diameter. This
contained four cavities each with diameter 1.02 $\pm$ 0.05 mm. An Aluminium (Al) and
PTFE (Polytetrafluoroethylene H_2F_4; commonly known as Teflon) pin of 1.00 $\pm$ 0.05 mm
diameter were inserted into two of the cavities to create a quaternary object (three materials
plus voids) with three distinct interfaces; these being air/PMMA, Aluminium/PMMA and
PTFE/PMMA (see Fig. 4.2). The δ and β values for the materials in the object, for 24 keV
X–rays, are listed in Table 4.1. The Aluminium/PMMA interface will be denoted as $j = 2$
and the PTFE/PMMA interface as $j = 3$.

4.3.2   Projection imaging

Here we use the theory of section 4.2.1 to implement 2D phase–amplitude retrieval of a
multi–material spatially quantized object with non–overlapping projections of embedded
features composed of different materials, noting that the assumption of non–overlapping

Table 4.1: Values of δ and β at 24 keV for materials used to construct the test object in Fig. 4.2.

Material	$\delta \times 10^{-7}$	$\mu \ (m^{-1})$
PMMA ($C_5H_8O_2$)	4.628	41.2
PTFE (H_2F_4)	7.789	119.8
Aluminium	9.396	502.6

embedded features will be dropped when moving to a tomographic analysis in section 4.3.3.

Absorption and phase contrast images of our test object (see Fig. 4.2) are shown in Fig. 4.4(a) and (c) for an orientation in which all embedded features, corresponding to different materials, are non–overlapping in projection. In the absorption contrast image, all interfaces except Al/PMMA exhibit weak contrast, since Al is significantly more attenuating than the other materials in the sample (see Table 4.1). Conversely, the phase contrast image displays a significantly greater signal–to–noise ratio (SNR), dramatically enhancing the PTFE/PMMA and air/PMMA interfaces and improving visualization of the object overall (Wilkins *et al*. [85]). Line profiles from left–to–right of the centre of the images in Fig. 4.4 (a) and (c) are shown in Fig. 4.4 (b) and (d), respectively. The profile in Fig. 4.4 (d) clearly reveals strong propagation-based phase contrast fringes formed at interface boundaries.

Figure 4.5 (a) shows an image of the projected thickness of the object computed via Eqn. (4.12), under the assumption that the object was composed entirely of PMMA. Here we have used the known values of δ_1 and μ_1 for PMMA listed in Table 4.1. The line profile in Fig. 4.5 (b) shows the distribution of the recovered projected thickness from the phase contrast image in Fig. 4.4 (c). From the profile it can be seen that the maximum projected thickness of the PMMA is close to the expected values (12.75 mm) and the boundaries of the air/PMMA interfaces are sharp (i.e. not blurred). Moreover, due to reasons mentioned in section 4.2.3, the Al/PMMA and PTFE/PMMA interfaces suffer from an "over–smoothing" and the associated projected thicknesses are also overestimated.

To recover the projected thicknesses of the Al and PTFE, that is $T_2(\mathbf{r}_\perp)$ and $T_3(\mathbf{r}_\perp)$, we "focus" on each of these individually using Eqn. (4.21). Since implementation of this algorithm requires knowledge of the total projected thickness, the function $A(\mathbf{r}_\perp)$ was generated with the assumption that the object was a cylinder with no internal voids, which results in negative values arising in the projected thickness in the presence of internal voids (see Fig. 4.5 (d) and (f)). To recover $T_2(\mathbf{r}_\perp)$, the values used for δ_2 and μ_2 correspond to Aluminium and δ_1 and μ_1 to PMMA (see Table 1). To recover $T_3(\mathbf{r}_\perp)$, the values used for δ_3 and μ_3 correspond to PTFE. The phase retrieved images are shown in Fig. 4.5 (c) and (e). The images show how the "selected" interfaces are sharply reconstructed and how the attenuated intensity due to PMMA is effectively removed. Line profiles in

Fig. 4.5 (d) and (f) illustrate this more clearly and reveal that the recovered projected thicknesses at the "selected" interfaces $T_2(\mathbf{r}_\perp)$ and $T_3(\mathbf{r}_\perp)$ are close to their expected thickness ($\approx$ 1 mm). Additionally, we see that the algorithm breaks down in regions where the encasing material exhibits strong phase contrast; however, this occurs at the boundary of the encasing material far from the interfaces of interest. These artefacts are expected since Eqn. (4.21) assumes that phase gradients due to the encasing material are negligible. Also, we now see that the interfaces where the density is less than that of Aluminium are now under–smoothed and slight residual fringing is still visible (see for example Fig. 4.5 (d), interfaces 1, 3 and 4; cf. section 4.2.3). Note that the upper intensity threshold in (e) has been reduced to enhance the PTFE as a linear palette obscures this feature, so the Al/PMMA interface appears saturated as a consequence.
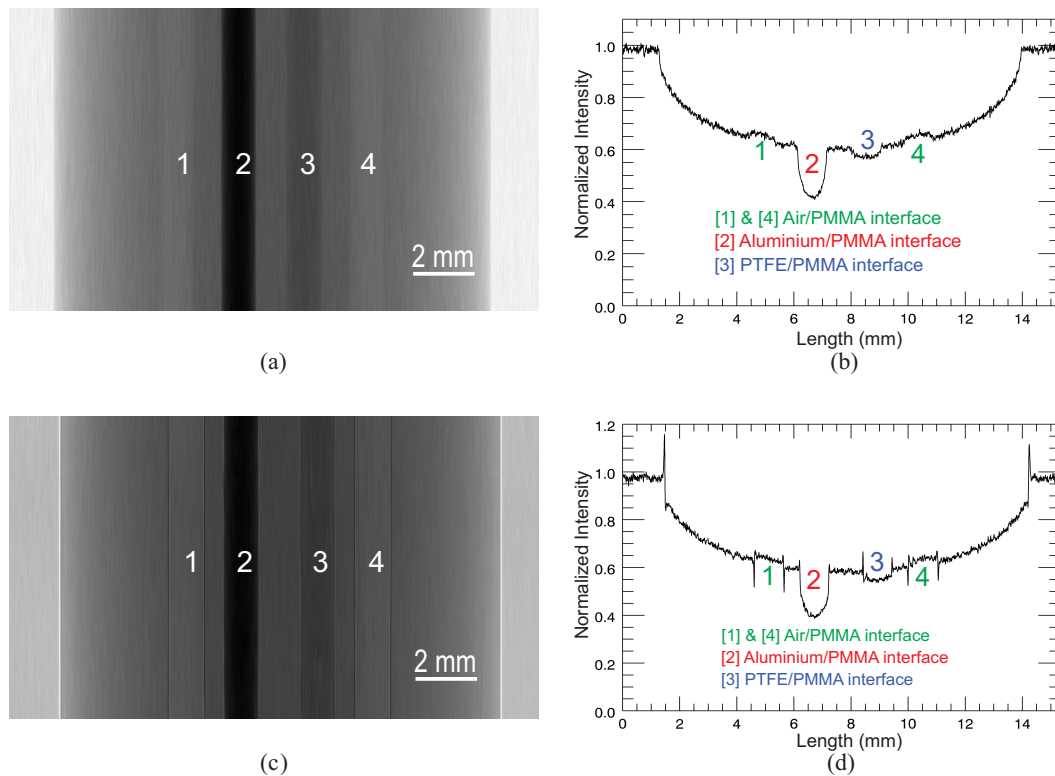
Figure 4.4: Projection images of the multi–material test sample. (a) Absorption contrast image acquired at d = 10 cm. The numbered regions correspond to the different interfaces in the object ([1]Air/PMMA (Green), [2]Al/PMMA (Red) and [3]PTFE/PMMA (Blue)). (b) Phase contrast image acquired at d = 1.0 m. Line profiles from the centre of the images on the left column are shown in (b) and (d), respectively.
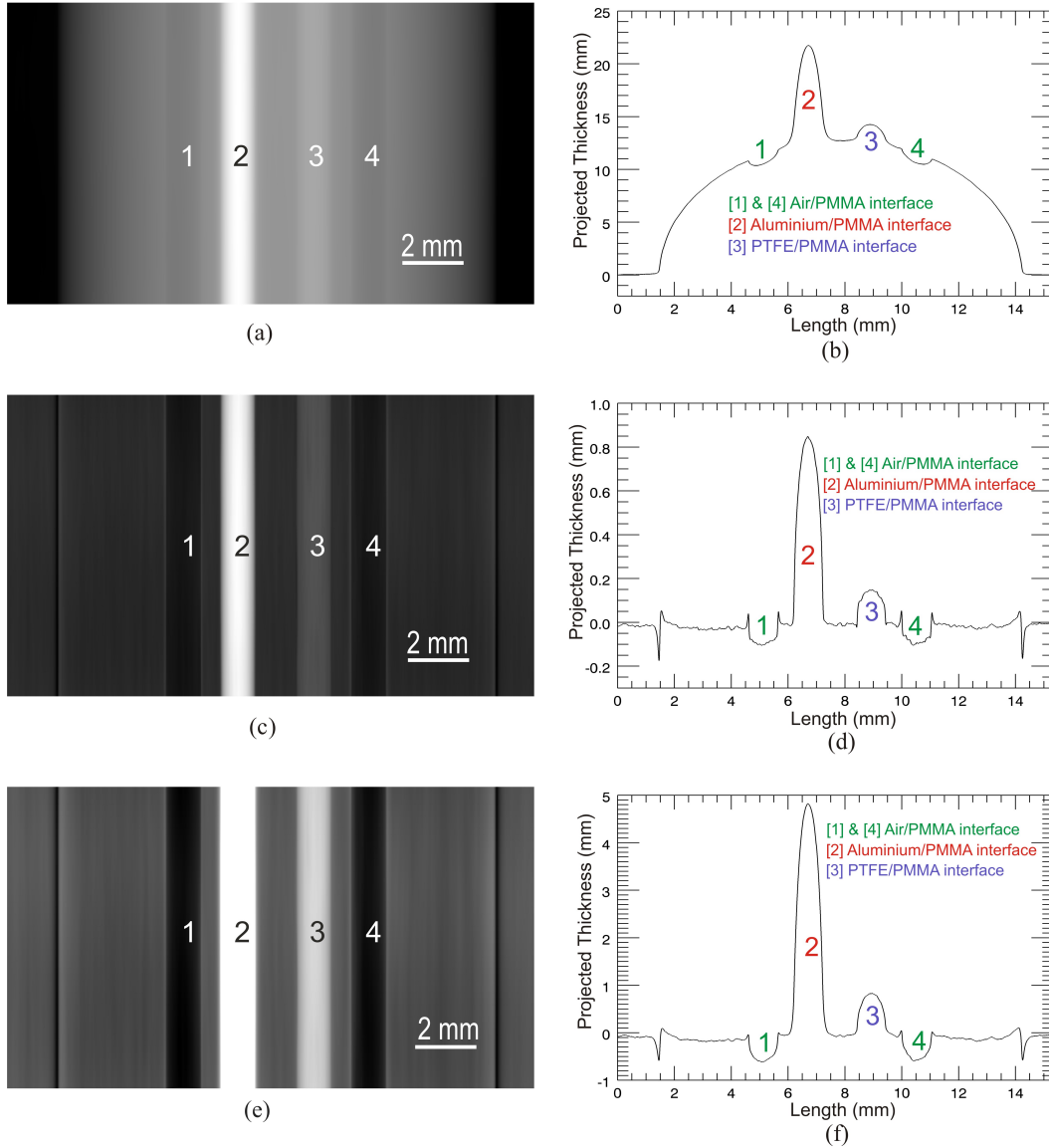
Figure 4.5: Phase–retrieved projection images of the multi–material test sample. (a) Phase retrieved image of Fig. 4.4 (c) using Eqn. (4.12) assuming the object was composed of PMMA. (c) and (e) are phase retrieved images of Fig. 4.4 (c) using Eqn. (4.21) with appropriate values of δ and μ for the Al/PMMA and PTFE/PMMA interfaces, respectively (see Table 4.1). Line profiles from the centre of the images on the left column are shown in (b), (d) and (f), respectively.

4.3.3 Interface–specific phase retrieval tomography

Here we present our results for interface-specific phase retrieval tomography, whereby a single phase–contrast image per projection has been used to selectively reconstruct a given interface between two given materials, in a spatially–quantized object.

For absorption-contrast FBP tomography, using the parameters described in sec-

tion 4.3.1, the reconstruction of a single slice of the sample is shown in Fig. 4.6 (a). Qualitatively the reconstruction shows good detail of the object features, particularly at the Al/PMMA interface where there is a large difference in absorption. In Fig. 4.6 (b) line profiles from left–to–right of the centre of each interface of Fig. 4.6 (a) are shown in a single plot. This displays the distribution of the attenuation coefficient at each interface where it can be seen that, on average, the attenuation coefficients are similar to the theoretical values in Table 4.1. However, the reconstruction also contains a substantial amount of high frequency noise making it difficult to define the boundaries at the interfaces where absorption contrast is poor (air/PMMA and PTFE/PMMA). Such noise is typically reduced in tomography by use of an additional low–pass filter during the filtered backprojection, but must be traded against a reduction in spatial resolution (Kak and Slaney [43]).

Figure 4.6 (c) shows a slice of a tomographic reconstruction obtained by applying FBP directly to the raw phase contrast images (cf. Cloetens *et al.* [18]), without any phase–amplitude retrieval. Like the absorption contrast result it also reveals good detail of the object features. The reconstruction allows us to see how the boundaries of each interface are enhanced as a result of the high SNR provided by phase contrast. Although phase contrast provides better feature visibility, the line profile in Fig. 4.6 (d) shows that non–physical negative values and sharp spikes arise in the attenuation coefficient map without the phase retrieval step.

Figure 4.7 (a) shows a slice of a tomographic reconstruction obtained using Eqn. (4.12) to yield $T_1(\mathbf{r}_\perp, \theta)$ for each projection angle, giving a series of two-dimensional projected-thickness maps that were then tomographically reconstructed using FBP (Gureyev *et al.* [38]). The reconstruction shows the distribution of $\delta_1(\mathbf{p}_\perp)$ along the plane $\mathbf{p}_\perp = (p_1, p_3)$ (see Fig. 4.1), which in this case is for PMMA ($j = 1$). It can be seen that the noise has been substantially suppressed whilst preserving the sharpness of the air/PMMA interface, as the line profile in Fig. 4.7 (b) indicates. Conversely, over–smoothing (cf. Section 4.2.3) is clearly apparent at the remaining interfaces. Despite this localized blurring of these regions the result shows that Eqn. (4.12) can be applied to multi–material objects and accurately reconstruct the voids as long as they are not near the vicinity of the over-smoothed interfaces. The line profile in Fig. 4.7 (b) shows that at the air/PMMA interface, the distribution of $\delta_1(\mathbf{p}_\perp)$ has an average value of 4.2×10^{-7}, which is within 10% of the theoretical value in Table 4.1. This is acceptable as it is known that attenuation coefficients have discrepancies of up to 10% between theoretical values (Chantler *et al.* [13]).

Figure 4.7 (c) and (e) show reconstructions of the same slice from phase retrieved images using Eqn. (4.21) to obtain $T_2(\mathbf{r}_\perp, \theta)$ and $T_3(\mathbf{r}_\perp, \theta)$ before using FBP to respectively recover the distributions of $\delta_2(\mathbf{p}_\perp)$ (Aluminium; $j = 2$) and $\delta_3(\mathbf{p}_\perp)$ (PTFE; $j = 3$). Figure 4.7 (c) focuses on the Al/PMMA interface and (e) focuses on the PTFE/PMMA interface. Due to the rotational symmetry of the surface of the cylinder the same $A(\mathbf{r}_\perp)$ fitted function was used for every projection. The distributions of $\delta_2(\mathbf{p}_\perp)$ and $\delta_3(\mathbf{p}_\perp)$ are shown in the line profiles in Fig. 4.7 (d) and (f). On average the values of $\delta_2(\mathbf{p}_\perp)$ and $\delta_3(\mathbf{p}_\perp)$ are 7.9×10^{-7} and 6.6×10^{-7} respectively, and are within 15% of the theoretical

values in Table 4.1.
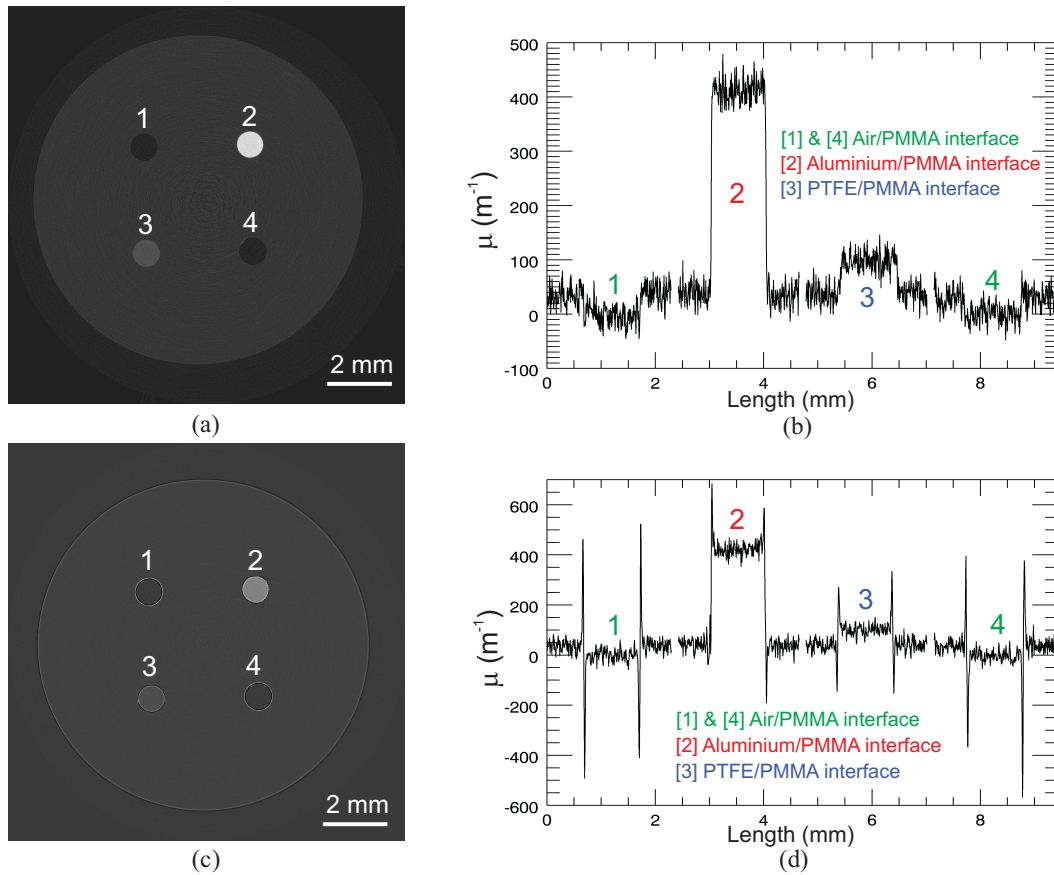
Figure 4.6: Tomographic reconstruction of the multi–material test sample using (a) conventional absorption images reconstructed via FBP; (b) phase contrast images reconstructed by applying FBP to raw PCI data. (b) and (d), respectively, show line profiles from left–t-o-right across the centre of the images in (a) and (c), respectively. Numbered regions correspond to different interfaces in the object ([1]Air/PMMA, (Green), [2]Al/PMMA (Red) and [3]PTFE/PMMA (Blue)).

4.3.4 Quantification of over-smoothing

By measuring the blurring at the Al/PMMA and PTFE/PMMA interfaces in Fig. 4.7 (b). The blurring was just visible up to a distance of 443 μm from the Al/PMMA interface and 454 μm from the PTFE/PMMA interface with an uncertainty of $\pm$30 μm. Evaluating $\sqrt{\alpha}$
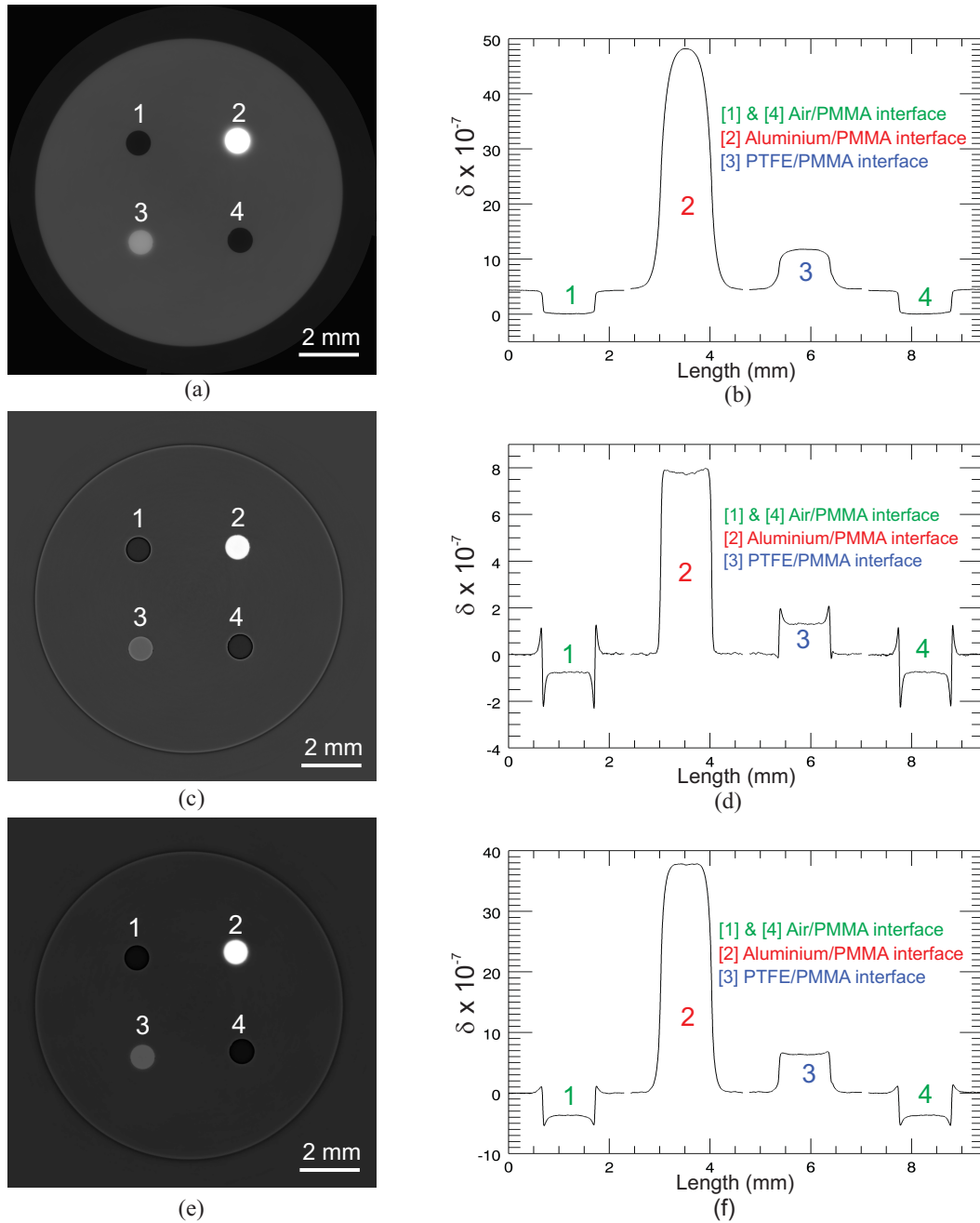
Figure 4.7: Interface-specific tomographic reconstruction of the multi–material test sample using (a) phase contrast images reconstructed using Eqn. (4.12) to calculate $T_1(\mathbf{r}_\perp, \theta)$ for each projection $j = 1$, followed by FBP. (c) and (e) are reconstructions using the same procedure as (c), after calculating $T_2(\mathbf{r}_\perp, \theta)$ and $T_3(\mathbf{r}_\perp, \theta)$ with Eqn. (4.21) for both Al and PTFE for each projection ($j = 2$ and $j = 3$). (b), (d) and (f) respectively, show line profiles from left–to–right across the centre of the images in (a), (c) and (e). Numbered regions correspond to different interfaces in the object ([1]Air/PMMA, (Green), [2]Al/PMMA (Red) and [3]PTFE/PMMA (Blue)).

for PMMA gives a value of 106 μm. The measured bleed widths are thus $4.17\times \sqrt{\alpha}$ for Al/PMMA and $4.28\times \sqrt{\alpha}$ for PTFE/PMMA. Experimentally, we find that the "bleed width" blurring typically extends between 3 and 5 times the lower bound in Eqn. (4.24). Hence the following rule–of–thumb is used to estimate the bleed width Δx:

$$3 \sqrt{\alpha} \geq \Delta \mathbf{x} \geq 5 \sqrt{\alpha}. \tag{4.26}$$

This formula gives a rough indication as to how far an over-smoothed interface will be blurred by the phase retrieval (cf. section 4.2.3). We also note that the Al/PMMA and PTFE/PMMA interfaces bleed almost the same amount. This provides empirical evidence that the parameter α is the only contributor to the smoothing artefact.

4.3.5   Spliced tomographic reconstruction

Having quantitatively reconstructed all three interfaces and established a rule–of–thumb to estimate the blurring widths (see Eqn. (4.26)), we can now combine these images to form a single "spliced" image of our quaternary (or higher order) object (cf. section 4.2.3). The image was constructed by digitally inserting the individually reconstructed interfaces in Fig. 4.7 (c) and (e) into the appropriate regions of the encasing material in Fig. 4.7 (a). The size of the region was chosen by considering the amount of blurring at these interfaces. The refractive index distribution of these segments were offset so that the background zeroes match that of the encasing material and the resulting amplitude was rescaled to maintain the original value. The spliced image is shown in Fig. 4.8 (a). Line profiles of the different interfaces of the image are shown in Fig. 4.8 (b). We now have a quantitative tomographic reconstruction of a multi–material object, at each point of which the refractive index takes one of N distinct values, using a single PCI image per projection.

To quantitatively compare our spliced reconstruction with the absorption–based reconstruction, the SNR was calculated for each medium. The formula used to calculate the SNR values was the following:

$$\mathrm{SNR} = \frac{\tilde{\mu}}{\sigma}, \tag{4.27}$$

where, $\tilde{\mu}$ is the mean signal and σ is the standard deviation of voxels in the subarray. The Al, PTFE and PMMA gave SNRs of 312, 309 and 98.9, respectively, where the signal is the average value inside the medium. This significantly improves the respective SNR values of 18.7, 5.19 and 1.17, which were calculated at the same regions in the absorption contrast reconstruction in Fig. 4.6 (a). The ordering of these SNRs is consistent with the relative amount of smoothing associated with the filters in Eqn. (4.12) and (4.21). The increase in SNR is largest ($\approx 85\times$) for the encasing material as the Fourier-space damping of high spatial frequencies is largest for the PMMA/air interface. Each of the SNRs were

calculated over a 90×90 pixel region of interest. The mathematical origin of the stability with respect to noise is due to the regularizing presence of a non–zero denominator in the Fourier filter of Eqns. (4.12) and (4.21), as the ratio $\frac{d\delta}{\mu}$ is always greater than zero and the ratio $\frac{d(\delta_j - \delta_1)}{\mu_j - \mu_1}$ is unlikely to be less than zero; also, since μ is never zero and $(\Delta\mu)_{j1}$ is generally a non-zero quantity. This avoids instability problems of the "division by zero" type that would arise if the denominator were zero (Paganin *et al.* [65]).
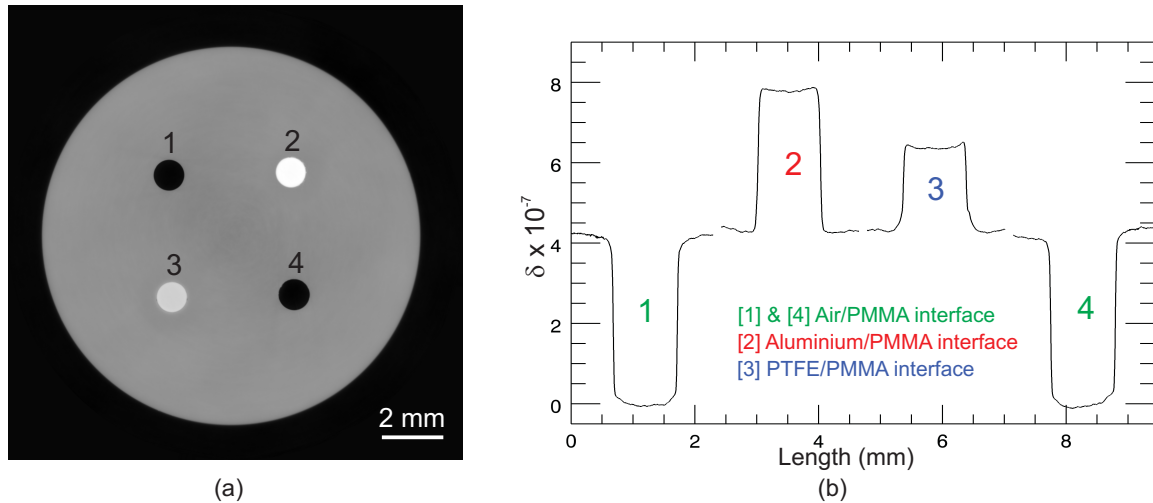
Figure 4.8: (a) Spliced tomographic reconstruction. (b) Line profile of the different interfaces in (a).

4.4   Concluding remarks

We have developed a numerically efficient phase retrieval algorithm to reconstruct the complex refractive index distribution of known materials embedded in a second medium from a single X–ray phase contrast image per projection. This interface–specific phase retrieval tomography algorithm requires *a priori* knowledge of each material's complex refractive index and the total projected thickness of the sample at each orientation. The algorithm was successfully applied to experimental data collected using X–ray synchrotron radiation. We have used our method to quantitatively reconstruct a quaternary object by reconstructing all interfaces separately. A complete tomographic reconstruction of all interfaces in the object was produced by splicing the individual reconstructions together. For the test sample used here, the improvement in the signal–to–noise ratio was between 17 and 85 fold over conventional absorption contrast CT.

5

Interface–specific X–ray phase retrieval tomography of complex biological organs

5.1 Introduction

This chapter[1] is concerned with the application of the methods presented in chapter 4 to perform and demonstrate interface–specific phase retrieval tomography of complex biological organs. No use is made of any chemical contrast enhancements and use is made of only a single view per projection. The complex biological organs used are the thorax of a newborn New Zealand white rabbit pup and the excised brain of an adult Sprague Dawley rat. Our aim was to determine whether our single-image phase retrieval technique could be applied to complex structures and to determine whether interface–specific phase retrieval can be used to help lower the dose to the tissue in comparison to conventional CT.

To enable interface–specific phase retrieval tomography to be performed, the following key assumptions were made: samples are composed of a finite number of materials which are spatially quantized such that (i) each material type within the sample may be adequately approximated by a single complex refractive index; (ii) the complex refractive index of each distinct material has a unique value; (iii) no more than two interfaces can be in direct contact at any given location. While any real sample will have variations in homogeneity within each given material, this was seen to have a minimal effect on both the tomographic reconstructions shown in chapter 4 and the reconstructions presented in this chapter. In this context, note also that the previously mentioned variations in homogeneity are often within the uncertainties of the real and imaginary parts of the complex refractive index for biological samples at diagnostic X–ray energies. Importantly, this technique retains the salient feature of requiring only a single phase-contrast image per projection.

The outline of the remainder of this chapter is as follows. Section 5.2 briefly reviews the methods presented in chapter 4 for interface–specific phase retrieval X–ray tomography of objects whose refractive indices take on one of a series of discrete values. Section 5.3 describes the setup and procedures used for the experimental implementation on two

---

[1]This chapter is based on the publication "Interface–specific X–ray phase retrieval tomography of complex biological organs", M. A. Beltran, D. M. Paganin, K. K. W. Siu, A. Fouras, S. B. Hooper, D. H. Reser and M. J. Kitchen, Phys. Med. Biol. 50, 7353–7369 (2011). See Appendix B.

complex biological samples, namely rabbit lung and rat brain tissue. Section 5.4 illustrates the results achieved using interface-specific tomography. Concluding remarks are given in section 5.5
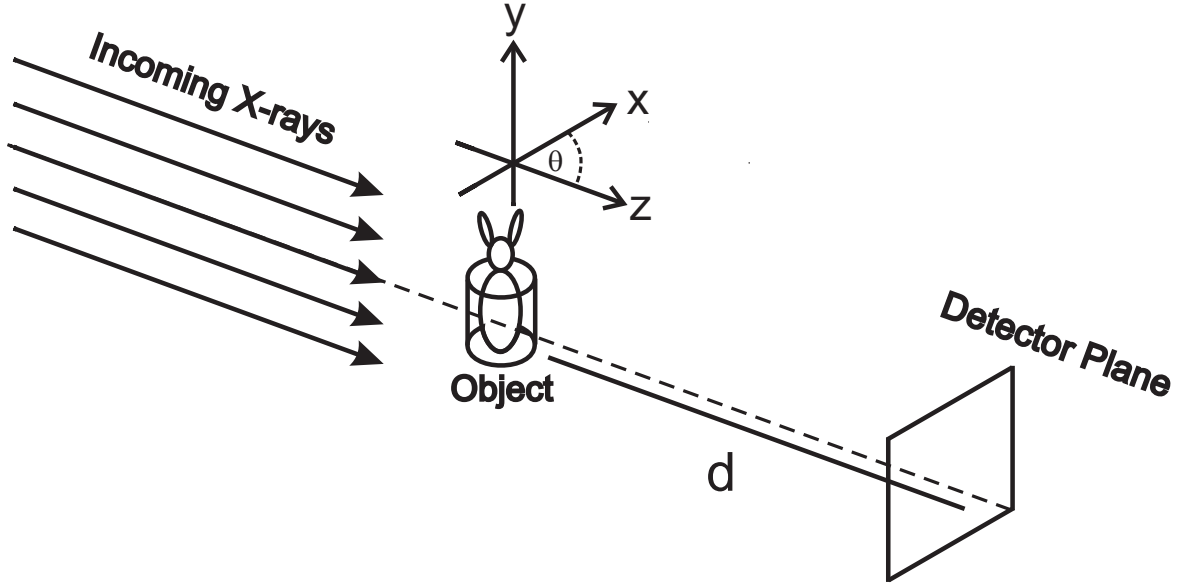
Figure 5.1: Experimental setup illustrating the geometry for propagation-based X–ray phase retrieval tomography, using a single view per projection.

5.2   Image processing algorithms

Here the phase retrieval methods developed in chapter 4 are implemented for complex biological organs (i.e. the lungs of preterm rabbit pup and excised rat brain). To three-dimensionally "focus in" on a particular interface, say the encasing medium (with its internal voids) which has complex refractive index $n_1 = 1 - \delta_1 + i\beta_1$, one needs to apply the algorithm below to each phase–contrast tomographic projection followed by filtered backprojections (see Eqn. (4.12)):

$$T_1(\mathbf{r}_\perp) = -\frac{1}{\mu_1}\ln\left(F_{\mathbf{k}_\perp}^{-1}\left\{\frac{1}{\frac{d\delta_1}{\mu_1}\mathbf{k}_\perp^2+1}F_{\mathbf{r}_\perp}\left[\frac{I(\mathbf{r}_\perp, z=d)}{I_0}\right]\right\}\right). \tag{5.1}$$

Here, $F_{\mathbf{r}_\perp}$ and $F_{\mathbf{k}_\perp}^{-1}$ respectively denote forward and inverse Fourier transforms. Now to three-dimensionally focus "in" on a medium "j" which is embedded in medium "1" once the encasing medium "1" has been reconstructed one then needs to apply the algorithm below to each phase–contrast tomographic projection also followed by filtered backprojections (see Eqn. (4.21)):

$$T_j(\mathbf{r}_\perp) = \frac{1}{\mu_j - \mu_1}\ln\left(F_{\mathbf{k}_\perp}^{-1}\left\{\frac{1}{\frac{d(\delta_j-\delta_1)}{(\mu_j-\mu_1)}\mathbf{k}_\perp^2+1}F_{\mathbf{r}_\perp}\left[\frac{I(\mathbf{r}_\perp, z=d)}{I_0\exp[-\mu_1 A(\mathbf{r}_\perp)]}\right]\right\}\right). \tag{5.2}$$

It is important to note that Eqns. (5.1) and (5.2) will not correctly reconstruct the projected thickness at all tomographic projections. This is especially relevant for multi–material samples in which distinct media overlap in projection. However, it will correctly reconstruct the three-dimensional distribution of interfaces of a given pair of distinct materials (see section 4.3.3).

5.3   Method

5.3.1   Image acquisition

High-resolution X–ray phase-contrast images were acquired in hutch 3 of beamline 20B2 at the SPring-8 synchrotron radiation source, Japan (Goto *et al*. [31]). The large source-to-object distance ($\sim$ 210 m) and the Si(1 1 1) double-crystal monochromator provided a near planar X–ray beam. We used 24 keV X–rays to provide strong phase and attenuation contrast of the biological specimens used here (see Kitchen *et al*. [45], Beltran *et al*. [6]), which included the thorax of a newborn New Zealand white rabbit pup and the excised brain of an adult Sprague Dawley rat. The beam size was collimated to be approximately 30 mm wide and 30 mm high, which was large enough to completely illuminate each sample. A 4000 $\times$ 2672 pixel Hamamatsu CCD camera (C9300-124F) with a 1.8:1 ratio fibre optic taper, having an effective pixel size of 16.2 μm, was used to collect the tomographic tilt series of propagation-based X–ray phase-contrast images (see Fig. 5.1).

For imaging the rabbit pup thorax, the detector was positioned a distance $d = 50$ cm from the object. This relatively small sample-to-detector propagation distance was sufficient to render visible strong phase-contrast fringes from the air-tissue interfaces within the lung at this energy (see, e.g., Suzuki *et al*. [78] and Beltran *et al*. [6]). A total of 1500 projections were collected over 180° of rotation, with each having an exposure time of 250 ms. Flat field images (with no object in the beam) were recorded at the start and end of each scan to normalize the image intensity. Dark field images were also collected to correct for the detector's dark current offset.

The same setup was used for imaging the rat brain as for the rabbit pup thorax with the exception of the object-to-detector distance, which was set to 5.0 m. A large propagation distance was required to increase the phase contrast between the materials within the sample due to the highly similar refractive indices of the materials (namely grey and white brain matter) within the sample. A total of 1800 tomographic projections were acquired with an exposure time of 2.5 s each. The exposure time for the thorax was kept short relative to that of the brain in order to minimize potential motion artefacts introduced by movement of the pliable lung tissue during the scan.

We note that the large number of projections used here is required for adequate sampling of the tomographic reconstruction to adequately resolve the phase-contrast fringes, which typically have maxima separated by $50 - 100 \, \mu$m. Although a considerably lower dose could be achieved using larger pixels with fewer projections, we chose to maximize the

phase sensitivity of these applications to properly demonstrate the potential of phase retrieval tomography.

5.3.2   Image processing

For the selected energy (24 keV), the δ and β values for lung tissue and cortical bone are listed in Table 5.1. The δ and β values considered to be present in the agar-embedded brain sample are listed in Table 5.2. According to the NIST[2] database, grey and white matter (the main tissue types present in the brain) are virtually identical in reference to diagnostic energy X–ray interactions and are herein treated as identical. We justify this statement by reference to Eqns (5.1) and (5.2) where we see that it is the ratio of the real and imaginary components of the refractive indices, or the difference ratio (see Eqn (5.2)), that is important for the Fourier filtering by the phase retrieval algorithms. Figure 5.2 illustrates this point by comparing the four Fourier-space filters used in this research. Distinct differences can be seen for the lung tissue/air interface filter against those of the brain tissue/agar and bone/lung tissue interfaces. Remarkably, the agar/air filter is almost identical to the brain tissue/agar filter despite the interfaces having very different density gradients, which arises because the ratio of δ to μ is nearly identical for brain tissue and agar (see Table 5.2). Therefore, either filter (Eqns (5.1) or (5.2)) can be applied with essentially the same results.

Table 5.1: Values of δ and μ at 24 keV X–rays for water (soft-tissue equivalent) and cortical bone tissue. These were calculated from the NIST[2] database.

Material	$\delta \times 10^{-7}$	μ (m^{-1})
Water (lung tissue equivalent)	3.992	54.9
Bone tissue	7.145	461.1

Table 5.2: Values of δ and μ at 24 keV X–rays for grey/white matter and agar. These were calculated from the NIST[2] database.

Material	$\delta \times 10^{-7}$	μ (m^{-1})
Grey/white matter	4.842	56.3
Agar	3.432	40.2

Since Eqns (5.1) and (5.2) involve ratios of δ and μ, concerns regarding sample inhomogeneity can be partly allayed. Both δ and μ are proportional to the density of a given material; hence, their ratio in Eqns (5.1) will be independent of changes in density for a given material. The same holds true for Eqns (5.2) when the density of material 'j'

---

[2]The National Institute of Standards and Technology (NIST) internet website where X–ray/matter interactions factors can be found is http://www.nist.gov/index.html.
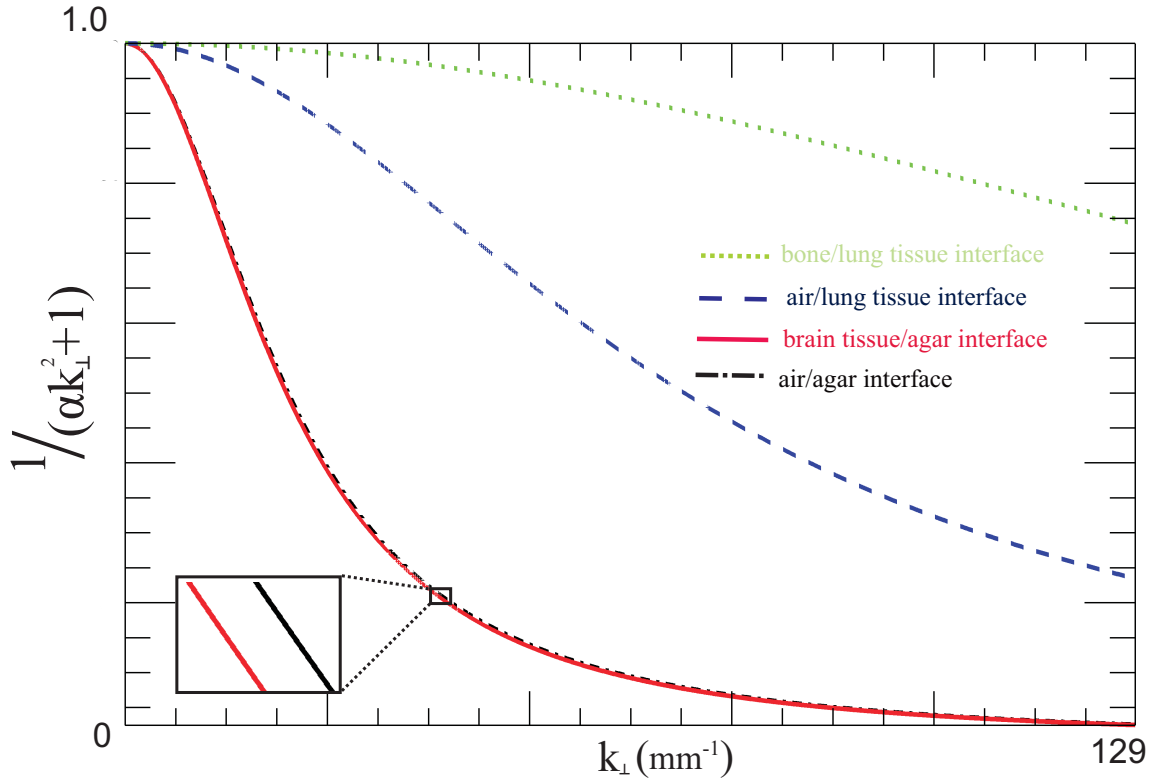
Figure 5.2: Fourier filters of the form $1/(\alpha \mathbf{k}_\perp^2 + 1)$ for different ratios of $\alpha = d\delta/\mu$ or $\alpha = d\Delta\delta/\Delta\mu$ (see Eqns (5.1) and (5.2)). The dashed line corresponds to the ratio used for the air/lung tissue interface, $\alpha = d\delta_{water}/\mu_{water}$ with $d = 50$ cm. The dotted line corresponds to the ratios used for the bone/lung tissue interface, $\alpha = d(\delta_{bone} - \delta_{water})/(\mu_{bone} - \mu_{water})$ with $d = 50$ cm. The solid line corresponds to the ratio used for the air/agar interface, $\alpha = d\delta_{agar}/\mu_{agar}$ with $d = 5$ m, and the dashed-dotted line corresponds to the ratios used for the brain tissue (grey/white matter; denoted 'gw')/agar interface, $\alpha = d(\delta_{gw} - \delta_{agar})/(\mu_{gw} - \mu_{agar})$ with $d = 5$ m. The magnified inset is used to illustrate the minute difference between filters for brain tissue/agar and air/agar, respectively.

and that of material '1' are equal. Moreover, variations in density of a few per cent of either material will typically have little effect on the shape of the filter in Eqn (5.2). It is therefore a valid approximation to employ a single filter for a given interface despite small density variations in inhomogeneous samples.

5.3.3 Animal procedures

All animal procedures were approved by the Monash University Animal Ethics Committee and the SPring-8 Animal Care and Use Committee. A pregnant New Zealand white rabbit at 31 days of gestation was anaesthetized by intravenous injection of propofol (Rapinovet; 12 mg kg^{-1} bolus, 40 mg h^1 infusion). The pup was delivered by caesarean section and

then humanely killed via anaesthetic overdose. Following death, an endotracheal tube was inserted via a tracheotomy into the mid-cervical trachea and connected to a custom-designed ventilator (Kitchen *et al.* [47]). The pup was placed in a water-filled cylindrical plethysmograph made of PMMA. The head of the pup was located outside the chamber and a thin rubber diaphragm formed a seal around its neck. Once correctly placed in the plethysmograph, the lungs were inflated with air and inflation was maintained by the application of a constant airway pressure of 25 cmH$_2$O, as was required to keep the terminal airways inflated.

The Sprague Dawley rat was humanely killed via an overdose of sodium pentothal (100 mg/kg, i.p.) and then transcardially perfused with heparinized 0.1 M phosphate buffered saline (PBS) followed by 4% paraformaldehyde (PFA) in 0.1 M PBS. The brain was carefully removed from the skull and postfixed overnight in 4% PFA/0.1 M PBS. The brain was then serially dehydrated in increasing concentrations of sucrose (up to 30%) in 4% PFA. The fixed brain was next suspended inside a 2.6 cm diameter plastic specimen container containing warm 2% gel agar diluted with 4% PFA. After the agar hardened, the container was refrigerated until imaging. After synchrotron imaging was complete, the brain was extracted from the agar and sectioned in the coronal plane (50 μm thickness) using a cryostat. Alternating brain sections were stained with Nissl substance, which densely stains the rough endoplasmic reticulum in neuronal cell bodies, and used to locate anatomical landmarks in the propagation-based X–ray phase-contrast images. Anatomical localization was performed with the aid of the stereotaxic atlas of Pellegrino *et al.* [68].

5.4   Results and discussion

5.4.1   Chest imaging

A single PBI image of the tomographic data set is shown in Fig. 5.3 (a). Even with the relatively small object-to-detector distance, the bulk of the lung tissue is rendered visible as a speckled intensity pattern as a result of multiple refraction of the X–ray beam through minor airways that overlap in projection (Kitchen *et al.* [46]).

By applying filtered backprojection (Kak and Slaney [43]) using a ramp (Ram-Lak) filter directly to the phase-contrast images, without performing phase retrieval (Cloetens *et al.* [17]), we obtain a qualitative reconstruction of the thorax as shown in Fig. 5.3 (b). Here, the phase–contrast fringes formed at the edges between the interfaces (i.e. air/lung and bone/lung tissues) are seen in the reconstruction as residual phase-contrast fringes in the tomogram. We note that slight motion artefacts are also evident due to difficulties in keeping the object stationary for the $\sim$ 7 minutes of scan time. The phase contrast can aid the visualization of features such as the major airways by highlighting their boundaries. However, the edge enhancement can obscure finer features and restricts quantitative analysis of the tissue morphology (Suzuki *et al.* [78]). To perform interface–specific phase retrieval tomography, we apply Eqns (5.1) and (5.2) to each tomographic
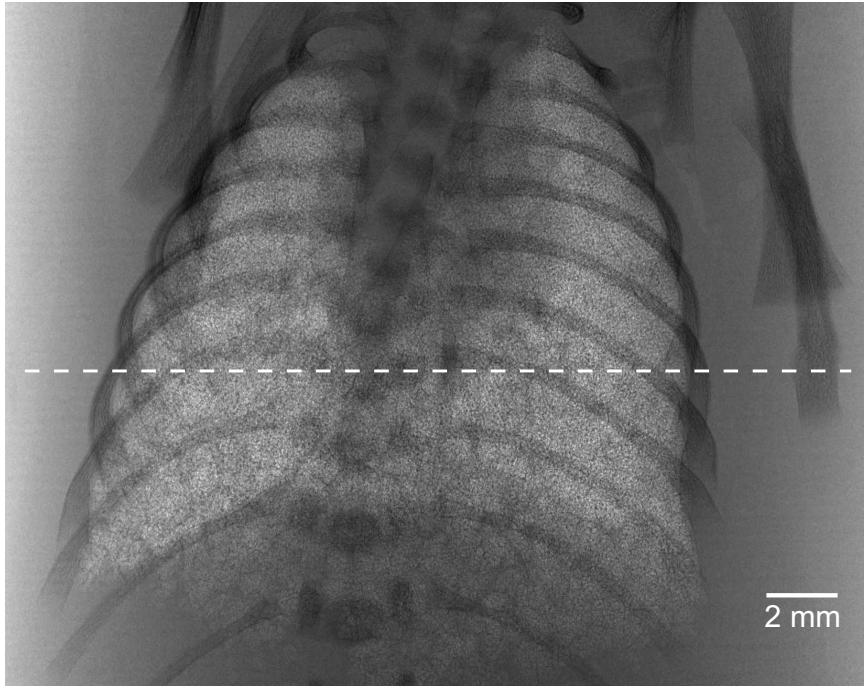
(a)
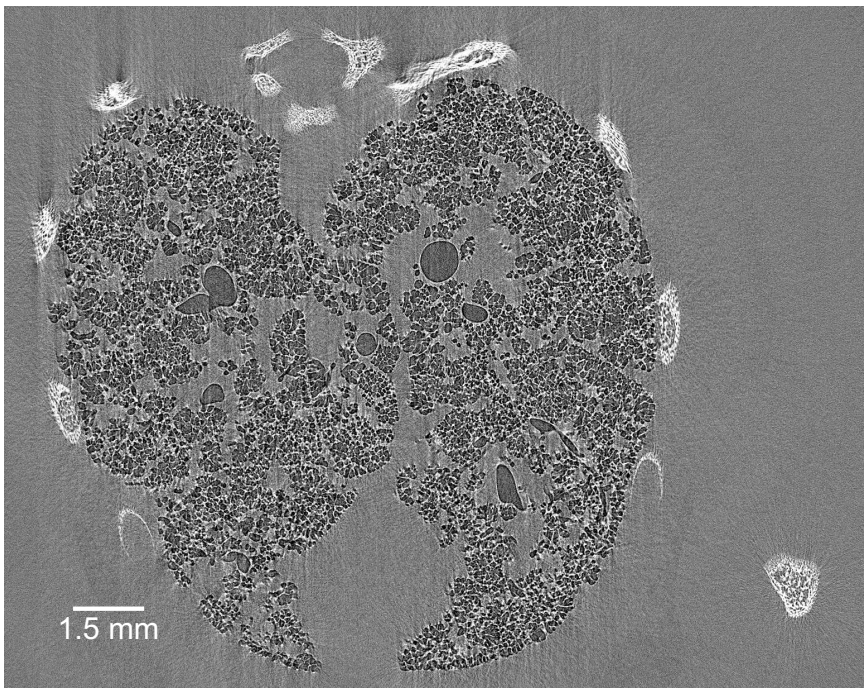
(b)

Figure 5.3: Propagation-based X–ray phase-contrast image of the lungs of a preterm rabbit pup. X–ray energy of 24 keV, propagation distance=50 cm. (b) Tomographic reconstruction of a single slice (see the dashed line in (a)) from the raw phase-contrast images utilizing filtered backprojection.

image followed by filtered backprojection. Depending on which interface one wishes to focus on, the corresponding δ and μ or $\Delta\delta = \delta_2 - \delta_1$ and $\Delta\mu = \mu_2 - \mu_1$ are input into Eqns (5.1) and (5.2), respectively. Here we denote $j = 2$ as the bone/lung tissue interface.
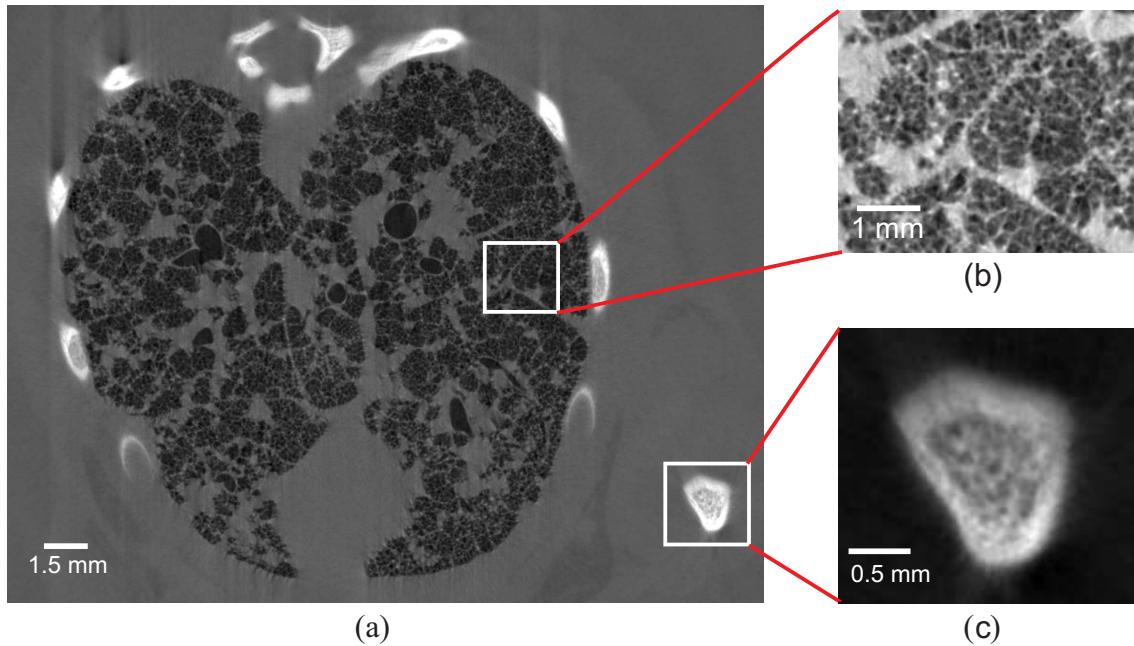
Figure 5.4: Interface–specific tomographic reconstruction of a newborn rabbit pup thorax focusing on the air/lung interface. (b) shows a magnified section of (a) to aid visibility of the terminal airways. (c) shows a magnified section of (a) in which the bone/lung tissue interface appears blurred as a result of the chosen phase retrieval filter. Note, this figure was republished in the review article by Bravin *et al*. [9].

In our analysis, we consider lung tissue to be the encasing material. Therefore, to focus in on the air/lung tissue interface, we apply Eqns (5.1) to each tomographic image. Here, the δ and μ values for water were inserted into Eqns (5.1) as soft tissues and water have similar refractive and absorptive properties at the selected X–ray energy (Kitchen *et al*. [45]). A tomographic reconstruction that focuses on the air/lung tissue interface is shown in Fig. 5.4 (a) . This image illustrates that the phase-contrast fringes have been removed, leaving the air/lung tissue interfaces sharply reconstructed, while we can also see that the bone/lung tissue interface has been locally blurred as a result of incorrect choices of δ and μ in the phase retrieval process, which contaminates the local vicinity surrounding this interface (Beltran *et al*. [6]). Figure 5.4 (b) shows a zoomed-in region of Fig. 5.4 (a) in which individual terminal airways (alveoli) are clearly visible.

An important benefit of the phase-retrieved reconstruction (Fig. 5.4) is the clearly improved SNR over the raw tomographic dataset (Fig. 5.3 (b)). Using three 50×50 pixel regions containing soft tissue only, an SNR of 30 ± 6 (mean $\pm$ standard deviation) was calculated. By comparison, the same area in the raw reconstruction yielded just 1.8 ± 0.3. Note, these values were calculated using the formula in Eqn. 4.27 (see section 4.3.5). However, since no pure absorption-contrast image could be collected due to the finite

object-to-detector distance, the latter SNR value was calculated in a region of Fig. 5.3 where only absorption-contrast signal exists (i.e. away from residual phase-contrast fringes). Thus, we found an improvement in the soft-tissue SNR of 16 ± 4 fold over absorption contrast for our particular experimental setup. This same improvement in the SNR was also observed (within uncertainties) in the large airspaces (bronchioles). It is not surprising that the noise was so heavily reduced since the phase retrieval algorithms naturally suppress high-frequency noise.

Employing phase contrast with an appropriate phase retrieval algorithm has enabled us to clearly visualize the terminal airways. Whilst similar quality data may have been obtained from absorption-contrast tomography, for instance by increasing the X–ray exposure, the corresponding dose increase would be prohibitive. This has important implications for studying the health of the lungs and other organs. Emphysema, for example, is a disease of the distal airways that is characterized by the loss of alveolar structures. The ability to clearly observe these fine structures could lead to improved diagnosis of early lung disease. We have used this dataset to measure the range of alveolar dimensions found within this animal. The diameters of the alveoli were measured to be between 109 and 162 μm, which is consistent with the previously measured values found in a rabbit pup model (Hooper *et al*. [40]). We further demonstrate the fidelity of the reconstruction in the online supplementary movie (available at stacks.iop.org/PMB/56/7353/mmedia) that takes us into the airway tree of the pup, with remarkable clarity all the way to the terminal airsacs (alveoli). This movie was made using commercial software (Amira v 5.2, Visage Imaging, Inc.) upon thresholding the image stack such that the airways were transparent and the tissues opaque.

To retrieve quantitative information from the in-focus interface, a line profile across a major airway, shown in Fig. 5.5 (a), is plotted in Fig. 5.5 (b). Here the distribution of the refractive index decrement averages around the expected value listed in Table 5.1. Also, a line profile is plotted across the magnified (blurred) bone feature seen in Fig. 5.5 (c), which helps us to observe the over-smoothing of the bone/soft-tissue interface and the quantitatively incorrect reconstruction of δ (see Table 5.1).

Referring back to Fig. 5.4 (a) we note that other soft tissues can be seen as amorphous shapes surrounding the chest wall in the phase retrieved reconstruction. These tissues are more evident than in the raw reconstruction in Fig. 5.3 (b). We attribute this increased clarity to the shape of the Fourier filter required for the lung tissue/air interface used in Eqns (5.1) being likely very similar to that used in Eqns (5.2) that would be used to focus on soft-tissue interfaces. This filter has suppressed the noise, making the other soft tissue more readily visible.

To focus on the bone/lung tissue interface, we instead process every image with Eqn. (5.2) before tomographically reconstructing each slice. To apply this equation, we use the δ and μ values for bone as well as those for water together with *a priori knowledge* of the total projected thickness A($\mathbf{r}_\perp$). A($\mathbf{r}_\perp$) is required to determine the attenuation that the object would provide if it were made entirely of a single homogenous material, which is

used in the normalization term $I_0 \exp\left[-\mu_1 A(\mathbf{r}_\perp)\right]$ of Eqn (5.2). Here we have approximated the normalization term by fitting a parabolic curve to the intensity profile at each projection. This only works well since the animal was inside a water-filled cylinder and because the lungs are approximately circular in projection and were located near the centre of the tube. Although this approximation will reduce the accuracy of the reconstruction, we see no artefacts in the resulting reconstruction, justifying its use.

(a)   (b)

(c)   (d)
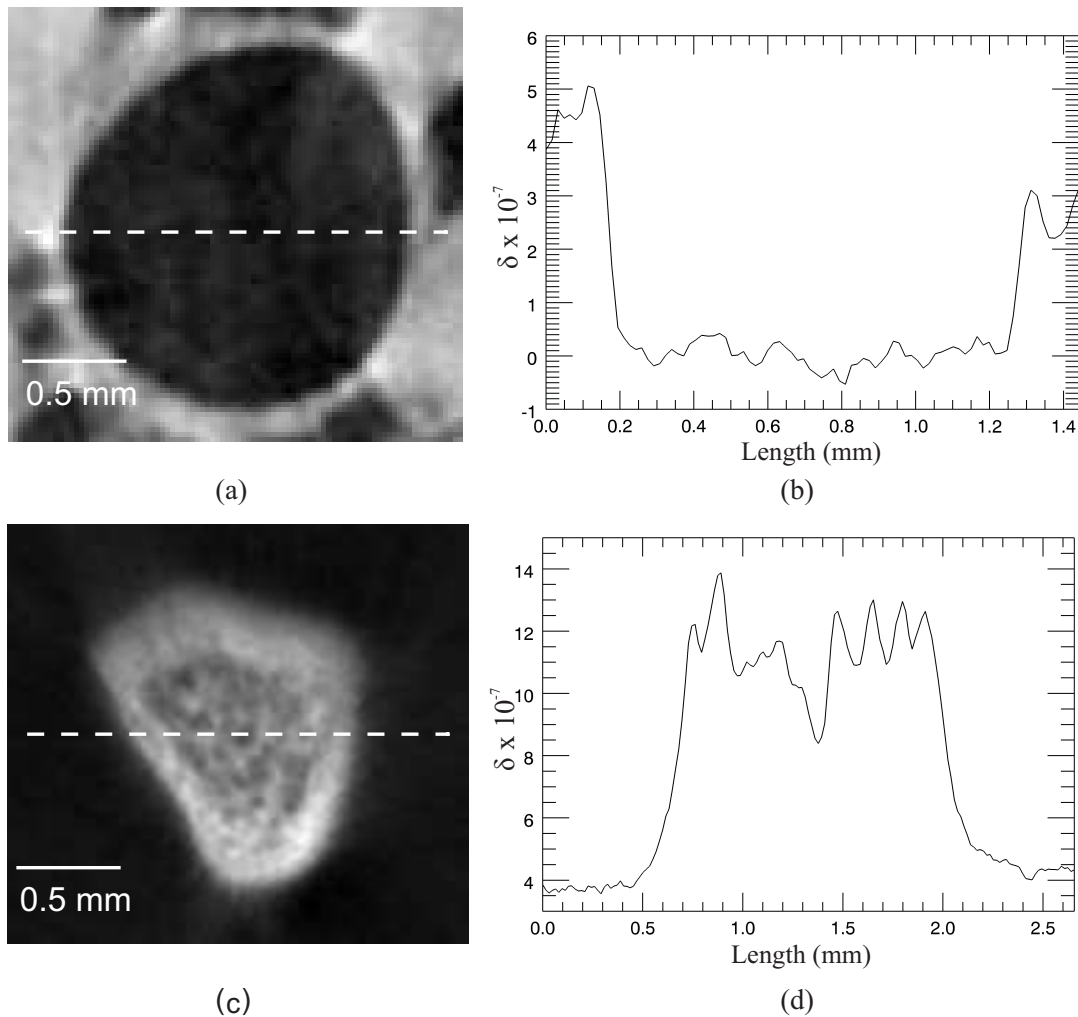
Figure 5.5: (a) Magnified region of Fig. 5.4 (a) showing a major airway. Its line profile is plotted from left to right from the centre of the image and is shown in (b) displaying the distribution of its refractive index decrement. (c) The same image as in Fig. 5.4 (c) with its line profile shown in (d).

In Fig. 5.6 (a), a tomographic reconstruction of the same slice as in Fig. 5.3 (b) and Fig. 5.4 (a) is shown, which now focuses on the bone/lung tissue interfaces. From this image, we see that the interfaces of interest have now been correctly reconstructed, yielding a sharp boundary between the media. This can be better appreciated in Fig. 5.6 (b), which

shows the same zoomed-in region as in Fig. 5.4 (c), but now the boundaries and features are highly visible. Additionally, the line profile in Fig. 5.6 (c) shows the quantitative measure of the refractive index decrement, δ. The large fluctuations in δ arise from the porosity of the bone. The maximum value underestimates the expected value from Table 5.1. We believe that this discrepancy arises because the tabulated values are calculated for mature, fully calcified bone, whilst the immature bones of the newborn rabbit will differ considerably in their average density and composition (i.e. They are not fully calcified), compared to those of an adult rabbit, thereby lowering the measured δ value.

To compare the improvement in the SNR before and after the phase retrieval for the bone/tissue interface, we observed the cortical bone (outer edge) of the bone segment seen in Fig. 5.6 (c). The cortical bone contains fewer pores than the internal trabecular bone and enables comparison against the raw image far from phase-contrast fringes (i.e. a measure of approximately pure attenuation by bone). We measured the mean signal within small areas of cortical bone and measured the noise from the nearby soft tissue that was also free of phase-contrast effects. For bone, the SNR in the raw "absorption-contrast" image was only 5 ± 1 compared to the same area in the phase retrieved image with an SNR of 47 ± 12. On average, we found an improvement in the SNR of 9 ± 3 times afforded by phase retrieval. Whilst this is less than the improvement seen for the soft-tissue reconstruction, this results from the reduced level of spatial filtering in Eqns (5.1) due to the reduced phase gradients present at the bone/tissue interface compared to the air/tissue interface.

Finally, we draw attention to the air/lung tissue interfaces in Fig. 5.6 (a), which have now been over-sharpened, or insufficiently filtered, by the phase retrieval process resulting from under-compensation of the phase-contrast fringes. Therefore, the air/tissue interfaces have been incorrectly reconstructed.

Upon reconstructing all interfaces of interest, we now combine the images in Fig. 5.4 (a) and Fig. 5.6 (a) to compose a spliced reconstruction shown in Fig. 5.7. To produce the spliced image, one cannot simply manually insert the appropriate region into the corresponding regions of another image. We began by using the soft-tissue image (Fig. 5.4) and exploited the fact that the relatively highly attenuating bones appear blurred, realizing that the true bone interfaces must lie within those blurred regions. The large contrast enabled the image to be thresholded until the blurred bones were invisible, thereby creating a binary "soft-tissue-only" mask. The inverse of this mask was then applied to the image containing the correctly reconstructed bones (Fig. 5.6). By smoothing each binary mask, and ensuring both masks summed to unity before multiplying with the relevant image, a continuous and smooth spliced image was formed by adding the masked images together. One additional step involved adjusting any offsets so that the background encasing material had the same average value in each image before creating the spliced image.

The spliced image shows all interfaces both quantitatively and sharply reconstructed, which demonstrates the key result that we are able to perform phase and amplitude tomography of multi-material objects that are spatially quantized with only one PBI image per tomographic orientation.
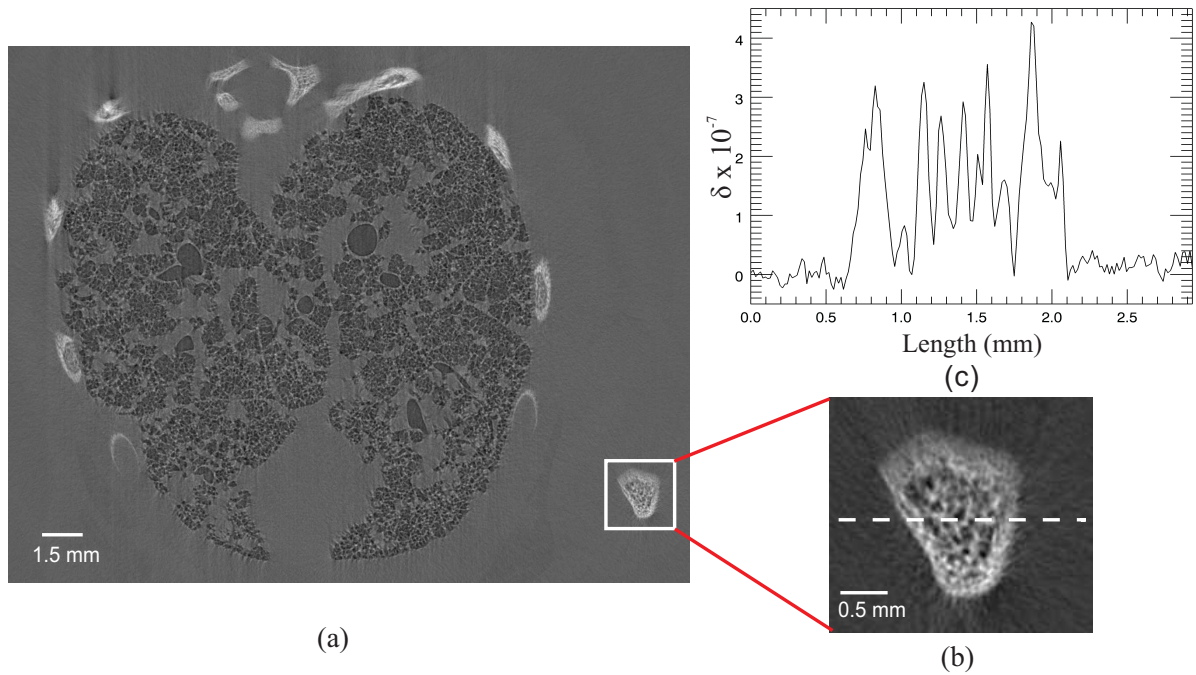
Figure 5.6: (a) Interface–specific tomographic reconstruction of a preterm rabbit pup thorax, focusing on the bone/lung tissue interface. (b) shows a magnified section of (a) which now yields a sharp and quantitative reconstruction of the same images seen in Fig. 5.4 (c) and Fig. 5.5 (c). (c) Line profile from left to right across the centre of (b) showing the distribution of the refractive index decrement of the porous bone.

One drawback of our image splicing is that the objects in question should be spatially separated by an amount equal to the bleeding (pollution length) associated with over-smoothing the second interface. In section 4.3.4 it was shown that this bleed width (Δx) depends only on the refractive index of the encasing material, where

$$\Delta x \geqslant \sqrt{d\delta_1/\mu_1}. \tag{5.3}$$

It was experimentally verified that a distance of three to five times (Δx) was sufficient to avoid locally polluting nearby objects of a different refractive index. For our experiment, this distance should therefore be at least 180 μm, but no more than 300 μm. This reduces the accuracy of the reconstruction where the bone encroaches on the airways. Interestingly, we see very little evidence of the contamination between media in the spliced reconstruction of Fig. 5.7 even though some of the bones were close to the lung tissue.

5.4.2 Brain imaging

Figure 5.8 (a) shows a single PBI image from the CT dataset of a rat brain prepared as described in section 5.3.3. Due to the similar complex refractive indices of brain and agar (Table 5.2), the brain is not visible in a single projection image even with the very long
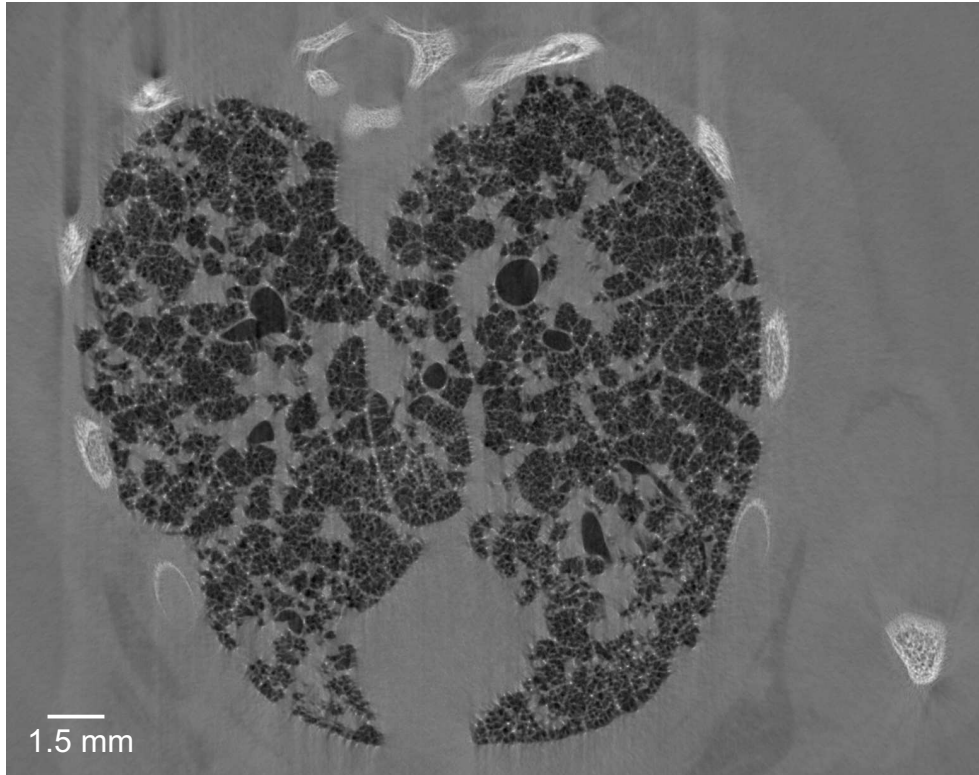
Figure 5.7: Spliced tomographic reconstruction of preterm rabbit pup lungs, constructed by splicing Fig. 5.4 (a) and Fig. 5.6 (a).

propagation distance of 5.0 m. However, if we apply filtered backprojection directly to the set of raw PBI brain images (Fig. 5.8 (b)), a small amount of anatomical detail becomes visible and structures are resolved relative to the gel agar matrix. This is principally due to the averaging effect caused by acquiring images from multiple projections which improves the SNR. Figure 5.8 (b) shows a single tomographic slice in a para-frontal orientation at an approximate anterior-posterior distance of 9.4 mm caudal to bregma. The bright white flares seen in the image are possibly caused by attenuation due to Bragg diffraction from crystallite regions in the agar matrix.

Phase retrieval was then applied before performing the tomographic reconstruction. As described above, all materials in the brain sample effectively refract and attenuate X–rays to a similar degree; hence the sample behaves somewhat like a single-material object and thus we need to utilize Eqn (5.1) only (see Fig. 5.2). We used the δ and μ values for grey/white matter listed in Table 5.2. The same slice in Fig. 5.8 (b) is shown in Fig. 5.9, now with the phase retrieval process included. Despite the subtle differences in complex refractive index, the tomogram yields clearly demarcated tissue borders at the grey/white matter boundaries. Considerable detail can be seen in the brainstem, including the ventral cochlear nucleus (vCN), spinal tract of the trigeminal nerve (TST) and inferior cerebellar peduncle (iCP).

SNR values were calculated for six 30×30 pixel regions of grey or white matter in both
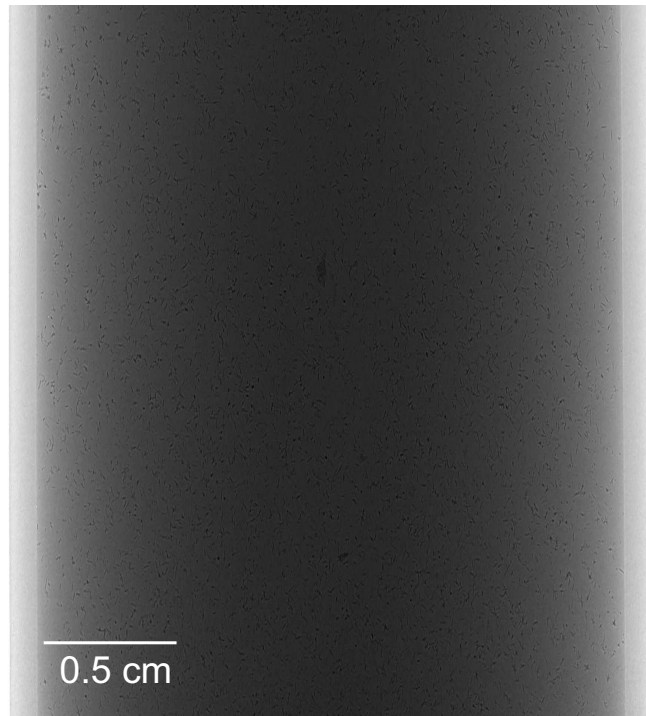
(a)
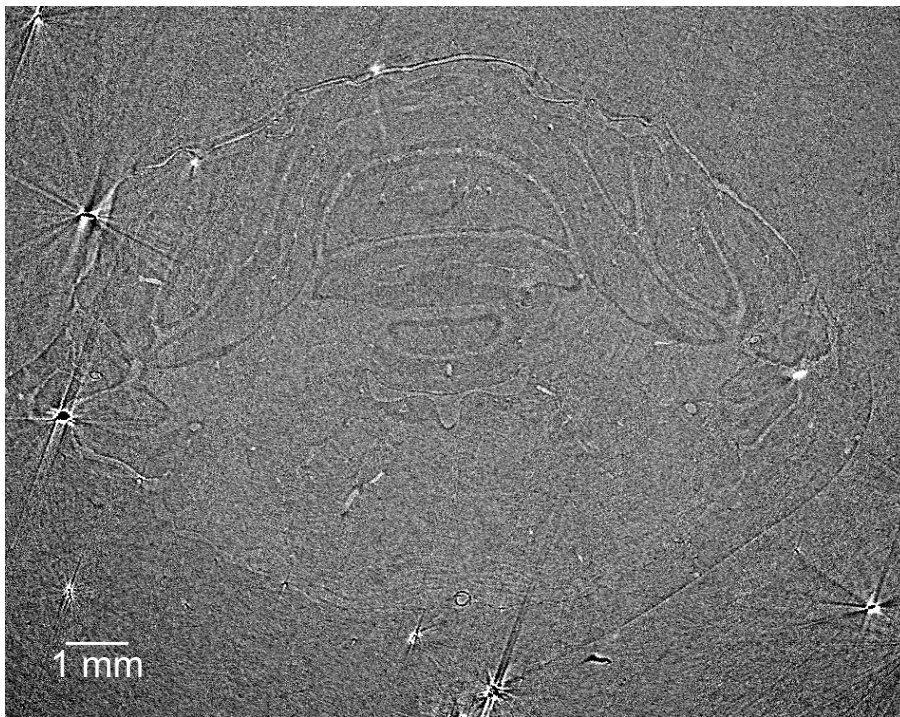
(b)

Figure 5.8: (a) PBI image of a excised rat brain submerged in an agar solution. X–ray energy of 24 keV, propagation distance $d = 5.0$ m. (b) Tomographic reconstruction of a single slice from the raw brain PBI images using filtered backprojection.
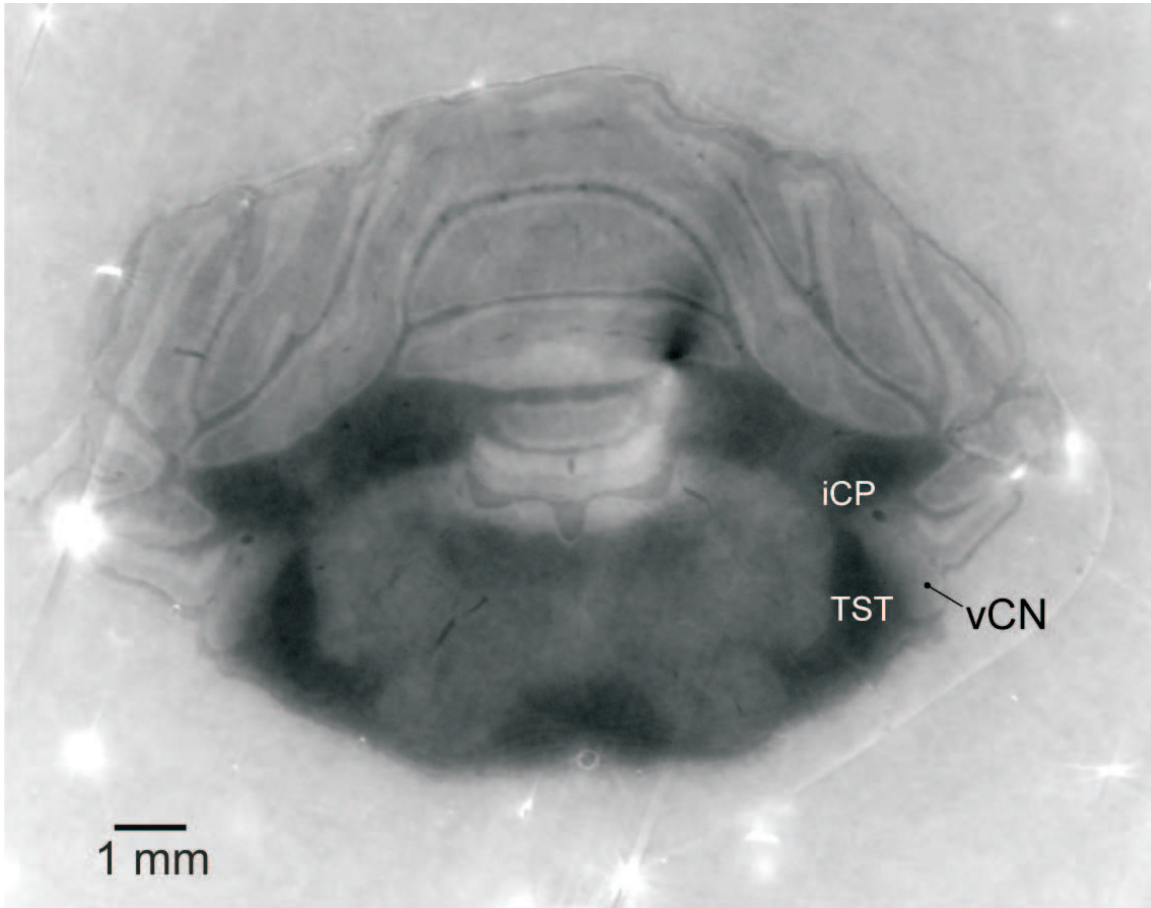
Figure 5.9: Tomographic reconstruction of the same slice as shown in Fig. 5.8 (b). Equation (5.1) was applied to each image before tomographically reconstructing.

Fig. 5.8 (b) and Fig. 5.9 yielding values of 2.1 ± 0.2 and 440 ± 120, respectively. Again we note that the regions selected for the calculations did not contain any phase-contrast signal. For brain imaging with this geometry, we found a net gain in the SNR of 200 ± 50 over absorption contrast. This exceptional improvement is a consequence of the relatively large propagation distance of 5.0 m used to render the brain visible, which translates to heavy spatial filtering (see Fig. 5.2) and associated strong noise suppression in the phase retrieval step (Eqn (5.1)); this effect was also discussed by (Arhatari *et al*. [3]). Note that if one were to use too large a propagation distance, the validity conditions of the underlying transport-of-intensity equation would be violated.

Phase-contrast modalities that are more sensitive to weak phase gradients, such as grating interferometry, can render visible the tissues of the brain with even higher contrast than that presented above (Pfeiffer *et al*. [70]). However, the extra sensitivity of such methods makes them less robust for imaging objects that simultaneously contain strong phase gradients such as the air/soft-tissue boundaries within the lung. Moreover, phase retrieval in that context requires multiple images to be acquired for every projection (Pfeiffer *et al*. [70]), thereby significantly increasing the X–ray dose to the sample. The

benefits of our approach include the simple imaging geometry, with no requirement for post-sample optical elements, and only a single exposure per projection required for phase retrieval.

5.5   Concluding remarks

We have demonstrated that interface–specific X–ray phase retrieval tomography, using the method developed in chapter 4, can be performed on complex biological objects. The method makes use of only a single PBI image per tomographic orientation and requires *a priori* information of the sample's total projected thickness at each orientation and knowledge of each material's complex refractive index present in the sample. Note that for a sample containing no internal voids, the total projected thickness at each orientation is completely determined by knowledge of the surface of the object. The method was successfully implemented on experimental propagation-based phase-contrast tomographic data of the thorax and brain of small animals collected using X–ray synchrotron radiation. For the thorax data, quantitative reconstructions of air/lung tissue and bone/lung tissue interfaces were performed separately and were then spliced together to yield a complete reconstruction. A tomographic reconstruction of a rat brain was made under the assumption that it comprised of a single material of variable density, which resulted in an image able to clearly distinguish between grey and white matter. SNR calculations were carried out and showed our technique to be superior to conventional absorption contrast by factors ranging from 9 to 200 fold. This gain in SNR can potentially be used to lower the radiation dose. This can be demonstrated in a simple calculation that considers Poisson statistics using the following formula:

$$\text{SNR} = \sqrt{N} \tag{5.4}$$

where, N represents the number of photons. From Eqn. (5.4), it can be seen that for the SNR to increase $10\times$ then N must be increased by $100\times$. If we assume that N is directly proportional to dose then, according to this calculation one would require $100\times$ the dose with conventional absorption contrast CT to produce the image contrast achieved using our method. In other words, the radiation dose could be reduced $100\times$ compared to that used with conventional CT to maintain the SNR. This is more significant for an SNR increase of $200\times$, which would see a potential radiation dose reduction of $40,000\times$. However, the relation between SNR and dose still requires experimental investigation. This would be advantageous given that estimated surface entrance doses were ~69 Gy for the lungs of the rabbit pup and ~828 Gy for the excised rat brain, which are extremely high.

6

Aberration–induced phase contrast imaging in partially coherent fields transmitted through a linear shift–invariant imaging system

6.1 Introduction

So far this thesis has dealt with a single X–ray phase contrast imaging modality (propagation-based phase contrast (PBI)) and we have assumed that the radiation source is a well behaved, fully coherent field. In this chapter we drop the assumptions of a single phase contrast modality and full coherence and generalize to arbitrary differential phase contrast modes utilizing partially coherent fields. To make such a generalization, phase contrast effects are treated as a form of optical aberration that distorts an input image. The optical system is assumed to be linear and shift–invariant such that it can be characterized by a transfer function. To incorporate the effects of partial coherence the space–frequency description formulated by Wolf [88] is utilized (see section 2.6.5). Including the effect of partial coherence would add a greater degree of quantitativeness in the analysis of phase contrast images that are acquired using more accessible X–ray sources (i.e. laboratory sources). Also, establishing a mathematical expression that describes the forward problem under the conditions of partial coherence naturally leads to the study of the inverse problem under such effects. This could potentially reveal more information about a sample than traditional phase retrieval methods.

This chapter[1] generalizes the work of Paganin and Gureyev [64], Petrucelli *et al*. [69], Gureyev [34], and Zysk *et al*. [94]. Paganin and Gureyev [64] generalised arbitrary phase contrast linear shift-invariant imaging systems via the use of optical aberration theory, but excluded the effects of partial coherence. On the other hand, Petrucelli *et al*. [69],

---

[1]This chapter is based on the manuscript "Aberrations in shift-invariant linear optical imaging systems using partially coherent fields", M. A. Beltran, M. J. Kitchen, and D. M. Paganin. This manuscript was uploaded into the arXiv website and is currently in the process of publication. See Appendix C.

Gureyev [34], and Zysk *et al.* [94] included the effects of partial coherence specifically for propagation–based phase–contrast imaging based on the transport–of–intensity equation.

Some relevant background material on the theory of aberrated linear systems is reviewed in section 6.2. In section 6.3 we obtain an equation that describes the action of shift–invariant linear systems, using partially coherent fields, under the assumption that the object under study is a pure thin phase object. A two–dimensional transverse Cartesian coordinate system is used in the derivation. In section 6.4 expressions for the spectral density are derived, restricting consideration to only one transverse spatial variable for simplicity. Three different types of sample are considered: Samples that satisfy; i) the weak–phase object approximation; ii) the weak phase–amplitude approximation and; iii) the single material weak phase–amplitude approximation. Section 6.5 studies in depth the features of the transfer function used in this formalism.

6.2 Linear shift–invariant imaging systems and optical aberrations

In this thesis we consider optical systems that; (i) satisfy the property of linearity and; (ii) exhibit shift–invariance. For any optical system the output is related to the input wavefield via the operation (Goodman [30]):

$$\Psi_{out}(x, y) = \mathfrak{L}\left\{\Psi_{in}(x, y)\right\} \tag{6.1}$$

where $\mathfrak{L}$ represents a mathematical operator acting on the input wavefield $\Psi_{in}(x, y)$. A system is said to be linear if for any input composed by a linear combination of separate weighted wavefields then the output will also be the corresponding linear combination of weighted wavefields. In mathematical terms this is implies the following:

$$
\begin{aligned}
\mathfrak{L}\left\{a\Psi_{in}^{(1)}(x, y) + b\Psi_{in}^{(2)}(x, y)\right\} &= a\mathfrak{L}\left\{\Psi_{in}^{(1)}(x, y)\right\} + b\mathfrak{L}\left\{\Psi_{in}^{(2)}(x, y)\right\} \\
&= a\Psi_{out}^{(1)}(x, y) + b\Psi_{out}^{(2)}(x, y).
\end{aligned}
\tag{6.2}
$$

Here, a and b are arbitrary complex constants. In the case of shift–invariance, if the input wavefield is shifted by a certain distance in the transverse direction then the output wavefield will also be shifted by an equal distance in the same transverse direction. That is;

$$\Psi_{out}(x - a, y - b) = \mathfrak{L}\left\{\Psi_{in}(x - a, y - b)\right\}. \tag{6.3}$$

Optical aberrations for shift–invariant linear systems for fully coherent complex scalar wavefields are described by the transfer function formalism. For such optical systems the
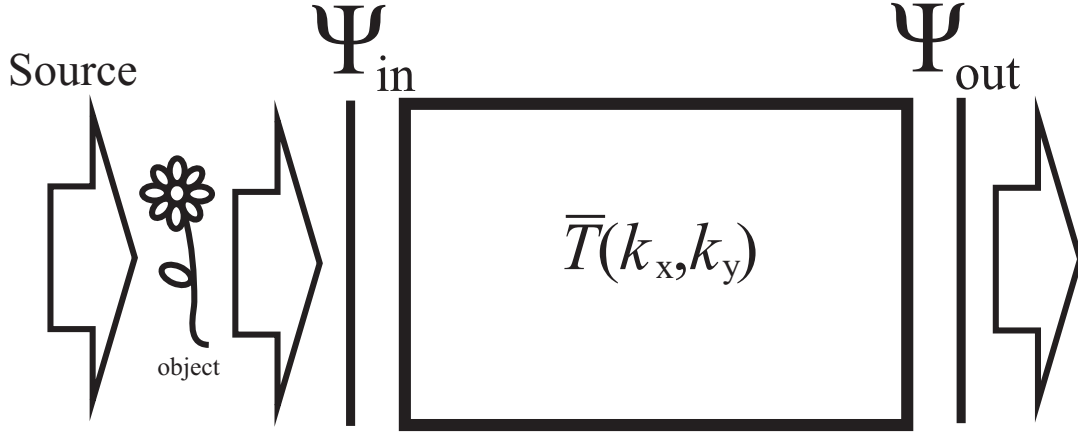
Figure 6.1: Schematic illustration of the action of an aberrated shift–invariant linear optical system for imaging fully coherent complex scalar wavefields under the transfer function formalism. Input and output complex fields are related by the transfer function formalism according to Eq. (6.4).

output field $\Psi_{out}(x, y)$ is related to the input field $\Psi_{in}(x, y)$ by a Fourier–space filtration that can be written in operator form as (Paganin and Gureyev [64]):

$$\Psi_{out}(x, y) = \mathrm{F}^{-1}_{k_x,k_y} \overline{T}(k_x, k_y) \mathrm{F}_{x,y} \left\{ \Psi_{in}(x, y) \right\} . \tag{6.4}$$

Here, $\overline{T}(k_x, k_y)$ is the transfer function characterizing the optical system, (k_x, k_y) are Fourier conjugate coordinates dual to (x, y), F and F^{-1} respectively represent the forward and inverse Fourier transform operations, and all operators are taken to act from right to left. Thus, the above equation states that F is applied to the input field $\Psi_{in}(x, y)$, before multiplying by the transfer function $\overline{T}(k_x, k_y)$ and then applying the operator F^{-1}, so as to yield the output field $\Psi_{out}(x, y)$ (see Fig. 6.1).

We recall the forward and inverse Fourier transform operation conventions used in this thesis:

$$\widehat{G}(k_x, k_y) = \frac{1}{2\pi} \iint_{-\infty}^{\infty} G(x, y) e^{-i(k_x x + k_y y)} dx dy, \tag{6.5a}$$

$$G(x, y) = \frac{1}{2\pi} \iint_{-\infty}^{\infty} \widehat{G}(k_x, k_y) e^{i(k_x x + k_y y)} dk_x dk_y. \tag{6.5b}$$

Here, $\widehat{G}(k_x, k_y) \equiv \mathrm{F}\{G(x, y)\}$.

To proceed further, we follow Paganin and Gureyev [64] and make the restricting assumption that the transfer function $\overline{T}(k_x, k_y)$ is sufficiently well behaved for its logarithm to admit a Taylor–series representation. Note that a necessary condition for this assumption to be valid is that the transfer function does not possess any zeros over the patch of Fourier space for which the modulus of $\mathrm{F}\{\Psi_{in}(x, y)\}$ is non–negligible, a region which may be termed the "essential spectral support" of the input field.

While this key assumption will fail for imaging systems such as Schlieren optics, which completely block certain spatial frequencies in the essential spectral support of the input disturbance, the assumption will hold for a variety of important imaging systems such as out–of–focus contrast (Wilkins *et al.* [85]), inline holography (Gabor [27]), interferometric phase contrast (Bonse and Hart [7]), differential phase contrast (Pfeiffer *et al.* [71]), and analyzer–based phase contrast of weakly scattering samples (Förster *et al.* [26]), etc. With this in mind, our simplifying assumption allows us to express the transfer function in the classic form that is standard, for example in transmission electron microscopy, namely (Paganin and Gureyev [64], Paganin [67], Cowley [19]):

$$\overline{T}\left(k_x, k_y\right) = \exp\left(i \sum_{m,n=0}^{\infty} \widetilde{\alpha}_{mn} k_x^m k_y^n\right). \tag{6.6}$$

Under this representation we denote the set of complex numbers $\{\widetilde{\alpha}_{mn}\}$ as the "aberration coefficients" where m and n are non–negative integers that label the order of the aberration. The real part of each such coefficient is termed a coherent aberration, with the corresponding imaginary part being termed an incoherent aberration. The reader is encouraged to see Paganin and Gureyev [64] for a direct link between these complex aberration coefficients and the Seidel aberrations (e.g., piston, defocus, astigmatism, spherical aberration, chromatic aberration etc.) of classical aberration theory (Born and Wolf [8]). Optical devices in the majority of cases are designed with cylindrical geometry (i.e. microscopes, telescopes). Therefore it is often advantageous to describe optical aberration coefficients and transfer functions in terms of Zernike polynomials for which the aberration function is expressed as a series expansion in polar coordinates over the unit circle. However, this is not the case in this thesis where Cartesian coordinates are used to suit a more arbitrary geometry. Nevertheless this formalism can be related to Zernike coefficients and polynomials using appropriate transformations (Lakshminarayanan and Fleck [48]).

Expanding the complex exponential in Eqn. (6.6) as a Taylor–series, we obtain:

$$\overline{T}\left(k_x, k_y\right) \equiv 1 + i \sum_{m,n=0}^{\infty} \alpha_{mn} k_x^m k_y^n. \tag{6.7}$$

The above expression serves to define the set of coefficients $\{\alpha_{mn}\}$. The set of coefficients $\{\alpha_{mn}\}$ is defined in terms of the set of aberration coefficients $\{\widetilde{\alpha}_{mn}\}$. This form is particularly useful for studying the effect of transfer functions that differ only slightly from unity, namely for weakly aberrated shift–invariant imaging systems. We shall later pick up on this point in section 6.5.

6.3   Optical aberrations in shift–invariant linear imaging systems using partially coherent fields considering two transverse spatial coordinates

In this section we include the the effects of partial coherence for an aberrated shift–invariant linear optical system. It proves convenient to express the output complex disturbances which are related to the input complex disturbances in terms of the transfer function formalism (i.e. Eqn. (6.4)) in terms of the Fourier space integral shown in Eqn. (6.5b) (b):

$$\Psi_{out}(x,y) \;=\; \frac{1}{2\pi} \iint_{-\infty}^{\infty} \overline{T}\left(k_x, k_y\right) e^{i(k_x x + k_y y)} \widehat{\Psi}_{in}(k_x, k_y) \, dk_x dk_y,$$

$$(6.8)$$

where $\widehat{\Psi}_{in}(k_x, k_y)$ denotes the Fourier transform of $\Psi_{in}(x,y)$ with respect to x and y. The above integral–form expression describes the output wavefield for an optical system that is linear and shift–invariant for incoming wavefields that are fully coherent.
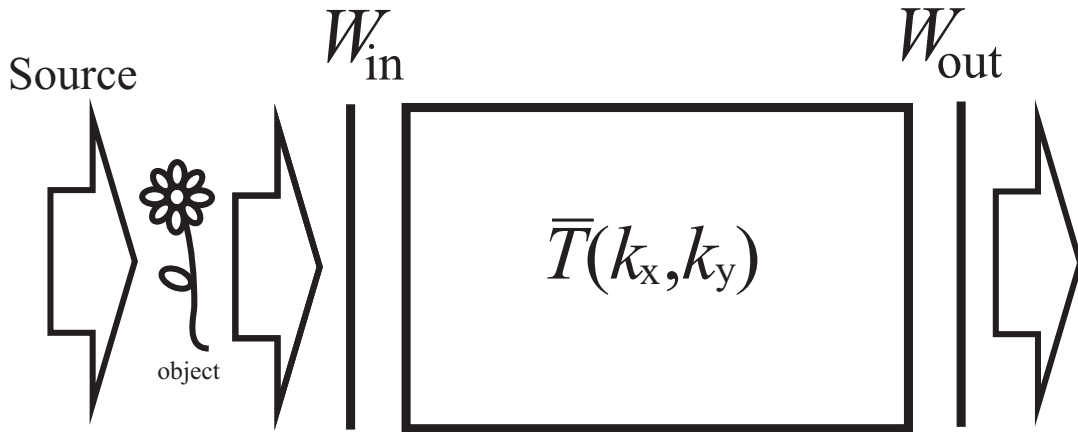
Figure 6.2: Schematic illustration of the action of an aberrated shift–invariant linear optical imaging system, for statistically stationary partially coherent complex scalar fields, under the transfer function formalism. Input (W_{in}) and output (W_{out}) cross–spectral densities are related by the generalized transfer function formalism according to Eqn. (6.11).

For the reasons outlined earlier, it is desirable to extend this theory to partially coherent fields. This corresponds to the generalization shown in Fig. 6.2. Here, W_{in} is the cross–spectral density incident upon a linear shift–invariant aberrated optical system, yielding the corresponding output cross–spectral density W_{out}.

Under the space–frequency description of partial coherence developed by (Wolf [8, 88]), the output cross–spectral density at a specified angular frequency ω may be constructed using an ensemble of strictly monochromatic fields all of the same angular frequency, via (see chapter 2):

$$W_{out}(x_1, y_1, x_2, y_2) = \left\langle \Psi_{out}^*(x_1, y_1)\Psi_{out}(x_2, y_2) \right\rangle_\omega. \tag{6.9}$$

Here, angular brackets denote the ensemble average.

Putting this equation to one side for the moment, note that we can express $\Psi_{out}^*(x_1, y_1)$ and $\Psi_{out}(x_2, y_2)$ in terms of the Fourier transform of $\Psi_{in}^*(x_1, y_1)$ and $\Psi_{in}(x_2, y_2)$, respectively, using the conventions in Eqn. (6.5a) and (6.5b), which gives the following:

$$\Psi_{out}^*(x_1, y_1) = \frac{1}{(2\pi)} \iint_{-\infty}^{\infty} \overline{T}^*\left(k_{x_1}, k_{y_1}\right) e^{i^*(k_{x_1}x_1 + k_{y_1}y_1)} \widehat{\Psi}_{in}^*(k_{x_1}, k_{y_1}) dk_{x_1} dk_{y_1}, \tag{6.10a}$$

$$\Psi_{out}(x_2, y_2) = \frac{1}{(2\pi)} \iint_{-\infty}^{\infty} \overline{T}\left(k_{x_2}, k_{y_2}\right) e^{i(k_{x_2}x_2 + k_{y_2}y_2)} \widehat{\Psi}_{in}(k_{x_2}, k_{y_2}) dk_{x_2} dk_{y_2}. \tag{6.10b}$$

By substituting the above expressions into Eqn. (6.9), one can obtain the output cross–spectral density in terms of the input cross–spectral density as (Gbur and Visser [28]):

$$\begin{aligned}
W_{out} &= \frac{1}{(2\pi)^2} \iiiint_{-\infty}^{\infty} \overline{T}^*\left(k_{x_1}, k_{y_1}\right) \overline{T}\left(k_{x_2}, k_{y_2}\right) e^{[i^*(k_{x_1}x_1 + k_{y_1}y_1) + i(k_{x_2}x_2 + k_{y_2}y_2)]} \\
&\quad \times \left\langle \widehat{\Psi}_{in}^*(k_{x_1}, k_{y_1})\widehat{\Psi}_{in}(k_{x_2}, k_{y_2}) \right\rangle_\omega dk_{x_1} dk_{y_1} dk_{x_2} dk_{y_2}.
\end{aligned} \tag{6.11}$$

Equation (6.11) can be visualized pictorially in the diagram shown in Fig. 6.2. For the present we restrict considerations to ensembles of input wavefields, each member of which is described by the "phase object approximation" that, by definition, are wavefields that only vary in phase but not in amplitude, that is $\Psi_{in}(x, y) = e^{i\phi_{in}(x,y)}$. This way our final expression will be a series of terms that have operations on the input phase $\phi_{in}(x, y)$, which is a real function. Later in this chapter we generalize to include absorption. Expanding the complex exponential in this expression as a Taylor series, which implies no loss of generality on account of the infinite radius of convergence of this series, we obtain:

$$\Psi_{in}(x, y) = 1 + \sum_{p=1}^{\infty} \frac{i^p}{p!} \phi_{in}^p(x, y). \tag{6.12}$$

Taking the Fourier transform of the above expression with respect to x and y, we can then write down the following expressions for the terms $\widehat{\Psi}_{in}^*(k_{x_1}, k_{y_1})$ and $\widehat{\Psi}_{in}(k_{x_2}, k_{y_2})$ in

Eqn. (6.11):

$$\widehat{\Psi}_{in}^*(k_{x_1}, k_{y_1}) = \widehat{\delta}(k_{x_1}, k_{y_1}) + \sum_{p=1}^{\infty} \frac{(i^p)^*}{p!} \widehat{\phi}_{in}^{p\,*}(k_{x_1}, k_{y_1}), \tag{6.13a}$$

$$\widehat{\Psi}_{in}(k_{x_2}, k_{y_2}) = \widehat{\delta}(k_{x_2}, k_{y_2}) + \sum_{q=1}^{\infty} \frac{i^q}{q!} \widehat{\phi}_{in}^{p}(k_{x_2}, k_{y_2}), \tag{6.13b}$$

where $\widehat{\delta}(k_x, k_y)$ denotes the Dirac delta.

From Eqn. (6.7) we may also write:

$$\overline{T}^*\left(k_{x_1}, k_{y_1}\right) = 1 + i^* \sum_{m,n=0}^{\infty} \alpha_{mn}^* k_{x_1}^m k_{y_1}^n, \tag{6.14a}$$

$$\overline{T}\left(k_{x_2}, k_{y_2}\right) = 1 + i \sum_{\gamma,\nu=0}^{\infty} \alpha_{\gamma\nu} k_{x_2}^{\gamma} k_{y_2}^{\nu}. \tag{6.14b}$$

We now substitute Eqs. (6.13a), (6.13b), (6.14a) and (6.14a) into Eqn. (6.11) and expand. A total of sixteen terms appear in the expansion making it a very lengthy expression to display; however, similar mathematical manipulation is performed in each term that can be illustrated by using one term as an example. The longest term that appears is;

$$\left\langle \sum_{p,q,m,n,\gamma,\nu=1}^{\infty} \frac{(i^{p+1})^* i^{q+1} \alpha_{mn}^* \alpha_{\gamma\nu}}{p!q!(i^{m+n})^*(i^{\gamma+\nu})} \frac{1}{2\pi} \iint_{-\infty}^{\infty} (i^* k_{x_1})^m (i^* k_{y_1})^n e^{[i^*(k_{x_1} x_1 + k_{y_1} y_1)]} \widehat{\phi}_{in}^{p\,*}(k_{x_1}, k_{y_1}) dk_{x_1} dk_{y_1} \right.$$
$$\left. \times \frac{1}{2\pi} \iint_{-\infty}^{\infty} (ik_{x_2})^{\gamma} (ik_{y_2})^{\nu} e^{[i(k_{x_2} x_2 + k_{y_2} y_2)]} \widehat{\phi}_{in}^{q}(k_{x_2}, k_{y_2}) dk_{x_2} dk_{y_2} \right\rangle_{\omega}. \tag{6.15}$$

By the Fourier derivative theorem, the terms inside the double integrals can be expressed as;

$$(i^* k_{x_1})^m (i^* k_{y_1})^n e^{[i^*(k_{x_1} x_1 + k_{y_1} y_1)]} = \frac{\partial^m}{\partial x_1^m} \frac{\partial^n}{\partial y_1^n} e^{[i^*(k_{x_1} x_1 + k_{y_1} y_1)]}, \tag{6.16a}$$

$$(ik_{x_2})^{\gamma} (ik_{y_2})^{\nu} e^{[i(k_{x_2} x_2 + k_{y_2} y_2)]} = \frac{\partial^{\gamma}}{\partial x_2^{\gamma}} \frac{\partial^{\nu}}{\partial y_2^{\nu}} e^{[i(k_{x_2} x_2 + k_{y_2} y_2)]}. \tag{6.16b}$$

The indices m, n, γ and ν are positive integers that denote the order of differentiation. With this re–expression we see that the integrals represent the inverse Fourier transforms of the functions:

$$\frac{\partial^m}{\partial x_1^m} \frac{\partial^n}{\partial y_1^n} \widehat{\phi}_{in}^{p}(k_{x_1}, k_{y_1}), \text{ and} \tag{6.17a}$$

$$\frac{\partial^{\gamma}}{\partial x_2^{\gamma}} \frac{\partial^{\nu}}{\partial y_2^{\nu}} \widehat{\phi}_{in}^{q}(k_{x_2}, k_{y_2}). \tag{6.17b}$$

Hence the entire term in Eqn. (6.15) simplifies to:

$$\sum_{p,q,m,n,\gamma,\nu=1}^{\infty} \frac{(i^{p+1})^* i^{q+1} \alpha_{mn}^* \alpha_{\gamma\nu}}{p!q!(i^{m+n})^*(i^{\gamma+\nu})} \left\langle \left[\frac{\partial^m}{\partial x_1^m} \frac{\partial^n}{\partial y_1^n} \phi_{in}^p(x_1,y_1) \right] \left[\frac{\partial^\gamma}{\partial x_2^\gamma} \frac{\partial^\nu}{\partial y_2^\nu} \phi_{in}^q(x_2,y_2) \right] \right\rangle_\omega .$$

(6.18)

Using similar mathematical manipulation and logic used to get from Eq. (6.15) to (6.18) and applying it to all the terms which appear in the expansion of Eq. (6.11), one finds that the cross–spectral density for a shift–invariant linear system whose transfer function has infinitely many orders of aberrations is given by:

$$
\begin{aligned}
W_{out} \;=\; & 1 + \sum_{p=1}^{\infty} \frac{(i^p)^*}{p!} \left\langle \phi_{in}^p(x_1,y_1) \right\rangle_\omega + \sum_{q=1}^{\infty} \frac{i^q}{q!} \left\langle \phi_{in}^q(x_2,y_2) \right\rangle_\omega + \sum_{p,q=1}^{\infty} \frac{(i^p)^* i^q}{p!q!} \left\langle \phi_{in}^p(x_1,y_1)\phi_{in}^q(x_2,y_2) \right\rangle_\omega \\[2mm]
& + \sum_{p,m,n=1}^{\infty} \frac{\alpha_{mn}^*(i^{p+1})^*}{p!(i^{m+n})^*} \left\langle \frac{\partial^m}{\partial x_1^m} \frac{\partial^n}{\partial y_1^n} \phi_{in}^p(x_1,y_1) \right\rangle_\omega + \sum_{q,\gamma,\nu=1}^{\infty} \frac{\alpha_{\gamma\nu}(i^{q+1})}{q!(i^{\gamma+\nu})} \left\langle \frac{\partial^\gamma}{\partial x_2^\gamma} \frac{\partial^\nu}{\partial y_2^\nu} \phi_{in}^q(x_2,y_2) \right\rangle_\omega \\[2mm]
& + \sum_{p,q,m,n=1}^{\infty} \frac{\alpha_{mn}^*(i^{p+1})^* i^q}{p!q!(i^{m+n})^*} \left\langle \left[\frac{\partial^m}{\partial x_1^m} \frac{\partial^n}{\partial y_1^n} \phi_{in}^p(x_1,y_1) \right] \phi_{in}^q(x_2,y_2) \right\rangle_\omega \\[2mm]
& + \sum_{p,q,\gamma,\nu=1}^{\infty} \frac{\alpha_{\gamma\nu}(i^{p+1})(i^q)^*}{p!q!(i^{\gamma+\nu})} \left\langle \phi_{in}^p(x_1,y_1) \left[\frac{\partial^\gamma}{\partial x_2^\gamma} \frac{\partial^\nu}{\partial y_2^\nu} \phi_{in}^q(x_2,y_2) \right] \right\rangle_\omega \\[2mm]
& + \sum_{p,q,m,n,\gamma,\nu=1}^{\infty} \frac{(i^{p+1})^* i^{q+1} \alpha_{mn}^* \alpha_{\gamma\nu}}{p!q!(i^{m+n})^*(i^{\gamma+\nu})} \left\langle \left[\frac{\partial^m}{\partial x_1^m} \frac{\partial^n}{\partial y_1^n} \phi_{in}^p(x_1,y_1) \right] \left[\frac{\partial^\gamma}{\partial x_2^\gamma} \frac{\partial^\nu}{\partial y_2^\nu} \phi_{in}^q(x_2,y_2) \right] \right\rangle_\omega .
\end{aligned}
$$

(6.19)

Eqn. (6.19) is a key result of this chapter. We speak of Eqn. (6.19) as exhibiting a *generalized form of differential phase contrast*, in the sense that it is a representation in which the transverse derivatives of all orders of the phase distribution of each monochromatic field in the ensemble are statistically averaged and weighted in constructing the output cross–spectral density. The weighting coefficients are proportional to the generalized aberration coefficients drawn from the complex set $\{\alpha_{mn}\}$, thereby demonstrating how individual generalized aberration coefficients contribute to particular orders of transverse derivative of the phase of each monochromatic component in the statistical ensemble.

6.4 Optical aberrations in shift–invariant linear imaging systems using partially coherent fields considering different types of sample, using a single transverse spatial coordinate

In this section we will apply the formalism of the preceding section to three different types of sample, starting with samples that satisfy the weak–phase approximation (section 6.4.1), followed by samples that satisfy the weak phase–amplitude approximation (section 6.4.2) and finally samples made from a single–material that also satisfy the weak phase–amplitude approximation (section 6.4.3). Such types of sample have already been introduced in previous chapters; however, here we more thoroughly explore the underpinning mathematical and physical arguments justifying these expressions. In the interests of physical transparency of the resulting expressions, we will drop the number of transverse dimensions from two down to one.

6.4.1 Samples that satisfy the weak–phase approximation

The weak–phase approximation implies that when an object is illuminated by a wavefield the object itself causes very small changes in the phase of the incident field, as the scattering effects are relatively weak. We saw how under the "phase object approximation" one may express Ψ_{in} as a Taylor series (see Eq.(6.12)). In the one–dimensional perfectly coherent case this is written as:

$$\Psi_{in}(x) = 1 + \sum_{p=1}^{\infty} \frac{i^p}{p!} \phi_{in}^p(x). \tag{6.20}$$

For samples that satisfy the weak–phase approximation, we can ignore anything higher than first–order terms in the phase, that is:

$$\Psi_{in}(x) \approx 1 + i\phi_{in}(x). \tag{6.21}$$

Physically, this corresponds to each strictly monochromatic component of the input statistical ensemble having a transverse phase variation whose magnitude is much smaller than one radian. Such a strong limiting assumption of course implies significant loss of generality, a drawback which may be counterpointed with the very widespread use of the weak phase object approximation in visible–light imaging, X–ray imaging and electron imaging (Cowley [19], Cloetens *et al*. [15]).

In most cases relating to weak phase objects, including such terms only up to first order in $\phi_{in}(x)$ is acceptable. However, when we calculate the cross–spectral density W_{out} we take

the product of two wave fields, which causes second–order terms in ϕ to appear that cannot be ignored. This simply means expanding sums over p and q in Eq. (6.19) and retaining terms that are no higher than second order in ϕ. By doing this the one–dimensional version of the cross–spectral density (W_{out}) for samples that satisfy the weak–phase approximation is:

$$
\begin{aligned}
W_{out} \;=\; & 1 + i^* \langle \phi_{in}(x_1) \rangle_\omega + i \langle \phi_{in}(x_2) \rangle_\omega - \frac{1}{2} \langle \phi_{in}^2(x_1) \rangle_\omega - \frac{1}{2} \langle \phi_{in}^2(x_2) \rangle_\omega \\
& + \langle \phi_{in}(x_1)\phi_{in}(x_2) \rangle_\omega - \sum_{m=1}^{\infty} \left(\frac{\alpha_m}{i^m} \right)^* \left\langle \frac{\partial^m}{\partial x_1^m} \phi_{in}(x_1) \right\rangle_\omega - \sum_{n=1}^{\infty} \left(\frac{\alpha_n}{i^n} \right) \left\langle \frac{\partial^n}{\partial x_2^n} \phi_{in}(x_2) \right\rangle_\omega \\
& - \sum_{m=1}^{\infty} \left(\frac{\alpha_m}{i^{m-1}} \right)^* \left\langle \frac{\partial^m}{\partial x_1^m} \phi_{in}^2(x_1) \right\rangle_\omega - \sum_{n=1}^{\infty} \left(\frac{\alpha_n}{i^{n-1}} \right) \left\langle \frac{\partial^n}{\partial x_2^n} \phi_{in}^2(x_2) \right\rangle_\omega \\
& + \sum_{m=1}^{\infty} \left(\frac{\alpha_m}{i^{m-1}} \right)^* \left\langle \left[\frac{\partial^m}{\partial x_1^m} \phi_{in}(x_1) \right] \phi_{in}(x_2) \right\rangle_\omega + \sum_{n=1}^{\infty} \left(\frac{\alpha_n}{i^{n-1}} \right) \left\langle \phi_{in}(x_1) \left[\frac{\partial^n}{\partial x_2^n} \phi_{in}(x_2) \right] \right\rangle_\omega \\
& + \sum_{m,n=1}^{\infty} \left(\frac{\alpha_m}{i^m} \right)^* \left(\frac{\alpha_n}{i^n} \right) \left\langle \left[\frac{\partial^m}{\partial x_1^m} \phi_{in}(x_1) \right] \left[\frac{\partial^n}{\partial x_2^n} \phi_{in}(x_2) \right] \right\rangle_\omega .
\end{aligned}
$$

(6.22)

The associated spectral density $S_{out}(x, \omega) \equiv W_{out}(x, x, \omega)$ is:

$$
\begin{aligned}
S_{out} \;=\; & 1 - 2 \sum_{m=1}^{\infty} \mathrm{Re} \left(\frac{\alpha_m}{i^m} \right) \left\langle \frac{\partial^m}{\partial x^m} \phi_{in}(x) \right\rangle_\omega - 2 \sum_{m=1}^{\infty} \mathrm{Re} \left(\frac{\alpha_m}{i^{m-1}} \right) \left\langle \frac{\partial^m}{\partial x^m} \phi_{in}^2(x) \right\rangle_\omega \\
& + 2 \sum_{m=1}^{\infty} \mathrm{Re} \left(\frac{\alpha_m}{i^{m-1}} \right) \left\langle \left[\frac{\partial^m}{\partial x^m} \phi_{in}(x) \right] \phi_{in}(x) \right\rangle_\omega \\
& + \sum_{m,n=1}^{\infty} \left(\frac{\alpha_m}{i^m} \right)^* \left(\frac{\alpha_n}{i^n} \right) \left\langle \left[\frac{\partial^m}{\partial x^m} \phi_{in}(x) \right] \left[\frac{\partial^n}{\partial x^n} \phi_{in}(x) \right] \right\rangle_\omega .
\end{aligned}
$$

(6.23)

Our earlier comments regarding generalized phase contrast are also applicable here. Thus, for the case of weak phase objects imaged by an aberrated linear shift–invariant optical system, the output spectral density consists of a weighted sum of various orders of transverse derivative of the phases of each component of each strictly monochromatic member of the statistical ensemble, quantifying the input stochastic process. The associated weighting coefficients are again proportional to the real or imaginary parts of the generalized aberration coefficients given by the complex set $\{\alpha_{mn}\}$.

It is important to realize that in equation (6.23) we can directly see that four terms have no imaginary parts, which is expected since the spectral density is the monochromatic spatial component of the square modulus of a wave-field (see section 2.6.5). Having said this, the last term must also not have imaginary parts. If we analyse the last term

more carefully it can be shown that no imaginary parts arise from $\sum_{m,n=1}^{\infty} \left(\frac{\alpha_m}{i^m}\right)^* \left(\frac{\alpha_n}{i^n}\right)$. To demonstrate this we need to consider two separate cases. First, consider the case where $m = n$. The expansion terms are:

$$|\alpha_1|^2 + |\alpha_2|^2 + |\alpha_3|^2 + ... \tag{6.24}$$

Second, consider the case where $m \neq n$. The expansion terms are:

$$\left(\frac{\alpha_1}{i}\right)^* \left(\frac{\alpha_2}{i^2}\right) + \left(\frac{\alpha_2}{i^2}\right)^* \left(\frac{\alpha_1}{i}\right) + \left(\frac{\alpha_1}{i}\right)^* \left(\frac{\alpha_3}{i^3}\right) + \left(\frac{\alpha_3}{i^3}\right)^* \left(\frac{\alpha_1}{i}\right)$$
$$+ \left(\frac{\alpha_1}{i}\right)^* \left(\frac{\alpha_4}{i^4}\right) + \left(\frac{\alpha_4}{i^4}\right)^* \left(\frac{\alpha_1}{i}\right) + ... \tag{6.25}$$

By analysing the expansions in Eqns (6.24) and (6.25) for the two separate cases, one can logically deduce that the last summation term in Eqn (6.23) can be re-expressed as two separate summations:

$$\sum_{m=1}^{\infty} |\alpha_m| \left\langle \left[\frac{\partial^m}{\partial x^m}\phi_{in}(x)\right] \left[\frac{\partial^n}{\partial x^n}\phi_{in}(x)\right] \right\rangle_\omega$$
$$+2 \sum_{m,n=1}^{\infty} \mathrm{Re}\left[\left(\frac{\alpha_m}{i^m}\right)^* \left(\frac{\alpha_n}{i^n}\right)\right] [1 - \widehat{\delta}_{mn}] \left\langle \left[\frac{\partial^m}{\partial x^m}\phi_{in}(x)\right] \left[\frac{\partial^n}{\partial x^n}\phi_{in}(x)\right] \right\rangle_\omega . \tag{6.26}$$

This re-expression demonstrates that no complex components will appear in S_{out}. The symbol $\widehat{\delta}_{mn}$ is the Kronecker delta. Although this re-expression firmly illustrates that there are no imaginary components in S_{out}, we find it more convenient to express the last term of equation (6.23) as originally stated.

If we ignore terms in Eqn. (6.23) that are higher than first order in ϕ and assume a perfectly coherent field (i.e. no ensemble average is required) then this equation reduces to the one dimensional form of the expression derived in the paper by Paganin and Gureyev [64] for linear shift–invariant imaging systems for fully coherent fields given by:

$$S_{out} = 1 - 2 \sum_{m=1}^{\infty} \mathrm{Re}\left(\frac{\alpha_m}{i^m}\right) \frac{\partial^m}{\partial x^m}\phi_{in}(x). \tag{6.27}$$

Some interesting effects result when terms higher than first order in $\phi_{in}(x)$ are retained. For example, if we truncate Eqn. (6.23) up to $m = 1$ and $n = 1$ the spectral density becomes:

$$S_{out} = 1 - 2\mathrm{Re}\left(\frac{\alpha_1}{i}\right)\left\langle\frac{\partial}{\partial x}\phi_{in}(x)\right\rangle_\omega - 2\mathrm{Re}(\alpha_1)\left\langle\frac{\partial}{\partial x}\phi_{in}^2(x)\right\rangle_\omega$$
$$+ 2\mathrm{Re}(\alpha_1)\left\langle\left[\frac{\partial}{\partial x}\phi_{in}(x)\right]\phi_{in}(x)\right\rangle_\omega + |\alpha_1|^2\left\langle\left[\frac{\partial}{\partial x}\phi_{in}(x)\right]\left[\frac{\partial}{\partial x}\phi_{in}(x)\right]\right\rangle_\omega .$$

$$(6.28)$$

Here we have explicitly chosen a system that only displays first derivative contrast in the phase ϕ. Now notice how invoking the product rule one may rewrite certain terms such as:

$$\frac{\partial\phi_{in}^2(x)}{\partial x} = 2\left[\frac{\partial\phi_{in}(x)}{\partial x}\right]\phi_{in}(x) \tag{6.29}$$

and

$$\left[\frac{\partial\phi_{in}(x)}{\partial x}\right]\left[\frac{\partial\phi_{in}(x)}{\partial x}\right] = \frac{\partial}{\partial x}\left(\left[\frac{\partial}{\partial x}\phi_{in}(x)\right]\phi_{in}(x)\right) - \left[\frac{\partial^2}{\partial x^2}\phi_{in}(x)\right]\phi_{in}(x), \tag{6.30}$$

So that Eqn. (6.28) can be written as:

$$S_{out} = 1 - 2\mathrm{Re}\left(\frac{\alpha_1}{i}\right)\left\langle\frac{\partial}{\partial x}\phi_{in}(x)\right\rangle_\omega - 2\mathrm{Re}(\alpha_1)\left\langle\left[\frac{\partial}{\partial x}\phi_{in}(x)\right]\phi_{in}(x)\right\rangle_\omega$$
$$+ |\alpha_1|^2\left\langle\frac{\partial}{\partial x}\left\{\left[\frac{\partial}{\partial x}\phi_{in}(x)\right]\phi_{in}(x)\right\}\right\rangle_\omega - |\alpha_1|^2\left\langle\left[\partial_x^2\phi_{in}(x)\right]\phi_{in}(x)\right\rangle_\omega .$$

$$(6.31)$$

Notice how the final term yields a second derivative in the ensemble of phases. This is popularly referred to in the imaging field as "Laplacian contrast" (Teague *et al.* [82]). It is surprising that even though the system in Eqn. (6.31) has been restricted to tilt aberrations α_1 of first order, Laplacian contrast still arises.

6.4.2 Samples that satisfy the weak phase–amplitude approximation

The next class of samples considered are those that satisfy the weak phase–amplitude approximation. This approximation takes into consideration the variations in both amplitude and phase that the wavefield incurs as it travels though the sample. Again, since we are working under the space–frequency description of partial coherence, these statements apply to each strictly monochromatic component of the illuminating beam, which is elastically scattered by the sample to yield the ensemble of monochromatic fields that is input into the shift invariant linear imaging system.

Bearing the above statements in mind, the weak phase–amplitude approximation corresponds to the sample's scattering and absorptive properties being weak in the sense of the first Born approximation (Born and Wolf [8]). For samples that induce changes in both phase and amplitude, the one dimensional wavefield exiting the object is expressed as (Cowley [19]):

$$\Psi_{in}(x) = \exp[i\phi_{in}(x) - \mu_{in}(x)]. \tag{6.32}$$

The real function function $\mu_{in}(x)$ is related to the transverse variations in intensity and, like $\phi_{in}(x)$, it is also a real function. It again proves convenient to express exponential functions as a Taylor series. In this case $\Psi_{in}(x)$ is given by:

$$\Psi_{in}(x) = 1 + \sum_{p=1}^{\infty} \frac{[i\phi_{in}(x) - \mu_{in}(x)]^p}{p!}. \tag{6.33}$$

Like the weak–phase object approximation the weak phase–amplitude approximation also involves ignoring terms higher than first order, allowing the wavefield to be expressed as:

$$\Psi_{in}(x) \approx 1 + i\phi_{in}(x) - \mu_{in}(x). \tag{6.34}$$

To obtain W_{out} one simply needs to replace the terms $\phi_{in}(x_1)$ and $\phi_{in}(x_2)$ with $i\phi_{in}(x_1) - \mu_{in}(x_1)$ and $i\phi_{in}(x_2) - \mu_{in}(x_2)$ in Eqn. (6.22), respectively. Note that second–order terms need to be included for the same reasons argued for the weak–phase approximation. Once we have W_{out}, we then set $x_1 = x_2 = x$ to obtain an expression for the spectral density $S_{out}(x, \omega)$ for samples that are weak in phase and amplitude variations. In this case the spectral density is given by the following expression, which again demonstrates generalized differential phase contrast in the sense defined earlier:

$$
\begin{aligned}
S_{out} = & \; 1 - 2\left\langle \mu_{in}(x)\right\rangle_\omega - 2\sum_{m=1}^{\infty}\mathrm{Re}\left(\frac{\alpha_m}{i^m}\right)\left\langle\frac{\partial^m}{\partial x^m}\phi_{in}(x)\right\rangle_\omega - 2\sum_{m=1}^{\infty}\mathrm{Re}\left(\frac{\alpha_m}{i^{m-1}}\right)\left\langle\frac{\partial^m}{\partial x^m}\mu_{in}(x)\right\rangle_\omega \\
& -2\sum_{m=1}^{\infty}\mathrm{Re}\left(\frac{\alpha_m}{i^{m-1}}\right)\left\langle\frac{\partial^m}{\partial x^m}\phi_{in}^2(x)\right\rangle_\omega + 2\sum_{m=1}^{\infty}\mathrm{Re}\left(\frac{\alpha_m}{i^{m-1}}\right)\left\langle\frac{\partial^m}{\partial x^m}\mu_{in}^2(x)\right\rangle_\omega \\
& +6\sum_{m=1}^{\infty}\mathrm{Re}\left(\frac{\alpha_m}{i^{m-2}}\right)\left\langle\left[\frac{\partial^m}{\partial x^m}\phi_{in}(x)\right]\mu_{in}(x)\right\rangle_\omega + 2\sum_{m=1}^{\infty}\mathrm{Re}\left(\frac{\alpha_m}{i^{m-1}}\right)\left\langle\left[\frac{\partial^m}{\partial x^m}\phi_{in}(x)\right]\phi_{in}(x)\right\rangle_\omega \\
& +2\sum_{m=1}^{\infty}\mathrm{Re}\left(\frac{\alpha_m}{i^{m-2}}\right)\left\langle\left[\frac{\partial^m}{\partial x^m}\mu_{in}(x)\right]\phi_{in}(x)\right\rangle_\omega + 2\sum_{m=1}^{\infty}\mathrm{Re}\left(\frac{\alpha_m}{i^{m-1}}\right)\left\langle\left[\frac{\partial^m}{\partial x^m}\mu_{in}(x)\right]\mu_{in}(x)\right\rangle_\omega \\
& +\sum_{m,n=1}^{\infty}\left(\frac{\alpha_m}{i^m}\right)^*\left(\frac{\alpha_n}{i^n}\right)\left\langle\left[\frac{\partial^m}{\partial x^m}\phi_{in}(x)\right]\left[\frac{\partial^n}{\partial x^n}\phi_{in}(x)\right]\right\rangle_\omega \\
& +\sum_{m,n=1}^{\infty}\left(\frac{\alpha_m}{i^m}\right)^*\left(\frac{\alpha_n}{i^n}\right)\left\langle\left[\frac{\partial^m}{\partial x^m}\mu_{in}(x)\right]\left[\frac{\partial^n}{\partial x^n}\mu_{in}(x)\right]\right\rangle_\omega .
\end{aligned}
$$

$$(6.35)$$

Similar to the previous case in section 6.4, if second order terms in ϕ and μ are neglected and we remove the angular brackets, assuming a fully coherent wave, then Eq. (6.35) reduces to the one derived by Paganin and Gureyev [64] when dealing with the weak phase–amplitude approximation, namely:

$$
S_{out} = 1 - 2\mu_{in}(x) - 2\sum_{m=1}^{\infty}\mathrm{Re}\left(\frac{\alpha_m}{i^m}\right)\frac{\partial^m}{\partial x^m}\phi_{in}(x) - 2\sum_{m=1}^{\infty}\mathrm{Re}\left(\frac{\alpha_m}{i^{m-1}}\right)\frac{\partial^m}{\partial x^m}\mu_{in}(x).
$$

$$(6.36)$$

6.4.3 Single–material samples that satisfy the weak phase–amplitude approximation

The final kind of sample that we consider is those that are comprised of a single material and also have the transverse phase and intensity variations of the wavefield being small as it travels though the sample. For single–material samples the complex refractive index is constant throughout the volume of the sample (Paganin [67]):

$$
n = 1 - \delta + i\beta.
$$

$$(6.37)$$

If the projected thickness along the orientation of a particular direction of propagation for paraxial illumination is denoted as $T(x)$, then using the real numbers δ and β we can

relate the functions $\phi_{in}(x)$ and $\mu_{in}(x)$ to T(x) via (see section 4.2.1):

$$\phi_{in}(x) = -k\delta T(x), \tag{6.38a}$$

$$\mu_{in}(x) = \beta k T(x). \tag{6.38b}$$

Here, k is the radiation wavenumber corresponding to the wavelength λ. This permits us to write the input wavefield as:

$$\Psi_{in}(x) = \exp[k(\beta - i\delta)T(x)]. \tag{6.39}$$

Under the single–material weak phase–amplitude object approximation $\Psi_{in}(x)$ is approximated as:

$$\begin{aligned} \Psi_{in}(x) \;&= \exp[k(\beta - i\delta)T(x)] \\ &\approx 1 - k(\beta - i\delta)T(x). \end{aligned} \tag{6.40}$$

Here we see that the "single–material weak phase–amplitude object approximation" is none other than the "weak phase–amplitude object approximation" that uses that fact that when a weak object is made out of only one material the functions $\phi_{in}(x)$ and $\mu_{in}(x)$ become proportional to each other. Bearing this in mind, to obtain an expression for the spectral density $S_{out}(x)$ for systems that are linear and shift–invariant when the object satisfies the "single–material weak phase–amplitude object approximation", all that is needed is to replace $\phi_{in}(x)$ and $\mu_{in}(x)$ in Eqn.(6.35) with $-k\delta T(x)$ and $\beta k T(x)$ respectively to yield:

$$\begin{aligned} S_{out} \;=\; & 1 - 2\beta k \left\langle T(x) \right\rangle_\omega - 2 \sum_{m=1}^{\infty} \mathrm{Re}\left[\frac{\alpha_m k(i\beta + \delta)}{i^m} \right] \left\langle \frac{\partial^m}{\partial x^m} T(x) \right\rangle_\omega \\ & + 2 \sum_{m=1}^{\infty} \mathrm{Re}\left[\frac{\alpha_m k(\delta + \beta)}{i^{m-1}} \right] \left\langle \frac{\partial^m}{\partial x^m} T^2(x) \right\rangle_\omega \\ & + 2 \sum_{m=1}^{\infty} \mathrm{Re}\left[\frac{\alpha_m k^2(4\delta - \beta^2 + i\delta^2)}{i^m} \right] \left\langle \left[\frac{\partial^m}{\partial x^m} T(x) \right] T(x) \right\rangle_\omega \\ & + \sum_{m,n=1}^{\infty} \sigma \left(\frac{\alpha_m}{i^m} \right)^* \left(\frac{\alpha_n}{i^n} \right) \left\langle \left[\frac{\partial^m}{\partial x^m} T(x) \right] \left[\frac{\partial^n}{\partial x^n} T(x) \right] \right\rangle_\omega, \end{aligned} \tag{6.41}$$

where $\sigma = k^2(\delta + \beta)$, and ensemble averages are taken over the sample projected thickness (i.e. $\left\langle T(x) \right\rangle_\omega$). This implies taking the average sum of projected line-integrals along the sample over a range of angular orientations for the case where the incident ensemble of

monochromatic fields consists of a set of plane waves. We see that the single–material assumption significantly simplifies the expression for the spectral density S_{out} in Eqn. (6.35). One of the advantages about making the "single–material weak phase–amplitude object approximation" is that it allows one to relate the measured image directly to morphological detail of the sample, bypassing the idea of ensembles of phase maps. For instance, take a special case of Eqn. (6.41) where the system has a finite set of non–vanishing aberrations (all of which are known *a priori*), and we take the spectral density S_{out} to be the measured quantity, leaving $\langle T(x) \rangle_{\omega}$ as the unknown variable. This effectively brings about an inverse problem, where from an aberrated image one seeks to infer information about the dimensions of a sample. Usually this is done using some iterative or non–iterative algorithm and in most cases a perfectly coherent monochromatic wavefield is assumed. In the context of this paper we see that the idea of "phase retrieval" is somewhat redundant since we have considered wavefields that are partially coherent and therefore do not have a characteristic phase ϕ, but rather have a statistical signature $\left\langle \frac{\partial^m}{\partial x^m} \phi_{in} \right\rangle_{\omega}$. This highlights the importance of Eqn. (6.41) as it makes more sense to want to recover information about the morphology of the imaged sample as opposed to the phase ϕ of a wavefield; since technically the latter does not exist in the context of partial coherence (Wolf [89]).

6.5   The transfer function for shift–invariant linear systems with infinitely many orders of aberration

The transfer function formalism to study image formation is widely used to describe optical systems. This section discusses in detail the properties and characteristics of the transfer function used in the development of this theory (see Eqn. (6.6)). The expressions for spectral densities for all three types of sample described in section 6.4 are here derived under the Taylor series form of the transfer function, which is written in terms of the coefficients α_m. For this reason it is important to state that the actual aberration coefficients, namely those directly corresponding to the Seidel aberrations, are those denoted by $\widetilde{\alpha}_m$. For example, $\widetilde{\alpha}_2$ is directly proportional to defocus "z" as is $\widetilde{\alpha}_4$ to spherical aberration "C_s" (Paganin and Gureyev [64]). The main goal of this section will be to illustrate how we are able to express the transfer function as a Taylor–series expansion that eventually will lead to another problem in finding a standard formula on how to relate the coefficients α_m to the aberration coefficients $\widetilde{\alpha}_m$; a problem which is solved using a combinatorial approach. Also, we will continue to use only one spatial dimension in order to keep all mathematical manipulations simple.

We begin by re–stating the transfer function in one spatial dimension:

$$\overline{T}(k_x) = \exp\left(i \sum_{m=0}^{\infty} \widetilde{\alpha}_m k_x^m \right). \tag{6.42}$$

We remind the reader that the set of complex numbers $\{\widetilde{\alpha}_m\}$ are labelled here as "aberration coefficients" whose objective is to characterise a particular state of the linear imaging system. Each such coefficient can be expressed as:

$$\widetilde{\alpha}_m \equiv \widetilde{\alpha}_m^{(R)} + i\widetilde{\alpha}_m^{(I)}, \tag{6.43}$$

where $\widetilde{\alpha}_m^{(R)}$ denotes the real part and $\widetilde{\alpha}_m^{(I)}$ denotes the imaginary part. It was assumed in Paganin and Gureyev [64] that at the Fourier–space origin the transfer function must equal unity; that is $\overline{T}(k_x = 0) = 1$. Such an assumption implies a trivial loss of generality for all systems that posses a transfer function that does not vanish at the Fourier space origin. Also under this assumption we may set $\widetilde{\alpha}_0 = 0$.

Now we want to represent Eqn. (6.42) as a Taylor–series, something that in Paganin and Gureyev [64] was only stated but not shown. Here we provide a more detailed explanation of how this is achieved. First, let the summation in Eqn. (6.42) be labelled $X \equiv i \sum_{m=1}^{\infty} \widetilde{\alpha}_m k_x^m$. Notice that we have now commenced the summation from $m = 1$. This is due to assumption made earlier that $\overline{T}(k_x = 0) = 1$, which in turn allowed us to set $\widetilde{\alpha}_0 = 0$. The Taylor–series of an exponential function is given by:

$$e^X = 1 + \sum_{l=1}^{\infty} \frac{X^l}{l!}, \tag{6.44}$$

where, $l = 1, 2, ...$ is also a non–negative integer. If we now substitute $X \equiv i \sum_{m=1}^{\infty} \widetilde{\alpha}_m k_x^m$ then Eqn. (6.42) becomes:

$$\overline{T}(k_x) = 1 + i \sum_{l=1}^{\infty} \frac{i^{l-1}}{l!} \left(\sum_{m=1}^{\infty} \widetilde{\alpha}_m k_x^m \right)^l. \tag{6.45}$$

Writing the summation $\sum_{m=1}^{\infty} \widetilde{\alpha}_m k_x^m$ explicitly we get:

$$\overline{T}(k_x) = 1 + i \sum_{l=1}^{\infty} \frac{i^{l-1}}{l!} \left(\widetilde{\alpha}_1 k_x + \widetilde{\alpha}_2 k_x^2 + \widetilde{\alpha}_3 k_x^3 + \widetilde{\alpha}_4 k_x^4 + \cdots \right)^l. \tag{6.46}$$

We now turn our focus to the summation in Eqn. (6.46). If one writes down the first few l terms, say $l = 1, 2, 3, 4$, it can be seen that all the common powers of k_x can be collected. For example:

$$l = 1, \qquad \left(\widetilde{\alpha}_1 k_x + \widetilde{\alpha}_2 k_x^2 + \widetilde{\alpha}_3 k_x^3 + \widetilde{\alpha}_4 k_x^4 + \cdots \right)^1$$

$$l = 2, \qquad + \frac{i}{2!} \left(\widetilde{\alpha}_1 k_x + \widetilde{\alpha}_2 k_x^2 + \widetilde{\alpha}_3 k_x^3 + \widetilde{\alpha}_4 k_x^4 + \cdots \right)^2$$

$$l = 3, \qquad - \frac{1}{3!} \left(\widetilde{\alpha}_1 k_x + \widetilde{\alpha}_2 k_x^2 + \widetilde{\alpha}_3 k_x^3 + \widetilde{\alpha}_4 k_x^4 + \cdots \right)^3$$

$$l = 4, \qquad - \frac{i}{4!} \left(\widetilde{\alpha}_1 k_x + \widetilde{\alpha}_2 k_x^2 + \widetilde{\alpha}_3 k_x^3 + \widetilde{\alpha}_4 k_x^4 + \cdots \right)^4.$$

(6.47)

Once we collect all the common powers of k_x we see that the entire summation in Eqn. (6.46) can be expressed in the alternative form:

$$\overbrace{(\widetilde{\alpha}_1)}^{\alpha_1} k_x + \overbrace{(\widetilde{\alpha}_2 + \frac{i}{2}\widetilde{\alpha}_1^2)}^{\alpha_2} k_x^2 + \overbrace{(\widetilde{\alpha}_3 + i\widetilde{\alpha}_1\widetilde{\alpha}_2 - \frac{1}{6}\widetilde{\alpha}_1^3)}^{\alpha_3} k_x^3 +$$

$$\overbrace{(\widetilde{\alpha}_4 + i\widetilde{\alpha}_1\widetilde{\alpha}_3 + \frac{i}{2}\widetilde{\alpha}_2^2 - \frac{1}{2}\widetilde{\alpha}_1^2\widetilde{\alpha}_2 - \frac{i}{24}\widetilde{\alpha}_1^4)}^{\alpha_4} k_x^4 + \cdots = \sum_{l=1}^{\infty} \alpha_l k_x^l.$$

(6.48)

These mathematical manipulations reveal that we are able to represent the transfer function as the following Taylor–series:

$$\overline{T}(k_x) = 1 + i \sum_{m=1}^{\infty} \alpha_m k_x^m.$$

(6.49)

We have re–labelled the non–negative integer l with m in order to remain consistent with our original notation. Also, notice that each α_m term is composed of a finite series of $\widetilde{\alpha}_m$ terms where the higher the order of m the higher number the of terms that will appear. The fact that the series are finite turns out to be advantageous. On this note we see that another problem arises, that is, if one is dealing with aberrations that are higher in order than say α_5, we saw from the above examples that computing all its terms in the series this can be tedious. This motivates us to seek a Standard Series Formula that can allow us to calculate any α_m for this problem by simply substituting fixed parameters to avoid such lengthy and tedious computations. This can be achieved if one visualises the problem as a combinatorial one. The first indication that tells us that this can be solved combinatorially is when the term $\left(\widetilde{\alpha}_1 k_x + \widetilde{\alpha}_2 k_x^2 + \cdots \right)^l$ arises where we see that this is none other than a multinomial expansion which reveals its combinatorial nature. The multinomial expansion formula has the form:

$$(c_1 + c_2 + \ldots + c_m)^l = \sum_{m_1 + m_2 + \ldots + m_j = l} \binom{l}{m_1, m_2, \cdots, m_j} c_1^{m_1} c_2^{m_2} \ldots c_j^{m_j}$$

(6.50)

where $c_1, c_2, ..., c_m$ are variables and l, m, j, m_j are integers. From this we can deduce that the terms in the series will have coefficients which can be calculated with the multinomial coefficients formula:

$$\binom{l}{m_1, m_2, \cdots, m_j} = \frac{l!}{m_1! m_2! \cdots m_j!}.$$ (6.51)

Notice that for any α_m we find that the sum of the exponent times its subscript in each of its corresponding $\widetilde{\alpha}$ terms will always be equal. For instance take $\alpha_3 = \widetilde{\alpha}_3 + i\widetilde{\alpha}_1\widetilde{\alpha}_2 - \frac{1}{6}\widetilde{\alpha}_1^3$; each of its $\widetilde{\alpha}$ terms in the expansion can be written as $\widetilde{\alpha}_3^1$, $\widetilde{\alpha}_1^1\widetilde{\alpha}_2^1$ and $\widetilde{\alpha}_1^3$. Now notice how the sum of the product of the exponents times its subscript for each term all equate to 3; we have $\widetilde{\alpha}_3^1$ ($1 \times 3 = 3$), $\widetilde{\alpha}_1^1\widetilde{\alpha}_2^1$ ($1 \times 1 + 1 \times 2 = 3$) and $\widetilde{\alpha}_3^1$ ($3 \times 1 = 3$). If we do this for any α_m this condition will still hold.

Our next step is to try to decode a particular pattern for any α_m series. Let's focus on $\alpha_2 = \widetilde{\alpha}_2 + \frac{i}{2}\widetilde{\alpha}_1^2$. Here we see that the highest power is 2 and therefore one can also deduce that the highest power for any $\widetilde{\alpha}$ is never greater than m. We know that each expansion has a combinatorial nature so let's consider the terms that compose α_2 are elements from the set $\{\widetilde{\alpha}_1, \widetilde{\alpha}_2\}$ and its corresponding exponents are combinations from the set $\{0, 1, 2\}$. We also see that the coefficients will be given by the multinomial coefficients formula. If we write down all possible combinations with their corresponding multinomial coefficients (including the factor $i^{l-1}/l!$, starting with $m = 0$ for completeness) it displays as:

$$\overset{0(1)+0(2)=0}{\frac{i^{-1}}{0!}\binom{0}{0,0}\widetilde{\alpha}_1^0\widetilde{\alpha}_2^0} + \overset{0(1)+1(2)=2}{\frac{i^0}{1!}\binom{1}{0,1}\widetilde{\alpha}_1^0\widetilde{\alpha}_2^1} + \overset{1(1)+0(2)=1}{\frac{i^0}{1!}\binom{1}{1,0}\widetilde{\alpha}_1^1\widetilde{\alpha}_2^0}$$
$$+ \overset{0(1)+2(2)=4}{\frac{i}{2!}\binom{2}{0,2}\widetilde{\alpha}_1^0\widetilde{\alpha}_2^2} + \overset{2(1)+0(2)=2}{\frac{i}{2!}\binom{2}{2,0}\widetilde{\alpha}_1^2\widetilde{\alpha}_2^0} + \overset{1(1)+1(2)=3}{\frac{i}{2!}\binom{2}{1,1}\widetilde{\alpha}_1^1\widetilde{\alpha}_2^1}.$$ (6.52)

As a convenient notation, notice that the sum of the product of the exponents times their corresponding subscripts have been deliberately placed above each combinatorial term. This helps us to see that if we only allow the terms in which the product of the exponents times their corresponding subscripts equals the order of the coefficient α_m, in this case $m = 2$ and neglect those that do not fulfil this condition, then the surviving terms in the expansion will be the following:

$$\alpha_2 = \frac{i^0}{1!}\binom{1}{0,1}\widetilde{\alpha}_1^0\widetilde{\alpha}_2^1 + \frac{i}{2!}\binom{2}{2,0}\widetilde{\alpha}_1^2\widetilde{\alpha}_2^0$$
$$= \widetilde{\alpha}_2 + \frac{i}{2}\widetilde{\alpha}_1^2.$$ (6.53)

Notice how applying this fusion of combinatorics and pattern decoding has arrived at the same answer for the α_2 terms in Eqn. (6.48). Now we can employ the same strategy

for $\alpha_3 = \widetilde{\alpha}_3 + i\widetilde{\alpha}_1\widetilde{\alpha}_2 - \frac{1}{6}\widetilde{\alpha}_1^3$ where now all the terms are elements from the set $\{\widetilde{\alpha}_1, \widetilde{\alpha}_2, \widetilde{\alpha}_3\}$ and its exponents are combinations from the set $\{0, 1, 2, 3\}$. Writing down the possible combinations will give:

$$
\begin{array}{ccc}
\overset{0(1)+0(2)+0(3)=0}{\frac{i^{-1}}{0!}\binom{0}{0,0,0}\widetilde{\alpha}_1^0\widetilde{\alpha}_2^0\widetilde{\alpha}_3^0} & + \overset{1(1)+0(2)+0(3)=1}{\frac{i^0}{1!}\binom{1}{1,0,0}\widetilde{\alpha}_1^1\widetilde{\alpha}_2^0\widetilde{\alpha}_3^0} & + \overset{0(1)+1(2)+0(3)=2}{\frac{i^0}{1!}\binom{1}{0,1,0}\widetilde{\alpha}_1^0\widetilde{\alpha}_2^1\widetilde{\alpha}_3^0} \\[2ex]
+ \overset{0(1)+0(2)+1(3)=3}{\frac{i^0}{1!}\binom{1}{0,0,1}\widetilde{\alpha}_1^0\widetilde{\alpha}_2^0\widetilde{\alpha}_3^1} & + \overset{2(1)+0(2)+0(3)=2}{\frac{i^1}{2!}\binom{2}{2,0,0}\widetilde{\alpha}_1^2\widetilde{\alpha}_2^0\widetilde{\alpha}_3^0} & + \overset{0(1)+2(2)+0(3)=4}{\frac{i^1}{2!}\binom{2}{0,2,0}\widetilde{\alpha}_1^0\widetilde{\alpha}_2^2\widetilde{\alpha}_3^0} \\[2ex]
+ \overset{0(1)+0(2)+2(3)=6}{\frac{i^1}{2!}\binom{2}{0,0,2}\widetilde{\alpha}_1^0\widetilde{\alpha}_2^0\widetilde{\alpha}_3^2} & + \overset{1(1)+1(2)+0(3)=3}{\frac{i^1}{2!}\binom{2}{1,1,0}\widetilde{\alpha}_1^1\widetilde{\alpha}_2^1\widetilde{\alpha}_3^0} & + \overset{1(1)+0(2)+1(3)=4}{\frac{i^1}{2!}\binom{2}{1,0,1}\widetilde{\alpha}_1^1\widetilde{\alpha}_2^0\widetilde{\alpha}_3^1} \\[2ex]
+ \overset{0(1)+1(2)+1(3)=5}{\frac{i^1}{2!}\binom{2}{0,1,1}\widetilde{\alpha}_1^0\widetilde{\alpha}_2^1\widetilde{\alpha}_3^1} & + \overset{3(1)+0(2)+0(3)=3}{\frac{i^2}{3!}\binom{3}{3,0,0}\widetilde{\alpha}_1^3\widetilde{\alpha}_2^0\widetilde{\alpha}_3^0} & + \overset{0(1)+3(2)+0(3)=6}{\frac{i^2}{3!}\binom{3}{0,3,0}\widetilde{\alpha}_1^0\widetilde{\alpha}_2^3\widetilde{\alpha}_3^0} \\[2ex]
+ \overset{0(1)+0(2)+3(3)=9}{\frac{i^2}{3!}\binom{3}{0,0,3}\widetilde{\alpha}_1^0\widetilde{\alpha}_2^0\widetilde{\alpha}_3^3} & + \overset{1(1)+1(2)+1(3)=6}{\frac{i^2}{3!}\binom{3}{1,1,1}\widetilde{\alpha}_1^1\widetilde{\alpha}_2^1\widetilde{\alpha}_3^1} & + \overset{2(1)+1(2)+0(3)=4}{\frac{i^2}{3!}\binom{3}{2,1,0}\widetilde{\alpha}_1^2\widetilde{\alpha}_2^1\widetilde{\alpha}_3^0} \\[2ex]
+ \overset{2(1)+0(2)+1(3)=5}{\frac{i^2}{3!}\binom{3}{2,0,1}\widetilde{\alpha}_1^2\widetilde{\alpha}_2^0\widetilde{\alpha}_3^1} & + \overset{1(1)+2(2)+0(3)=5}{\frac{i^2}{3!}\binom{3}{1,2,0}\widetilde{\alpha}_1^1\widetilde{\alpha}_2^2\widetilde{\alpha}_3^0} & + \overset{1(1)+0(2)+2(3)=7}{\frac{i^2}{3!}\binom{3}{1,0,2}\widetilde{\alpha}_1^1\widetilde{\alpha}_2^0\widetilde{\alpha}_3^2} \\[2ex]
& + \overset{0(1)+1(2)+2(3)=8}{\frac{i^2}{3!}\binom{3}{0,1,2}\widetilde{\alpha}_1^0\widetilde{\alpha}_2^1\widetilde{\alpha}_3^2}. &
\end{array}
$$

$$(6.54)$$

Like the case for α_2, if we only consider the terms where the sum of the exponents times their corresponding subscript equal $m = 3$ and neglect the rest then the only terms which survive are:

$$
\begin{aligned}
\alpha_3 &= \overset{0(1)+0(2)+0(3)=3}{\frac{i^0}{1!}\binom{0}{0,0,1}\widetilde{\alpha}_1^0\widetilde{\alpha}_2^0\widetilde{\alpha}_3^1} + \overset{1(1)+1(2)+0(3)=3}{\frac{i^1}{2!}\binom{2}{1,1,0}\widetilde{\alpha}_1^1\widetilde{\alpha}_2^1\widetilde{\alpha}_3^0} + \overset{3(1)+0(2)+0(3)=3}{\frac{i^2}{3!}\binom{3}{3,0,0}\widetilde{\alpha}_1^3\widetilde{\alpha}_2^0\widetilde{\alpha}_3^0} \\
&= \widetilde{\alpha}_3 + i\widetilde{\alpha}_1\widetilde{\alpha}_2 - \frac{1}{6}\widetilde{\alpha}_1^3.
\end{aligned}
$$

$$(6.55)$$

By extending the above logic one is able deduce the following standard formula to compute any α_m:

$$
\alpha_m = \sum_{v} \sum_{m_1+m_2+\ldots+m_j=v} \frac{i^{v-1}}{v!}\binom{v}{m_1, m_2, \cdots, m_j}\widetilde{\alpha}_1^{m_1}\widetilde{\alpha}_2^{m_2}\ldots\widetilde{\alpha}_j^{m_j}
$$

$$
\text{where,} \sum_{j} m_j \times j = m.
$$

$$(6.56)$$

Here, $v = 0, 1, 2, ..., m$, $j = 1, 2, ..., m$ and $m_j = 0, 1, 2, ..., m$. To verify this standard formula we calculate another α_m and see if we arrive at the same result to that obtained by collecting terms, as done previously in Eqn. (6.48). We do this by calculating α_4 where

according to the set condition one only needs to consider the terms that satisfy $\sum_j m_j \times j = 4$. Below we display all the relevant terms:

$$
\begin{aligned}
\alpha_4 &= \frac{i^0}{1!}\overset{0(1)+0(2)+0(3)+1(4)=4}{\binom{1}{0,0,0,1}}\widetilde{\alpha}_1^0\widetilde{\alpha}_2^0\widetilde{\alpha}_3^0\widetilde{\alpha}_4^1 + \frac{i}{2!}\overset{1(1)+0(2)+1(3)+0(4)=4}{\binom{2}{1,0,1,0}}\widetilde{\alpha}_1^1\widetilde{\alpha}_2^0\widetilde{\alpha}_3^1\widetilde{\alpha}_4^0 \\
&+ \frac{i}{2!}\overset{0(1)+2(2)+0(3)+0(4)=4}{\binom{2}{0,2,0,0}}\widetilde{\alpha}_1^0\widetilde{\alpha}_2^2\widetilde{\alpha}_3^0\widetilde{\alpha}_4^0 + \frac{i^2}{3!}\overset{2(1)+1(2)+0(3)+0(4)=4}{\binom{3}{2,1,0,0}}\widetilde{\alpha}_1^2\widetilde{\alpha}_2^1\widetilde{\alpha}_3^0\widetilde{\alpha}_4^0 \\
&+ \frac{i^3}{4!}\overset{4(1)+0(2)+0(3)+0(4)=4}{\binom{4}{4,0,0,0}}\widetilde{\alpha}_1^4\widetilde{\alpha}_2^0\widetilde{\alpha}_3^0\widetilde{\alpha}_4^0 \\
&= \widetilde{\alpha}_4 + i\widetilde{\alpha}_1\widetilde{\alpha}_3 + \frac{i}{2}\widetilde{\alpha}_2^2 - \frac{1}{2}\widetilde{\alpha}_1^2\widetilde{\alpha}_2 - \frac{i}{24}\widetilde{\alpha}_1^4.
\end{aligned}
\tag{6.57}
$$

The computation above is in agreement with calculating α_4 via the standard formula and the more lengthy method that involves collecting term of k_x^4 powers, as was done in Eqn. (6.48).

To end this section we return to the case where the transfer function contains two spatial dimensions transverse to the imaging direction. For such cases the combinatorial analysis is more complex. Nevertheless, using a similar strategy to the one used to formulate the standard formula for the one–dimensional case, one is also able to deduce a formula for the more common imaging scenario with two spatial dimensions. Setting $\widetilde{\alpha}_{00} = 0$ yields a "two spatial dimensions standard formula" of the form:

$$
\alpha_{mn} = \sum_{v}^{m+n} \sum_{m_{01}+m_{10}+...+m_{jv}=v} \frac{i^{v-1}}{v!}\binom{v}{m_{01},m_{10},\cdots,m_{jv}}\widetilde{\alpha}_{01}^{m_{01}}\widetilde{\alpha}_{10}^{m_{10}}...\widetilde{\alpha}_{jv}^{m_{jv}}
$$
$$
\text{where,} \sum_{j,v} m_{jv} \times (j+v) = m+n,
$$

$$\tag{6.58}$$

where $v = 0, 1, 2, ..., m+n$, $j = 0, 1, 2, ..., m$, $v = 0, 1, 2, ..., n$ and $m_{jv} = 0, 1, 2, ..., m+n$. Since we have set $\widetilde{\alpha}_{00} = 0$ we must impose the condition that when $j = 0$ then $v \neq 0$ and vice versa. It is possible to make further simplification of the formula if rotational symmetry is also assumed (i.e. $\widetilde{\alpha}_{10} = \widetilde{\alpha}_{01}$).

6.6 Concluding remarks

In this chapter we have treated the general problem of phase contrast in terms of optical aberrations for partially coherent complex scalar wavefields imaged by optical systems characterized by a transfer function that is both linear and shift–invariant. We have derived expressions for the output cross–spectral density W_{out} using only one spatial

variable for samples that satisfy the "phase object approximation", the "weak–phase object approximation", the "weak phase–amplitude approximation" and finally the "single–material weak phase–amplitude approximation". Also, for the three classes of samples mentioned, an expression for the spectral density S_{out} was calculated for which we saw how, under restrictions, the equations reduced to those derived by Paganin and Gureyev [64] where partial coherence was not considered. The transfer function was studied where we emphasized how one obtains the coefficients of the Taylor–series representation of the transfer function. This lead to a different problem involved with finding a standard formula that can allow the calculation of any coefficient α_m in terms of its corresponding aberration coefficients $\widetilde{\alpha_m}$ for an infinite number of aberration orders.

7

Summary, future work and conclusion

This chapter summarises the original research results that form the core of this thesis, namely chapters 4, 5 and 6. Augmenting this summary is a series of questions which open possible avenues where this research may lead. We then finalise with an overall conclusion of this thesis.

In chapter 4 a method of tomographic phase retrieval was developed for multi–material objects whose components each have a distinct complex refractive index. The phase retrieval algorithm, based on the Transport–of–Intensity equation, utilizes propagation–based X–ray phase contrast images acquired at a single defocus distance for each tomographic projection. The method requires *a priori* knowledge of the complex refractive index for each material present in the sample, together with the total projected thickness of the object at each orientation. The requirement of only a single defocus distance per projection simplifies the experimental setup and imposed no additional dose compared to conventional tomography. The method was implemented using phase contrast data acquired at the SPring–8 synchrotron radiation facility in Japan. The three–dimensional (3D) complex refractive index distribution of a multi–material test object was quantitatively reconstructed using a single X–ray phase–contrast image per projection. The technique was found to be highly robust in the presence of noise compared to conventional absorption based tomography. When it comes to imaging multi–material objects, our technique proves superior to conventional absorption contrast in terms of the signal–to–noise ratio (SNR). For the test sample used here, the improvement in the SNR was between 17 and 85 fold.

Chapter 5 applies the method developed in chapter 4 to complex biological organs. Specifically, chapter 5 performs interface–specific propagation-based X–ray phase retrieval tomography of the thorax and brain of small animals. For the biological samples used here, there was a 9–200 fold improvement in the signal–to–noise ratio of the phase–retrieved tomograms over the conventional attenuation-contrast signal. This gain depended on the material in question and the experimental setup, but can potentially be traded against a reduction in X–ray dose. For the values reported here, this could potentially reduce the dose 100–40,000×. This enhances the dose reduction already made over alternative implementations of phase retrieval since only a single image per projection is required. However, this huge potential reduction in dose remains to be verified experimentally by

reducing the dose by these factors and seeing SNR can be maintained by using phase retrieval. Given these results, combined with the simplicity of our technique, we anticipate that it will potentially be a useful tool in the field of biomedical X–ray imaging.

A key finding of chapter 5 was that the single–material phase retrieval algorithm (Eqn. (5.1)) was suitable for the sample containing brain tissue (containing both grey and white matter) in agar. This considerably simplified and sped up the analysis as only a single tomographic reconstruction was required. It remains to be seen whether other material combinations, including soft tissues, can be analysed in the same way. For example, it may be valid to make the single–material approximation in a sample exclusively comprised of soft tissues. It also remains to be seen whether a clear image of the brain can be reconstructed when the brain is *in situ*, inside the skull, using either phase retrieval algorithm.

With a view to ultimately applying the method presented in chapter 4 to laboratory–based PBI using polychromatic radiation (e.g., Wilkins *et al.* [85]), it would be very useful to generalize it to a polychromatic spectrum. This will be a stepping stone allowing the technique to be used for routine biomedical imaging, with potential clinical implications, since PBI is already being used in the clinic for breast imaging (Tanaka *et al.* [81]). We note that several groups have made inroads into the problem of phase retrieval using polychromatic radiation in the contexts of both two- and three–dimensional imaging (Arhatari *et al.* [4], Myers *et al.* [61]).

Finally, we note that spatially quantized objects are in some sense sparse, insofar as the interfaces between the various volumetric regions of the object are intrinsically two–dimensional surfaces. No attempt has been made to utilize this sparseness in this analysis of the present thesis. Progress has been made in using the intrinsically sparse nature of spatially quantized objects in the context of phase retrieval in the work of Myers *et al.* [60, 61, 59] and the work on gradient–sparse objects by Sidky *et al.* [75]). Furthermore, the burgeoning field of compressive sensing (Baraniuk [5]) has also made inroads into the tomography of sparse objects, albeit via a different form of sparsity in which the majority of features in the object are confined to a small fraction of the volume occupied by the object. It might be interesting to investigate whether these methods of compressive sensing may be adapted to spatially quantized objects, in which the volume occupied by interfaces is sparse (cf. Sidky *et al.* [75]). In this context, the concept of a quasi–one–dimensional object, developed by Gureyev and Evans [36], might also prove useful. A particular driver is the quest to reduce the number of required projections, and therefore the dose to the sample by making use of the sparseness of interface–occupying voxels in a typical spatially quantized object.

In chapter 6 the role and influence of aberrations in optical imaging systems employing partially coherent complex scalar fields was studied. All phase contrast imaging systems require aberrations to yield contrast in the output image. These linear optical aberrated systems were characterised in terms of a transfer function. For linear shift–invariant optical systems, an expression was derived for the output cross–spectral density under the

space–frequency formulation of statistically stationary partially coherent fields. We also derived expressions for the output cross–spectral density and associated spectral density for weak–phase, weak–phase–amplitude, and single–material objects in one transverse spatial dimension. For the single material case the possibility of phase retrieval was briefly explored, giving rise to the idea of carrying out morphological studies of imaged samples utilizing partially coherent light and aberrated imaging systems. This idea may have several applications in many areas such as geology, microbiology, materials science, etc.

Chapter 6 was finalised with an analysis of the generalized Fourier space transfer function. Here a standard formula was developed that related the coefficients α_m to the aberration coefficients $\widetilde{\alpha}_m$. This standard formula brings many advantages not only in the sense that it is not limited to a finite order of aberrations, but also allows for broader considerations in "aberration balancing". Aberration balancing is the act of seeking certain conditions for which the aberrations present in an optical system are negated by the system itself. To be more concise, one seeks to balance out the aberrations in an optical system against one another. This is somewhat similar to the notion of Scherzer defocus, where defocus is tuned to balance out spherical aberration (Scherzer [74]). For example, consider the spectral density in Eqn. (6.36) for the "weak–phase object approximation" case. Suppose one aimed to find the conditions for which all aberrations present balanced out one another such that the output image displayed only first order differential contrast, that is;

$$S_{out} = 1 - 2 \left\langle \frac{\partial}{\partial x} \phi_{in}(x) \right\rangle_{\omega}. \tag{7.1}$$

This would require the following balancing conditions in order to achieve such an output image:

$$\alpha_1^{(I)} = 1, \mathrm{Re}\left(\frac{\overset{m \neq 0}{\alpha_m}}{i^m}\right) = 0, \mathrm{Re}\left(\frac{\alpha_m}{i^{m-1}}\right) = 0, \left(\frac{\alpha_m}{i^m}\right)^* \left(\frac{\alpha_n}{i^n}\right) = 0. \tag{7.2}$$

For systems with infinitely many aberrations, the above balancing equation could in principle be solved with the help of the standard formula (Eqn. (6.56)) without the need for truncating the system.

Quantitative X–ray phase contrast imaging using fully and partially coherent fields is an area of study that leaves numerous open avenues for new research developments and potential applications. The benefits of the original methods presented in chapter 4, 5 and 6 of this thesis include being able to perform high quality quantitative phase contrast imaging of objects applying easily numerically implemented algorithms as well a laying the mathematical foundations of generalised differential phase contrast systems using partially coherent radiation. Considering the latter, we can forecast a number of experimental

applications that are based on the mathematical foundations set in this thesis. For example, the idea of investigating interface–specific X–ray phase retrieval tomography methods for spatially quantized objects given an arbitrary phase contrast modality is an interesting one. This can be taken further by incorporating the effects of partial coherence as it would see a far greater applicability for use with conventional radiation sources that can only provide partial coherence. To finalise, we hope that the original work in this thesis inspires future researchers to take these ideas further.

References

[1] A. Abrami, F Arfelli, C. Barroso, A. Bergamaschi, F. Bille, P. Bregant F. Brizzi, K. Casarin, E. Castelli, V. Chenda, L. Dalla Palma, D. Dreossi, C. Fava, R. Mongo, L. Mancini, R. H. Menk, F. Montanari, A. Olivo, S. Zanconati, A. Zanetti, and F. Zanini. Medical applications of sychrotron radiation a the SYRMEP beamline of ELETTRA. *Nucl. Instrum. Meth. A*, 548:221–227, 2005.

[2] Jens Als-Nielsen and Des McMorrow. *Elements of Modern X-ray Physics*. Wiley, New York, 1st edition, 2001.

[3] B. D. Arhatari, W. P. Gates, and A. G. Eshtiaghi, N. Peele. Phase-retrieval tomography in the presence of noise. *J. Appl. Phys.*, 107:113704, 2010.

[4] B. D. Arhatari, K. A. Nugent, A. G. Peele, and J. Thornton. Phase contrast radiography. ii. imaging of complex objects. *Rev. Sci. Instrum.*, 76:113704, 2005.

[5] R. G. Baraniuk. Compressive sensing. *IEEE Signal Process. Mag.*, 24:118–121, 2007.

[6] M. A. Beltran, D. M. Paganin, K. Uesugi, and M. J. Kitchen. 2D and 3D x-ray phase retrieval of multi-material objects using a single defocus distance. *Opt. Express*, 18:6423–6436, 2010.

[7] U. Bonse and M. Hart. An x-ray interferometer. *Appl. Phys. Lett.*, 6:155–156, 1965.

[8] M. Born and E. Wolf. *Principles of Optics*. Cambridge University Press New York, 7th edition, 1999.

[9] A. Bravin, P. Coan, and P. Suortti. X-ray phase-contrast imaging: from pre-clinical applications towards clinics. *Phys. Med. Biol.*, 58:R1–R35, 2013.

[10] H. Bremmer. On the asymptotic evaluation of diffraction integrals with a special view to the theory of defocusing and optical contrast. *Physica*, 18:469–485, 1952.

[11] A. V. Bronnikov. Reconstruction formulas in phase-contrast tomography. *Opt. Commun.*, 171:239–244, 1999.

[12] A.V. Bronnikov. Theory of quantitative phase-contrast computed tomography. *J. Opt. Soc. Am. A*, 19:472–480, 2002.

[13] C. T. Chantler, C. Q. Tran, Z. Barnea, D. Paterson, D. J. Cookson, and D. X. Baliac. Measurement of x-ray mass attenuation coefficient of copper using 8.55–20 keV sychrotron radiation. *Phys. Rev. A.*, 64:062506, 2001.

[14] D. Chapman, W. Thomlinson, R. E. Johnston, D. Washburn, E. Pisano, N. Gmur, Z. Zhong, R. Menk, F. Arfelli, and D. Sayers. Diffraction enhanced x-ray imaging. *Phys. Med. Biol.*, 42:2015–2025, 1997.

[15] P. Cloetens, R. Barrett, J. Baruchel, J. P. Guigay, and M. Schlenker. Phase objects in synchrotron radiation hard x-ray imaging. *J. Phys. D: Appl. Phys.*, 29:133–146, 1996.

[16] P. Cloetens, W. Ludwig, J. Baruchel, D. Van Dyck, J. Van Landuyt, JP Guigay, and M. Schlenker. Holotomography: Quantitative phase tomography with micrometer resolution using hard synchrotron radiation x rays. *Appl. Phys. Lett.*, 75:2912–2914, 1999.

[17] P. Cloetens, M. Salomé-Pateyron, J. Buffière, G. Peix, J. Baruchel, F. Peyrin, and M. Schlenker. Observation of microstructure and damage in materials by phase sensitive radiography and tomography. *J. Appl. Phys.*, 81:5878–5886, 1997.

[18] P. Cloetens, L. Wolfgang, J. Baruchel, J. Guigay, P. Pernot-Rejmánková, M. Salomé-Pateyron, M. Schlenker, J. Buffière, E. Maire, and G. Peix. Hard x-ray phase imaging using simple propagation of a coherent synchrotron radiation beam. *J. Phys. D: Appl. Phys.*, 32:A145–A151, 1999.

[19] J. M. Cowley. *Diffraction Physics*. North-Holland and Elsevier, 3rd edition, 1995.

[20] C. David, B. Nohammer, and H.H. Solak. Differential x-ray phase contrast imaging using a shearing interferometer. *Appl. Phys. Lett.*, 81:3287–3289, 2002.

[21] T. J. Davis. X-ray diffraction imaging using perfect crystals. *X-Ray Sci. Technol.*, 6:317–342, 1996.

[22] T. J. Davis, D. Gao, T. E. Guryev, A. W. Stevenson, and S. W. Wilkins. Phase-contrast imaging of weakly absorbing materials using hard x-rays. *Nature*, 373:595–598, 1995.

[23] T. J. Davis, T. E. Gureyev, D. Gao, A. W. Stevenson, and S. W. Wilkins. X-ray image contrast from a simple phase object. *Phys. Rev. Lett.*, 74:3173–3176, 1995.

[24] T. J. Davis and A. W. Stevenson. Direct measurement of the phase shift of an x-ray beam. *J. Opt. Soc. Am. A*, 13:1193–1198, 1996.

[25] T. Donath, F. Pfeiffer, O. Bunk, C. Grünzweig, E. Hempel, S. Popescu, P. Vock, and C. David. Towards clinical x-ray phase-contrast CT: demonstration of enhanced soft-tissue contrast in human specimen. *Invest. Radiol.*, 45:445–452, 2010.

[26] E. Förster, K. Goetz, and P. Zaumseil. Double crystal diffractometry for the characterization of targets for laser fusion experiments. *Krist. Tech.*, 15:937–945, 1980.

[27] D. Gabor. A new microscopic principle. *Nature*, 161:777–778, 1948.

[28] G. Gbur and T. V. Visser. Phase singularities and coherence vortices in linear optical systems. *Opt. Commun.*, 259:428–435, 2006.

[29] R. W. Gerchberg and W. O. Saxton. A practical algorithm for the determination of the phase from image and diffraction plane pictures. *Optik*, 35:237–246, 1972.

[30] J. W. Goodman. *Introduction to Fourier Optics*. Roberts and Company Publishers, Greenwood Village, 1st edition, 2005.

[31] S. Goto, K. Takeshita, Y. Suzuki, H. Ohashi, Y. Asano, H. Kimura, T. Matsushita, N. Yagi, M. Isshiki, H. Yamazaki, Y Yoneda, K Umetani, and T Ishikawa. Construction and commissioning of a 215-m-long beamline at spring-8. *Nucl. Instrum. Meth. A*, 467:682–685, 2001.

[32] H. S. Green and E. Wolf. A scalar representation of electromagnetic fields. *Proc. Phys. Soc. A.*, 66:1129–1137, 1953.

[33] J. P. Guigay. Fourier transform analysis of Fresnel diffraction patterns and in-line holograms. *Optik*, 49:121–125, 1977.

[34] T. E. Gureyev. Transport of intensity equation for beams in an arbitrary state of temporal and spatial coherence. *Optik*, 110:263–266, 1999.

[35] T. E. Gureyev. Composite techniques for phase retrieval in the Fresnel region. *Opt. Commun.*, 220:49–58, 2003.

[36] T. E. Gureyev and R. Evans. An extension of quasi-one-dimensional tomography. *Appl. Opt.*, 37:2628–36, 1998.

[37] T. E. Gureyev and K. A. Nugent. Rapid quantitative phase imaging using the transport of intensity equation. *Opt. Commun.*, 133:339–346, 1997.

[38] T. E. Gureyev, D. M. Paganin, G.R. Myers, Y. I. Nesterets, and S. W. Wilkins. Phase-and-amplitude computer tomography. *Appl. Phys. Lett.*, 89:034102, 2006.

[39] J. Herzen, T. Donath, F. Pfeiffer, O. Bunk, C. Padeste, F. Beckmann, A. Schreyer, and C. David. Quantitative phase-contrast tomography of a liquid phantom using a conventional x-ray tube. *Opt. Express.*, 17:10010–8, 2009.

[40] S.B. Hooper, M.J. Kitchen, M.J. Wallace, N. Yagi, K. Uesugi, M.J. Morgan, C. Hall, K.K.W. Siu, I.M. Williams, M. Siew, S. C. Irvine, K. Pavlov, and R. A. Lewis. Imaging lung aeration and lung liquid clearance at birth. *FASEB J.*, 21:3329–3337, 2007.

[41] V. N. Ingal and E. Beliaevskaya. X-ray plane-wave topography observation of the phase contrast from a non-crystalline object. *J. Phys. D: Appl. Phys.*, 28:2314–2317, 1995.

[42] J. D. Jackson. *Classical Electrodynamics*. Wiley, New York, 3rd edition, 1999.

[43] A. C. Kak and M. Slaney. *Principles of Computerized Tomographic Imaging*. Society of Industrial and Applied Mathematics, New York, 2001.

[44] B. Kaulich, T. Wilhein, E. Di Fabrizio, F. Romanato, M. Altissimo, and S. Cabrini. Differential interference contrast x-ray microscopy with twin zone plates. *J. Opt. Soc. Am. A.*, 19:797–806, 2002.

[45] M. J. Kitchen, R. A. Lewis, M. J. Morgan, M. J. Wallace, M. L. Siew, K. K. W. Siu, A. Habib, A. Fouras, N. Yagi, K. Uesugi, and S. B. Hooper. Dynamic measures of regional lung air volume using phase contrast x-ray imaging. *Phys. Med. Biol.*, 53:6065–6077, 2008.

[46] M. J. Kitchen, D. Paganin, R. A. Lewis, N. Yagi, K. Uesugi, and S. T. Mudie. On the origin of speckle in x-ray phase contrast images of lung tissue. *Phys. Med. Biol.*, 49:4335–4348, 2004.

[47] M.J. Kitchen, A. Habib, A. Fouras, S. Dubsky, R.A. Lewis, M.J. Wallace, and S.B. Hooper. A new design for high stability pressure-controlled ventilation for small animal lung imaging. *J. Intrum.*, 5:T02002, 2010.

[48] V. Lakshminarayanan and A. Fleck. Zernike polynomials: a guide. *J. Mod. Opt.*, 58:545–561, 2011.

[49] R. A. Lewis, K. D. Rogers, C. J. Hall, A. P. Hufton, S. Evans, R. H. Menk, G. Tromba, F. Arfelli, L. Rigon, A. Olivo, A Evans, S. E. Pinder, E. Jacobs, I. O. Ellis, and D. R. Dance. Diffraction-enhanced imaging: improved contrast and lower dose x-ray imaging. *Proc. SPIE*, 4682:286–297, 2002.

[50] L. Mandel and E. Wolf. *Optical Coherence and Quantum Optics*. Cambridge University Press, Cambridge, 1995.

[51] A. S. Marathay and G. B. Parrent Jr. Use of scalar theory in optics. *J. Opt. Soc. Am.*, 60:243–245, 1970.

[52] S. C. Mayo, T. J. Davis, T. E. Gureyev, P. R. Miller, D. Paganin, A. Pogany, A. W. Stevenson, and S. W. Wilkins. X-ray phase-contrast microscopy and microtomography. *Opt. Express.*, 11:2289–2302, 2003.

[53] S. A. McDonald, F. Marone, C. Hintermuller, G. Mikuljan, C. David, F. Pfeiffer, and M. Stampanoni. Advanced phase-contrast imaging using a grating interferometer. *J. Synchrotron Radiat.*, 16:562–572, 2009.

[54] A. Momose. Phase-contrast x-ray imaging based on interferometry. *J. Synchrotron Radiat.*, 9:136–142, 2002.

[55] Atsushi Momose, Shinya Kawamoto, Ichiro Koyama, Yoshitaka Hamaishi, Kengo Takai, and Yoshio Suzuki. Demonstration of x-ray Talbot interferometry. *Jpn. J. Appl. Phys.*, 42:L866–L868, 2003.

[56] K. S. Morgan, P. Modregger, S. C. Irvine, S. Rutishauser, V. A. Guzenko, M. Stampanoni, and C. David. A sensitive x-ray phase contrast technique for rapid imaging using a single phase grid analyzer. *Opt. Express.*, 38:4605–4608, 2013.

[57] K. S. Morgan, D. P. Paganin, and K. K. W. Siu. Quantitative single-exposure x-ray phase contrast imaging using a single attenuation grid. *Opt. Express.*, 19:19781–9, 2011.

[58] K. S. Morgan, D. P. Paganin, and K. K. W. Siu. Quantitative x-ray phase contrast imaging using a single grating of comparable pitch to sample feature size. *Opt. Lett.*, 36:55–57, 2011.

[59] G. Myers, D. L. Thomas, D. M. Paganin, T. E. Gureyev, and J. G. Clement. A general few-projection method for tomographic reconstruction of samples consisting of several distinct materials. *Appl. Phys. Lett.*, 96:021105, 2010.

[60] G. R. Myers, T. E. Gureyev, D. M. Paganin, and S. C. Mayo. The binary dissector: Phase contrast tomography of two- and three-material objects from few projections. *Opt. Express.*, 16:16736–16749, 2008.

[61] G. R. Myers, S. C. Mayo, T. E. Gureyev, D. M. Paganin, and S. W. Wilkins. Polychromatic cone-beam phase-contrast tomography. *Phys. Rev. A*, 76:045804, 2007.

[62] U. Neuhäusler, G. Schneider, W. Ludwig, M. A. Meyer, E. Zschech, and D. Hambach. X-ray microscopy in zernike phase contrast mode at 4 kev photon energy with 60 nm resolution. *J. Phys. D: Appl Phys.*, 36:A79–A82, 2003.

[63] M Nieto-Vesperinas. *Scattering and Diffraction in Physical Optics*. World Scientific Publishing, New Jersey, 2nd edition, 2006.

[64] D. Paganin and T. Gureyev. Phase contrast, phase retrieval and aberration balancing in shift–invariant linear imaging systems. *Opt. Commun.*, 281:965–981, 2008.

[65] D. Paganin, S. C. Mayo, T. E. Guryev, P. R. Miller, and S. W. Wilkins. Simultaneous phase and amplitude extraction from a single defocused image of a homogeneous object. *J. Microsc.*, 206:33–40, 2002.

[66] D. Paganin and K. A. Nugent. Noninterferometric phase imaging with partially coherent light. *Phys. Rev. Lett.*, 80:2586–2589, 1998.

[67] D. M. Paganin. *Coherent X-ray Optics.* Oxford University Press, New York, 2006.

[68] L. G. Pellegrino. *A Stereotaxic Atlas of the Rat Brain.* New York: Plentum, New York, 1979.

[69] J. Petruccell, L. Tian, and G. Barbastathis. The transport of intensity equation for optical path length recovery using partially coherent illumination. *Opt. Express.*, 21:14430–41, 2013.

[70] F. Pfeiffer, O. Bunk, C. David, M. Bech, G. Le Duc, A. Bravin, and P. Cloetens. High-resolution brain tumor visualization using three-dimensional x-ray phase contrast tomography. *Phys. Med. Biol.*, 52:6923–6930, 2007.

[71] F. Pfeiffer, T. Weitkamp, O. Bunk, and C. David. Phase retrieval and differential phase-contrast imaging with low-brilliance x-ray sources. *Nature Physics*, 2:258–261, 2006.

[72] J. Radon. Über die Bestimmung von Funktionen durch ihre Integralwerte längs gewisser Mannigfaltigkeiten. *Berichte über die Verhandlungen der Königlich-Sächsischen Akademie der Wissenschaften zu Leipzig, Mathematisch-Physische Klasse*, 69:262–277, 1917.

[73] G. N. Ramachandran and A. V. Lakshminarayanan. Three-dimensional reconstruction from radiographs and electron micrographs: application of convolutions instead of Fourier transforms. *Proc. Natl. Sci. Acad. USA*, 68:2236–2240, 1971.

[74] O. Scherzer. The theoretical resolution limit of the electron microscope. *A. Appl. Phys.*, 20, 1949.

[75] E. Y. Sidky, M. A. Anastasio, and X. Pan. Image reconstruction exploiting object sparsity in boundary-enhanced x-ray phase-contrast tomography. *Opt. Express.*, 18:10404–22, 2010.

[76] V. A. Somenkov, A. K. Tkalich, S. S. H. Shil'Shtein, and M. E. Alferieff. Refraction contrast in x-ray introscopy. *Sov. Phys. Tech. Phys.-U.*, 36(11):1309–1311, 1991.

[77] D. Stutman, T. J. Beck, J. A. Carrino, and C. O. Bingham. Talbot phase-contrast x-ray imaging for small joints of the hand. *Phys. Med. Bio.*, 56:5697–720, 2011.

[78] Y. Suzuki, N. Yagi, and K. Uesugi. X-ray refraction-enhanced imaging and a method for phase retrieval for a simple object. *J. Synchrotron Radiat.*, 9:160–165, 2002.

[79] Y. Takeda, W. Yashiro, T. Hattori, A. Takeuchi, Y. Suzuki, and A. Momose. Differential phase x-ray imaging microscopy with x-ray Talbot interferometer. *Appl. Phys. Express*, 1:117002, 2008.

[80] H. F. Talbot. Facts relating to optical science no. iv. *Philos. Mag*, 9:419–427, 1836.

[81] T. Tanaka, C. Honda, S. Matsuo, K. Noma, H. Oohara, N. Nitta, S. Ota, K. Tsuchiya, Y. Sakashita, A. Yamada, M. Yamasaki, A. Furukawa, M. Takahashi, and K. Murata. The first trial of phase contrast imaging for digital full-field mammography using a practical molybdenum x-ray tube. *Invest. Radiol.*, 40:385–396, 2005.

[82] M. R. Teague. Deterministic phase retrieval: a Green's function solution. *J. Opt. Soc. Am. A*, 73:1434, 1983.

[83] L. D. Turner, B. B. Dhal, J. P. Hayes, A. P. Mancuso, K. A. Nugent, D. Paterson, R. E. Scholten, C. Q. Tran, and A. G. Peele. X-ray phase imaging: Demonstration of extended conditions with homogeneous objects. *Opt. Express.*, 12:2960–2965, 2004.

[84] T. Weitkamp, A. Diaz, C. David, F. Pfeiffer, M. Stampanoni, P. Cloetens, and E. Ziegler. X-ray phase imaging with a grating interferometer. *Opt. Express.*, 13:6296–6304, 2005.

[85] S. W. Wilkins, T. E. Gureyev, D. Gao, A. Pogany, and A. W. Stevenson. Phase-contrast imaging using polychromatic hard x-rays. *Nature*, 384:335–338, 1996.

[86] J. T. Winthrop and C. R. Worthington. Convolution formulation of Fresnel diffraction. *J. Opt. Soc. Am*, 56:588–591, 1966.

[87] E. Wolf. A scalar representation of electromagnetic fields: II. *Proc. Phys. Soc. A.*, 74:269–280, 1959.

[88] E. Wolf. New theory of partial coherence in space-frequency domain. *J. Opt. Soc. Am.*, 3:77–85, 1986.

[89] E. Wolf. Solution ot phase problem in the theory of stucture determination of crystals from x-ray diffraction experiments. *Phys. Rev. Lett.*, 103:075501, 1986.

[90] E. Wolf. *Introduction to the Theory of Coherence and Polarization of Light*. Cambridge University Press, New York, 2007.

[91] X.Wu, H. Liu, and A. Yan. X-ray phase attenuation duality and phase retrieval. *Opt. Lett.*, 30:379–381, 2005.

[92] J. Zambelli, N. Bevins, Z. Qi, and G. Chen. Radiantion dose efficiency comparison between differential phase contrast ct and conventional absorption. *Med. Phys.*, 37:2473–2479, 2010.

[93] F. Zernike. Phase contrast, a new method for the microscopic observation of transparent objects. *Physica*, 7:686–698, 1942.

[94] A. Zysk, R. Schoonover, P. Carney, and M. Anastasio. Transport of intensity and the spectrum for partially coherent fields. *Opt. Lett.*, 35:2239–2241, 2010.

Appendices: Publications arising from this thesis

Appendix A

2D and 3D X-ray phase retrieval of multi-material objects using a single defocus distance.

by M. A. Beltran, D. M. Paganin, K. Uesugi, and M. J. Kitchen.

Published in Optics Express **25**, pp. 6423-36, 2010.

2D and 3D X-ray phase retrieval of multi-material objects using a single defocus distance

M.A. Beltran[1,*], D.M. Paganin[1], K. Uesugi[2], and M.J. Kitchen[1]

[1]School of Physics, Monash University, VIC 3800, Australia
[2]SPring-8/JASRI, Sayo, Hyogo 679-5198, Japan

Abstract: A method of tomographic phase retrieval is developed for multi-material objects whose components each have a distinct complex refractive index. The phase-retrieval algorithm, based on the Transport-of-Intensity equation, utilizes propagation-based X-ray phase contrast images acquired at a single defocus distance for each tomographic projection. The method requires *a priori* knowledge of the complex refractive index for each material present in the sample, together with the total projected thickness of the object at each orientation. The requirement of only a single defocus distance per projection simplifies the experimental setup and imposes no additional dose compared to conventional tomography. The algorithm was implemented using phase contrast data acquired at the SPring-8 Synchrotron facility in Japan. The three-dimensional (3D) complex refractive index distribution of a multi-material test object was quantitatively reconstructed using a single X-ray phase-contrast image per projection. The technique is robust in the presence of noise, compared to conventional absorption based tomography.

OCIS codes: (100.5070) Phase retrieval; (100.6950) Tomographic image processing; (090.1995) Digital holography; (340.7440) X-ray imaging.

References and links

1. A. C. Kak, and M. Slaney, *Principles of Computerized Tomographic Imaging* (IEEE Press, New York, 1988).
2. S. Bayat, G. Le Duc, L. Porra, G. Berruyer, C. Nemoz, S. Monfraix, S. Fiedler, W. Thomlinson, P. Suortti, C. G. Standertskjöld-Nordenstam, and A. R. A. Sovijärvi, "Quantitative functional lung imaging with synchrotron radiation using inhaled xenon as contrast agent," Phys. Med. Biol. **46**(12), 3287–3299 (2001).
3. S. Monfraix, S. Bayat, L. Porra, G. Berruyer, C. Nemoz, W. Thomlinson, P. Suortti, and A. R. A. Sovijärvi, "Quantitative measurement of regional lung gas volume by synchrotron radiation computed tomography," Phys. Med. Biol. **50**(1), 1–11 (2005).
4. B. Driehuys, and L. W. Hedlund, "Imaging techniques for small animal models of pulmonary disease: MR microscopy," Toxicol. Pathol. **35**(1), 49–58 (2007).
5. D. P. Schuster, A. Kovacs, J. Garbow, and D. Piwnica-Worms, "Recent advances in imaging the lungs of intact small animals," Am. J. Respir. Cell Mol. Biol. **30**(2), 129–138 (2004).
6. U. Bonse, and M. Hart, "An x-ray interferometer," Appl. Phys. Lett. **6**(8), 155–156 (1965).
7. E. Förster, K. Goetz, and P. Zaumseil, "Double crystal diffractometry for the characterization of targets for laser fusion experiments," Krist. Tech. **15**(8), 937–945 (1980).
8. F. Pfeiffer, T. Weitkamp, O. Bunk, and O. David, "Phase retrieval and differential phase-contrast imaging with low-brilliance X-ray sources," Nature **2**, 258–261 (2006).
9. A. Snigirev, I. Snigireva, V. Kohn, S. Kuznetsov, and I. Schelokov, "On the possibilities of x-ray phase contrast microimaging by coherent high-energy synchrotron radiation," Rev. Sci. Instrum. **66**(12), 5486–5492 (1995).
10. S. W. Wilkins, T. E. Gureyev, D. Gao, A. Pogany, and A. W. Stevenson, "Phase-contrast imaging using polychromatic hard X-rays," Nature **384**(6607), 335–338 (1996).
11. P. Cloetens, R. Barrett, J. Baruchel, J.-P. Guigay, and M. Schlenker, "Phase objects in synchrotron radiation hard X-ray imaging," J. Phys. D Appl. Phys. **29**(1), 133–146 (1996).
12. M. R. Teague, "Deterministic phase retrieval: a Green's function solution," J. Opt. Soc. Am. **73**(11), 1434–1441 (1983).

13. T. E. Gureyev, and K. A. Nugent, "Phase retrieval with the transport-of-intensity equation. II. Orthogonal series solution for nonuniform illumination," J. Opt. Soc. Am. A **13**(8), 1670–1682 (1996).
14. T. E. Gureyev, and K. A. Nugent, "Rapid quantitative phase imaging using the transport of intensity equation," Opt. Commun. **133**(1-6), 339–346 (1997).
15. D. Paganin, and K. A. Nugent, "Noninterferometric phase imaging with partially coherent light," Phys. Rev. Lett. **80**(12), 2586–2589 (1998).
16. O. M. Bucci, L. Crocco, M. D'Urso, and T. Isernia, "Inverse scattering from phaseless measurements of the total field open lines," J. Opt. Soc. Am. A **23**(10), 2566–2577 (2006).
17. L. Crocco, M. D'Urso, and T. Isernia, "Faithful non-linear imaging from only-amplitude measurements of incident and total fields," Opt. Express **15**(7), 3804–3815 (2007).
18. J. P. Guigay, M. Langer, R. Boistel, and P. Cloetens, "Mixed transfer function and transport of intensity approach for phase retrieval in the Fresnel region," Opt. Lett. **32**(12), 1617–1619 (2007).
19. M. D'Urso, K. Belkerbir, L. Crocco, T. Isernia, and A. Litman, "Phaseless imaging with experimantal data: facts and challenges," J. Opt. Soc. Am. A **25**(1), 271–281 (2008).
20. A. Pogany, D. Gao, and S. W. Wilkins, "Contrast and resolution in imaging with a microfocus x-ray source," Rev. Sci. Instrum. **68**(7), 2774–2782 (1997).
21. P. Cloetens, W. Ludwig, J. Baruchel, D. van Dyck, J. van Landuyt, J. P. Guigay, and M. Schlenker, "Holotomography: Quantitative phase tomography with micrometer resolution using hard synchrotron radiation X-rays," Appl. Phys. Lett. **75**(19), 2912–2914 (1999).
22. D. Paganin, S. C. Mayo, T. E. Gureyev, P. R. Miller, and S. W. Wilkins, "Simultaneous phase and amplitude extraction from a single defocused image of a homogeneous object," J. Microsc. **206**(1), 33–40 (2002).
23. S. C. Mayo, T. J. Davis, T. E. Gureyev, P. R. Miller, D. Paganin, A. Pogany, A. W. Stevenson, and S. W. Wilkins, "X-ray phase-contrast microscopy and microtomography," Opt. Express **11**(19), 2289–2302 (2003).
24. T. E. Gureyev, D. M. Paganin, G. R. Myers, Y. I. Nesterets, and S. W. Wilkins, "Phase-and-amplitude computer tomography," Appl. Phys. Lett. **89**(3), 034102 (2006).
25. G. R. Myers, T. E. Gureyev, D. M. Paganin, and S. C. Mayo, "The binary dissector: phase contrast tomography of two- and three-material objects from few projections," Opt. Express **16**(14), 10736–10749 (2008).
26. A. V. Bronnikov, "Reconstruction formulas in phase-contrast tomography," Opt. Commun. **171**(4-6), 239–244 (1999).
27. A. V. Bronnikov, "Theory of quantitative phase-contrast computed tomography," J. Opt. Soc. Am. A **19**(3), 472–480 (2002).
28. J. Als-Nielsen, and D. McMorrow, *Elements of Modern X-ray Physics* (John Wiley & Sons, New York, 2001).
29. D. M. Paganin, *Coherent X-Ray Optics* (Oxford University Press, New York, 2006).
30. X. Wu, H. Liu, and A. Yan, "X-ray phase-attenuation duality and phase retrieval," Opt. Lett. **30**(4), 379–381 (2005).
31. M. J. Kitchen, R. A. Lewis, M. J. Morgan, M. J. Wallace, M. L. Siew, K. K. W. Siu, A. Habib, A. Fouras, N. Yagi, K. Uesugi, and S. B. Hooper, "Dynamic measures of regional lung air volume using phase contrast x-ray imaging," Phys. Med. Biol. **53**(21), 6065–6077 (2008).
32. S. Goto, K. Takeshita, Y. Suzuki, H. Ohashi, Y. Asano, H. Kimura, T. Matsushita, N. Yagi, M. Isshiki, H. Yamazaki, Y. Yoneda, K. Umetani, and T. Ishikawa, "Construction and commissioning of a 215m-long beamline at SPring-8," Nucl. Instrum. Meth. A. **467-468**, 682–685 (2001).
33. A. Abrami, F. Arfelli, R. C. Barroso, A. Bergamaschi, F. Bille, P. Bregant, F. Brizzi, K. Casarin, E. Castelli, V. Chenda, L. Dalla Palma, D. Dreossi, C. Fava, R. Longo, L. Mancini, R.-H. Menk, F. Montanari, A. Olivo, S. Pani, A. Pillon, E. Quai, S. R. Kaiser, L. Rigon, T. Rokvic, M. Tonutti, G. Tromba, A. Vascotto, C. Venanzi, F. Zanconati, A. Zanetti, and F. Zanini, "Medical applications of synchrotron radiation at the SYRMEP beamline of ELETTRA," Nucl. Instrum. Meth. A **548**(1-2), 221–227 (2005).
34. P. Cloetens, W. Ludwig, J. Baruchel, J.-P. Guigay, P. Pernot-Rejmánková, M. Salomé-Pateyron, M. Schlenker, J.-Y. Buffière, E. Malre, and G. Peix, "Hard X-ray phase imaging using simple propagation of a coherent synchrotron radiation beam," J. Phys. D Appl. Phys. **32**(10A), 145–151 (1999).
35. C. T. Chantler, C. Q. Tran, Z. Barnea, D. Paterson, D. J. Cookson, and D. X. Balaic, "Measurement of the x-ray mass attenuation coefficient of copper using 8.85-20 keV synchrotron radiation," Phys. Rev. A **64**(6), 062506 (2001).

1. Introduction

X-ray absorption is a powerful tool for imaging objects comprised of multiple materials. In this absorptive imaging regime, the logarithm of the intensity image formed over the detector is proportional to the projection of the object's X-ray linear attenuation coefficient along a series of straight-line raypaths [1]. However, features that exhibit poor absorption contrast, such as biological soft tissues, can be difficult to resolve with this method.

Numerous techniques have been developed to successfully overcome this difficulty, including K-edge subtraction imaging [2, 3], magnetic resonance imaging [4, 5], positron

emission tomography [5], X-ray interferometry [6], analyzer-based phase contrast [7], and X-ray grating methods [8].

The technique utilized in the present paper, which differs from the abovementioned techniques insofar as it employs no optical elements between the illuminating radiation and the detector, is propagation-based X-ray phase contrast imaging (PBI) [9–11]. In this imaging modality, the act of free-space propagation—from the exit surface of a sample illuminated by a spatially coherent source, to the surface of a two-dimensional position-sensitive detector—renders visible the transverse phase shifts imparted by the sample upon the illuminating radiation (see Fig. 1).

Although PBI can improve the visualization of weakly absorbing features in a sample, quantitative information cannot be directly obtained from the raw phase contrast X-ray images. Phase-retrieval methods for extracting quantitative information from intensity measurements alone have been developed (see e.g. [12–21]) to obtain the projected phase and absorption information of the object. Notwithstanding their successes, these methods often require multiple intensity measurements, impose strong restrictions on the object under study or apply iterative solution techniques. Acquiring multiple images can prove problematic for correct alignment of images and induces a higher radiation dose, which is important for biomedical applications. Several phase retrieval methods require the object to be 'weak' such that they provide little to no absorption contrast with limited phase gradients introduced by the sample [18, 20, 21]. Since most inanimate materials and biological tissues cannot be considered as 'weak objects', phase retrieval algorithms developed under these approximations have only limited use for biomedical imaging or materials science applications. Iterative phase retrieval algorithms can also be problematic as convergence to the correct solution cannot be guaranteed and are computationally more intensive than analytic solutions.
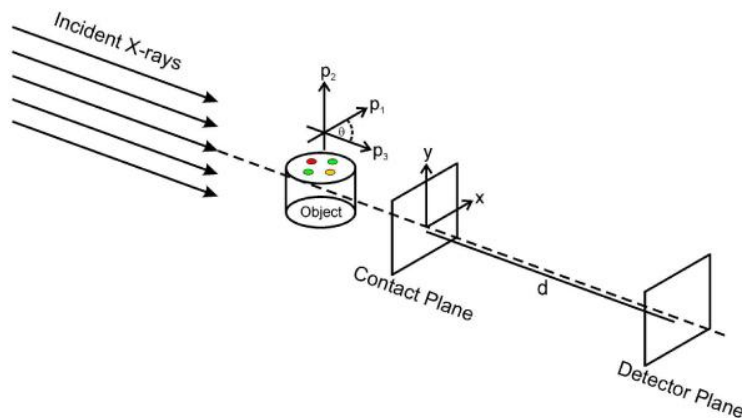

Fig. 1. Experimental setup showing the imaging geometry and coordinate system, for propagation-based phase contrast tomography of a multi-material object from a single propagation-based phase contrast image per projection.

For the case of a single-material object illuminated by paraxial coherent X-rays, Paganin *et al.* [22] developed a noise-robust deterministic phase-retrieval algorithm to reconstruct the projected linear attenuation coefficient from a single PBI image, which has been subsequently utilized in a number of tomographic studies [23–25]. These phase-contrast tomography investigations, which incorporate the effects of both absorption and phase contrast, generalize the seminal work for the phase-contrast tomography of pure phase objects by Bronnikov [26,27].

In this paper, we extend the work of Paganin *et al.* [22] and Mayo *et al.* [23] to enable analytic propagation-based phase-retrieval tomography to be performed on a multi-material

object in which the spatially-dependent complex refractive index is quantized, *i.e.* it takes one of a series of distinct values. The algorithm makes use of a single PBI image per projection, separately and selectively reconstructing each interface between any given pair of distinct materials. Having separately reconstructed the interfaces between different distinct pairs of materials, a "spliced" image of all materials present in the sample can then be computed. Section 2 of the paper develops the underlying theory for our method, with an experimental implementation in Section. 3.

2. Theory

Here we outline the theory for quantitative phase–amplitude tomography of a multi-material object with a quantized distribution of complex refractive indices ("spatially-quantized object"). Section 2.1 reviews an existing theory for two-dimensional (2D) single-image propagation-based phase-retrieval of a one-material object, with Section 2.2 generalizing this to the case of 2D single-image phase retrieval of an object of a given material which is embedded in a matrix of a second material. Section 2.3 generalizes this result to the case of three-dimensional (3D) propagation-based phase-contrast imaging of spatially-quantized objects, given a single image per projection.

2.1 Two-dimensional phase retrieval for a binary object

Consider an object with complex refractive index distribution $n(\mathbf{p}) = 1 - \delta(\mathbf{p}) + i\beta(\mathbf{p})$, where δ and $\beta = \lambda\mu/4\pi$ respectively quantify the refractive and absorptive properties of the object, λ is the radiation wavelength and μ is the linear attenuation coefficient [28]. The position vector $\mathbf{p} = (p_1, p_2, p_3)$ represents the object's coordinate system as illustrated in Fig. 1. For an object composed of a single material "1" (including voids; herein referred to as a binary object), $n(\mathbf{p})$ takes only the values $1 - \delta_1 + i\beta_1$ or unity. For such objects, and under the assumptions of paraxial monochromatic scalar electromagnetic-wave illumination and optical thinness, the intensity and phase of the wavefield downstream of the object obey the Transport-of-Intensity equation (TIE) [12]:

$$\nabla_\perp \cdot \left[I(\mathbf{r}_\perp, z) \nabla_\perp \varphi(\mathbf{r}_\perp, z) \right] = -k \partial_z I(\mathbf{r}_\perp, z). \quad (1)$$

Here, the intensity and phase of the wavefield are denoted by $I(\mathbf{r}_\perp, z)$ and $\varphi(\mathbf{r}_\perp, z)$, $\mathbf{r}_\perp = (x, y)$ is the position vector perpendicular to the optic axis z, $\nabla_\perp = (\partial_x, \partial_y)$ is the transverse gradient operator, $k = 2\pi/\lambda$ is the wave number and ∂_m denotes differentiation with respect to $m = x, y, z$. For normally incident plane-wave illumination of an optically-thin object, the intensity and phase at the contact plane $(z = 0)$ is given by the projection approximation (see e.g. [29]), such that $I(\mathbf{r}_\perp, z = 0) = I_0 \exp[-\mu_1 T_1(\mathbf{r}_\perp)]$ and $\varphi(\mathbf{r}_\perp, z = 0) = -k\delta_1 T_1(\mathbf{r}_\perp)$. The former expression is the Beer–Lambert law of absorption, $T_1(\mathbf{r}_\perp)$ is the projected thickness of the object (projected in the z direction) and I_0 is the uniform incident intensity. By substituting $I(\mathbf{r}_\perp, z = 0)$ and $\varphi(\mathbf{r}_\perp, z = 0)$ into Eq. (1) one can solve for the projected thickness as [22]:

$$T_1(\mathbf{r}_\perp) = -\frac{1}{\mu_1} \log_e \left(\mathbf{F}^{-1} \left\{ \frac{1}{(d\delta_1/\mu_1)\mathbf{k}_\perp^2 + 1} \mathbf{F} \left[\frac{I(\mathbf{r}_\perp, z = d)}{I_0} \right] \right\} \right). \quad (2)$$

Here, $\mathbf{F}$ and $\mathbf{F}^{-1}$ are the two-dimensional forward and inverse Fourier transforms with respect to $\mathbf{r}_\perp$, $\mathbf{k}_\perp = (k_x, k_y)$ are the Fourier coordinates corresponding to $\mathbf{r}_\perp$, and d is the propagation distance between the exit-surface of the object and the surface of the detector

(see Fig. 1). This algorithm assumes the "near field approximation" that d be sufficiently small that the Fresnel number $N_F = \ell^2 / [\lambda(D+d)]$ be significantly larger than unity, where ℓ is the characteristic transverse length scale associated with the wavefield at the exit surface of the object and D is the distance from the smallest feature to the exit surface (see e.g. [29]). For a given wavelength and spatial resolution we can therefore estimate the minimum feature size that can be imaged and still satisfy the near field approximation.

A mathematically identical form of Eq. (2) that allows for the recovery of the projected electron density $\rho(\mathbf{r}_\perp)$, has also been derived via a different approach by Wu *et al.* [30]. In their derivation, the authors make explicit use of the Klein-Nishina formula and assume the energies of the incident X-rays must range from 60 to 500 keV. Their derivation is not restricted to a single material object, but enables the same mathematical simplification as the single material assumption made in deriving Eq. (2) when lower energy X-rays are considered.

2.2 Two-dimensional phase retrieval for a ternary object

Here, the phase-retrieval algorithm in Eq. (2) is generalized to the case of a ternary object (two materials including voids). To this end, consider an object made of material "j" with projected thickness $T_j(\mathbf{r}_\perp)$, embedded in another object made of material "1" with projected thickness $T_1(\mathbf{r}_\perp)$. We seek to recover $T_j(\mathbf{r}_\perp)$ from a single PCI image. Introduce the total projected thickness [25]:

$$A(\mathbf{r}_\perp) = T_j(\mathbf{r}_\perp) + T_1(\mathbf{r}_\perp). \tag{3}$$

Under the projection approximation the intensity and phase at the contact plane are given by

$$I(\mathbf{r}_\perp, z = 0) = I_0 \exp\left[-\mu_j T_j(\mathbf{r}_\perp) - \mu_1 T_1(\mathbf{r}_\perp)\right], \tag{4}$$

$$\varphi(\mathbf{r}_\perp, z = 0) = -k\left[\delta_j T_j(\mathbf{r}_\perp) + \delta_1 T_1(\mathbf{r}_\perp)\right]. \tag{5}$$

We can solve for $T_j(\mathbf{r}_\perp)$ upon substitution of Eqs. (3), (4) and (5) into the TIE (Eq. (1)) and making the assumption that the projected thickness of the encasing material, $T_1(\mathbf{r}_\perp)$, varies slowly across the plane $\mathbf{r}_\perp = (x, y)$. Under this approximation, spatial derivatives of the encasing material are neglected. As such, the term $\delta_1 I_0 \exp[-\mu_1 A(\mathbf{r}_\perp)]\nabla_\perp \cdot \{\exp[-(\mu_j - \mu_1)T_j(\mathbf{r}_\perp)]\nabla_\perp A(\mathbf{r}_\perp)\}$ appearing in the derivation is ignored, which leads to the following non-linear differential equation:

$$(\delta_j - \delta_1)I_0 \exp\left[-\mu_1 A(\mathbf{r}_\perp)\right]\nabla_\perp \cdot \left\{\exp\left[-(\mu_j - \mu_1)T_j(\mathbf{r}_\perp)\right]\nabla_\perp T_j(\mathbf{r}_\perp)\right\} = \partial_z I(\mathbf{r}_\perp, z). \tag{6}$$

Making use of the identity

$$\nabla_\perp \cdot \left\{\exp\left[-(\mu_j - \mu_1)T_j(\mathbf{r}_\perp)\right]\nabla_\perp T_j(\mathbf{r}_\perp)\right\} = -\frac{1}{\mu_j - \mu_1}\nabla_\perp^2 \exp\left[-(\mu_j - \mu_1)T_j(\mathbf{r}_\perp)\right], \tag{7}$$

and expressing the right hand side of Eq. (6) as a first-order difference approximation of two closely spaced measured intensities corresponding to the planes $z = 0$ and $z = d$, yields:

$$\left[-\frac{d(\delta_j - \delta_1)}{(\mu_j - \mu_1)}\nabla_\perp^2 + 1\right]\exp\left[-(\mu_j - \mu_1)T_j(\mathbf{r}_\perp)\right] = \frac{I(\mathbf{r}_\perp, z = d)}{I_0 \exp\left[-\mu_1 A(\mathbf{r}_\perp)\right]}. \tag{8}$$

Fourier transform both sides of Eq. (8), use the Fourier derivative theorem, and inverse transform to obtain the following expression for $T_j(\mathbf{r}_\perp)$:

$$T_j(\mathbf{r}_\perp) = -\frac{1}{\mu_j - \mu_1} \log_e \left(\mathbf{F}^{-1} \left\{ \frac{1}{\left[d(\delta_j - \delta_1)/(\mu_j - \mu_1) \right] \mathbf{k}_\perp^2 + 1} \mathbf{F} \left[\frac{I(\mathbf{r}_\perp, z = d)}{I_0 \exp\left[-\mu_1 A(\mathbf{r}_\perp) \right]} \right] \right\} \right). \quad (9)$$

To employ this algorithm one requires *a priori* knowledge of the total projected thickness $A(\mathbf{r}_\perp)$ in addition to the values δ_j, δ_1 and μ_j, μ_1 corresponding to the different materials in the object. If an object is of complicated shape and is known to contain no internal voids, then $A(\mathbf{r}_\perp)$ can be found using techniques such as laser profilometry [25]. In the case of tomography, a more convenient and practical approach to obtain $A(\mathbf{r}_\perp)$ for each projection angle can be used. By utilizing Eq. (2) the encasing material can first be correctly reconstructed tomographically. Internal and external voids can then be located by computationally searching for a predefined threshold in each slice of the reconstructed volume. $A(\mathbf{r}_\perp)$ may then be calculated for each projection angle. On an additional note, for point source illumination it is necessary to account for image magnification in both Eq. (2) and Eq. (9). Both equations will be altered by identical factors [31].

2.3 Three-dimensional phase retrieval: Quantitative phase–amplitude tomography of multi-material objects with quantized refractive-index distribution, from a single phase-contrast image per projection

For both absorption and phase contrast tomography we utilize a conventional filtered backprojection (FBP) algorithm to reconstruct a two-dimensional slice of the imaged object [1, 24]. Fourier-transform-based FBP utilizing projection phase-contrast images processed using Eq. (2), allows one to "focus in" on an interface between air (cavities) and the encasing object "1", enabling any voids within the encasing material to be quantitatively reconstructed. Here δ_1 and μ_1 take the values corresponding to the encasing object "1". For objects with spatially quantized refractive indices, such as shown in Fig. 2, the "correct" interfaces will be sharply reconstructed.
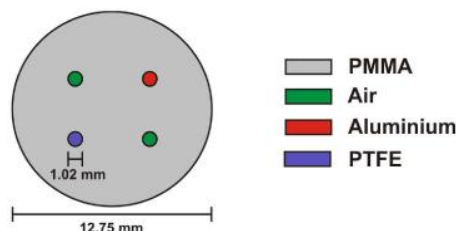

Fig. 2. Top view of the object, used as a test object to demonstrate interface-specific phase-retrieval tomography, using a single propagation-based X-ray phase contrast image per projection.

Interfaces between embedded objects "j" (where $j = 2, 3, ...$) and the encasing object "1", will be incorrectly reconstructed using this procedure. However, such incorrectly reconstructed interfaces will bear a characteristic local signature of either (i) residual phase-contrast fringes, or (ii) blurred interfaces. Moreover, such "incorrect" interfaces (e.g. between materials "j" and "1") may be quantitatively (sharply) reconstructed by repeating the FBP analysis using inputs derived by inserting $(\Delta\delta)_{j1} \equiv \delta_j - \delta_1$ and $(\Delta\mu)_{j1} \equiv \mu_j - \mu_1$ into Eq. (9), provided the material of interest is not in contact with or in the immediate vicinity of either another embedded object or a cavity. From a series of FBP analyses for each distinct pair of material interfaces present in the sample, one can build up a quantitative 3D map of all

materials. These can be spliced together into a composite tomographic reconstruction, in which all interfaces between each distinct pair of materials is sharply reconstructed. This is the core idea underpinning our procedure for phase–amplitude tomography of a multi-material object with spatially quantized complex refractive index distribution, given a single propagation-based phase contrast image per projection.

Crucial to the success of the splicing procedure described above is the idea that "incorrect" interfaces are only *locally* polluted (in three dimensions) by locally incorrect choices for δ and μ [23]. How may one quantify the smoothing artefacts for interfaces which are incurred as a result of a locally incorrect filtering parameter, $\alpha = d\delta/\mu$, being utilized in Eq. (2) at a given interface? In regions where over-smoothing occurs (*i.e.* where α is underestimated), the amount of blurring ("bleed width") of an "incorrect" interface can be estimated by analyzing the low-pass Fourier filter in Eq. (2), which has the form of a Lorentzian function. This Lorentzian can be rewritten as

$$\frac{1}{\alpha\mathbf{k}_\perp^2 + 1} = \frac{1}{\varepsilon\mathbf{k}_\perp^2 + 1} \times \frac{\varepsilon\mathbf{k}_\perp^2 + 1}{\alpha\mathbf{k}_\perp^2 + 1}. \tag{10}$$

In the case of a medium "j" embedded in an encasing medium "1", $\varepsilon = d(\delta_j - \delta_1)/(\mu_j - \mu_1)$ is the ratio that will correctly reconstruct this particular interface. Equation (10) allows us to approximately interpret the operation of Eq. (2) (using α rather than ε) on this interface as the correct Lorentzian function multiplied by the ratio of quadratic functions on the right side of Eq. (10). This quotient is a Fourier filter that locally causes either an over- or under-smoothing artefact in the vicinity of the "incorrect" interface. Incidentally, in the case of over-smoothing, when $\varepsilon/\alpha < 1$, this ratio of quadratic functions is a Lorentzian function that has been vertically scaled by a factor $(\alpha - \varepsilon)/\varepsilon$ and shifted positively along the vertical axis by (ε/α), with a maximum value of unity. In the opposite case, when $\varepsilon/\alpha > 1$, we have an inverted Lorentzian, giving rise to a high-pass filter that leaves a characteristic fringe representing under-compensated phase contrast. In either case, one has a clear signature associated with "incorrect" interfaces, which allows them to be unambiguously identified and thereby enabling one to "focus in" upon a particular material interface of interest.

The "bleed width" for over-smoothing can be estimated via the optical uncertainty principle:

$$\Delta\mathbf{x}\Delta\mathbf{k} \geq 1, \tag{11}$$

where $\Delta\mathbf{x}$ is the uncertainty in real space (*i.e.*, the "bleed width") and $\Delta\mathbf{k}$ is the uncertainty in reciprocal space. Take $\Delta\mathbf{k}$ as the half-width at half-maximum (HWHM) of the second quotient on the right-hand side of Eq. (10); this HWHM is taken relative to the asymptotic baseline of ε/α. Subsequently, using Eq. (11) we obtain a simple lower bound for the associated bleed width that is independent of ε:

$$\Delta\mathbf{x} \geq \sqrt{\alpha}. \tag{12}$$

We close this section by noting that this "bleed width", associated with interfaces *other* than those selected via a given choice for α, is constructive insofar as it "tags" particular over-smoothed interfaces as not corresponding to the particular interface of interest, but rather to an interface with $\varepsilon < \alpha$. Under-smoothed interfaces are also tagged, as corresponding to $\varepsilon > \alpha$, via the signature of incompletely-compensated phase contrast fringes.

3. Experimental results and discussion

Here we give an X-ray synchrotron-based experimental implementation of the theory developed above. Section 3.1 discusses the experimental setup. Section 3.2 reports 2D phase–

amplitude retrieval of multi-material spatially quantized objects with embedded features that are non-overlapping in projection (cf. Sections 2.1 and 2.2). This requirement for non-overlap in projection is relaxed is Section 3.3, which implements 3D phase–amplitude retrieval of multi-material spatially quantized objects, given a single propagation-based X-ray phase contrast image per projection (cf. Section 2.3).

3.1 Experimental setup for X-ray phase–amplitude imaging of spatially quantized objects

X-ray propagation-based phase–amplitude computed tomography experiments were performed in Hutch 3 of beamline 20B2 at the SPring-8 synchrotron radiation source, Japan (proposal 2009A1882). The beamline employs a bending magnet source with a Si(111) double-crystal monochromator [32]. An X-ray energy of 24 keV provided acceptable phase and attenuation contrast for materials of relatively low atomic number. This energy is also commensurate with the diagnostic X-ray energies used in mammography [33]. Phase and absorption contrast images were recorded with the detector positioned at distances of $d = 1\,\mathrm{m}$ and $d < 3\,\mathrm{cm}$ from the object, respectively, as shown in Fig. 1. An optically coupled Hamamatsu CCD camera (C4880-41S) with a 10 μm thick gadolinium oxysulfide (Gd_2O_2S) scintillator was used to acquire each data set. The images had a window size of 3000 x 1500 pixels and an effective pixel size of 5.9 μm, which gave a region of interest (ROI) of 17.70 mm (H) $\times$ 8.85 mm (V). For each tomographic data set, 1800 projections were collected over 180° of rotation, each acquired with an exposure time of 2.5 s. Flat field images (no object in the beam) were recorded every 43 projections. Frequent flat field recordings were required due to instabilities in beam position with time. Dark field images also were acquired with the main beam shutter closed at the beginning and end of each scan to correct for the detector dark current offset. Prior to quantitative analysis, all phase-contrast images were flat-field and dark-field corrected, to compensate for both illumination non-uniformities and CCD dark current.

The imaged object was a PMMA (Polymethyl-methacrylate ($C_5H_8O_2$); commonly known as Perspex) cylinder 10 mm in height and 12.75 $\pm$ 0.05 mm in diameter. This contained four cavities each with diameter 1.02 $\pm$ 0.05 mm. An Aluminium (Al) and PTFE (Polytetrafluoroethylene (H_2F_4); commonly known as Teflon) pin of 1.00 $\pm$ 0.05 mm diameter were inserted into two of the cavities to create a quaternary object (three materials plus voids) with three distinct interfaces, these being air/PMMA, Aluminium/PMMA and PTFE/PMMA (see Fig. 2). The δ and μ values for the materials in the object, for 24 keV X-rays, are listed in Table 1. The Aluminium/PMMA interface will be denoted as $j = 2$ and the PTFE/PMMA interface as $j = 3$.

Table 1. Values of δ and μ at 24 keV for materials used to construct the test object in Fig. 2. Values obtained from http://henke.lbl.gov/optical_constants/ (accessed Nov. 4, 2009).

Material	δ ($\times 10^{-7}$)	μ (m^{-1})
PMMA ($C_5H_8O_2$)	4.628	41.2
PTFE (H_2F_4)	7.789	119.8
Aluminium	9.396	502.6

3.2 Projection imaging

Here we use the theory of Section 2.2 to implement 2D phase–amplitude retrieval of a multi-material spatially quantized object with non-overlapping projections of embedded features composed of different materials, noting that the assumption of non-overlapping embedded features will be dropped when moving to a tomographic analysis in Section. 3.3.

Absorption and phase contrast images of our test object (see Fig. 2) are shown in Fig. 3(a) and (b), for an orientation in which all embedded features (corresponding to different materials) are non-overlapping in projection. In the absorption contrast image, all interfaces except Al/PMMA exhibit weak contrast, since Al is significantly more attenuating than the other materials in the sample (see Table 1). Conversely, the phase contrast image displays a significantly greater signal-to-noise ratio (SNR), dramatically enhancing the PTFE/PMMA and air/PMMA interfaces and improving visualization of the object overall [10]. Line profiles from left-to-right of the centre of the images in Fig. 3(a) and (b) are shown in Fig. 3(f) and (g), respectively. The profile in Fig. 3(g) clearly reveals strong propagation-based phase contrast fringes formed at interface boundaries [10].

Figure 3(c) shows an image of the projected thickness of the object computed via Eq. (2), under the assumption that the object was composed entirely of PMMA. Here we have used the known values of δ_1 and μ_1 for PMMA listed in Table 1. The line profile in Fig. 3(h) shows the distribution of the recovered projected thickness from the phase contrast image in Fig. 3(b). From the profile it can be seen that the maximum projected thickness of the PMMA is close to the expected values (12.75 mm) and the boundaries of the air/PMMA interfaces are sharp. Moreover, due to reasons mentioned in section 2.3, the Al/PMMA and PTFE/PMMA interfaces suffer from an "over smoothing" and the associated projected thicknesses are also overestimated.

To recover the projected thicknesses of the Al and PTFE, that is $T_2(\mathbf{r}_\perp)$ and $T_3(\mathbf{r}_\perp)$, we "focus" on each of these individually using Eq. (9). Since implementation of this algorithm requires knowledge of the total projected thickness, the function $A(\mathbf{r}_\perp)$ was generated with the assumption that the object was a cylinder with no internal voids, which results in negative values arising in the projected thickness in the presence of internal voids (see Fig. 3(i) and (j)). To recover $T_2(\mathbf{r}_\perp)$, the values used for δ_2 and μ_2 correspond to Aluminium and δ_1 and μ_1 to PMMA (see Table 1). To recover $T_3(\mathbf{r}_\perp)$, the values used for δ_3 and μ_3 correspond to PTFE. The phase-retrieved images are shown in Fig. 3(d) and (e). The images show how the "selected" interfaces are sharpened and how the attenuated intensity due to PMMA is effectively removed. Line profiles in Fig. 3(i) and (j) illustrate this more clearly and reveal that the recovered projected thicknesses at the "selected" interfaces $T_2(\mathbf{r}_\perp)$ and $T_3(\mathbf{r}_\perp)$ are close to their expected thickness (~1 mm). Additionally, we see that the algorithm breaks down in regions where the encasing material exhibits strong phase contrast; however, this occurs at the boundary of the encasing material far from the interfaces of interest. These artefacts are expected since Eq. (9) assumes that phase gradients due to the encasing material are negligible. Also, we now see that the interfaces where the density is less than that of Aluminium are now under-smoothed and slight residual fringing is still visible (see for example Fig. 3(i), interfaces 1, 3 and 4; cf. Section. 2.3). Note that the upper threshold in (e) has been reduced to enhance the PTFE, as a linear palette obscures this feature and the Al/PMMA interface appears saturated as a consequence.
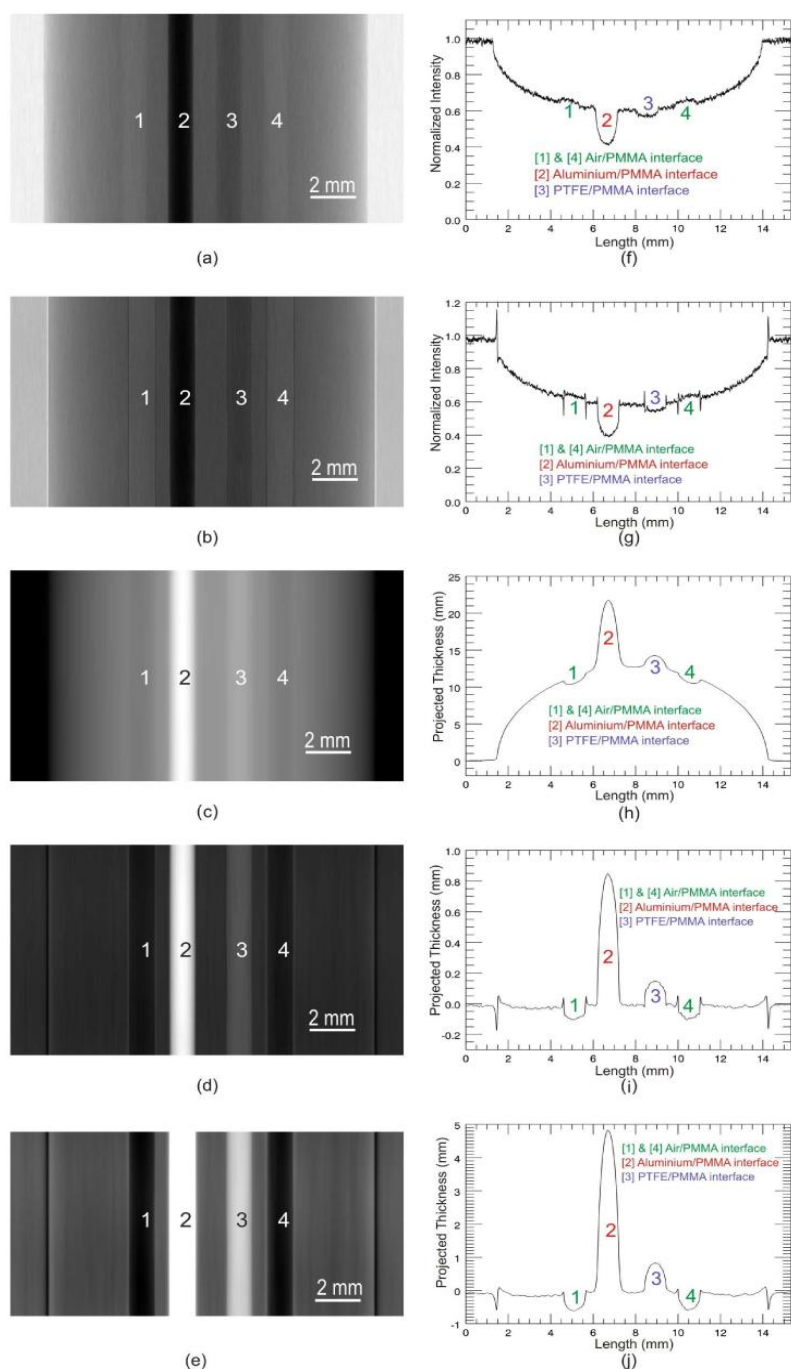
Fig. 3. Projection images of the multi-material test sample. (a) Absorption contrast image. The numbered regions correspond to the different interfaces in the object (Air/PMMA (Green), Al/PMMA (Red) and PTFE/PMMA (Blue)). (b) Phase contrast image acquired at d=1 m. (c) Phase retrieved image of (b) using Eq. (2). (d) and (e) Phase retrieved images of (b) using Eq. (9) with appropriate values of δ and μ for the Al/PMMA and PTFE/PMMA interface, respectively (see Table 1). Line profiles from the centre of the images on the left column are shown in (f), (g), (h), (i) and (j), respectively.

3.3 Tomography of spatially quantized objects, from a single phase-contrast image per projection

Section 3.3.1 presents our results for interface-specific phase-retrieval tomography, whereby a single phase-contrast image per projection may be used to selectively reconstruct a given interface between two given materials, in a spatially-quantized object. In Section 3.3.2, we experimentally test our uncertainty-principle estimate (see Eqs. (11) and (12)) for the "bleed width" associated with material interfaces other than that which is selectively reconstructed. In Section 3.3.3 we show how a complete set of material interfaces in a given spatially-quantized object may be spliced together, into a composite tomogram, given a single phase-contrast view per projection.

3.3.1 Interface-specific phase-retrieval tomography

For absorption-contrast FBP tomography, using the parameters described in Section 3.1, the reconstruction of a single slice of the sample is shown in Fig. 4(a). Qualitatively the reconstruction shows good detail of the object features, particularly at the Al/PMMA interface where there is a large difference in absorption. In Fig. 4(f) line profiles from left-to-right of the centre of each interface of Fig. 4(a) are shown in a single plot. This displays the distribution of the attenuation coefficient at each interface where it can be seen that, on average, the attenuation coefficients are similar to the theoretical values in Table 1. However, the reconstruction also contains a substantial amount of high frequency noise making it difficult to define the boundaries at the interfaces where absorption contrast is poor (air/PMMA and PTFE/PMMA). Such noise is typically reduced in tomography by use of an additional low-pass filter during the filtered backprojection, but must be traded against a reduction in spatial resolution [1].

Figure 4(b) shows a slice of a tomographic reconstruction obtained by applying FBP directly to the raw phase contrast images (cf. [34]), without any phase–amplitude retrieval. Like the absorption contrast result it also reveals good detail of the object features. The reconstruction allows us to see how the boundaries of each interface are enhanced as a result of the high SNR provided by phase contrast. Although phase contrast provides better feature visibility, the line profile in Fig. 4(g) shows that non-physical negative values and sharp spikes arise in the attenuation coefficient map without the phase retrieval step.

Figure 4(c) shows a slice of a tomographic reconstruction obtained using Eq. (2) to yield $T_1(\mathbf{r}_\perp, \theta)$ for each projection angle, giving a series of two-dimensional projected-thickness maps that were then tomographically reconstructed using FBP [24]. The reconstruction shows the distribution of $\delta_1(\mathbf{p}_\perp)$ along the plane $\mathbf{p}_\perp = (p_1, p_3)$ (see Fig. 1), which in this case is PMMA ($j = 1$). It can be seen that the noise has been substantially suppressed while preserving the sharpness of the air/PMMA interface, as the line profile in Fig. 4(h) indicates. Conversely, over-smoothing (cf. Section 2.3) is clearly apparent at the remaining interfaces. Despite this localized blurring of these regions the result shows that Eq. (2) can be applied to multi-material objects and accurately reconstruct the voids as long as they are not near the vicinity of the over-smoothed interfaces. The line profile in Fig. 4(h) shows that at the air/PMMA interface, the distribution of $\delta_1(\mathbf{p}_\perp)$ has an average value of 4.2×10^{-7}, which is within 10% of the theoretical value in Table 1. This is acceptable as it is known that attenuation coefficients have discrepancies of up to 10% between theoretical values [35].

Figure 4(d) and (e) show reconstructions of the same slice from phase retrieved images using Eq. (9) to obtain $T_2(\mathbf{r}_\perp, \theta)$ and $T_3(\mathbf{r}_\perp, \theta)$ before using FBP to respectively recover the distributions of $\delta_2(\mathbf{p}_\perp)$ (Aluminium; $j = 2$) and $\delta_3(\mathbf{p}_\perp)$ (PTFE; $j = 3$). Figure 4(d) focuses on the Al/PMMA interface and (e) focuses on the PTFE/PMMA interface. Due to the rotational symmetry of the surface of the cylinder the same $A(\mathbf{r}_\perp)$ fitted function was used for
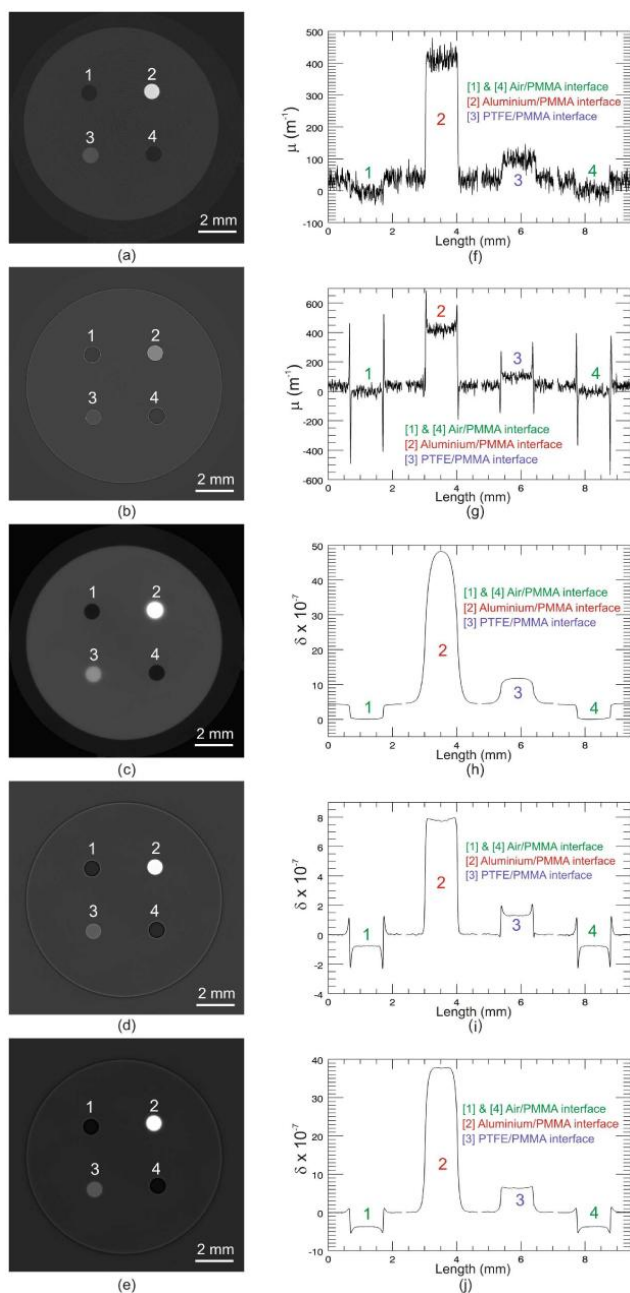
Fig. 4. Tomographic reconstruction of the multi-material test sample using (a) conventional absorption contrast images reconstructed via FBP; (b) phase contrast images reconstructed by applying FBP to raw PCI data. (c) Phase contrast images reconstructed using Eq. (2) to calculate $T_1(\mathbf{r}_\perp, \theta)$ for each projection ($j = 1$), followed by FBP. (d) and (e) are reconstructions using same procedure as (c), after calculating $T_2(\mathbf{r}_\perp, \theta)$ and $T_3(\mathbf{r}_\perp, \theta)$ with Eq. (9) for both Al and PTFE for each projection ($j = 2$ and $j = 3$). (f), (g), (h), (i) and (j) respectively, show line profiles from left-to-right across the centre of the images in (a), (b), (c), (d) and (e). Numbered regions correspond to different interfaces in the object (Air/PMMA (Green), Al/PMMA (Red) and PTFE/PMMA (Blue)).

every projection. The distribution of $\delta_2(\mathbf{p}_\perp)$ and $\delta_3(\mathbf{p}_\perp)$ are shown in the line profiles in Fig. 4(i) and (j). On average the values of $\delta_2(\mathbf{p}_\perp)$ and $\delta_3(\mathbf{p}_\perp)$ are 7.9×10^{-7} and 6.6×10^{-7} respectively, and are within 15% of the theoretical values in Table 1.

3.3.2 Quantification of over-smoothing

Experimentally, we find that the "bleed width" blurring typically extends between 3 and 5 times the lower bound in Eq. (12). Hence the following rule-of-thumb is used to estimate the bleed width $\Delta\mathbf{x}$:

$$3\sqrt{\alpha} \geq \Delta\mathbf{x} \geq 5\sqrt{\alpha}. \qquad (13)$$

This formula gives a rough indication as to how far an over-smoothed interface will be blurred by the phase retrieval (cf. Section 2.3). We tested this rule by measuring the blurring at the Al/PMMA and PTFE/PMMA interfaces in Fig. 4 (h). The blurring was just visible up to a distance of 443 μm from the Al/PMMA interface and 454 μm from the PTFE/PMMA interface with an uncertainty of ±30 μm. Evaluating $\sqrt{\alpha}$ for PMMA gives a value of 106 μm. The measured bleed widths are thus $4.17\times\sqrt{\alpha}$ for Al/PMMA and $4.28\times$ $\sqrt{\alpha}$ for PTFE/PMMA, which agrees with the inequality in Eq. (13). We also note that both interfaces bleed almost the same amount, providing empirical evidence that the parameter α is the only contributor to the smoothing artefact.

3.3.3 Spliced tomographic reconstruction

Having quantitatively reconstructed all three interfaces and established a rule-of-thumb to estimate the blurring widths (see Eq. (13)), we can now combine these images to form a single "spliced" image of our quaternary (or higher order) object (cf. Section. 2.3). The image was constructed by digitally inserting the individually reconstructed interfaces in Fig. 4(d) and (e) into the appropriate regions of the encasing material in Fig. 4(c). The size of the region was chosen by considering the amount of blurring at these interfaces. The refractive index of these segments were offset so that the background zeroes match that of the encasing material and the resulting amplitude was rescaled to maintain the original value. The spliced image is shown in Fig. 5(a). Line profiles of the different interfaces of the image are shown in Fig. 5(b). We now have a quantitative tomographic reconstruction of a multi-material object, at each point of which the refractive index takes one of N distinct values, using a single PCI image per projection.

To quantitatively compare our spliced reconstruction with the absorption-based reconstruction, the SNR was calculated for each medium. The Al, PTFE and PMMA gave SNRs of 312, 309 and 98.9, respectively, where the signal is the average value inside the medium. This significantly improves the respective SNR values of 18.7, 5.19 and 1.17, which were calculated at the same regions in the absorption contrast reconstruction in Fig. 4(a). The ordering of these SNRs is consistent with the relative amount of smoothing associated with the filters in Eqs. (2) and (9). The increase in SNR is largest (~85×) for the encasing material as the Fourier-space damping of high spatial frequencies is largest for the PMMA/air interface. Each of the SNRs were calculated over a 90×90 pixel region of interest. The mathematical origin of the stability with respect to noise is due to the regularizing presence of a non-zero denominator in the Fourier filter of Eqs. (2) and (9), as the ratio $d\delta/\mu$ is always greater than zero and the ratio $d(\delta_j - \delta_1)/(\mu_j - \mu_1)$ is unlikely to be less than zero; also, since μ is never zero and $(\Delta\mu)_{j1}$ is generally a non-zero quantity. This avoids instability problems of the 'division by zero' type that would arise if the denominator were zero [22].
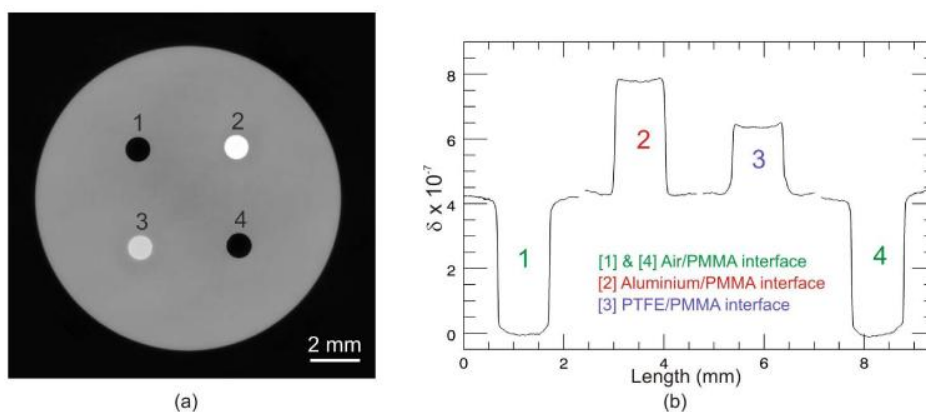
Fig. 5. (a) Spliced tomographic reconstruction. (b) Line profile of the different interfaces in (a).

4. Conclusion

We have developed a numerically efficient phase retrieval algorithm to reconstruct the complex refractive index distribution of known materials embedded in a second medium from a single X-ray phase contrast image per projection. This interface-specific phase-retrieval tomography algorithm requires *a priori* knowledge of each material's complex refractive index and the total projected thickness of the sample at each orientation. The algorithm was successfully applied to experimental data collected using X-ray synchrotron radiation. We have used our method to quantitatively reconstruct a quaternary object by reconstructing all interfaces separately. A complete tomographic reconstruction of all interfaces in the object was produced by splicing the individual reconstructions together. When it comes to imaging multi-material objects, our technique proves superior to conventional absorption contrast in terms of the signal-to-noise ratio (SNR). For the test sample used here, the improvement in the SNR was between 17 and 85 fold.

Given the success of our results, combined with the practicality of the technique, we anticipate that it will have applications in a number of different fields including medicine, biomedical science, geology and materials science. Our methodology may also be adapted to electron and visible light microscopy.

Appendix B

Interface-specific X-ray phase retrieval tomography of complex biological organs.

by M. A. Beltran, D. M. Paganin, K. K. W. Siu, A. Fouras, S. B. Hooper, D. H. Reser, and M. J. Kitchen.

Interface-specific x-ray phase retrieval tomography of complex biological organs

Interface-specific x-ray phase retrieval tomography of complex biological organs

M A Beltran[1]**, D M Paganin**[1]**, K K W Siu**[1,2,3]**, A Fouras**[4]**, S B Hooper**[5]**, D H Reser**[6] **and M J Kitchen**[1]

[1] School of Physics, Monash University, Victoria 3800, Australia
[2] Monash Biomedical Imaging, Monash University, Victoria 3800, Australia
[3] Australian Synchrotron, Victoria 3168, Australia
[4] Division of Biological Engineering, Monash University, Victoria 3800, Australia
[5] The Ritchie Centre, Monash Institute of Medical Research, Monash University, Victoria 3800, Australia
[6] Department of Physiology, Monash University, Victoria 3800, Australia

E-mail: ███████████████████

Abstract

We demonstrate interface-specific propagation-based x-ray phase retrieval tomography of the thorax and brain of small animals. Our method utilizes a single propagation-based x-ray phase-contrast image per projection, under the assumptions of (i) partially coherent paraxial radiation, (ii) a static object whose refractive indices take on one of a series of distinct values at each point in space and (iii) the projection approximation. For the biological samples used here, there was a 9–200 fold improvement in the signal-to-noise ratio of the phase-retrieved tomograms over the conventional attenuation-contrast signal. The ability to 'digitally dissect' a biological specimen, using only a single phase-contrast image per projection, will be useful for low-dose high-spatial-resolution biomedical imaging of form and biological function in both healthy and diseased tissue.

S Online supplementary data available from stacks.iop.org/PMB/56/7353/mmedia

(Some figures in this article are in colour only in the electronic version)

1. Introduction

Phase-contrast imaging is any optical technique whereby phase changes imparted by an object to the incident coherent, or partially coherent, radiation are rendered visible in the
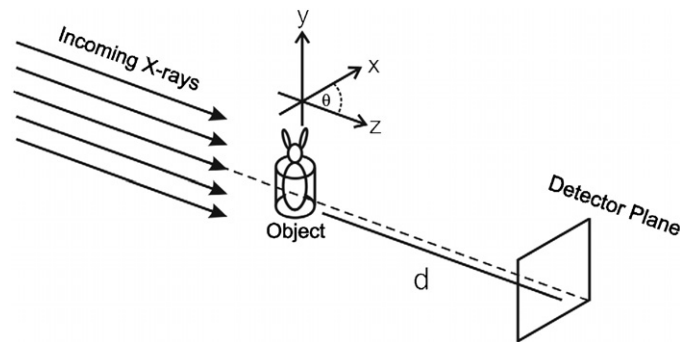
Figure 1. Experimental setup illustrating the geometry for propagation-based x-ray phase retrieval tomography, using a single view per projection.

measured intensity. Phase-contrast x-ray computed tomography (CT) can provide images with better signal-to-noise ratio (SNR) than conventional x-ray absorption-contrast CT for imaging samples in three dimensions that exhibit weak absorption, such as biological specimens (Mayo *et al* 2003, Arhatari *et al* 2010, Beltran *et al* 2010). The most common phase-contrast techniques are x-ray interferometry (Momose *et al* 1996), x-ray diffraction grating methods (Pfeiffer *et al* 2007), analyser-based phase-contrast imaging (ABI) (Förster *et al* 1980) and propagation-based phase-contrast imaging (PBI) (Snigirev *et al* 1995).

The technique used in the present paper is PBI. Unlike the other methods mentioned above, PBI does not require any additional optical elements between the sample and detector. In PBI, the act of free-space propagation—from the exit surface of a sample illuminated by a spatially coherent source to the surface of a two-dimensional position-sensitive detector—renders visible the transverse phase shifts imparted by the sample upon the illuminating radiation (Snigirev *et al* 1995, Wilkins *et al* 1996, Cloetens *et al* 1996, 1999, Pogany *et al* 1997) (see figure 1).

With PBI, visualization of poorly absorbing features in a sample can significantly improve in comparison to absorption-contrast alone. However, quantitative information about the phase cannot be directly inferred from the raw PBI images. In order to extract phase information, phase retrieval methods may be employed. Numerous phase retrieval algorithms that require intensity-only measurements have been developed to yield the projected phase and absorption information of an object (Teague 1983, Gureyev and Nugent 1996, 1997, Paganin and Nugent 1998, Cloetens *et al* 1999, Guigay *et al* 2007). Despite their success, many of these algorithms require the acquisition of multiple images per tomographic projection, or impose significant restrictions on the object under study (e.g., it must provide weak or no attenuation contrast). When it comes to using ionizing radiation to image biological specimens, taking more than one image per projection will induce a higher radiation dose, which can be detrimental. Dose consideration is particularly important for *in vivo* studies, and thus methods requiring large numbers of projections are of limited use for biomedical applications.

A significant amount of work has been done on the question of tomographic reconstruction using x-ray PBI. Key works include, but are not limited to, (i) Cloetens *et al* (1997), who reconstructed raw x-ray propagation-based phase-contrast data using filtered backprojection to give an edge-enhanced three-dimensional representation of the object; (ii) Cloetens *et al* (1999) on 'holotomography', which utilized through-focal-series phase retrieval methods originally developed in the field of electron microscopy, in the context of quantitative

x-ray phase-contrast tomography; (iii) x-ray phase-contrast tomography which incorporated the transport-of-intensity equation (Teague 1983) for the phase retrieval analysis of each projection prior to three-dimensional reconstruction (Mayo *et al* 2003, McMahon *et al* 2003); (iv) Bronnikov's merging of the phase retrieval and tomography steps into a single algorithm for the case of a transparent object (Bronnikov 2002), together with the generalization of this work by Gureyev *et al* (2006); (v) extension of Wolf's work on diffraction tomography (Wolf 1969), in the context of x-ray phase contrast, by Anastasio and Pan (2000); (vi) Myers *et al* (2010) on phase retrieval tomography of few-material objects using a limited number of views, together with work on gradient-sparse objects by Sidky *et al* (2010); and (vii) local phase-contrast tomography (Anastasio *et al* 2004, Shi *et al* 2005, Gureyev *et al* 2007). For a balanced overview of the contemporary state of the art in x-ray phase-contrast tomography, we refer to the proceedings of the *Conference on Developments in X-Ray Tomography VII*, edited by Stock (2010).

As a key ingredient of the work presented here, Paganin *et al* (2002) developed a phase retrieval algorithm that only requires a single PBI image per projection. Their algorithm was derived under the strong assumption that the sample be comprised of a single homogeneous material that is imaged under paraxial coherent x-ray illumination. It has proven to be very robust under the influence of noise and has also been utilized in a number of PBI tomographic studies (Mayo *et al* 2003, Gureyev *et al* 2006, Arhatari *et al* 2010). The work of Paganin *et al* (2002) was extended by Beltran *et al* (2010) to enable interface-specific phase retrieval tomography to be performed on samples composed of a finite number of materials which are spatially quantized, under the assumptions that (i) each material type within the sample may be adequately approximated by a single complex refractive index; (ii) the complex refractive index of each distinct material has a distinct value; (iii) no more than two interfaces can be in direct contact at any given location. While any real sample will have variations in homogeneity within each given material, this was seen to have a minimal effect on the tomographic reconstruction, both in the previously reported work by Beltran *et al* (2010) and in the new work reported in the present paper. In this context, note also that the previously mentioned variations in homogeneity are often within the uncertainties of the real and imaginary parts of the complex refractive index, for biological samples at diagnostic x-ray energies. Importantly, this technique retains the salient feature of requiring only a single phase-contrast image per projection. As a proof of principle, the authors tested their technique on PBI tomographic experimental data taken of a simple test phantom which contained three different materials. Each material was quantitatively reconstructed separately and spliced together into a complete reconstruction (Beltran *et al* 2010).

In this investigation, we apply the technique developed by Beltran *et al* (2010) to carry out interface-specific phase retrieval tomography, without using any chemical contrast enhancements, on complex biological organs including the thorax of a newborn New Zealand white rabbit pup and the excised brain of an adult Sprague Dawley rat. Our aim was to determine whether our single-image phase retrieval technique could be applied to complex structures and to measure the gain in the SNR of the reconstructed images over conventional CT.

The outline of our paper is as follows. Section 2 reviews the underlying theory of the method developed by Beltran *et al* (2010), for interface-specific phase retrieval x-ray tomography of objects whose refractive indices take on one of a series of discrete values. Section 3 describes the setup and procedures used for the experimental implementation on two complex biological samples, namely rabbit lung and rat brain tissue. Section 4 illustrates the results achieved using interface-specific tomography. We provide discussion for future work in section 5 and conclude with section 6.

2. Theory: phase retrieval for a single- and two-material sample

Underpinning our phase retrieval method is the algorithm developed by Paganin *et al* (2002), which requires only a single two-dimensional PBI image per tomographic projection. Its derivation was based on the transport of intensity equation (Teague 1983) for a paraxial monochromatic wavefield together with the assumption that the imaged object is comprised of a single homogeneous material. The algorithm has proven to be computationally efficient and robust under the presence of noise in a number of subsequent studies (e.g., Mayo *et al* 2003, Paganin *et al* 2004, Turner *et al* 2004, Kitchen *et al* 2008, Irvine *et al* 2008, Beltran *et al* 2010, Stevenson *et al* 2010).

For an object that is composed of material '1' which has complex refractive index $n = 1 - \delta_1 + i\beta_1$, an argument combining Teague's transport of intensity equation (Teague 1983) and Beer's law of attenuation implies that the projected thickness can be calculated from the measured intensity using (Paganin *et al* 2002):

$$T_1(\mathbf{r}_\perp) = -\frac{1}{\mu_1} \log_e \left(\mathbf{F}^{-1} \left\{ \frac{1}{(d\delta_1/\mu_1)\mathbf{k}_\perp^2 + 1} \mathbf{F} \left\{ \frac{I(\mathbf{r}_\perp, z = d)}{I_0} \right\} \right\} \right). \tag{1}$$

Here, $\mathbf{F}$ and $\mathbf{F}^{-1}$ respectively represent the forward and inverse Fourier transforms with respect to $\mathbf{r}_\perp = (x, y)$, $\mathbf{k}_\perp = (k_x, k_y)$ are the Fourier coordinates dual to $\mathbf{r}_\perp$, λ is the wavelength of the radiation, μ_1 is the linear coefficient related to the imaginary part of the complex refractive index via $\mu_1 = 4\pi\beta_1/\lambda$, $I(\mathbf{r}_\perp, z = d)$ is the intensity of the PBI image measured at a propagation distance d along the z-direction from the sample's exit surface plane to the detector plane and I_0 is the incident intensity. Equation (1) is only valid for the near-field approximation, that is, the propagation distance d is small enough such that the Fresnel number $N_F = \ell^2/\lambda d$ (where ℓ is the characteristic transverse length scale of the object's exit surface wave-field) is much larger than unity (Saleh and Teich 1991). Further assumptions, required for the validity of the above equation, include (i) the projection approximation, (ii) normally incident coherent plane-wave illumination and (iii) paraxiality of the exit-surface wavefield.

When applied to spatially quantized objects, whose three-dimensional complex refractive index takes on one of a series of distinct values, equation (1) will of course not correctly reconstruct the projected thickness of a given specific material. However, this problem can be alleviated when relative differences for μ and δ, corresponding to any pair of materials (i.e. a material–material interface), are incorporated into the equation. Thus, when a tilt series (i.e. a tomographic dataset of sample angular orientations) of the resulting retrieved 'projected thickness' maps are tomographically reconstructed, the reconstruction corresponding to the specified interface will be accurately obtained, superposed with a three-dimensional signal corresponding to the 'other' material interfaces that only locally pollute the boundary of the region containing the pair of materials of interest. This method was implemented for quantized ternary samples (containing two homogeneous materials plus voids) by Beltran *et al* (2010), for which we provide a brief review of the relevant theory and approximations.

If a medium of interest denoted by 'j' is embedded within a medium denoted as '1', their respective projected thicknesses are given by $T_j(\mathbf{r}_\perp)$ and $T_1(\mathbf{r}_\perp)$. $T_j(\mathbf{r}_\perp)$ can then be calculated using (Beltran *et al* 2010):

$$T_j(\mathbf{r}_\perp) = -\frac{1}{\mu_j - \mu_1} \log_e \left(\mathbf{F}^{-1} \left\{ \frac{1}{[d(\delta_j - \delta_1)/(\mu_j - \mu_1)]\mathbf{k}_\perp^2 + 1} \mathbf{F} \left\{ \frac{I(\mathbf{r}_\perp, z = d)}{I_0 \exp[-\mu_1 A(\mathbf{r}_\perp)]} \right\} \right\} \right) \tag{2}$$

for each projection; one can then run the resulting thickness maps through a conventional tomographic reconstruction algorithm, such as filtered backprojection. For the same reasons as

mentioned in the previous paragraph, equation (2) will not reconstruct the projected thickness of each member of the tilt series, but it will correctly reconstruct the three-dimensional distribution of interfaces between a given pair of distinct materials, with only local pollution of the nature previously described. Note also that equation (2) was derived under the assumption that the phase gradients imparted on the incident wavefield due to the object's total projected thickness, $A(\mathbf{r}_\perp)$, are slowly varying. Utilizing equation (2) requires *a priori* knowledge of $A(\mathbf{r}_\perp)$ in addition to the values δ_j, δ_1 and μ_j, μ_1 corresponding to the different materials in the object. In practice, to generate the function $A(\mathbf{r}_\perp)$ to reconstruct an object of a high degree of complexity, and which contains no internal voids, one can use techniques such as laser profilometry (Myers *et al* 2008a). In the case of tomographic studies, a more practical approach to obtain $A(\mathbf{r}_\perp)$ for each projection angle can be used. By applying equation (1) to each PBI image, the encasing material can first be tomographically reconstructed. Then, both internal and external voids can be located by computationally searching for a predefined threshold in each slice of the reconstructed volume, and thus $A(\mathbf{r}_\perp)$ may then be calculated for each projection angle. We also mention that for point source illumination, image magnification in equations (1) and (2) needs to be accounted for (see e.g., Kitchen *et al* 2008).

A benefit of equations (1) and (2) is their high degree of numerical stability, due to the fact that the images are smoothed by a low-pass Fourier space filter during the initial part of the phase retrieval process. This smoothing, via the phase-retrieval integral transform represented by equations (1) and (2), leads to a concomitant reduction in high-frequency noise in the images, thereby improving the SNR without blurring the boundaries between interfaces. This gain in the SNR can potentially be traded against an equivalent x-ray dose reduction.

3. Method

3.1. Image acquisition

High-resolution x-ray phase-contrast images were acquired in hutch 3 of beamline 20B2 at the SPring-8 synchrotron radiation source, Japan (Goto *et al* 2001). The large source-to-object distance ($\sim$210 m) and the Si(1 1 1) double-crystal monochromator provided a near planar x-ray beam. We used 24 keV x-rays to provide strong phase and attenuation contrast of the biological specimens used here (see Kitchen *et al* 2008, Beltran *et al* 2010), which included the thorax of a newborn New Zealand white rabbit pup and the excised brain of an adult Sprague Dawley rat. The beam size was collimated to be approximately 30 mm wide and 30 mm high, which was large enough to illuminate each sample. A 4000 $\times$ 2672 pixel Hamamatsu CCD camera (C9300-124F) with a 1.8:1 ratio fibre optic taper, having an effective pixel size of 16.2 μm, was used to collect the tomographic tilt series of propagation-based x-ray phase-contrast images (see figure 1).

For imaging the rabbit pup thorax, the detector was positioned a distance $d = 50$ cm from the object. This relatively small sample-to-detector propagation distance was sufficient to render visible strong phase-contrast fringes from the air–tissue interfaces within the lung at this energy (see, e.g., Suzuki *et al* 2002, Beltran *et al* 2010). A total of 1500 projections were collected over 180° of rotation, with each having an exposure time of 250 ms. Flat field images (with no object in the beam) were recorded at the start and end of each scan to normalize the image intensity. Dark field images were also collected to correct for the detector's dark current offset.

The same setup was used for imaging the rat brain as for the rabbit pup thorax with the exception of the object-to-detector distance, which was set to 5.0 m. A large propagation distance was required to increase the phase contrast between the materials within the sample

Table 1. Values of δ and μ at 24 keV x-rays for water (soft-tissue equivalent) and cortical bone tissue. These were calculated using the NIST database[7].

Material	δ ($\times 10^{-7}$)	μ (m^{-1})
Water (lung tissue equivalent)	3.992	54.9
Bone tissue	7.145	461.1

Table 2. Values of δ and μ at 24 keV x-rays for grey/white matter and agar. These were calculated using the NIST database[7].

Material	δ ($\times 10^{-7}$)	μ (m^{-1})
Grey/white matter	4.842	56.3
Agar	3.432	40.2

due to the highly similar refractive indices of the materials (namely grey and white brain matter) within the sample. A total of 1800 tomographic projections were acquired with an exposure time of 2.5 s each.

We note that the large number of projections used here is required for adequate sampling of the tomographic reconstruction, to adequately resolve the phase-contrast fringes which typically have maxima separated by 50–100 μm. Although a considerably lower dose could be achieved using larger pixels with fewer projections, we chose to maximize the phase sensitivity of these applications to take advantage of the high resolution of the camera. The exposure time for the thorax was kept short relative to that of the brain in order to minimize potential motion artefacts introduced by movement of the tissues during the scan.

3.2. Image processing

For the selected energy (24 keV), the δ and μ values for lung tissue and cortical bone are listed in table 1. The δ and μ values considered to be present in the agar-embedded brain sample are listed in table 2. According to the NIST database (http://www.nist.gov/index.html), grey and white matter (the main tissue types present in the brain) are virtually identical in reference to diagnostic energy x-ray interactions and are herein treated as identical. We justify this statement by reference to equations (1) and (2) where we see that it is the ratio of the real and imaginary components of the refractive indices, or the difference ratio (see equation (2)), that is important for the Fourier filtering by the phase retrieval algorithms. Figure 2 illustrates this point by comparing the four Fourier-space filters used in this research. Distinct differences can be seen for the lung tissue/air interface filter against those of the brain tissue/agar and bone/lung tissue interfaces. Remarkably, the agar/air filter is almost identical to the brain tissue/agar filter despite the interfaces having very different density gradients, which arises because the ratio of δ to μ is nearly identical for brain tissue and agar (see table 2). Therefore, either filter (equation (1) or (2)) can be applied with essentially the same results.

Since equations (1) and (2) involve ratios of δ and μ, concerns regarding sample inhomogeneity can be partly allayed. Both δ and μ are proportional to the density of a given material; hence, their ratio in equation (1) will be independent of changes in density for a given material. The same holds true for equation (2) when the density of material 'j' and that

---

[7] http://www.nist.gov/index.html (accessed 4 April and 10 November 2010).
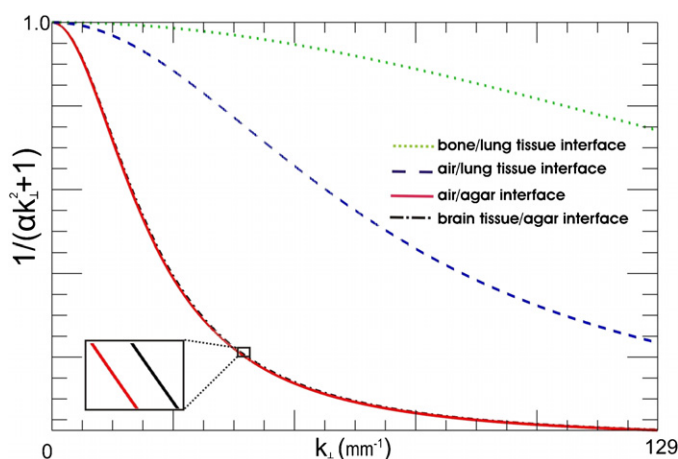
Figure 2. Fourier filters of the form $1/(\alpha \mathbf{k}_\perp^2 + 1)$ for different ratios of $\alpha = d\delta/\mu$ or $\alpha = d\Delta\delta/\Delta\mu$ (see equations (1) and (2)). The dashed line corresponds to the ratio used for the air/lung tissue interface, $\alpha = d\delta_{\text{water}}/\mu_{\text{water}}$ with $d = 50$ cm. The dotted line corresponds to the ratio used for the bone/lung tissue interface, $\alpha = d(\delta_{\text{bone}} - \delta_{\text{water}})/(\mu_{\text{bone}} - \mu_{\text{water}})$ with $d = 50$ cm. The solid line corresponds to the ratio used for the air/agar interface, $\alpha = d\delta_{\text{agar}}/\mu_{\text{agar}}$, with $d = 5$ m, and the dashed-dotted line corresponds to the ratio used for the brain tissue (grey/white matter; denoted 'gw')/agar interface, $\alpha = d(\delta_{\text{gw}} - \delta_{\text{agar}})/(\mu_{\text{gw}} - \mu_{\text{agar}})$ with $d = 5$ m. The magnified inset is used to illustrate the minute difference between filters for brain tissue/agar and air/agar, respectively.

of material '1' are equal. Moreover, variations in density of a few per cent of either material will typically have little effect on the shape of the filter in equation (2). It is therefore a valid approximation to employ a single filter for a given interface despite small density variations in inhomogeneous samples.

3.3. Animal procedures

All animal procedures were approved by the Monash University Animal Ethics Committee and the SPring-8 Animal Care and Use Committee. A pregnant New Zealand white rabbit at 31 days of gestation was anaesthetized by intravenous injection of propofol (Rapinovet; 12 mg kg^{-1} bolus, 40 mg h^{-1} infusion). The pup was delivered by caesarean section and then humanely killed via anaesthetic overdose. Following death, an endotracheal tube was inserted via a tracheotomy into the mid-cervical trachea and connected to a custom-designed ventilator (Kitchen *et al* 2010). The pup was placed in a water-filled cylindrical plethysmograph made of Perspex. The head of the pup was located outside the chamber and a thin rubber diaphragm formed a seal around its neck. Once correctly placed in the plethysmograph, the lungs were inflated with air and inflation was maintained by the application of a constant airway pressure of 25 cmH$_2$O, as was required to keep the terminal airways inflated.

The rat was humanely killed via an overdose of sodium pentothal (100 mg/kg, i.p.) and then transcardially perfused with heparinized 0.1 M phosphate buffered saline (PBS) followed by 4% paraformaldehyde (PFA) in 0.1 M PBS. The brain was carefully removed from the skull and postfixed overnight in 4% PFA/0.1M PBS. The brain was then serially dehydrated in increasing concentrations of sucrose (up to 30%) in 4% PFA. The fixed brain was next suspended inside a 2.6 cm diameter plastic specimen container containing warm 2% gel agar
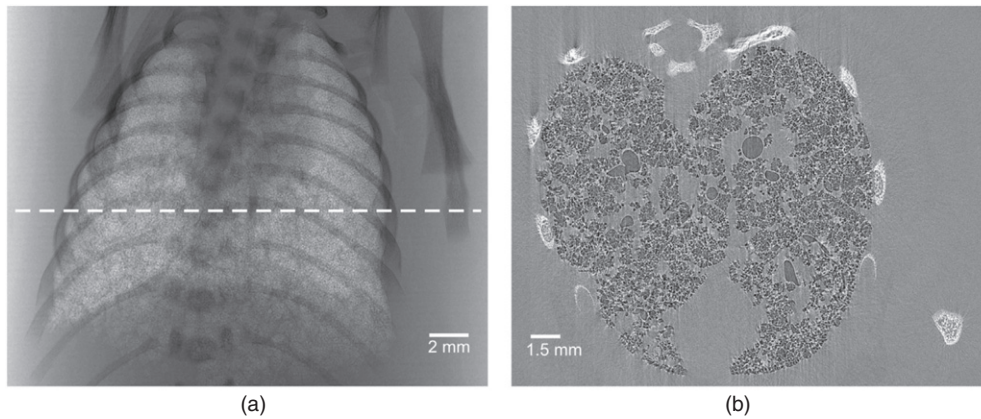
Figure 3. (a) Propagation-based x-ray phase-contrast image of the lungs of a preterm rabbit pup. X-ray energy = 24 keV, propagation distance = 50 cm. (b) Tomographic reconstruction of a single slice (see the dashed line in (a)) from the raw phase-contrast images utilizing filtered backprojection.

diluted with 4% PFA. After the agar hardened, the container was refrigerated until imaging. After synchrotron imaging was complete, the brain was extracted from the agar and sectioned in the coronal plane (50 μm thickness) using a cryostat. Alternating brain sections were stained for Nissl substance (which densely stains the rough endoplasmic reticulum in neuronal cell bodies) and used to locate anatomical landmarks in the propagation-based x-ray phase-contrast images. Anatomical localization was performed with the aid of the stereotaxic atlas of Pellegrino *et al* (1979).

4. Results and discussion

4.1. Chest imaging

A single PBI image of the tomographic data set is shown in figure 3(a). Even with the relatively small object-to-detector distance, the bulk of the lung tissue is rendered visible as a speckled intensity pattern as a result of multiple refraction of the x-ray beam through minor airways that overlap in projection (Kitchen *et al* 2004).

By applying filtered backprojection (Kak and Slaney 1988) using a ramp (Ram-Lak) filter directly to the phase-contrast images, without performing phase retrieval (Cloetens *et al* 1997), we obtain a qualitative reconstruction of the thorax as shown in figure 3(b). Here, the phase-contrast fringes formed at the edges between the interfaces (i.e. air/lung and bone/lung tissues) are seen in the reconstruction as residual phase-contrast fringes in the tomogram. We note that slight motion artefacts are also evident due to difficulties in keeping the object stationary for the ∼7 min of scan time. The phase contrast can aid the visualization of features such as the major airways by highlighting their boundaries. However, the edge enhancement can obscure finer features and restricts quantitative analysis of the tissue morphology (Suzuki *et al* 2002). To perform interface-specific phase retrieval tomography, we apply equations (1) and (2) to each tomographic image followed by filtered backprojection. Depending on which interface one wishes to focus on, the corresponding δ and μ or $\Delta\delta = \delta_2 - \delta_1$ and $\Delta\mu = \mu_2 - \mu_1$ are input into equations (1) and (2), respectively. Here we denote $j = 2$ as the bone/lung tissue interface.
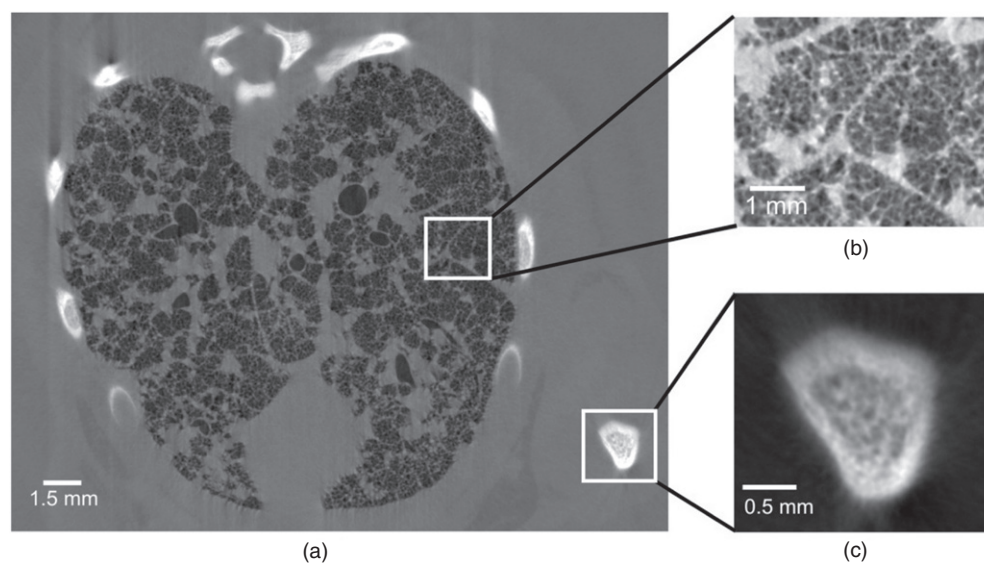
Figure 4. (a) Interface-specific tomographic reconstruction of a preterm rabbit pup thorax, focusing on the air/lung tissue interface. (b) Magnified section of (a) to aid visibility of the terminal airways. (c) Magnified section of (a) in which the bone/lung tissue interface appears blurred as a result of the chosen phase retrieval filter.

In our analysis, we consider lung tissue to be the encasing material. Therefore, to focus in on the air/lung tissue interface, we apply equation (1) to each tomographic image. Here, the δ and μ values for water were inserted into equation (1) as soft tissues and water have similar refractive and absorptive properties at the selected x-ray energy (Kitchen *et al* 2008). A tomographic reconstruction that focuses on the air/lung tissue interface is shown in figure 4(a). This image illustrates that the phase-contrast fringes have been removed, leaving the air/lung tissue interfaces sharply reconstructed, while we can also see that the bone/lung tissue interface has been locally blurred as a result of incorrect choices of δ and μ in the phase retrieval process, which contaminates the local vicinity surrounding this interface (Beltran *et al* 2010). Figure 4(b) shows a zoomed-in region of figure 4(a) in which individual terminal airways (alveoli) are clearly visible.

An important benefit of the phase-retrieved reconstruction (figure 4) is the dramatically improved SNR over the raw tomographic dataset (figure 3(b)). Using three 50×50 pixel regions containing soft tissue only, an SNR of 30 ± 6 (mean $\pm$ standard deviation) was calculated. By comparison, the same area in the raw reconstruction yielded just 1.8 ± 0.3. Here, we used the formula SNR $= \tilde{\mu}/\sigma$, where $\tilde{\mu}$ is the mean signal and σ is the standard deviation of voxels in the subarray. However, since no pure absorption-contrast image could be collected due to the finite object-to-detector distance, the latter SNR value was calculated in a region of figure 3 where only absorption-contrast signal exists (i.e. away from residual phase-contrast fringes). Thus, we found an improvement in the soft-tissue SNR of 16 ± 4 fold over absorption contrast for our particular experimental setup. This same improvement in the SNR was also observed (within uncertainties) in the large airspaces (bronchioles). It is not surprising that the noise was so heavily reduced since the phase retrieval algorithms naturally suppress the high-frequency noise.

Employing phase contrast with an appropriate phase retrieval algorithm has enabled us to clearly visualize the terminal airways. Whilst similar data may have been obtained from absorption-contrast tomography, for instance by decreasing the average energy to increase the soft-tissue absorption contrast, the corresponding dose increase would be prohibitive. This has important implications for studying the health of the lungs and other organs. Emphysema, for example, is a disease of the distal airways that is characterized by the loss of alveolar structures. The ability to clearly observe these fine structures could lead to improved diagnosis of early lung disease. We have used this dataset to measure the range of alveolar dimensions found within this animal. The diameters of the alveoli were measured to be between 109 and 162 μm, which is consistent with the previously measured values found in a rabbit pup model (Hooper *et al* 2007). We further demonstrate the fidelity of the reconstruction in the online supplementary movie (available at stacks.iop.org/PMB/56/7353/mmedia) that takes us into the airway tree of the pup, with remarkable clarity all the way to the terminal airsacs (alveoli). This movie was made using commercial software (Amira v 5.2, Visage Imaging, Inc.) upon thresholding the image stack such that the airways were transparent and the tissues opaque.

To retrieve quantitative information from the in-focus interface, a line profile across a major airway shown in figure 5(a) is plotted in figure 5(b). Here the distribution of the refractive index decrement averages around the expected value listed in table 1. Also, a line profile is plotted across the magnified (blurred) bone feature seen in figure 5(c), which helps us to observe the over-smoothing of the bone/soft-tissue interface and the quantitatively incorrect reconstruction of δ (see table 1).

We note here that other soft tissues can be seen as amorphous shapes surrounding the chest wall in the phase retrieved reconstruction in figure 4(a). These tissues are more evident than in the raw reconstruction in figure 3(b). We attribute this increased clarity to the shape of the Fourier filter required for the lung tissue/air interface used in equation (1) being likely very similar to that used in equation (2) that would be used to focus on soft-tissue interfaces.

To focus on the bone/lung tissue interface, we instead process every image with equation (2) before tomographically reconstructing each slice. To apply this equation, we use the δ and μ values for bone as well as those for water together with *a priori* knowledge of the total projected thickness $A(\mathbf{r}_\perp)$. $A(\mathbf{r}_\perp)$ is required to determine the attenuation that the object would provide if it were made entirely of a single homogenous material, which is used in the normalization term $I_0 \exp[-\mu_1 A(\mathbf{r}_\perp)]$ of equation (2). Here we have approximated the normalization term by fitting a parabolic curve to the intensity profile at each projection. This only works well since the animal was inside a water-filled cylinder and because the lungs are approximately circular in projection and were located near the centre of the tube. Although this approximation will reduce the accuracy of the reconstruction, we see no artefacts in the resulting reconstruction, justifying its use.

In figure 6(a), a tomographic reconstruction of the same slice as in figures 3(b) and 4(a) is shown, which now focuses on the bone/lung tissue interfaces. From this image, we see that the interfaces of interest have now been correctly reconstructed, yielding a sharp boundary between the media. This can be better appreciated in figure 6(b), which shows the same zoomed-in region as in figure 4(c) but now the boundaries and features are highly visible. Additionally, the line profile in figure 6(c) shows the quantitative measure of the refractive index decrement, δ. The large fluctuations in δ arise from the porosity of the bone, but the maximum value underestimates the expected value from table 1. We believe that this discrepancy arises because the tabulated values are calculated for mature, fully calcified bone, whilst the immature bones of the newborn rabbit will differ considerably in their average density and composition (i.e. not be fully calcified), compared to those of an adult rabbit, thereby lowering the measured δ value.
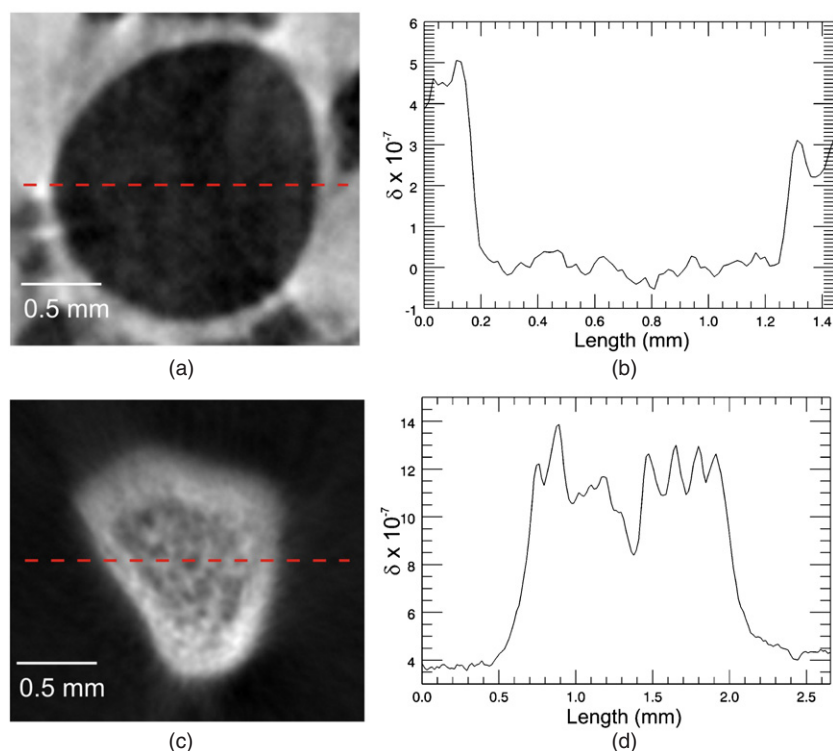
Figure 5. (a) Magnified region of figure 4(a) showing a major airway. Its line profile is plotted from left to right from the centre of the image and is shown in (b) displaying the distribution of its refractive index decrement. (c) The same image as in figure 4(c) with its line profile shown in (d).

To compare the improvement in the SNR before and after the phase retrieval for the bone/tissue interface, we observed the cortical bone (outer edge) of the bone segment seen in figure 6(c). The cortical bone contains fewer pores than the internal trabecular bone and enables comparison against the raw image far from phase-contrast fringes (i.e. a measure of approximately pure attenuation by bone). We measured the mean signal within small areas of cortical bone and measured the noise from the nearby soft tissue that was also free of phase-contrast effects. For bone, the SNR in the raw 'absorption-contrast' image was only 5 ± 1 compared to the same area in the phase retrieved image with an SNR of 47 ± 12. On average, we found an improvement in the SNR of 9 ± 3 times afforded by phase retrieval. Whilst this is less than the improvement seen for the soft-tissue reconstruction, this results from the reduced level of spatial filtering in equation (2) due to the reduced phase gradients present at the bone/tissue interface compared to the air/tissue interface.

Finally, we draw attention to the air/lung tissue interfaces in figure 6(a), which have now been over-sharpened, or insufficiently filtered, by the phase retrieval process resulting from under-compensation of the phase-contrast fringes. Therefore, the air/tissue interfaces have been incorrectly reconstructed.

Upon reconstructing all interfaces of interest, we now combine the images in figures 4(a) and 6(a) to compose a spliced reconstruction (figure 7). To produce the spliced image, one cannot simply manually insert the appropriate region into the corresponding regions of another image. We began by using the soft-tissue image (figure 4) and exploited the fact that the relatively highly attenuating bones appear blurred, realizing that the true bone interfaces
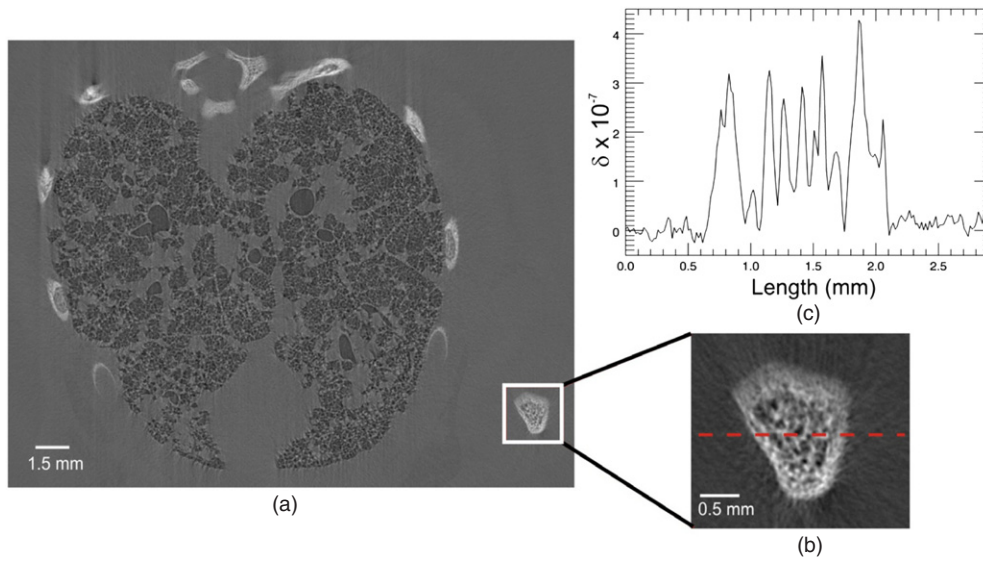
Figure 6. (a) Interface-specific tomographic reconstruction of a preterm rabbit pup thorax, focusing on the bone/lung tissue interface. (b) Magnified section of (a) which now shows a sharp and quantitative reconstruction of the same images seen in figures 4(c) and 5(c). (c) Line profile from left-to-right across the centre of (b) showing the distribution of the refractive index decrement of the porous bone.

must lie within those blurred regions. The large contrast enabled the image to be thresholded until the blurred bones were invisible, thereby creating a binary 'soft-tissue-only' mask. The inverse of this mask was then applied to the image containing the correctly reconstructed bones (figure 6). By smoothing each binary mask, and ensuring both masks summed to unity before multiplying with the relevant image, a continuous and smooth spliced image was formed by adding the masked images together. One additional step involved adjusting any offsets so that the background encasing material had the same average value in each image before creating the spliced image.

The spliced image shows all interfaces both quantitatively and sharply reconstructed, which demonstrates the key result that we are able to perform phase and amplitude tomography of multi-material objects that are spatially quantized with only one PBI image per tomographic orientation.

One drawback of our image splicing is that the objects in question should be spatially separated by an amount equal to the bleeding (pollution length) associated with over-smoothing the second interface. In Beltran *et al* (2010), it was shown that this bleed width (Δx) depends only on the refractive index of the encasing material, where $\Delta x \geqslant \sqrt{d\delta_1/\mu_1}$. It was experimentally verified that a distance of three to five times Δx was sufficient to avoid locally polluting nearby objects of a different refractive index. For our experiment, this distance should therefore be at least 180 μm, but no more than 300 μm. This reduces the accuracy of the reconstruction where the bone encroaches on the airways. Fortunately, we see very little evidence of the contamination between media in the spliced reconstruction of figure 7.

4.2. Brain imaging

Figure 8(a) shows a single PBI image from the CT dataset of a rat brain prepared as described in section 3.3. Due to the similar complex refractive indices of brain and agar (table 2), the

Figure 7. Spliced tomographic reconstruction of preterm rabbit pup lungs, constructed by splicing figures 4(a) and 6(a).

brain is not visible in a single projection image even with the very long propagation distance of 5.0 m. However, if we apply filtered backprojection directly to the set of raw PBI brain images (figure 8(b)), a small amount of anatomical detail becomes visible and structures are resolved relative to the gel agar matrix. This is principally due to the averaging effect caused by acquiring images from multiple projections which improves the SNR. Figure 8(b) shows a single tomographic slice in a para-frontal orientation at an approximate anterior–posterior distance of 9.4 mm caudal to bregma. The bright white flares seen in the image are possibly caused by attenuation due to Bragg diffraction from crystallite regions in the agar matrix.

Phase retrieval was then applied before performing the tomographic reconstruction. As described above, all materials in the brain sample effectively refract and attenuate x-rays to a similar degree; hence, the sample behaves somewhat like a single-material object and thus we need to utilize equation (1) only (see figure 2). We used the δ and μ values for grey/white matter listed in table 2. The same slice in figure 8(b) is shown in figure 9, now with the phase retrieval process included. Despite the subtle differences in complex refractive index, the tomogram yields clearly demarcated tissue borders at the grey/white matter boundaries. Considerable detail can be seen in the brainstem, including the ventral cochlear nucleus (vCN), spinal tract of the trigeminal nerve (TST) and inferior cerebellar peduncle (iCP).

SNR values were calculated for six 30×30 pixel regions of grey or white matter in both figures 8(b) and 9 yielding values of 2.1 ± 0.2 and 440 ± 120, respectively. Again we note that the regions selected for the calculations did not contain any phase-contrast signal. For brain imaging with this geometry, we found a net gain in the SNR of 200 ± 50 over absorption contrast. This exceptional improvement is a consequence of the relatively large propagation distance of 5.0 m used to render the brain visible, which translates to heavy spatial filtering (see figure 2) and associated strong noise suppression in the phase retrieval step (equation (1)); this effect was also discussed by Arhatari *et al* (2010). Note that if one were to use too large a propagation distance, the validity conditions of the underlying transport-of-intensity equation would be violated.

(a)   (b)
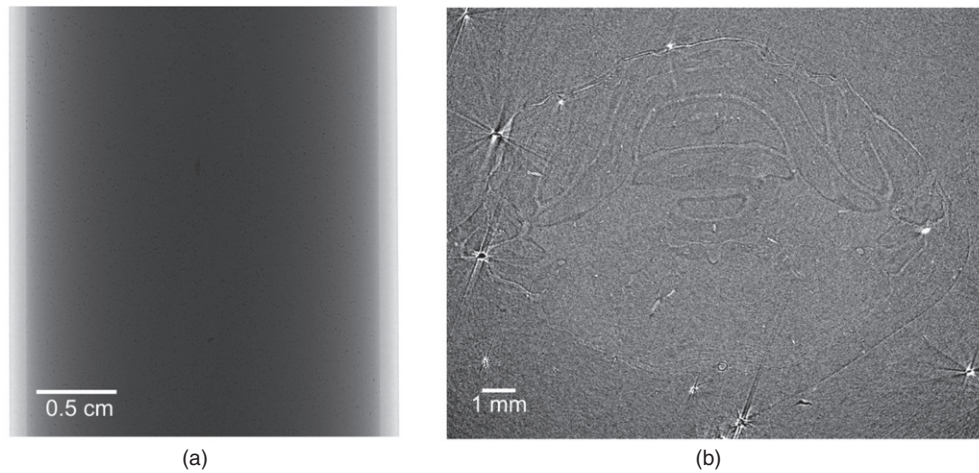
Figure 8. (a) PBI image of an excised rat brain submerged in an agar solution. X-ray energy $= 24$ keV, propagation distance $= 5.0$ m. (b) Tomographic reconstruction of a single slice from the raw brain PBI images using filtered backprojection.
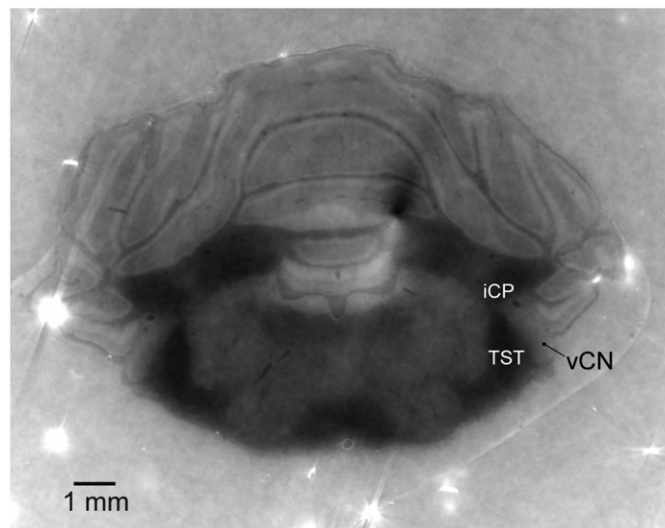
Figure 9. Tomographic reconstruction of the same slice as shown in figure 8(b). Equation (1) was applied to each image before tomographically reconstructing.

Phase-contrast modalities that are more sensitive to weak phase gradients, such as grating interferometry, can render visible the tissues of the brain with even higher contrast than that presented above (Pfeiffer *et al* 2007). However, the extra sensitivity of such methods makes them less robust for imaging objects that also contain strong phase gradients such as the air/soft-tissue boundaries within the lung. Moreover, phase retrieval in that context requires multiple images to be acquired for every projection (Pfeiffer *et al* 2007), thereby significantly increasing the x-ray dose to the sample. The benefits of our approach include the simple imaging geometry, with no requirement for post-sample optical elements, and only a single exposure per projection required for phase retrieval.

5. Future work

A key finding of this study was that the single-material phase retrieval algorithm (equation (1)) was sufficiently suitable for the sample containing brain tissue (containing both grey and white matter) in agar. This considerably simplified and sped up the analysis as only a single tomographic reconstruction was required. It remains to be seen whether other material combinations, including soft tissues, can be analysed in the same way. For example, it may be valid to make the single-material approximation in a sample exclusively comprised of soft tissues. It also remains to be seen whether a clear image of the brain can be reconstructed when the brain is *in situ*, inside the skull, using either phase retrieval algorithm.

With a view to ultimately applying our method to laboratory-based PBI using polychromatic radiation (e.g., Wilkins *et al* 1996), it would be very useful to generalize it to a polychromatic spectrum. This will be a stepping stone allowing the technique to be used for routine biomedical imaging, with potential clinical implications since PBI is already being used in the clinic for breast imaging (Tanaka *et al* 2005). We note that several groups have made inroads into the problem of phase retrieval using polychromatic radiation in the contexts of both two- and three-dimensional imaging (Arhatari *et al* 2005, Myers *et al* 2007).

Also, we note that spatially quantized objects are in some sense sparse, insofar as the interfaces between the various volumetric regions of the object are intrinsically two-dimensional surfaces. No attempt has been made to utilize this sparseness in this paper. Progress has been made in using the intrinsically sparse nature of spatially quantized objects in the context of phase retrieval in the work of Myers *et al* (2008a, 2008b, 2010) and the work on gradient-sparse objects by Sidky *et al* (2010). Furthermore, the burgeoning field of compressive sensing (Baraniuk 2007) has also made inroads into the tomography of sparse objects, albeit via a different form of sparsity in which the majority of features in the object are confined to a small fraction of the volume occupied by the object. It might be interesting to investigate whether these methods of compressive sensing may be adapted to spatially quantized objects, in which the volume occupied by *interfaces* is sparse (cf Sidky *et al* 2010). In this context, the concept of a quasi-one-dimensional object, developed by Gureyev and Evans (1998), might also prove useful. A particular driver is the quest to reduce the number of required projections (and therefore the dose to the sample) by making use of the sparseness of interface-occupying voxels in a typical spatially quantized object.

6. Conclusions

We have demonstrated that interface-specific x-ray phase retrieval tomography, using the method developed by Beltran *et al* (2010), can be performed on complex biological objects. The method makes use of only a single PBI image per tomographic orientation and requires *a priori* information of the sample's total projected thickness at each orientation and knowledge of each material's complex refractive index present in the sample. Note that for a sample containing no internal voids, the total projected thickness at each orientation is completely determined by knowledge of the surface of the object. The method was successfully implemented on experimental propagation-based phase-contrast tomographic data of the thorax and brain of small animals collected using x-ray synchrotron radiation. For the thorax data, quantitative reconstructions of air/lung tissue and bone/lung tissue interfaces were performed separately and were then spliced together to yield a complete reconstruction. A tomographic reconstruction of a rat brain was made under the assumption that it comprised of a single material of variable density, which resulted in an image able to clearly distinguish between grey and white matter. SNR calculations were carried out and showed our technique

to be superior to conventional absorption contrast by factors ranging from 9 to 200 fold. This gain depended on the material in question and the experimental setup, but can potentially be traded against a reduction in x-ray dose. This enhances the dose reduction already made over other implementations of phase retrieval since only a single image per projection is required. Given these results, combined with the simplicity of our technique, we anticipate that it will potentially be a useful tool in the field of biomedical x-ray imaging.

Acknowledgments

References

Anastasio M A and Pan X 2000 Computationally efficient and statistically robust image reconstruction in three-dimensional diffraction tomography *J. Opt. Soc. Am.* A **17** 391–400

Anastasio M A, Shi D, De Carlo F and Pan X 2004 Analytic image reconstruction in local phase-contrast tomography *Phys. Med. Biol.* **49** 121–44

Arhatari B D, Gates W P, Eshtiaghi N and Peele A G 2010 Phase retrieval tomography in the presence of noise *J. Appl. Phys.* **107** 034904

Arhatari B D, Nugent K A, Peele A G and Thornton J 2005 Phase contrast radiography: II. Imaging of complex objects *Rev. Sci. Instrum.* **76** 113704

Baraniuk R G 2007 Compressive sensing *IEEE Signal Process. Mag.* **24** 118–21

Beltran M A, Paganin D M, Uesugi K and Kitchen M J 2010 2D and 3D x-ray phase retrieval of multi-material objects using a single defocus distance *Opt. Express* **18** 6423–36

Bronnikov A V 2002 Theory of quantitative phase-contrast computed tomography *J. Opt. Soc. Am.* A **19** 472–80

Cloetens P, Barrett R, Baruchel J, Guigay J-P and Schlenker M 1996 Phase objects in synchrotron radiation hard x-ray imaging *J. Phys. D: Appl. Phys.* **29** 133–46

Cloetens P, Ludwig W, Baruchel J, van Dyck D, van Landuyt J, Guigay J P and Schlenker M 1999 Holotomography: quantitative phase tomography with micrometer resolution using hard synchrotron radiation x-rays *Appl. Phys. Lett.* **75** 2912–4

Cloetens P, Pateyron-Salomé M, Buffière J Y, Peix G, Baruchel J, Peyrin F and Schlenker M 1997 Observation of microstructure and damage in materials by phase sensitive radiography and tomography *J. Appl. Phys.* **81** 5878–86

Förster E, Goetz K and Zaumseil P 1980 Double crystal diffractometry for the characterization of targets for laser fusion experiments *Krist. Tech.* **15** 937–45

Goto S *et al* 2001 Construction and commissioning of a 215 m-long beamline at SPring-8 *Nucl. Instrum. Methods* A **467** 682–5

Guigay J P, Langer M, Renaud B and Cloetens P 2007 Mixed transfer function and transport of intensity approach for phase retrieval in the Fresnel region *Opt. Lett.* **32** 1617–9

Gureyev T E and Evans R 1998 An extension of quasi-one-dimensional tomography *Appl. Opt.* **37** 2628–36

Gureyev T E, Nesterets Y I and Mayo S C 2007 Quantitative quasi-local tomography using absorption and phase contrast *Opt. Commun.* **280** 39–48

Gureyev T E and Nugent K A 1996 Phase retrieval with the transport-of-intensity equation: II. Orthogonal series solution for nonuniform illumination *J. Opt. Soc. Am.* A **13** 1670–82

Gureyev T E and Nugent K A 1997 Rapid quantitative phase imaging using the transport of intensity equation *Opt. Commun.* **133** 339–46

Gureyev T E, Paganin D M, Myers G R, Nesterets Y I and Wilkins S W 2006 Phase-and-amplitude computer tomography *Appl. Phys. Lett.* **89** 034102

Hooper S B *et al* 2007 Imaging lung aeration and lung liquid clearance at birth *FASEB J.* **21** 3329–37

Irvine S C, Paganin D M, Dubsky W, Lewis R A and Fouras A 2008 Phase retrieval for improved three-dimensional velocimetry of dynamic x-ray blood speckle *Appl. Phys. Lett* **93** 153901

Kak A C and Slaney M 1988 *Principles of Computerized Tomographic Imaging* (New York: IEEE)

Kitchen M J *et al* 2008 Dynamic measures of regional lung air volume using phase contrast x-ray imaging *Phys. Med. Biol.* **53** 6065–77

Kitchen M J, Habib A, Fouras A, Dubsky S, Lewis R A, Wallace M J and Hooper S B 2010 A new design for high stability pressure-controlled ventilation for small animal lung imaging *J. Instrum.* **5** T02002

Kitchen M J, Paganin D, Lewis R A, Yagi N, Uesugi K and Mudie S T 2004 On the origin of speckle in x-ray phase contrast images of lung tissue *Phys. Med. Biol.* **49** 4335–48

Mayo S C, Davis T J, Gureyev T E, Miller P R, Paganin D, Pogany A, Stevenson A W and Wilkins S W 2003 X-ray phase-contrast microscopy and microtomography *Opt. Express* **11** 2289–302

McMahon P J, Peele A G, Paterson D, Lin J J A, Irving T H K, McNulty I and Nugent K A 2003 Quantitative x-ray phase tomography with sub-micron resolution *Opt. Commun.* **217** 53–8

Momose A, Takeda T, Itai Y and Hirano K 1996 Phase-contrast x-ray computed tomography for observing biological soft tissues *Nat. Med.* **2** 473–5

Myers G R, Gureyev T E, Paganin D M and Mayo S C 2008a The binary dissector: phase contrast tomography of two- and three- material objects from few projections *Opt. Express* **16** 16736–49

Myers G R, Mayo S C, Gureyev T E, Paganin D M and Wilkins S W 2007 Polychromatic cone-beam phase-contrast tomography *Phys. Rev.* A **76** 045804

Myers G R, Paganin D M, Gureyev T E and Mayo S C 2008b Phase-contrast tomography of single-material objects from few projections *Opt. Express* **16** 908–19

Myers G R, Thomas C D L, Paganin D M, Gureyev T E and Clement J G 2010 A general few-projection method for tomographic reconstruction of samples consisting of several distinct materials *Appl. Phys. Lett.* **96** 021105

Paganin D, Gureyev T E, Mayo S C, Stevenson A W, Nesterets Y A I and Wilkins S W 2004 X-ray omni microscopy *J. Microsc.* **214** 315–27

Paganin D, Mayo S C, Gureyev T E, Miller P R and Wilkins S W 2002 Simultaneous phase and amplitude extraction from a single defocused image of a homogeneous object *J. Microsc.* **206** 33–40

Paganin D and Nugent K A 1998 Noninterferometric phase imaging with partially coherent light *Phys. Rev. Lett.* **80** 2586–9

Pellegrino L J, Pellegrino A S and Cushman A J 1979 *A Stereotaxic Atlas of the Rat Brain* (New York: Plenum)

Pfeiffer F, Bunk O, David C, Bech M, Le Duc G, Bravin A and Cloetens P 2007 High-resolution brain tumor visualization using three-dimensional x-ray phase contrast tomography *Phys. Med. Biol.* **52** 6923–30

Pogany A, Gao D and Wilkins S W 1997 Contrast and resolution in imaging with a microfocus x-ray source *Rev. Sci. Instrum.* **68** 2774–82

Saleh B E A and Teich M C 1991 *Fundamentals of Photonics* (Toronto: Wiley)

Shi D, Anastasio M A and Pan X 2005 Reconstruction of refractive index discontinuities from truncated phase-contrast tomography projections *Appl. Phys. Lett.* **86** 034102

Sidky E Y, Anastasio M A and Pan X 2010 Image reconstruction exploiting object sparsity in boundary-enhanced x-ray phase-contrast tomography *Opt. Express* **18** 10404–22

Snigirev A, Snigireva I, Kohn V, Kuznetsov S and Schelokov I 1995 On the possibilities of x-ray phase contrast microimaging by coherent high-energy synchrotron radiation *Rev. Sci. Instrum.* **66** 5486–92

Stevenson A W, Mayo S C, Häusermann D, Maksimenko A, Garrett R F, Hall C J, Wilkins S W, Lewis R A and Myers D E 2010 First experiments on the Australian synchrotron imaging and medical beamline, including investigations of the effective source size in respect of x-ray imaging *J. Synchrotron Radiat.* **17** 75–80

Stock S R (ed) 2010 *Developments in X-Ray Tomography VII, Proc. SPIE* **7804** http://spie.org/x648.html?product_id=850961

Suzuki Y, Yagi N and Uesugi K 2002 X-ray refraction-enhanced imaging and a simple method for phase retrieval for a simple object *J. Synchrotron Radiat.* **9** 160–5

Tanaka T *et al* 2005 The first trial of phase contrast imaging for digital full-field mammography using a practical molybedenum x-ray tube *Invest. Radiol.* **40** 385–96

Teague M R 1983 Deterministic phase retrieval: a Green's function solution *J. Opt. Soc. Am.* **73** 1434–41

Turner D, Weber K P, Paganin D and Scholten R E 2004 Off-resonant defocus-contrast imaging of cold atoms *Opt. Lett.* **29** 232–4

Wilkins S W, Gureyev T E, Gao D, Pogany A and Stevenson A W 1996 Phase-contrast imaging using polychromatic hard x-rays *Nature* **384** 335–8

Wolf E 1969 Three-dimensional structure determination of semi-transparent objects from holographic data *Opt. Commun.* **1** 153–6

Appendix C

Aberrations in shift-invariant linear optical imaging systems using partially coherent fields.

by M. A. Beltran, M. J. Kitchen, and D. M. Paganin.

Aberrations in shift-invariant linear optical imaging systems using partially coherent fields

Mario A. Beltran,[1, *] Marcus J. Kitchen,[1] and David M. Paganin[1]

[1] *School of Physics, Monash University, Victoria 3800, Australia*

Here the role and influence of aberrations in optical imaging systems employing partially coherent complex scalar fields is studied. Imaging systems require aberrations to yield contrast in the output image. For linear shift–invariant optical systems, we develop an expression for the output cross–spectral density under the space–frequency formulation of statistically stationary partially coherent fields. We also develop expressions for the output cross–spectral density and associated spectral density for weak–phase, weak–phase–amplitude, and single–material objects in one transverse spatial dimension.

I. INTRODUCTION

When imaging transparent samples in an in-focus optical system such as a visible–light or x–ray microscope, the detected output image appears almost featureless if the system yields a reproduction of the input image that is incident upon the system [1]. This is what in optics is commonly defined as a perfect or near perfect imaging system in which there are no transverse spatial variations within the incident spectral density distribution as it propagates to the output detection plane. Note that the term "spectral density" is here used in the sense of optical partial coherence. As perfect systems are unable to visualize the refraction effects (phase contrast) caused by transparent samples, the presence of aberrations is a necessary condition for non–negligible contrast in the output spectral density to be attained [2]. In this context, an aberrated imaging system may be defined as one whose output transverse spatial distribution of spectral density is not equal to the input transverse spatial distribution of spectral density, up to transverse and multiplicative scale factors together with the smearing effects of finite resolution. Almost all aberrated imaging systems exhibit phase contrast, i.e. have an output spatial distribution of spectral density which is influenced by the functional form of the input wavefronts (input phase distribution). Examples of aberrated imaging systems yielding phase contrast include Zernike phase contrast, propagation–based phase contrast, differential phase contrast, inline holography, etc. [1, 3–5]

Work relating to a partially coherent treatment specifically for propagation–based phase contrast imaging based on the Transport–of–Intensity equation has been reported [6–8]. In this paper we consider the generalized differential phase contrast associated with aberrated linear shift–invariant optical imaging systems employing statistically stationary partially coherent scalar radiation, for which the output spatial distribution of spectral density (i.e., the output image) can be modelled using the transfer function formalism. This extends previously reported work by Paganin and Gureyev [2] which restricted

consideration to the generalized differential phase contrast of fully coherent scalar fields imaged using aberrated linear shift–invariant optical systems.

In Sec. II we obtain an equation that describes the action of shift–invariant linear systems using partially coherent fields, under the imaging assumption that the object under study is a pure thin phase object. A two–dimensional transverse Cartesian coordinate system is used in the derivation. In Sec. III expressions for the spectral density are derived, restricting consideration to only one transverse spatial variable for simplicity. Three different types of sample are considered: Samples that satisfy, i) the weak–phase object approximation, ii) the weak phase–amplitude approximation and; iii) the single material weak phase–amplitude approximation. Sec. IV studies in depth the features of the transfer function used in this formalism.

II. SHIFT–INVARIANT, LINEAR SYSTEMS FOR PARTIALLY COHERENT FIELDS USING TWO TRANSVERSE SPATIAL COORDINATES

In this section we derive an expression for partially coherent complex scalar fields imaged by an optical system that is shift–invariant and satisfies the property of linearity [10]. For such a system, the output complex disturbance is related to the input complex disturbance by the transfer function formalism [10]. Since most image collecting is normally done using two dimensional Cartesian grids it is natural to utilize a two–dimensional Cartesian system (x, y) in all calculations.

Before incorporating the effects of partial coherence in our derivations, we recall first a description of shift–invariant linear systems for fully coherent complex scalar wave–fields which are governed by the transfer function formalism. For such optical systems the output field $\Psi_{out}(x, y)$ is related to the input field $\Psi_{in}(x, y)$ by a Fourier–space filtration that can be written in operator form as [2]:

$$\Psi_{out}(x, y) = F^{-1} T(k_x, k_y) F \{\Psi_{in}(x, y)\}. \qquad (1)$$

Here, $T(k_x, k_y)$ is the transfer function characterizing the

* Corresponding author: ▮▮▮▮▮▮▮▮

optical system, (k_x, k_y) are Fourier conjugate coordinates dual to (x, y), F and F^{-1} respectively represent the forward and inverse Fourier transform operations, and all operators are taken to act from right to left. Thus, the above equation states that F is applied to the input field $\Psi_{in}(x, y)$, before multiplying by the transfer function $T(k_x, k_y)$ and then applying the operator F^{-1}, so as to yield the output field $\Psi_{out}(x, y)$ (see Fig. 1).
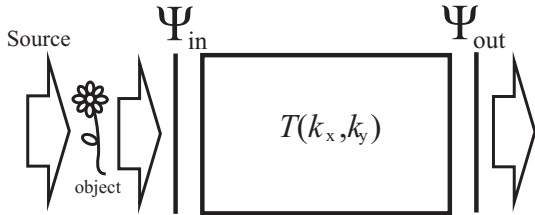

FIG. 1. Schematic illustration of the action of an aberrated shift–invariant linear optical system for imaging fully coherent complex scalar wave–fields, under the transfer function formalism. Input and output complex fields are related by the transfer function formalism according to Eq.(1).

In our derivation the forward and inverse Fourier transform operation conventions used are the following:

$$\widehat{G}(k_x, k_y) = \frac{1}{2\pi} \iint_{-\infty}^{\infty} dxdy \, G(x,y)e^{-i(k_x x + k_y y)}, \quad (2a)$$

$$G(x,y) = \frac{1}{2\pi} \iint_{-\infty}^{\infty} dk_x dk_y \widehat{G}(k_x, k_y)e^{i(k_x x + k_y y)}. \quad (2b)$$

Here, $\widehat{G}(k_x, k_y) \equiv F\{G(x,y)\}$.

To proceed further, we follow Paganin and Gureyev [2] and make the restricting assumption that the transfer function $T(k_x, k_y)$ is sufficiently well behaved for its logarithm to admit a Taylor–series representation. Note that a necessary condition for this assumption to be valid is that the transfer function does not possess any zeros over the patch of Fourier space for which the modulus of $F\{\Psi_{in}(x,y)\}$ is non–negligible, a region which may be termed the "essential spectral support" of the input field.

While this key assumption will fail for imaging systems such as Schlieren optics which completely block certain spatial frequencies in the essential spectral support of the input disturbance, the assumption will hold for a variety of important imaging systems such as out–of–focus contrast [3], inline holography [5], interferometric phase contrast [11], differential phase contrast [12], and analyzer–based phase contrast of weakly scattering samples [4] etc.

With the above in mind, our simplifying assumption allows us to express the transfer function in the classic form that is standard e.g. in transmission electron microscopy, namely [2, 13, 14]:

$$T(k_x, k_y) = \exp\left(i \sum_{m,n=0}^{\infty} \widetilde{\alpha}_{mn} k_x^m k_y^n \right). \quad (3)$$

Under this representation we denote the set of complex numbers $\{\widetilde{\alpha}_{mn}\}$ as the "aberration coefficients" where m and n are non–negative integers and label the order of the aberration. The real part of each such coefficient is termed a coherent aberration, with the corresponding imaginary part being termed an incoherent aberration. See Paganin and Gureyev [2] for a direct link between these complex aberration coefficients, and the Siedel aberrations [15] (e.g., piston, defocus, astigmatism, spherical aberration, chromatic aberration etc.) of classical aberration theory.

Expanding the complex exponential in Eq. (3) as a Taylor–series, we obtain:

$$T(k_x, k_y) = 1 + i \sum_{m,n=0}^{\infty} \alpha_{mn} k_x^m k_y^n. \quad (4)$$

The above expression serves to define the set of coefficients $\{\alpha_{mn}\}$. The set of coefficients $\{\alpha_{mn}\}$ is defined in terms of the set of aberration coefficients $\{\widetilde{\alpha}_{mn}\}$. We note that like Eq. (3), Eq. (4) disallows the presence of any zeros in the transfer function $T(k_x, k_y)$. This form is particularly useful for studying the effect of transfer functions which differ only slightly from unity, namely for weakly aberrated shift–invariant imaging systems. We shall pick up on this point later in the paper.

It is useful to write the operator form of Eq. (1) in terms of the following integral:

$$\Psi_{out}(x, y) = \frac{1}{2\pi} \iint_{-\infty}^{\infty} dk_x dk_y T(k_x, k_y) \, e^{i(k_x x + k_y y)}$$
$$\times \widehat{\Psi}_{in}(k_x, k_y), \quad (5)$$

where $\widehat{\Psi}_{in}(k_x, k_y)$ denotes the Fourier transform of $\Psi_{in}(x, y)$ with respect to x and y. The above integral–form expression describes the output wave–field for an optical system that is linear and shift–invariant for incoming wave–fields that are fully coherent.

We now turn to the extension of this theory of fully coherent fields to partially coherent fields. This corresponds to the generalization shown in Fig. 2. Here, W_{in} is the cross–spectral density incident upon a linear shift–invariant aberrated optical system, yielding the corresponding output cross–spectral density W_{out}.

Under the space–frequency description of partial coherence developed by Wolf [15, 16], the output cross–spectral density at a specified angular frequency ω may be constructed using an ensemble of strictly monochromatic fields all of the same angular frequency, via:
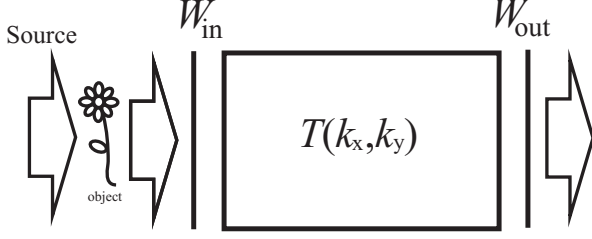
FIG. 2. Schematic illustration of the action of an aberrated shift–invariant linear optical imaging system, for statistically stationary partially coherent complex scalar fields, under the transfer function formalism. Input and output cross–spectral densities, W_{in} and W_{out} respectively, are related by the generalized transfer function formalism according to Eq. (8).

$$W_{out}(x_1, y_1, x_2, y_2) = \langle \Psi^*_{out}(x_1, y_1) \Psi_{out}(x_2, y_2) \rangle_\omega . \quad (6)$$

Here, angular brackets denote the ensemble average.

Putting this equation to one side for the moment, note that we can express $\Psi^*_{out}(x_1, y_1)$ and $\Psi_{out}(x_2, y_2)$ in terms of the Fourier transform of $\Psi^*_{in}(x_1, y_1)$ and $\Psi_{in}(x_2, y_2)$ respectively using the conventions in Eq. (2a) and (2b) which give the following:

$$\Psi^*_{out}(x_1, y_1) = \frac{1}{(2\pi)} \iint_{-\infty}^{\infty} dk_{x_1} dk_{y_1} T^*(k_{x_1}, k_{y_1})$$
$$\times e^{i^*(k_{x_1} x_1 + k_{y_1} y_1)} \widehat{\Psi}^*_{in}(k_{x_1}, k_{y_1}), \quad (7a)$$

$$\Psi_{out}(x_2, y_2) = \frac{1}{(2\pi)} \iint_{-\infty}^{\infty} dk_{x_2} dk_{y_2} T(k_{x_2}, k_{y_2})$$
$$\times e^{i(k_{x_2} x_2 + k_{y_2} y_2)} \widehat{\Psi}_{in}(k_{x_2}, k_{y_2}). \quad (7b)$$

By substituting the above expressions into Eq. (6), one can obtain the cross–spectral density in terms of the input cross–spectral density as [17]:

$$W_{out} = \frac{1}{(2\pi)^2} \iiiint_{-\infty}^{\infty} dk_{x_1} dk_{y_1} dk_{x_2} dk_{y_2} T^*(k_{x_1}, k_{y_1})$$
$$\times T(k_{x_2}, k_{y_2}) e^{[i^*(k_{x_1} x_1 + k_{y_1} y_1) + i(k_{x_2} x_2 + k_{y_2} y_2)]}$$
$$\times \left\langle \widehat{\Psi}^*_{in}(k_{x_1}, k_{y_1}) \widehat{\Psi}_{in}(k_{x_2}, k_{y_2}) \right\rangle_\omega . \quad (8)$$

Eq. (8) can be visualized pictorially in the diagram shown in Fig. 2. In the present we consider input wave–fields that are described by the "phase object approximation" which by definition are wave–fields that only vary in phase but not in amplitude, that is $\Psi_{in}(x, y) = e^{i\phi_{in}(x,y)}$, this way our final expression will be a series of terms which have operations on the input phase $\phi_{in}(x, y)$ which

is a real function. Later in the paper we generalize to include absorption. Expanding the complex exponential in this expression as a Taylor series, which implies no loss of generality on account of the infinite radius of convergence of this series, we obtain:

$$\Psi_{in}(x, y) = 1 + \sum_{p=1}^{\infty} \frac{i^p}{p!} \phi^p_{in}(x, y). \quad (9)$$

Taking the Fourier transform of the above expression with respect to x and y, we can then write down the following expressions for the terms $\widehat{\Psi}^*_{in}(k_{x_1}, k_{y_1})$ and $\widehat{\Psi}_{in}(k_{x_2}, k_{y_2})$ in Eq. (8):

$$\widehat{\Psi}^*_{in}(k_{x_1}, k_{y_1}) = \delta(k_{x_1}, k_{y_1}) + \sum_{p=1}^{\infty} \frac{(i^p)^*}{p!} \widehat{\phi^p_{in}}^*(k_{x_1}, k_{y_1}), \quad (10a)$$

$$\widehat{\Psi}_{in}(k_{x_2}, k_{y_2}) = \delta(k_{x_2}, k_{y_2}) + \sum_{q=1}^{\infty} \frac{i^q}{q!} \widehat{\phi^p_{in}}(k_{x_2}, k_{y_2}), \quad (10b)$$

where $\delta(k_x, k_y)$ denotes the Dirac delta.

We may also write:

$$T^*(k_{x_1}, k_{y_1}) = 1 + i^* \sum_{m,n=0}^{\infty} \alpha^*_{mn} k_{x_1}^m k_{y_1}^n, \quad (11a)$$

$$T(k_{x_2}, k_{y_2}) = 1 + i \sum_{\gamma,\nu=0}^{\infty} \alpha_{\gamma\nu} k_{x_2}^\gamma k_{y_2}^\nu. \quad (11b)$$

We now substitute Eqs. (10a), (10b), (11a) and (11a) into Eq. (8) and expand. A total of sixteen terms appear in the expansion making it a very lengthy expression to display, however similar mathematical manipulation is performed in each term which can be illustrated by using one term as an example. The longest term that appears is

$$\left\langle \sum_{p,q,m,n,\gamma,\nu=1}^{\infty} \frac{(i^{p+1})^* i^{q+1} \alpha^*_{mn} \alpha_{\gamma\nu}}{p! q! (i^{m+n})^* (i^{\gamma+\nu})} \right.$$
$$\frac{1}{2\pi} \iint_{-\infty}^{\infty} dk_{x_1} dk_{y_1} (i^* k_{x_1})^m (i^* k_{y_1})^n e^{[i^*(k_{x_1} x_1 + k_{y_1} y_1)]}$$
$$\times \widehat{\phi^p_{in}}^*(k_{x_1}, k_{y_1})$$
$$\frac{1}{2\pi} \iint_{-\infty}^{\infty} dk_{x_2} dk_{y_2} (i k_{x_2})^\gamma (i k_{y_2})^\nu e^{[i(k_{x_2} x_2 + k_{y_2} y_2)]}$$
$$\left. \times \widehat{\phi^q_{in}}(k_{x_2}, k_{y_2}) \right\rangle_\omega . \quad (12)$$

By the Fourier derivative theorem [14], the terms $(i^* k_{x_1})^m (i^* k_{y_1})^n e^{[i^*(k_{x_1} x_1 + k_{y_1} y_1)]}$ and

$(ik_{x_2})^\gamma (ik_{y_2})^\nu e^{[i(k_{x_2}x_2 + k_{y_2}y_2)]}$ inside the double integrals can be expressed as $\partial_{x_1}^m \partial_{y_1}^n e^{[i^*(k_{x_1}x_1 + k_{y_1}y_1)]}$ and $\partial_{x_2}^\gamma \partial_{y_2}^\nu e^{[i(k_{x_2}x_2 + k_{y_2}y_2)]}$ respectively. The symbols $\partial_{x_1}^m$, $\partial_{y_1}^n$, $\partial_{x_2}^\gamma$ and $\partial_{y_2}^\nu$ denote partial derivatives with respect to the variables x_1, y_1, x_2 and y_2 and the indices m, n, γ and ν are positive integers that denote the order of differentiation. With this re–expression we see that the integrals represent the inverse Fourier transforms of the functions $\partial_{x_1}^m \partial_{y_1}^n \widehat{\phi_{in}^p}(k_{x_1}, k_{y_1})$ and $\partial_{x_2}^\gamma \partial_{y_2}^\nu \widehat{\phi_{in}^q}(k_{x_2}, k_{y_2})$ and hence the entire term in Eq. (12) simplifies to

$$\sum_{p,q,m,n,\gamma,\nu=1}^{\infty} \frac{(i^{p+1})^* i^{q+1} \alpha_{mn}^* \alpha_{\gamma\nu}}{p! q! (i^{m+n})^* (i^{\gamma+\nu})}$$
$$\times \left\langle [\partial_{x_1}^m \partial_{y_1}^n \phi_{in}^p(x_1, y_1)][\partial_{x_2}^\gamma \partial_{y_2}^\nu \phi_{in}^q(x_2, y_2)] \right\rangle_\omega .$$

$$(13)$$

Using similar mathematical manipulation and logic used to get from Eq. (12) to (13) and applying it to all the terms which appear in the expansion of Eq. (8), one finds that the cross–spectral density for a shift–invariant linear system whose transfer function has infinitely many orders of aberrations is:

$$W_{out} = 1 + \sum_{p=1}^{\infty} \frac{(i^p)^*}{p!} \langle \phi_{in}^p(x_1, y_1) \rangle_\omega + \sum_{q=1}^{\infty} \frac{i^q}{q!} \langle \phi_{in}^q(x_2, y_2) \rangle_\omega$$
$$+ \sum_{p,q=1}^{\infty} \frac{(i^p)^* i^q}{p! q!} \langle \phi_{in}^p(x_1, y_1) \phi_{in}^q(x_2, y_2) \rangle_\omega$$
$$+ \sum_{p,m,n=1}^{\infty} \frac{\alpha_{mn}^* (i^{p+1})^*}{p! (i^{m+n})^*} \langle \partial_{x_1}^m \partial_{y_1}^n \phi_{in}^p(x_1, y_1) \rangle_\omega$$
$$+ \sum_{q,\gamma,\nu=1}^{\infty} \frac{\alpha_{\gamma\nu} (i^{q+1})}{q! (i^{\gamma+\nu})}$$
$$\times \langle \partial_{x_2}^\gamma \partial_{y_2}^\nu \phi_{in}^q(x_2, y_2) \rangle_\omega$$
$$+ \sum_{p,q,m,n=1}^{\infty} \frac{\alpha_{mn}^* (i^{p+1})^* i^q}{p! q! (i^{m+n})^*}$$
$$\times \langle [\partial_{x_1}^m \partial_{y_1}^n \phi_{in}^p(x_1, y_1)] \phi_{in}^q(x_2, y_2) \rangle_\omega$$
$$+ \sum_{p,q,\gamma,\nu=1}^{\infty} \frac{\alpha_{\gamma\nu} (i^{p+1})(i^q)^*}{p! q! (i^{\gamma+\nu})}$$
$$\times \langle \phi_{in}^p(x_1, y_1)[\partial_{x_2}^\gamma \partial_{y_2}^\nu \phi_{in}^q(x_2, y_2)] \rangle_\omega$$
$$+ \sum_{p,q,m,n,\gamma,\nu=1}^{\infty} \frac{(i^{p+1})^* i^{q+1} \alpha_{mn}^* \alpha_{\gamma\nu}}{p! q! (i^{m+n})^* (i^{\gamma+\nu})}$$
$$\times \langle [\partial_{x_1}^m \partial_{y_1}^n \phi_{in}^p(x_1, y_1)][\partial_{x_2}^\gamma \partial_{y_2}^\nu \phi_{in}^q(x_2, y_2)] \rangle_\omega .$$

$$(14)$$

This is a key result of the present paper. We speak of it as exhibiting a *generalized form of differential phase contrast*, in the sense that it is a representation in which the transverse derivatives of all orders of the phase distribution of each monochromatic field in the statistical ensemble, which are statistically averaged and weighted in constructing the output cross–spectral density. The weighting coefficients are proportional to the generalized aberration coefficients drawn from the complex set $\{\alpha_{mn}\}$, thereby demonstrating how individual generalized aberration coefficients contribute to particular orders of transverse derivative, of the phase of each monochromatic component in the statistical ensemble.

III. SHIFT–INVARIANT, LINEAR SYSTEMS FOR PARTIALLY COHERENT FIELDS CONSIDERING DIFFERENT TYPES OF SAMPLES USING ONE TRANSVERSE SPATIAL COORDINATE

In this section we will apply the formalism of the preceding section to three different types of sample, starting with samples which satisfy the weak–phase approximation (Sec. III A), followed by samples that satisfy the weak phase–amplitude approximation (Sec. III B) and finally samples made from a single–material which also satisfy the weak phase–amplitude approximation (Sec. III C). In the interests of physical transparency of the resulting expressions, we will drop the number of transverse dimensions from two down to one.

A. Samples that satisfy the weak–phase approximation

The weak–phase approximation implies that when an object is illuminated by a wave–field the object itself causes very small changes in the phase of the incident field, as the scattering effects are relatively weak. We saw how under the "phase object approximation" one may express Ψ_{in} as a Taylor series (see Eq.(9)). In the one–dimensional perfectly coherent case this is written as

$$\Psi_{in}(x) = 1 + \sum_{p=1}^{\infty} \frac{i^p}{p!} \phi_{in}^p(x) \qquad (15)$$

For samples which satisfy the weak–phase approximation, we can ignore anything higher than first–order terms in the phase, that is:

$$\Psi_{in}(x) \approx 1 + i\phi_{in}(x). \qquad (16)$$

Physically, this corresponds to each strictly monochromatic component of the input statistical ensemble having a transverse phase variation whose magnitude is much smaller than one radian. Such a strong limiting assumption of course implies significant loss of generality, a drawback which may be counterpointed with the

very widespread use of the weak phase object approximation in visible–light imaging, x–ray imaging and electron imaging [13, 18].

In most cases relating to weak phase objects including such terms only up to first order in $\phi_{in}(x)$ is acceptable, however when we calculate the cross–spectral density W_{out} we take the product of two wave fields which cause second–order terms in ϕ to appear which cannot be ignored. This simply means expanding sums over p and q in Eq. (14) up until terms that are no higher than second order in ϕ. By doing this the one–dimensional version of the cross–spectral density W_{out} for samples that satisfy the weak–phase approximation is

$$
\begin{aligned}
W_{out} = {} & 1 + i^* \langle \phi_{in}(x_1) \rangle_\omega + i \langle \phi_{in}(x_2) \rangle_\omega \\
& - \frac{1}{2} \langle \phi_{in}^2(x_1) \rangle_\omega - \frac{1}{2} \langle \phi_{in}^2(x_2) \rangle_\omega \\
& + \langle \phi_{in}(x_1)\phi_{in}(x_2) \rangle_\omega \\
& - \sum_{m=1}^{\infty} \left(\frac{\alpha_m}{i^m} \right)^* \langle \partial_{x_1}^m \phi_{in}(x_1) \rangle_\omega \\
& - \sum_{n=1}^{\infty} \left(\frac{\alpha_n}{i^n} \right) \langle \partial_{x_2}^n \phi_{in}(x_2) \rangle_\omega \\
& - \sum_{m=1}^{\infty} \left(\frac{\alpha_m}{i^{m-1}} \right)^* \langle \partial_{x_1}^m \phi_{in}^2(x_1) \rangle_\omega \\
& - \sum_{n=1}^{\infty} \left(\frac{\alpha_n}{i^{n-1}} \right) \langle \partial_{x_2}^n \phi_{in}^2(x_2) \rangle_\omega \\
& + \sum_{m=1}^{\infty} \left(\frac{\alpha_m}{i^{m-1}} \right)^* \langle [\partial_{x_1}^m \phi_{in}(x_1)]\phi_{in}(x_2) \rangle_\omega \\
& + \sum_{n=1}^{\infty} \left(\frac{\alpha_n}{i^{n-1}} \right) \langle \phi_{in}(x_1)[\partial_{x_2}^n \phi_{in}(x_2)] \rangle_\omega \\
& + \sum_{m,n=1}^{\infty} \left(\frac{\alpha_m}{i^m} \right)^* \left(\frac{\alpha_n}{i^n} \right) \\
& \times \langle [\partial_{x_1}^m \phi_{in}(x_1)][\partial_{x_2}^n \phi_{in}(x_2)] \rangle_\omega .
\end{aligned}
$$

$$\tag{17}$$

The associated spectral density $S_{out}(x,\omega) \equiv W_{out}(x,x,\omega)$ is

$$
\begin{aligned}
S_{out} = {} & 1 - 2 \sum_{m=1}^{\infty} \mathrm{Re} \left(\frac{\alpha_m}{i^m} \right) \langle \partial_x^m \phi_{in}(x) \rangle_\omega \\
& - 2 \sum_{m=1}^{\infty} \mathrm{Re} \left(\frac{\alpha_m}{i^{m-1}} \right) \langle \partial_x^m \phi_{in}^2(x) \rangle_\omega \\
& + 2 \sum_{m=1}^{\infty} \mathrm{Re} \left(\frac{\alpha_m}{i^{m-1}} \right) \langle [\partial_x^m \phi_{in}(x)]\phi_{in}(x) \rangle_\omega \\
& + \sum_{m,n=1}^{\infty} \left(\frac{\alpha_m}{i^m} \right)^* \left(\frac{\alpha_n}{i^n} \right) \\
& \times \langle [\partial_x^m \phi_{in}(x)][\partial_x^n \phi_{in}(x)] \rangle_\omega .
\end{aligned}
$$

$$\tag{18}$$

Our earlier comments regarding generalized phase contrast are also applicable here. Thus, for the case of weak phase objects imaged by an aberrated linear shift–invariant optical system, the output spectral density consists of a weighted sum of various orders of transverse derivative of the phases of each component of each strictly monochromatic member of the statistical ensemble quantifying the input stochastic process. The associated weighting coefficients are again proportional to the real or imaginary parts of the generalized aberration coefficients given by the complex set $\{\alpha_{mn}\}$.

If we ignore terms in Eq. (18) that are higher than first order in ϕ and assume a perfectly coherent field (i.e. no ensemble average is required) then this equation reduces to the one dimensional form of the expression derived in the paper by Paganin and Gureyev [2] for linear shift–invariant imaging systems for fully coherent fields given by:

$$
S_{out} = 1 - 2 \sum_{m=1}^{\infty} \mathrm{Re} \left(\frac{\alpha_m}{i^m} \right) \partial_x^m \phi_{in}(x).
$$

$$\tag{19}$$

Some interesting effects result when terms higher than first order in $\phi_{in}(x)$ are retained. For example, if we truncate Eq. (18) up to $m = 1$ and $n = 1$ the spectral density becomes

$$
\begin{aligned}
S_{out} = {} & 1 - 2\mathrm{Re} \left(\frac{\alpha_1}{i} \right) \langle \partial_x \phi_{in}(x) \rangle_\omega - 2\mathrm{Re}(\alpha_1) \langle \partial_x \phi_{in}^2(x) \rangle_\omega \\
& + 2\mathrm{Re}(\alpha_1) \langle [\partial_x \phi_{in}(x)]\phi_{in}(x) \rangle_\omega \\
& + |\alpha_1|^2 \langle [\partial_x \phi_{in}(x)][\partial_x \phi_{in}(x)] \rangle_\omega .
\end{aligned}
$$

$$\tag{20}$$

Here we have explicitly chosen a system that only displays first derivative contrast in the phase ϕ. Now notice how invoking the product rule one may rewrite certain terms such as $\partial_x \phi_{in}^2 = 2[\partial_x \phi_{in}]\phi_{in}$ and $[\partial_x \phi_{in}][\partial_x \phi_{in}] = \partial_x([\partial_x \phi_{in}]\phi_{in}) - [\partial_x^2 \phi]\phi$ which makes Eq. (20) appear as

$$S_{out} = 1 - 2\text{Re}\left(\frac{\alpha_1}{i}\right) \langle \partial_x \phi_{in}(x) \rangle_\omega$$
$$-2\text{Re}(\alpha_1) \langle [\partial_x \phi_{in}(x)]\phi_{in}(x) \rangle_\omega$$
$$+ |\alpha_1|^2 \langle \partial_x \{[\partial_x \phi_{in}(x)]\phi_{in}(x)\} \rangle_\omega$$
$$- |\alpha_1|^2 \langle [\partial_x^2 \phi_{in}(x)]\phi_{in}(x) \rangle_\omega .$$

$$(21)$$

Notice how the final term yields a second derivative in the ensemble of phases. This is popularly referred to in the imaging field as "Laplacian contrast" [9]. It is surprising that even though the system in Eq. (21) has been restricted to tilt aberrations α_1 of first order that Laplacian contrast still arises.

B. Samples that satisfy the weak phase–amplitude approximation

The next class of samples considered are those which satisfy the weak phase–amplitude approximation. This approximation takes into consideration the variations in both amplitude and phase that the wave–field incurs as it travels though the sample. Again, since we are working under the space–frequency description of partial coherence, these statements apply to each strictly monochromatic component of the illuminating beam which is elastically scattered by the sample to yield the ensemble of monochromatic fields which is input into the shift invariant linear imaging system.

Bearing the above in mind, the weak phase–amplitude approximation corresponds to the sample's scattering and absorptive properties being weak in the sense of the first Born approximation. For samples that induce changes in both phase and amplitude the one dimensional wave–field exiting is expressed as [13]:

$$\Psi_{in}(x) \equiv \exp[i\phi_{in}(x) - \mu_{in}(x)]. \quad (22)$$

The real function function $\mu_{in}(x)$ is related to the transverse variations in intensity and like $\phi_{in}(x)$ it is also a real function. It again proves convenient to express exponential functions as a Taylor series. In this case $\Psi_{in}(x)$ is given by

$$\Psi_{in}(x) = 1 + \sum_{p=1}^\infty \frac{[i\phi_{in}(x) - \mu_{in}(x)]^p}{p!}. \quad (23)$$

Like the weak–phase object approximation the weak phase–amplitude approximation also involves ignoring higher than first order terms allowing the wave–field to be expressed as

$$\Psi_{in}(x) \approx 1 + i\phi_{in}(x) - \mu_{in}(x). \quad (24)$$

Now, to obtain W_{out} one simply needs to replace the terms $\phi_{in}(x_1)$ and $\phi_{in}(x_2)$ with $i\phi_{in}(x_1) - \mu_{in}(x_1)$ and $i\phi_{in}(x_2) - \mu_{in}(x_2)$ in Eq. (17), respectively. Note that second–order terms need to be included for the same reasons argued for the weak–phase approximation. Once we have W_{out} then set $x_1 = x_2 = x$ to obtain an expression for the spectral density $S_{out}(x, \omega)$ for samples that are weak in phase and amplitude variations. In this case the spectral density is given by the following expression which again demonstrates generalized differential phase contrast in the sense defined earlier:

$$S_{out} = 1 - 2\langle \mu_{in}(x) \rangle_\omega - 2\sum_{m=1}^\infty \text{Re}\left(\frac{\alpha_m}{i^m}\right) \langle \partial_x^m \phi_{in}(x) \rangle_\omega$$

$$-2\sum_{m=1}^\infty \text{Re}\left(\frac{\alpha_m}{i^{m-1}}\right) \langle \partial_x^m \mu_{in}(x) \rangle_\omega$$

$$-2\sum_{m=1}^\infty \text{Re}\left(\frac{\alpha_m}{i^{m-1}}\right) \langle \partial_x^m \phi_{in}^2(x) \rangle_\omega$$

$$+2\sum_{m=1}^\infty \text{Re}\left(\frac{\alpha_m}{i^{m-1}}\right) \langle \partial_x^m \mu_{in}^2(x) \rangle_\omega$$

$$+6\sum_{m=1}^\infty \text{Re}\left(\frac{\alpha_m}{i^{m-2}}\right) \langle [\partial_x^m \phi_{in}(x)]\mu_{in}(x) \rangle_\omega$$

$$+2\sum_{m=1}^\infty \text{Re}\left(\frac{\alpha_m}{i^{m-1}}\right) \langle [\partial_x^m \phi_{in}(x)]\phi_{in}(x) \rangle_\omega$$

$$+2\sum_{m=1}^\infty \text{Re}\left(\frac{\alpha_m}{i^{m-2}}\right) \langle [\partial_x^m \mu_{in}(x)]\phi_{in}(x) \rangle_\omega$$

$$+2\sum_{m=1}^\infty \text{Re}\left(\frac{\alpha_m}{i^{m-1}}\right) \langle [\partial_x^m \mu_{in}(x)]\mu_{in}(x) \rangle_\omega$$

$$+\sum_{m,n=1}^\infty \left(\frac{\alpha_m}{i^m}\right)^* \left(\frac{\alpha_n}{i^n}\right) \langle [\partial_x^m \phi_{in}(x)][\partial_x^n \phi_{in}(x)] \rangle_\omega$$

$$+\sum_{m,n=1}^\infty \left(\frac{\alpha_m}{i^m}\right)^* \left(\frac{\alpha_n}{i^n}\right) \langle [\partial_x^m \mu_{in}(x)][\partial_x^n \mu_{in}(x)] \rangle_\omega .$$

$$(25)$$

Similar to the previous case if second order terms in ϕ and μ are neglected and we remove the angular brackets assuming a fully coherent wave then Eq. (25) reduces to the one derived in Paganin and Gureyev [2] when dealing with the weak phase–amplitude approximation, namely:

$$S_{out} = 1 - 2\mu_{in}(x) - 2\sum_{m=1}^\infty \text{Re}\left(\frac{\alpha_m}{i^m}\right) \partial_x^m \phi_{in}(x)$$

$$-2\sum_{m=1}^\infty \text{Re}\left(\frac{\alpha_m}{i^{m-1}}\right) \partial_x^m \mu_{in}(x).$$

$$(26)$$

C.   Single–material samples that satisfy the weak phase–amplitude approximation

The final kind of sample that we consider is those that are comprised of a single material and also have the transverse phase and intensity variations of the wave–field being small as it travels though the sample. Utilizing terminology commonly used by the x–ray optics community, assume that the single–material sample has a constant complex refractive index [14]:

$$n = 1 - \delta + i\beta. \tag{27}$$

If the projected thickness along the orientation of a particular direction of propagation for paraxial illumination is denoted as $T_{proj}(x)$, then the real numbers δ and β are related to functions $\phi_{in}(x)$ and $\mu_{in}(x)$ via [14]:

$$\phi_{in}(x) = -k\delta T_{proj}(x), \tag{28a}$$
$$\mu_{in}(x) = \beta k T_{proj}(x). \tag{28b}$$

Here, k is the radiation wavenumber corresponding to the wavelength λ. This permits us to write the input wave–field as

$$\Psi_{in}(x) = \exp[k(\beta - i\delta)T_{proj}(x)], \tag{29}$$

Under the single–material weak phase–amplitude object approximation $\Psi_{in}(x)$ is approximated as

$$\Psi_{in}(x) = \exp[k(\beta - i\delta)T_{proj}(x)]$$
$$\approx 1 - k(\beta - i\delta)T_{proj}(x). \tag{30}$$

Here we see that the "single–material weak phase–amplitude object approximation" is none other than the "weak phase–amplitude object approximation" that uses that fact that when a weak object is made out of only one material the functions $\phi_{in}(x)$ and $\mu_{in}(x)$ become proportional to each other. Bearing this in mind, to obtain an expression for the spectral density $S_{out}(x)$ for systems that are linear and shift–invariant when the object under study satisfies the "single–material weak phase–amplitude object approximation" all that is needed is to replace $\phi_{in}(x)$ and $\mu_{in}(x)$ in Eq.(25) with $-k\delta T_{proj}(x)$ and $\beta k T_{proj}(x)$ respectively to yield

$$S_{out} = 1 - 2\beta k \langle T_{proj}(x) \rangle_\omega$$
$$-2 \sum_{m=1}^{\infty} \mathrm{Re} \left[\frac{\alpha_m k(i\beta + \delta)}{i^m} \right] \langle \partial_x^m T_{proj}(x) \rangle_\omega$$
$$+2 \sum_{m=1}^{\infty} \mathrm{Re} \left[\frac{\alpha_m k(\delta + \beta)}{i^{m-1}} \right] \langle \partial_x^m T_{proj}^2(x) \rangle_\omega$$
$$+2 \sum_{m=1}^{\infty} \mathrm{Re} \left[\frac{\alpha_m k^2(4\delta - \beta^2 + i\delta^2)}{i^m} \right]$$
$$\times \langle [\partial_x^m T_{proj}(x)] T_{proj}(x) \rangle_\omega$$
$$+ \sum_{m,n=1}^{\infty} \sigma \left(\frac{\alpha_m}{i^m} \right)^* \left(\frac{\alpha_n}{i^n} \right)$$
$$\times \langle [\partial_x^m T_{proj}(x)][\partial_x^n T_{proj}(x)] \rangle_\omega, \tag{31}$$

where $\sigma = k^2(\delta + \beta)$, and ensemble averages are take over the sample projected thickness (i.e. $\langle T_{proj}(x) \rangle_\omega$). This implies taking the average sum of projected path integrals along the sample over a range of angular orientations, for the case where the incident ensemble of monochromatic fields consist of a set of plane waves. We see that the single–material assumption significantly simplifies the expression for the spectral density S_{out}. One of the advantages about making the "single–material weak phase–amplitude object approximation" is that it allows one to relate the measured image directly to morphological detail of the sample bypassing the idea of ensembles of phase maps. For instance take a special case of Eq. (31) where the system has a finite set of non–vanishing aberrations (all of which are known 'a priori'), and we take the spectral density S_{out} to be the measured quantity, leaving $\langle T_{proj}(x) \rangle_\omega$ as the unknown variable. This effectively brings about an inverse problem, where from an aberrated image one seeks to infer information about the size of sample. This is very common in the imaging world and can be related to the technique known as "phase retrieval", which as the name says involves retrieving the phase ϕ of the wave–field Ψ once the field has travelled through the sample from either one or multiple intensity measurements. Usually this is done using some iterative or non–iterative algorithm and in most cases a perfectly coherent monochromatic wave–field is assumed. In the context of this paper we see that the idea of "phase retrieval" is somewhat redundant since we have considered wave–fields that are partially coherent and that therefore do not have a characteristic phase ϕ but rather have a statistical signature $\langle \partial_x^m \phi_{in} \rangle_\omega$. This, highlights the importance of Eq. (31) as it makes more sense to want to recover information about the morphology of the imaged sample as opposed to phase ϕ of a wave–field technically the latter does not exist in the context of partial coherence [19].

IV. THE TRANSFER FUNCTION FOR SHIFT–INVARIANT LINEAR SYSTEMS WITH INFINITELY MANY ORDERS OF ABERRATIONS

The transfer function formalism to study image formation is widely used to describe optical systems. This section discusses in detail the properties and characteristics of the transfer function used in the development of this theory (see Eq. (3)). The expressions for spectral densities for all three types of sample are derived under the Taylor series form of the transfer function which is written in terms of the coefficients α_m. For this reason, it is important to state that actual aberration coefficients, namely those directly corresponding to the seidel aberrations, are those denoted by $\widetilde{\alpha}_m$. For example, $\widetilde{\alpha}_2$ is directly proportional to defocus "z" as is $\widetilde{\alpha}_4$ to spherical aberration [2] "C_s". The main goal of this section will be to illustrate to the reader how we are able to express the transfer function as a Taylor–series expansion, which, eventually will lead us to another problem in finding a standard formula on how to relate the coefficients α_m to the aberration coefficients $\widetilde{\alpha}_m$, a problem which is solved using a combinatorial approach. Also, we will continue to use only one spatial dimension as in Sec. III in order to keep all mathematical manipulations simple.

We begin by re–stating the transfer function in one spatial dimension

$$T(k_x) = \exp\left(i \sum_{m=0}^{\infty} \widetilde{\alpha}_m k_x^m\right) \tag{32}$$

We remind the reader that the set of complex numbers $\{\widetilde{\alpha}_m\}$ are labelled here as "aberration coefficients" whose object is to characterise a particular state of the linear imaging system. Each such coefficient is denoted

$$\widetilde{\alpha}_m \equiv \widetilde{\alpha}_m^{(R)} + i\widetilde{\alpha}_m^{(I)}, \tag{33}$$

where $\widetilde{\alpha}_m^{(R)}$ denotes the real part and $\widetilde{\alpha}_m^{(I)}$ denotes the imaginary part. It was assumed in Paganin and Gureyev [2] that at the Fourier–space origin the transfer function must equal unity, that is $T(k_x = 0) = 1$. Such an assumption implies a trivial loss of generality for all systems that posses a transfer function that does not vanish at the Fourier space origin. Also under this assumption we may set $\widetilde{\alpha}_0 = 0$.

Now, we want to represent Eq. (32) as a Taylor–series, something that in Paganin and Gureyev [2] was only stated but not shown. Here, we provide a more detailed explanation of how this is achieved. Firstly, let the entire sum in Eq. (32) be labelled $X \equiv i \sum_{m=1}^{\infty} \widetilde{\alpha}_m k_x^m$. The Taylor–series of an exponential function is given by

$$e^X = 1 + \sum_{l=1}^{\infty} \frac{X^l}{l!}, \tag{34}$$

where, l is also a non–negative integer $l = 1, 2, \dots$. If we now substitute $X \equiv i \sum_{m=1}^{\infty} \widetilde{\alpha}_m k_x^m$ then Eq. (32) becomes

$$T(k_x) = 1 + i \sum_{l=1}^{\infty} \frac{i^{l-1}}{l!} \left(\sum_{m=1}^{\infty} \widetilde{\alpha}_m k_x^m\right)^l. \tag{35}$$

Notice how now we have commenced the summation from $m = 1$. This is due to assumption made earlier that $T(k_x = 0) = 1$ which in turn allowed to set $\widetilde{\alpha}_0 = 0$. Writing the summation $\sum_{m=1}^{\infty} \widetilde{\alpha}_m k_x^m$ explicitly we get

$$T(k_x) = 1 + i \sum_{l=1}^{\infty} \frac{i^{l-1}}{l!} \left(\widetilde{\alpha}_1 k_x + \widetilde{\alpha}_2 k_x^2 + \widetilde{\alpha}_3 k_x^3 + \widetilde{\alpha}_4 k_x^4 + \cdots\right)^l \tag{36}$$

We now turn our focus to the summation in Eq. (36). If one writes down the first few l terms, say $l = 1, 2, 3, 4$, it can be seen that all the common powers of k_x can be collected. For example:

$$l = 1, \quad \left(\widetilde{\alpha}_1 k_x + \widetilde{\alpha}_2 k_x^2 + \widetilde{\alpha}_3 k_x^3 + \widetilde{\alpha}_4 k_x^4 + \cdots\right)^1$$
$$l = 2, \quad + \frac{i}{2!} \left(\widetilde{\alpha}_1 k_x + \widetilde{\alpha}_2 k_x^2 + \widetilde{\alpha}_3 k_x^3 + \widetilde{\alpha}_4 k_x^4 + \cdots\right)^2$$
$$l = 3, \quad - \frac{1}{3!} \left(\widetilde{\alpha}_1 k_x + \widetilde{\alpha}_2 k_x^2 + \widetilde{\alpha}_3 k_x^3 + \widetilde{\alpha}_4 k_x^4 + \cdots\right)^3$$
$$l = 4, \quad - \frac{-i}{4!} \left(\widetilde{\alpha}_1 k_x + \widetilde{\alpha}_2 k_x^2 + \widetilde{\alpha}_3 k_x^3 + \widetilde{\alpha}_4 k_x^4 + \cdots\right)^4. \tag{37}$$

Once we collect all the common powers of k_x we see that the entire summation in Eq. (36) can be expressed in the alternative form

$$\overbrace{(\widetilde{\alpha}_1)}^{\alpha_1} k_x + \overbrace{(\widetilde{\alpha}_2 + \frac{i}{2}\widetilde{\alpha}_1^2)}^{\alpha_2} k_x^2 + \overbrace{(\widetilde{\alpha}_3 + i\widetilde{\alpha}_1\widetilde{\alpha}_2 - \frac{1}{6}\widetilde{\alpha}_1^3)}^{\alpha_3} k_x^3 +$$
$$\overbrace{(\widetilde{\alpha}_4 + i\widetilde{\alpha}_1\widetilde{\alpha}_3 + \frac{i}{2}\widetilde{\alpha}_2^2 - \frac{1}{2}\widetilde{\alpha}_1^2\widetilde{\alpha}_2 - \frac{i}{24}\widetilde{\alpha}_1^4)}^{\alpha_4} k_x^4 + \cdots = \sum_{l=1}^{\infty} \alpha_l k_x^l. \tag{38}$$

These mathematical manipulations reveal that we are able to represent the transfer function as the following Taylor–series.

$$T(k_x) = 1 + i \sum_{m=1}^{\infty} \alpha_m k_x^m \tag{39}$$

We have re–labelled the non–negative integer l with m in order to remain consistent with our original notation. Also, notice that each α_m term is composed of a finite series of $\widetilde{\alpha}_m$ terms where the higher the order of m the higher number the of terms that will appear. The fact

that the series are finite turns out to be advantageous. On this note we see that another problem arises, that is, if one is dealing with aberrations that are higher in order than say α_5, we saw from the above examples that computing all its terms in the series this can be tedious. This motivates us to seek a Standard Series Formula which can allow us to calculate any α_m for this problem by simply substituting fixed parameters to avoid such lengthy and tedious computations. This can be achieved if one visualises the problem as a combinatorial one. The first indication that tells us that this is solved combinatorially is when the term $\left(\widetilde{\alpha}_1 k_x + \widetilde{\alpha}_2 k_x^2 + \widetilde{\alpha}_3 k_x^3 + \cdots\right)^l$ arises where we see that this is none other than a multinomial expansion which reveals its combinatorial nature. From this we can deduce that the terms in the series will have coefficients which can be calculated with the multinomial coefficients formula

$$\binom{v}{m_1, m_2, \cdots, m_j} = \frac{v!}{m_1! m_2! \cdots m_j!}. \qquad (40)$$

Notice that for any α_m we find that the sum of the exponent times its subscript in each of its corresponding $\widetilde{\alpha}$ terms will always be equal. For instance take $\alpha_3 = \widetilde{\alpha}_3 + i\widetilde{\alpha}_1\widetilde{\alpha}_2 - \frac{1}{6}\widetilde{\alpha}_1^3$; each of its $\widetilde{\alpha}$ terms in the expansion can be written as $\widetilde{\alpha}_3^1$, $\widetilde{\alpha}_1^1\widetilde{\alpha}_2^1$ and $\widetilde{\alpha}_1^3$. Now notice how the sum of the product of the exponents times its subscript for each term all equate to 3, we have $\widetilde{\alpha}_3^1$ $(1 \times 3 = 3)$, $\widetilde{\alpha}_1^1\widetilde{\alpha}_2^1$ $(1 \times 1 + 1 \times 2 = 3)$ and $\widetilde{\alpha}_1^3$ $(3 \times 1 = 3)$. If we do this for any α_m this condition will still hold.

Now our next step is to try to decode a particular pattern for any α_m series. Let's focus on $\alpha_2 = \widetilde{\alpha}_2 + \frac{i}{2}\widetilde{\alpha}_1^2$. Here we can see that the highest power is 2 and therefore one can also deduce that the highest power for any $\widetilde{\alpha}$ is never greater than m. We know that each expansion has a combinatorial nature so let's consider the terms that compose α_2 are elements from the set $\{\widetilde{\alpha}_1, \widetilde{\alpha}_2\}$ and its corresponding exponents are combinations from the set $\{0, 1, 2\}$. We also see that the coefficients will be given by the multinomial coefficients formula. If we write down all possible combinations with their corresponding coefficients it displays as

$$\overset{0(1)+0(2)=0}{\frac{i^{-1}}{0!}\binom{0}{0,0}\widetilde{\alpha}_1^0\widetilde{\alpha}_2^0} + \overset{0(1)+1(2)=2}{\frac{i^0}{1!}\binom{1}{0,1}\widetilde{\alpha}_1^0\widetilde{\alpha}_2^1} + \overset{1(1)+0(2)=1}{\frac{i^0}{1!}\binom{1}{1,0}\widetilde{\alpha}_1^1\widetilde{\alpha}_2^0}$$
$$+ \overset{0(1)+2(2)=4}{\frac{i}{2!}\binom{2}{0,2}\widetilde{\alpha}_1^0\widetilde{\alpha}_2^2} + \overset{2(1)+0(2)=2}{\frac{i}{2!}\binom{2}{2,0}\widetilde{\alpha}_1^2\widetilde{\alpha}_2^0} + \overset{1(1)+1(2)=3}{\frac{i}{2!}\binom{2}{1,1}\widetilde{\alpha}_1^1\widetilde{\alpha}_2^1}$$
$$(41)$$

As a convenient notation, notice that the sum of the product of the exponents times their corresponding subscripts have been deliberately placed above each combinatorial term. This helps us to see that if we only allow the terms in which the product of the exponents times

their corresponding subscripts equals the order of the coefficient α_m, in this case $m = 2$ and neglect those which do not fulfill this condition then the surviving terms in the expansion will be the following

$$\alpha_2 = \frac{i^0}{1!}\binom{1}{0,1}\widetilde{\alpha}_1^0\widetilde{\alpha}_2^1 + \frac{i}{2!}\binom{2}{2,0}\widetilde{\alpha}_1^2\widetilde{\alpha}_2^0$$
$$= \widetilde{\alpha}_2 + \frac{i}{2}\widetilde{\alpha}_1^2. \qquad (42)$$

Notice how applying this fusion of combinatorics and pattern decoding has arrived at the same answer for the α_2 terms in Eq. (38). Now, we can employ the same strategy for $\alpha_3 = \widetilde{\alpha}_3 + i\widetilde{\alpha}_1\widetilde{\alpha}_2 - \frac{1}{6}\widetilde{\alpha}_1^3$ where now all the terms are elements from the set $\{\widetilde{\alpha}_1, \widetilde{\alpha}_2, \widetilde{\alpha}_3\}$ and its exponents are combinations from the set $\{0, 1, 2, 3\}$. Writing down the possible combinations will give

$$\overset{0(1)+0(2)+0(3)=0}{\frac{i^{-1}}{0!}\binom{0}{0,0,0}\widetilde{\alpha}_1^0\widetilde{\alpha}_2^0\widetilde{\alpha}_3^0} + \overset{1(1)+0(2)+0(3)=1}{\frac{i^0}{1!}\binom{1}{1,0,0}\widetilde{\alpha}_1^1\widetilde{\alpha}_2^0\widetilde{\alpha}_3^0} + \overset{0(1)+1(2)+0(3)=2}{\frac{i^0}{1!}\binom{1}{0,1,0}\widetilde{\alpha}_1^0\widetilde{\alpha}_2^1\widetilde{\alpha}_3^0}$$
$$+ \overset{0(1)+0(2)+1(3)=3}{\frac{i^0}{1!}\binom{1}{0,0,1}\widetilde{\alpha}_1^0\widetilde{\alpha}_2^0\widetilde{\alpha}_3^1} + \overset{2(1)+0(2)+0(3)=2}{\frac{i^1}{2!}\binom{2}{2,0,0}\widetilde{\alpha}_1^2\widetilde{\alpha}_2^0\widetilde{\alpha}_3^0} + \overset{0(1)+2(2)+0(3)=4}{\frac{i^1}{2!}\binom{2}{0,2,0}\widetilde{\alpha}_1^0\widetilde{\alpha}_2^2\widetilde{\alpha}_3^0}$$
$$+ \overset{0(1)+0(2)+2(3)=6}{\frac{i^1}{2!}\binom{2}{0,0,2}\widetilde{\alpha}_1^0\widetilde{\alpha}_2^0\widetilde{\alpha}_3^2} + \overset{1(1)+1(2)+0(3)=3}{\frac{i^1}{2!}\binom{2}{1,1,0}\widetilde{\alpha}_1^1\widetilde{\alpha}_2^1\widetilde{\alpha}_3^0} + \overset{1(1)+0(2)+1(3)=4}{\frac{i^1}{2!}\binom{2}{1,0,1}\widetilde{\alpha}_1^1\widetilde{\alpha}_2^0\widetilde{\alpha}_3^1}$$
$$+ \overset{0(1)+1(2)+1(3)=5}{\frac{i^1}{2!}\binom{2}{0,1,1}\widetilde{\alpha}_1^0\widetilde{\alpha}_2^1\widetilde{\alpha}_3^1} + \overset{3(1)+0(2)+0(3)=3}{\frac{i^2}{3!}\binom{3}{3,0,0}\widetilde{\alpha}_1^3\widetilde{\alpha}_2^0\widetilde{\alpha}_3^0} + \overset{0(1)+3(2)+0(3)=6}{\frac{i^2}{3!}\binom{3}{0,3,0}\widetilde{\alpha}_1^0\widetilde{\alpha}_2^3\widetilde{\alpha}_3^0}$$
$$+ \overset{0(1)+0(2)+3(3)=9}{\frac{i^2}{3!}\binom{3}{0,0,3}\widetilde{\alpha}_1^0\widetilde{\alpha}_2^0\widetilde{\alpha}_3^3} + \overset{1(1)+1(2)+1(3)=6}{\frac{i^2}{3!}\binom{3}{1,1,1}\widetilde{\alpha}_1^1\widetilde{\alpha}_2^1\widetilde{\alpha}_3^1} + \overset{2(1)+1(2)+0(3)=4}{\frac{i^2}{3!}\binom{3}{2,1,0}\widetilde{\alpha}_1^2\widetilde{\alpha}_2^1\widetilde{\alpha}_3^0}$$
$$+ \overset{2(1)+0(2)+1(3)=5}{\frac{i^2}{3!}\binom{3}{2,0,1}\widetilde{\alpha}_1^2\widetilde{\alpha}_2^0\widetilde{\alpha}_3^1} + \overset{1(1)+2(2)+0(3)=5}{\frac{i^2}{3!}\binom{3}{1,2,0}\widetilde{\alpha}_1^1\widetilde{\alpha}_2^2\widetilde{\alpha}_3^0} + \overset{1(1)+0(2)+2(3)=7}{\frac{i^2}{3!}\binom{3}{1,0,2}\widetilde{\alpha}_1^1\widetilde{\alpha}_2^0\widetilde{\alpha}_3^2}$$
$$+ \overset{0(1)+1(2)+2(3)=8}{\frac{i^2}{3!}\binom{3}{0,1,2}\widetilde{\alpha}_1^0\widetilde{\alpha}_2^1\widetilde{\alpha}_3^2}$$
$$(43)$$

Like the case for α_2, if we only consider the terms where the sum of the exponents times their corresponding subscript equal $m = 3$ and neglect the rest then the only terms which survive are

$$\alpha_3 = \overset{0(1)+0(2)+1(3)=3}{\frac{i^0}{1!}\binom{0}{0,0,1}\widetilde{\alpha}_1^0\widetilde{\alpha}_2^0\widetilde{\alpha}_3^1} + \overset{1(1)+1(2)+0(3)=3}{\frac{i^1}{2!}\binom{2}{1,1,0}\widetilde{\alpha}_1^1\widetilde{\alpha}_2^1\widetilde{\alpha}_3^0}$$
$$+ \overset{3(1)+0(2)+0(3)=3}{\frac{i^2}{3!}\binom{3}{3,0,0}\widetilde{\alpha}_1^3\widetilde{\alpha}_2^0\widetilde{\alpha}_3^0}$$
$$= \widetilde{\alpha}_3 + i\widetilde{\alpha}_1\widetilde{\alpha}_2 - \frac{1}{6}\widetilde{\alpha}_1^3$$
$$(44)$$

By extending the above logic one is able deduce the following standard formula to compute any α_m:

$$\alpha_m = \sum_v^m \sum_{m_1+m_2+...+m_j=v} \frac{i^{v-1}}{v!} \begin{pmatrix} v \\ m_1, m_2, \cdots, m_j \end{pmatrix}$$
$$\widetilde{\alpha}_1^{m_1} \widetilde{\alpha}_2^{m_2}...\widetilde{\alpha}_j^{m_j}$$
$$\text{where,} \sum_j m_j \times j = m.$$
(45)

Here, $v = 0, 1, 2, ..., m$, $j = 1, 2, ..., m$ and $m_j = 0, 1, 2, ..., m$. To verify this standard formula, we calculate another α_m and see if we arrive at the same result to that obtained by collecting terms as done previously in Eq. (38). We do this by calculating α_4 where according to the set condition one only needs to consider the terms which satisfy $\sum_j m_j \times j = 4$. Below we display all the relevant terms

$$\alpha_4 = \frac{i^0}{1!} \overset{0(1)+0(2)+0(3)+1(4)=4}{\begin{pmatrix} 1 \\ 0,0,0,1 \end{pmatrix}} \widetilde{\alpha}_1^0 \widetilde{\alpha}_2^0 \widetilde{\alpha}_3^0 \widetilde{\alpha}_4^1 + \frac{i}{2!} \overset{1(1)+0(2)+1(3)+0(4)=4}{\begin{pmatrix} 2 \\ 1,0,1,0 \end{pmatrix}} \widetilde{\alpha}_1^1 \widetilde{\alpha}_2^0 \widetilde{\alpha}_3^1 \widetilde{\alpha}_4^0$$
$$+ \frac{i}{2!} \overset{0(1)+2(2)+0(3)+0(4)=4}{\begin{pmatrix} 2 \\ 0,2,0,0 \end{pmatrix}} \widetilde{\alpha}_1^0 \widetilde{\alpha}_2^2 \widetilde{\alpha}_3^0 \widetilde{\alpha}_4^0 + \frac{i^2}{3!} \overset{2(1)+1(2)+0(3)+0(4)=4}{\begin{pmatrix} 3 \\ 2,1,0,0 \end{pmatrix}} \widetilde{\alpha}_1^2 \widetilde{\alpha}_2^1 \widetilde{\alpha}_3^0 \widetilde{\alpha}_4^0$$
$$+ \frac{i^3}{4!} \overset{4(1)+0(2)+0(3)+0(4)=4}{\begin{pmatrix} 4 \\ 4,0,0,0 \end{pmatrix}} \widetilde{\alpha}_1^4 \widetilde{\alpha}_2^0 \widetilde{\alpha}_3^0 \widetilde{\alpha}_4^0$$
$$= \widetilde{\alpha}_4 + i\widetilde{\alpha}_1 \widetilde{\alpha}_3 + \frac{i}{2}\widetilde{\alpha}_2^2 - \frac{1}{2}\widetilde{\alpha}_1^2 \widetilde{\alpha}_2 - \frac{i}{24}\widetilde{\alpha}_1^4 \qquad (46)$$

The computation above is in agreement with calculating α_4 via the standard formula and the more lengthy method which involves collecting term of k_x^4 powers as was done in Eq. (38).

To end this section we return to the case where the transfer function contains two spatial dimensions transverse to the imaging direction. For such cases the combinatorial analysis is more complex. Nevertheless, using a similar strategy to the one used to formulate the standard formula for the one–dimensional case one is also able to deduce a formula for the more common imaging scenario with two spatial dimensions. Setting $\widetilde{\alpha}_{00} = 0$ yield a "two spatial dimensions standard formula" of the form

$$\alpha_{mn} = \sum_v^{m+n} \sum_{m_{01}+m_{10}+...+m_{j\nu}=v} \frac{i^{v-1}}{v!} \begin{pmatrix} v \\ m_{01}, m_{10}, \cdots, m_{j\nu} \end{pmatrix}$$
$$\widetilde{\alpha}_{01}^{m_{01}} \widetilde{\alpha}_{10}^{m_{10}}...\widetilde{\alpha}_{j\nu}^{m_{j\nu}}$$
$$\text{where,} \sum_{j,\nu} m_{j\nu} \times (j+\nu) = m+n$$
(47)

where $v = 0, 1, 2, ..., m+n$, $j = 0, 1, 2, ..., m$ $\nu = 0, 1, 2, ..., n$ and $m_{j\nu} = 0, 1, 2, ..., m+n$. Since we have set

$\widetilde{\alpha}_{00} = 0$ we must impose the condition that when $j = 0$ then $\nu \neq 0$ and vice versa. It is possible to make further simplification of the formula if rotational symmetry is also assumed (i.e. $\widetilde{\alpha}_{10} = \widetilde{\alpha}_{01}$).

V. DISCUSSION AND SUMMARY

In this work we have treated the problem of aberrations for partially coherent complex scalar wave–fields imaged by optical systems characterized by a transfer function which is both linear and shift–invariant. We have derived expressions for the output cross–spectral density W_{out} using only one spatial variable for samples that satisfy the "phase object approximation", the "weak–phase object approximation", the "weak phase–amplitude approximation" and finally the "single–material weak phase–amplitude approximation". Also, for the three classes of samples mentioned, an expression for the spectral density S_{out} was calculated in which we saw how under certain restrictions the equations reduced to those derived in Paganin and Gureyev [2] where partial coherence is not considered. For the single material case the idea of "phase retrieval" was mentioned, however in the context of partial coherence this was rather redundant but nonetheless gave rise to the idea of carrying out morphological studies of imaged samples partially coherent light and aberrated imaging systems. This idea may have several applications in many areas such as geology, microbiology, material science, etc.

The transfer function was studied where we emphasized how one obtains the coefficients of Taylor–series representation of the transfer function. This lead to a different problem involved finding a standard formula which can allow the calculation of any coefficient α_m in terms of its corresponding aberration coefficients $\widetilde{\alpha_m}$ for an infinite number of aberration orders. This standard formula brings many advantages not only in the sense that it is not limited to a finite order of aberrations but also allows for broader considerations in "aberration balancing". Aberration balancing is the act of seeking certain conditions in which the aberrations present in an optical system are negated by the system itself. To be more concise, one seeks to balance out the aberrations in an optical system against one another. This is somewhat similar to the notion of Scherzer defocus, where defocus is tuned to balance out spherical aberration [20]. For example, consider the spectral density in Eq. (26) for the "weak–phase object approximation" case. Suppose one aimed to find the conditions for which all aberrations present balanced out one another such that the output image displayed only first order differential contrast, that is,

$$S_{out} = 1 - 2 \langle \partial_x \phi_{in}(x) \rangle_\omega . \qquad (48)$$

This would require the following balancing conditions in order to achieve such an output image:

$$\alpha_1^{(I)} = 1, \mathrm{Re}\left(\overset{m \neq 0}{\frac{\alpha_m}{i^m}}\right) = 0, \mathrm{Re}\left(\frac{\alpha_m}{i^{m-1}}\right) = 0,$$
$$\left(\frac{\alpha_m}{i^m}\right)^* \left(\frac{\alpha_n}{i^n}\right) = 0.$$

(49)

For systems with infinitely many aberrations (Eq. (45)) the above balancing equation could be in principle solved with the help of the standard formula without the need for truncating the system.

[1] F. Zernike, "Phase contrast, a new method for the microscopic observation of transparent objects," Physica IX, 7, 686-698, 1942.

[2] D. M. Paganin and T. E. Gureyev, "Phase contrast, phase retrieval and aberration balancing in shift–invariant linear imaging systems," Opt. Commun, 281, 965-981, 2008.

[3] S. W. Wilkins, T. E. Gureyev, D. Gao, A. Pogany and A. W. Stevenson, "Phase contrast imaging using polychromatic hard x-rays," Nature, 384, 335-338, 1996.

[4] E. Förster, K. Goetz and P. Zaumseil, "Double crystal diffractometry for the characterization of targets for laser fusion experiments," Krist. Tech, 15, 937-945, 1980.

[5] D. Gabor, "A New Microscopic Principle," Nature, 161, 777-778, 1948.

[6] J. C. Petruccelli, L. Tian and G. Barbastathis, " The transport of intensity equation for optical path length recovery using partially coherent illumination," Opt. Express, 21, 14430-14441, 2013.

[7] T. Gureyev, "Transport of intensity equation for beams in an arbitrary state of temporal and spatial coherence." Optik, 110, 236-226, 1999.

[8] A. Zysk, R. Schoonover, P. Carney and M. Anastasio, "Transport of intensity and spectrum for partially coherent fields," Opt. Lett, 35, 2239-2241, 2010.

[9] M. R. Teague, "Deterministic phase retrieval: a Green's function solution," J. Opt. Soc. Am, 73, 1434-1441, 1983.

[10] R. H. Goodman, *Introduction to Fourier optics*, (John Wiley & Sons, New York, 1985).

[11] U. Bonse and M. Hart, "An x–ray interferometer," Appl. Phys. Lett, 6, 155-156, 1965.

[12] F. Pfeiffer, T. Weitkamp, O. Bunk, and O. David, "Phase retrieval and differential phase contrast imaging with low-brilliance x–ray sources," Nature, 2, 258-261, 2006.

[13] J. M. Cowley, *Diffraction Physics*, (North-Holland Personal Library, Amsterdam, 1995).

[14] D. Paganin, *Coherent X–ray Optics*, (Oxford University Press, Oxford, 2006).

[15] E. Wolf, "New theory of partial coherence in the space-frequency domain. Part II: Steady-state fields and higher-order correlations," J. Opt. Soc. Am. A, 3, 77-85, 1986.

[16] M. Born and E. Wolf, *Principles of optics*, (Cambridge University Press, Cambridge, 2003).

[17] G. Gbur and T. D. Visser, "Phase singularities and coherence vortices in linear optical systems," Opt. Commun, 259, 428-435, 2006.

[18] P. Cloetens, R. Barrett, J. Baruchel, J. Guigay and M. Schlenker, "Phase objects in synchrotron radiation hard x–ray imaging," J. Phys. D: Appl. Phys, 29, 133-146, 1996.

[19] E. Wolf, "Solution of the phase problem in the theory of structure determination of crystals from x–ray diffraction experiments" Phys. Rev. Lett, 103, 075501, 2009.

[20] O. Scherzer, "The theoretical resolution limit of the electron microscope," J. Appl. Phys, 20, 1949.